Characterisation of the Anisotropic Fracture Toughness and Crack-Tip Shielding Mechanisms in Elephant Dentin

A thesis submitted to the University of Manchester for the degree of Doctor of Philosophy in the Faculty of Engineering and Physical Science

2015

Xuekun Lu

School of Materials Science

Contents

Word Count: 53,888

List of Figures

List of Tables

ABSTRACT

The University of Manchester
Xuekun Lu, PhD in the Faculty of Engineering and Physical Sciences
Characterisation of the Anisotropic Fracture Toughness and Crack-Tip Shielding Mechanisms in Elephant Dentin

Teeth trauma has become one of the most serious physical problems that people are suffering from in the past years. Early diagnosis and management are desperately needed to improve tooth survival, functionality and avoid the tooth loss. However, the diagnosis of cracked tooth could be challenging due to the small size of the crack. Therefore, a mechanics understanding of the tooth fracture is demanding from the perspective of developing a framework for failure prediction in clinical research and bio-mimetic restorative materials.

This study focuses on characterising the anisotropic fracture behaviour and the crack shielding mechanisms in elephant dentin. This is often used as a structural analogue for human dentin due to the similarities in microstructure and chemical composition, in order to avoid the test-piece size restrictions, given the larger size of ivory than human teeth. Compact tension test-pieces were extracted from different locations on the ivory tusk so as to have different crack growth directions relative to the microstructure to inspect the fracture anisotropies. The fracture toughness as a function of the crack extension was assessed in terms of fracture resistance curves (R-curve). The accumulative crack-tip strain fields were also measured for the first time in dentin using digital image correlation technique (DIC) to investigate the capability of crack-tip elastic/plastic deformation before material failure. Investigation of crack morphologies, the interaction between crack and the microstructures, the fracture surfaces using both 2-D and 3-D techniques could provide with insights into extrinsic shielding mechanisms.

Surface and volume crack opening displacement (COD) were measured for the first time optically and by X-ray computed tomography to investigate the effect of extrinsic crack-tip shielding. The displacement fields around the crack-tip obtained by DIC were fitted using Westergaard's analytical solution to extract the effective stress intensity factor, by comparing this to the applied load, the efficiency of the crack-tip shielding could be evaluated.

A novel cohesive element model (traction-separation law) was then established based on the COD results to simulate the physical process of crack-tip shielding. It is the first time the cohesive model has been adapted to studying the direct crack behaviour measured by in-situ experiment to predict the crack growth. This model was then validated using the crack-tip strain field and R-curve obtained from the experiment measurement.

DECLARATION

The University of Manchester

PhD by published work Candidate Declaration

Candidate Name: Xuekun Lu

Faculty: Engineering and Physical Sciences

Title: Characterisation of the Anisotropic Fracture Toughness and Crack-Tip Shielding Mechanisms in Elephant Dentin

Declaration to be completed by the candidate:

I declare that no portion of this work referred to in this thesis has been submitted in support of an application for another degree or qualification of this or any other university or other institute of learning.

Signed Xuekun Lu

Date: 30th August 2015

COPYRIGHT

ACKNOWLEDGEMENTS

First and foremost, I'd like to express my sincere gratitude to my supervisor, Prof. Philip Withers. Without your guidance, I would be nowhere close to who I am today. Thank you for always pointing in the right direction I should go for my scientific research. Thank you for teaching me how to understand the experiment result with analytical thinking, motivating me to become a better researcher, encouraging me when I was depressed. Sorry for torturing you with my dreadful scientific writing skills during this four years. Fortunately, I think I am improving.

Secondly, a massive thank you to my girlfriend, Bo Yu. When I was down and my soul was weary, when troubles came and my heart was burdened, I was still and waited in the silence, until you came and sit awhile with me. You raised me up to more than I can be. My parents also gave me great support during my PhD life. You are the source of my belief to overcome every single problem, to be stronger.

Moreover, I'd like to express the appreciation to my colleagues. Dr. Joanna Walsh, you acted as my adviser and helped with my scientific writing and logic thinking. Dr. Sam McDonald, and Dr. Tim Burnett, who always gave me a hand when I was in trouble, never said 'No' to me; Dr. Rob Bradley, whom I learnt most my X-ray tomography techniques from, is a permanent idol in my life. You were never stingy to teach me whatever you knew and whatever I wanted; Dr. Kate Meade, thank you for revising my thesis time after time; Mr. Stuart Morse, you helped me out with my mechanical tests, giving me constructive advice on the experiment designs; Mr. Mark from the machinery workshop. Despite a Manchester City fan of you, I still want to express my sincere gratitude to you. You processed the loading rig for me. Whenever I visited you with urgent task, you always finished my work in time, with perfect accuracy.

I will always memorize the kind help and convenience offered by Prof. David Watts and Mr. Brian Daber from the School of Dentistry. During my PhD life, I frequently bothered you in the lab to use your equipment preparing my test-pieces. Without you, I may get stuck at the step of notch-cutting for a long time. You were concerned with the progress of my research and gave me useful advice. Thank you so much !

NOMENCLATURE

COD	crack opening displacement (μm)
SDEG	overall value of the scalar damage variable (in ABAQUS)
HAH	test piece with crack in hoop-axial plane and grow in hoop direction
RAR	test piece with crack in radial-axial plane and grow in radial direction
HRH	test piece with crack in hoop-radial plane and grow in hoop direction
CT	computed tomography
DIC	digital image correlation
SEM	scanning electron microscopy
LEFM	linear elastic fracture mechanics
EPFM	elastic plastic fracture mechanics
ASTM	American Society for Testing and Materials
E	Young's modulus (GPa)
E_p	Young's modulus in the elastic isotropic plane
E_t	Young's modulus vertical to the elastic isotropic plane
G_t	Shear modulus vertical to the elastic isotropic plane
v_t	Poisson's ratio vertical to the elastic isotropic plane
K_i	stress intensity factors, i = I, II, III ($MPa\sqrt{m}$)
K_{IC}	critical value of K_i , i = I, II, III ($MPa\sqrt{m}$)
el	elastic deformation
pl	plastic deformation
J	J-integral, parameter representing the stress level at the crack-tip
G_{IC}	critical value of strain energy release rate, i = I, II, III
P	Load (N)
a	crack length (μm)
υ	Poisson's ratio
Δu	displacement of crack walss (μm)
ε_{ii}	strain in ii direction, $ii = xx, yy$
δ_n	cohesive separation in normal direction (μm)
σ_{ys}	yielding strength (MPa)
σ_n	traction in normal direction (MPa)
δ_0	the separation when cohesive element starts to degrade (μm)
σ_0	peak traction when the cohesive element starts to degrade (MPa)
δ_u	final separation when the cohesive element fails (μm)
δ_f	separation at the turning point of the two softening segments in the cohesive law
σ_f	corresponding traction at δ_f (MPa)
K_n	initial stiffness of the material in the ascending section of the cohesive law (GPa/mm)
k_1	the initial gradient of the COD vs load
k_2	the gradient at higher load on the COD vs load curve
δ_t	the transition point between k_1 and k_2
μ	absorption coefficient of X-ray
I	intensity of the X-ray beam

Chapter 1

INTRODUCTION

The aims of present study are to understand the anisotropic fracture properties of elephant dentin by correlating the fracture toughness and strain capabilities with the underlying intrinsic and extrinsic crack-tip shielding mechanisms, favoured by a variety of 2-D and 3-D characterising techniques. This can benefit the clinical research in terms of early crack detection, failure prediction and also development of the bio-mimetic restorative materials with high toughness and strength. In this chapter, the background knowledge about teeth problem, the clinical treatment, the challenging, and the significance of present study was briefly introduced, followed by a diagram showing the studying strategy and the structure of this thesis.

1.1 Research Background

Teeth trauma has always been one of the most painful physical problems that people are suffering from in the past years. Tooth fractures can range from minor damage (involving chipping of the outer tooth layers, i.e. enamel and dentin) to severe failure (involving vertical, diagonal, or horizontal fractures of the tooth and/or root). Dental fractures are most common in children, youth, and young adults. An estimated 50% of the children all over the world encounter a dental injury before age 18 years, and most children are aged 7-14 years at the time of teeth traumatizing. A tooth may crack, often occurring in molars, due to a variety of factors [1]: (1) chewing on hard objects such as nuts, hard candy and ice; (2) exposure of tooth to extreme environment, e.g. acid beverage, ice water; (3) brittleness of tooth that undergone root canal treatment for restorations; (4) grinding and clenching the tooth. Early diagnosis and management are desperately needed to improve tooth survival, functionality and avoid the tooth loss.

When the enamel layer becomes weakened, it may break off or it may have to be removed by the dentist (Fig. 1.1a) [2]. A fractured enamel layer rarely damages the pulp, therefore the tooth will usually be restored with a full crown by the dentist. Another type of the damage is that the crack may extend from the chewing surface of the tooth vertically towards the root. The patient often feels the pain since the pulp area is damaged in this case. But the cracked tooth remains intact (Fig. 1.1b). Early diagnosis is crucial in this stage to prevent the loss of the tooth. Considering the size of the crack, it is challenging to identify the crack using the traditional methods such as high magnification optical observation and special lighting. A split tooth is often the consequence of the long term propagation of a crack (Fig. 1.1c). The whole tooth splits into separate segments. A split tooth cannot be saved intact. The position and extent of the crack, however, will determine whether any portion of the tooth can be saved. The last type of the damage is the crack initiates from the bottom of the root and extend toward the chewing surface (Fig. 1.1d). It show minimal signs and symptoms and may therefore go unnoticed for some time. It is often discovered when the surrounding bone and gum get infected.

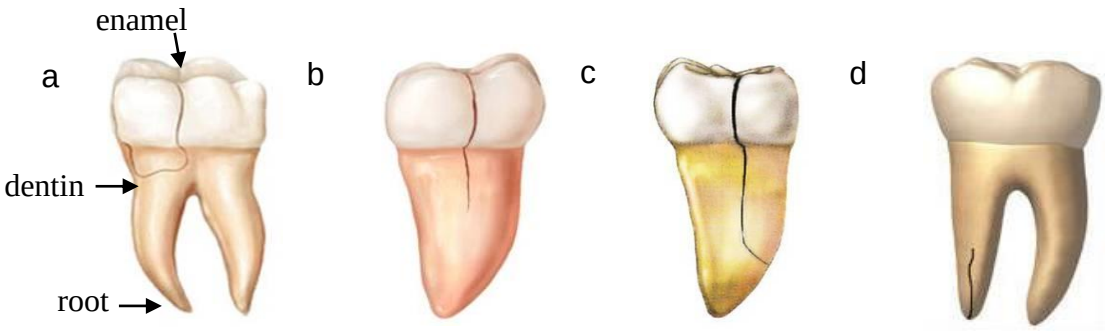

Fig. 1.1 Different types of human tooth fracture [3].

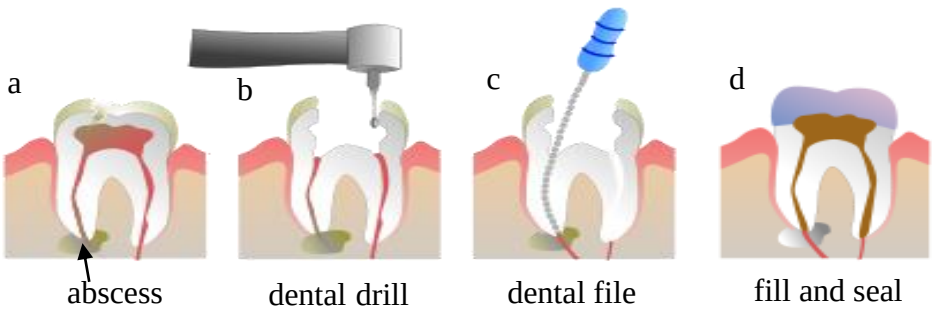

Fig. 1.2 Schematic illustrating the root canal treatment [4].

Root canal treatment is needed when the nerve of a tooth is affected by decay or infection (Fig. 1.2), which otherwise would die and have to be removed. During the procedure, a hole will be drilled into the tooth to reveal the infection and allow the dentist to remove away the pulp and infection together through the root canal (Fig. 1.2b-c). All the root canals in the specific tooth should be cleaned to ensure the infection is removed entirely. Upon the removal of the pulp, which keeps the teeth alive, the blood supply and essential nutrients are cut off. When the emergency dentist has removed the infected pulp from inside the tooth, the substance is replaced with a special root filler, which is a nature latex called gutta-percha [5]. Its use allows the tooth to remain rooted into the jawbone and the infection will be unable to return once the tooth has been refilled. An all-ceramic crown or porcelain-fused-to-metal crown is usually placed over the root filled tooth to provide further protection (Fig. 1.2d), even if the outer layers were unaffected by the infection.

However, the diagnosis of cracked tooth could be challenging due to the small size of the crack. The dentist may use a sharp instrument called an explorer to identify the cracks and inspect the gums around the tooth for irregularities [6]. X-ray radiography is another option, but the tiny size of the crack makes it challenging to detect. The third way is to use a fiber-optic light on the tooth or stain it with a special dye to search for a crack. Therefore, a mechanics understanding of the tooth fracture is needed so that the knowledge such as the crack initiation point, the most preferable crack growth direction and growth rate can be known, which is important from the perspective of developing a framework for failure prediction in clinical research.

Apart from the significance in the way of early diagnosis, research on the dental fracture is also beneficial to develop bio-mimetic restorative materials [7]. Natural dentin materials are complex composites, whose mechanical properties are often outstanding. The hierarchical, characteristic and multifunctional structures are the result of hundreds of million years evolution, inspiring the dental scientific research to develop novel materials with high fracture resistance, high strength and good biological compatibility.

1.2 Thesis Layout

This thesis composes of a literature survey covering the knowledge of dentin composition, structure and research background and also the basic theories of the techniques used in this study (Chapter 2), followed by the general introductions of experimental methods used (Chapter 3), if not covered by later chapters. The research is

covered in 4 main papers (alternative format) and the contents and aims of which are summarised in Fig. 1.3 so as to understand the anisotropic fracture properties of elephant dentin and its intrinsic and extrinsic shielding mechanisms step by step. The whole thesis ends with Chapter 8 covering the conclusions and further work.

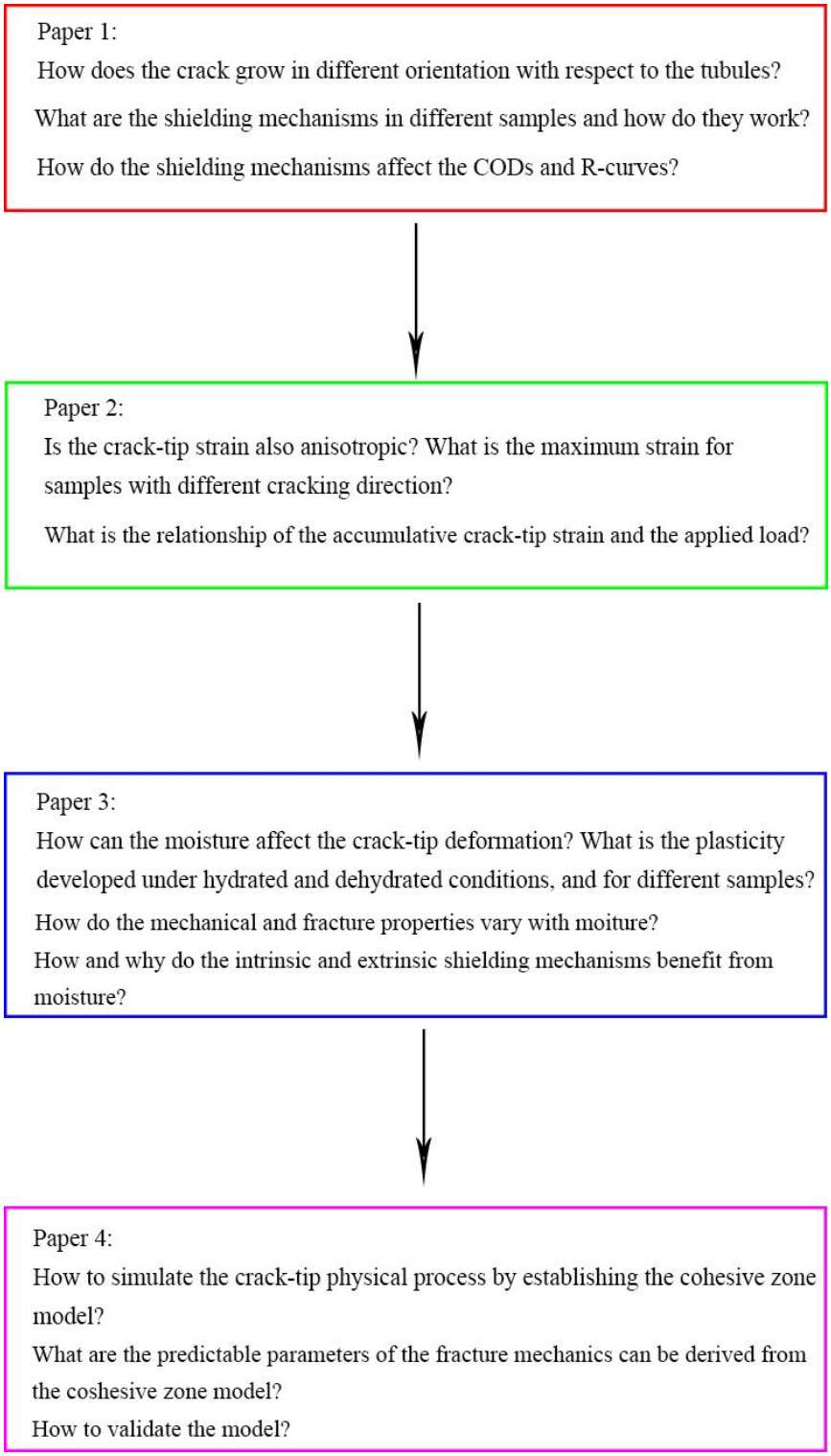

Fig. 1.3 The workflow of the PhD thesis.

References

[1] Fractured and Broken Teeth. http://wwwsimplestepsdentalcom/SS/ihtSS/r==/st32579/t32592/pr3html 21. 07. 2015.
[2] Cracked Teeth. http://wwwaaeorg/patients/symptoms/cracked-teethaspx 04. 02. 2015.
[3] Niemczyk SP. Cracked Teeth. Endodontic Microsurgical Innovations 09.04.2015;http://www.endomicrosurg.net/cracked-teeth.html.
[4] Root Canal Treatment. One Dental Specialties 12.04.2015;http://www.onedentalspecialties.com/general-services/root-canal-treatment/.
[5] Manogue M, Patel S, Walker RT. The principles of endodontics: Oxford University Press Oxford; 2005.
[6] Cracked Tooth Syndrome. http://wwwcolgateprofessionalcom/patient-education/articles/cracked-tooth-syndrome 30. 06. 2015.
[7] Meyers MA, Chen P-Y, Lin AY-M, Seki Y. Biological materials: structure and mechanical properties. Progress in Materials Science 2008;53:1-206.

Chapter 2

Literature Review

In this chapter, the knowledge of dentin composition, structure and research background are reviewed. The theories of linear elastic fracture mechanics, elastic/plastic fracture mechanics are briefly introduced. The principles and algorithms of the characterisation techniques are discussed.

2.1 Hierarchical Structure of Dentin

The long-term success of dental restorations is often limited by cavosurface margin adhesion, tooth fracture and recurrent caries, which cause the likelihood of the restored tooth failure ~40%. Previous studies have shown strong correlations between tooth fracture and dental restorations [1, 2], which shows that among the fractured teeth studied, more than 85% of them have been previously restored. Though not the most common cause of restoration failure, tooth fracture may be the most undesirable as it often results in subgingival cracking and may require total tooth extraction. It is already known that there is an anisotropy of mechanical properties such as fracture toughness and elasticity/plasticity.

The aim of present study is to improve the mechanics understanding of the anisotropies of the mechanical properties of dentin. This is important from the perspective of developing a framework for failure prediction in clinical research, to develop biomimetic restorative materials or oral treatments, and to understand the effect of the wide variety of restorative or esthetical dental procedures [3].

Dentin, the mineralized tissue of most mammals teeth that forms the bulk of the tooth, lies between the enamel and the pulp chamber, serving as a cushion for the hard, wear-resistant enamel during mastication and can absorb a great amount of mechanical energy [4]. Dentin is a composite with a complex hierarchical structure consisting of nanocrystalline inorganic hydroxyapatite platelets (45% by volume) embedded within an

amorphous protein matrix which consists of collagen (30% by volume). Fluid-filled pores and dentinal tubules (25% by volume) radiate from the inner pulp to the outer enamel layer, which is the significant structural feature of dentin (Fig. 2.1) [5, 6]. Some of the tubules are filled with carbonated hydroxyapatite, which is very common in the aged dentin and elephant dentin (Fig. 2.1b). The orientation of the tubules determines the anisotropic mechanical properties [7-9]. The mineralized collagen fibrils are arranged orthogonal to the tubules (1–2.5 μm diameter), forming a planar, felt-like structure called the intertubular dentin (ITD) (Fig. 2.1a and c). Closely around the tubules is a cuff of highly mineralized peritubular dentin (PTD) [8, 10-12]. The highly mineralized hydroxyapatite (HAP) improves the stiffness of teeth, while collagen provides toughness [13].

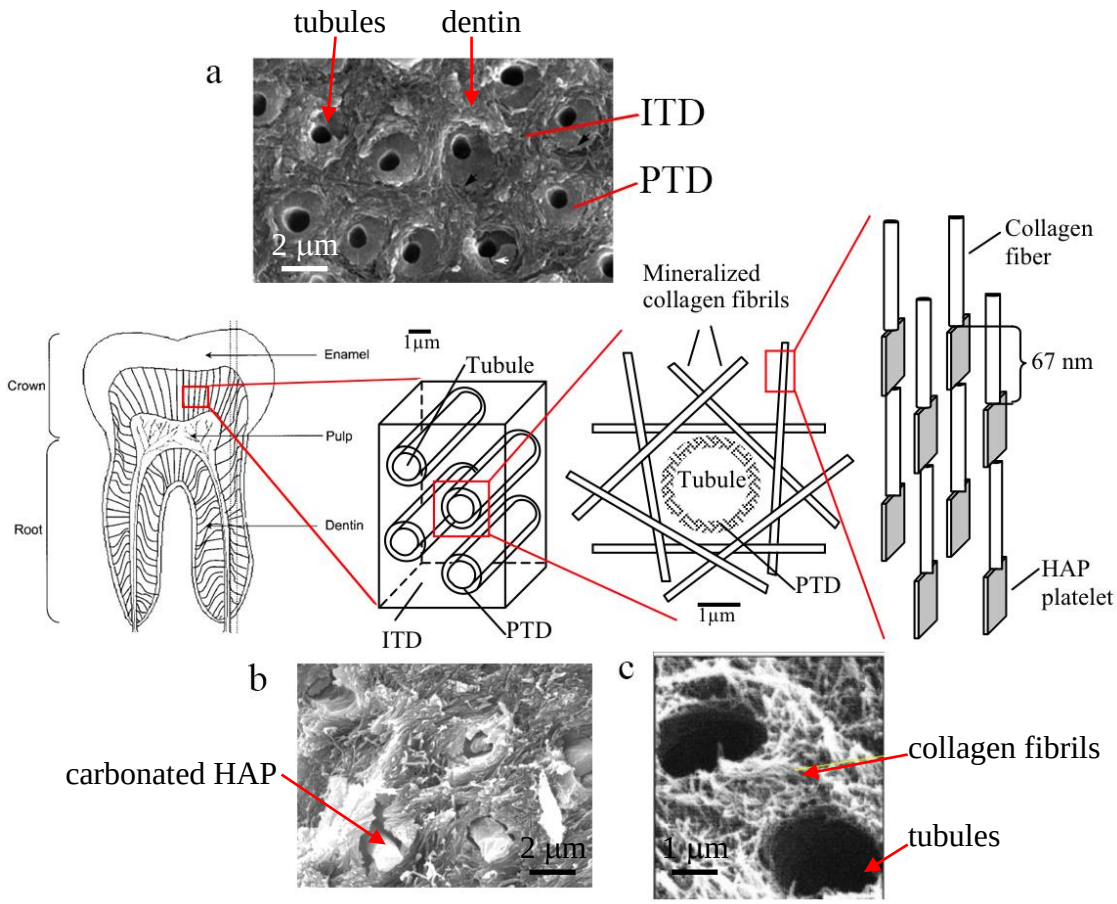

Fig. 2.1 Schematic of the hierarchical structure of teeth starting with the whole tooth molar (far left). Followed by the tubules surrounded by peritubular dentin (PTD) and intertubular dentin (ITD). This ITD is further composed of tangential mineralized collagen fibrils which are themselves hydroxyapatite and collagen composites (far right). Electron microscopic images show (a) the dentinal tubules and the ITD, PTD [6] (b) tubules occlusion by carbonated apatite (c) woven collagen between tubules respectively [14].

2.2 Human teeth *vs* Elephant tusk

Biologically, tusks are not particularly different from teeth in ways other than size. Similar with teeth, tusks grow and extend from mouth and embedded in the soft tissue from the jaw. Elephant tusk is often used as a proxy for human teeth in the study of fracture properties. The similarities and differences between them are discussed below.

2.2.1 Composition and Structure

Natural tusk is one of the most valuable biomaterials that can be referred to develop novel materials by scientists through biomimetic approach [15]. Structurally, tusk is composed of the same components as teeth: enamel, cememtum, dentin and pulp, from outside to core, and it is often used as a structural analogue for human dentin due to the similarities in microstructure and chemical composition [16]. One difference between the tusk and the teeth is the collagen fibrils. In tusk, the diameter of the collagen fibrils is smaller than that in human dentin [17, 18]. Moreover, the tubules in elephant dentin are elliptical and slightly bigger [19] than the round tubules in human teeth. The elliptical tubules may enhance the anisotropy of the tusk. The peritubular dentin (PTD) is comparatively smaller in elephant tusk. The most significant difference between the human teeth and tusk is the tubules arrangement.

Different with the dentinal tubules in human teeth, some of the tubules in tusk are not hollow. They are filled with carbonated hydroxyapatite (HAP), as is seen in Fig. 2.1b. They stack one above the other axially to form microlaminae, most commonly in the radial/axial plane (Fig. 2.2B–J) . Dentinal tubules and ground substance are sometimes calcified , suggesting that they may have a collagen base. Stacking of dentinal tubules into microlaminae is universal, but their shape, orientation, and positioning is variable for each kind of ivory. They can be curled into waves (Fig. 2.2B) or, straight (Fig. 2.2C). The microlaminae also has different orientation relative to the axis of the tusk (Fig. 2.2D-H). The orientation of the tubules can also vary between the neighbouring microlaminae (Fig. 2.2I-J). Fig. 2.3 clearly demonstrates the curled tubules arrangement in the tusk seen from different orientation.

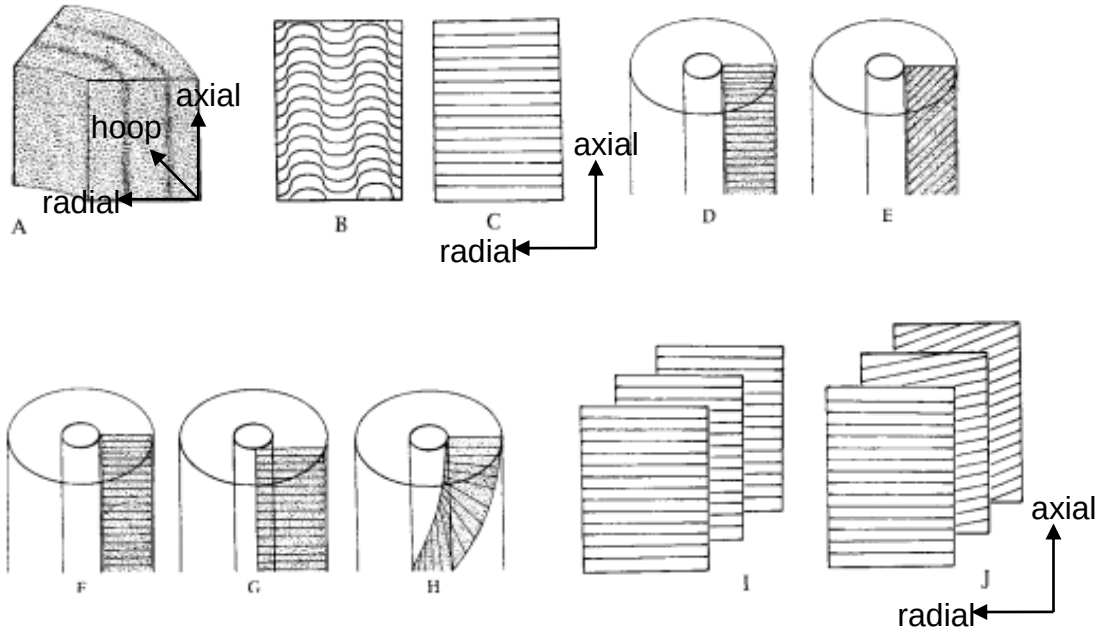

Fig. 2.2 Overview of tusk structure. (A) Macroscopic view of the tusk. The black lines correspond to the growth layers, the spotty pattern represents the radial tubules; (B) curled tubules into waves; (C) straight tubules. (B) and (C) are radial profiles. (D) and (E) show the microlaminae that are made of different oriented tubules. (F-H) indicate that the microlaminae can be radial/axial (F), axial but angled to the forming face (G), or radial but helical(H). Different microlaminae can have the identical orientations (I), or varying orientations to get the helicoidal pattern(J) [20].

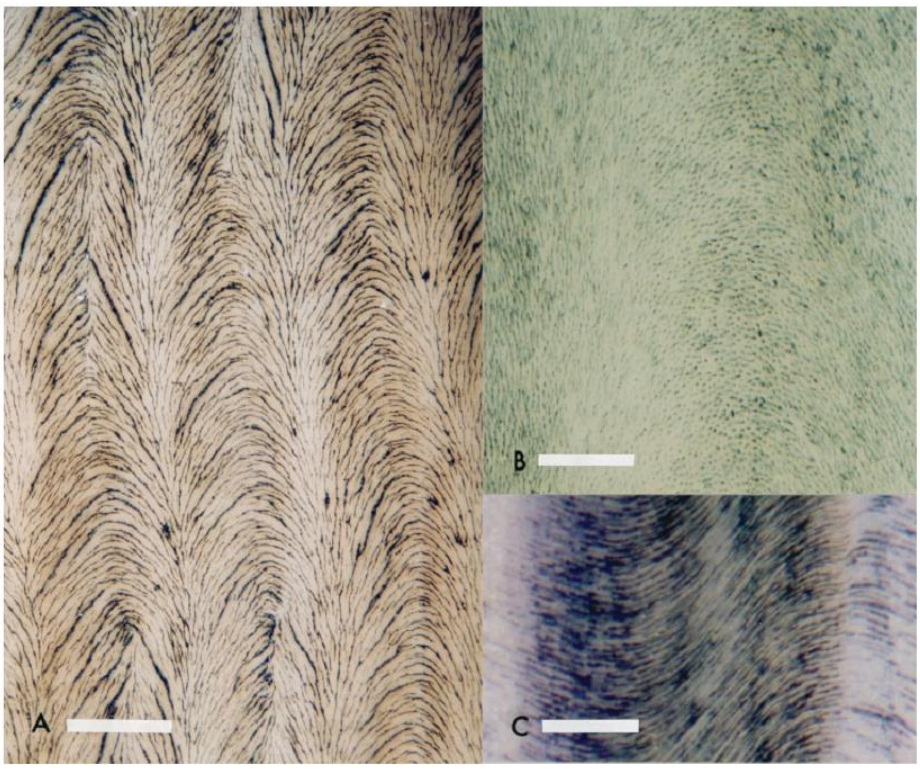

Fig. 2.3 Tubules of the tusk possess helicoidal arrangement. (A) Tangential profile of the cracks along the tubules orientation below cementum layer. (B) tubules on the surface viewed obliquely to the tangential profile. The axially aligned tubules are seen as vertical black lines, and the radially tubules are as spots. The change of the tubules orientation is apparent. (C) Radial profile of the tubules alignment, showing a wave-like pattern of dentinal tubules. Scale marker in A = 1mm; B,C = 100 mm [20].

2.2.2 Mechanical Properties

Despite the remarkable difference of the tubules alignment in the tusk and teeth, their mechanical properties are found to be identical. Depending on different test methods and sample geometries, the measured values can vary substantially. The average recorded values of the mechanical properties for human and elephant dentin are listed below:

Table 2.1 Comparisons of the mechanical properties between hydrated human and elephant dentin.

	Human Dentin	Elephant Dentin
Fracture toughness ($MPa\sqrt{m}$)	1.2~3.08 [21]	1.6 ~ 2.6 [22]
Young's modulus (*GPa*)	12 $\pm$ 0.3 [23]	15 $\pm$ 2 [22]
Yielding strength (*MPa*)	~ 60 [22]	50 - 65 [22]
Ultimate Strength %	48.7 $\pm$ 16 [24]	75 $\pm$ 5 [25]
Hardness, *GPa*	0.30 $\pm$ 0.05 [26]	0.30 $\pm$ 0.12 [27]

It is found that the fracture toughness of elephant dentin is within the fluctuation of the toughness in human dentin. The ultimate strength are higher than human dentin, but the yielding strength and hardness are identical.

2.2.3 Function

Elephant tusk is an incisor. Different from human teeth, which is designed to bite, crush and chew food, elephant tusk is not known to cut food, instead, they are often used as weapons to defend themselves, ward off the potential predators like tigers, dig and strip the bark off trees and move heavy objects. A high flexure strength and toughness are entailed so that it won't break perpendicular to the long axis of the tusk.

It is concluded that the elephant dentin can be used as a proxy of the human dentin for the study of fracture problems, evidenced by listed identical mechanical properties of the two materials. The similar microstructure composition, size and orientation could contribute to the same physical process of the crack growth and the comparable crack-tip shielding mechanisms as well.

2.3 Anisotropic Mechanical Properties

Dentin demonstrates significantly anisotropic fracture toughness with respect to the different orientations of the tubules and the alignment of the collagen fibrils. The

mechanical properties also vary between the hydrated and dehydrated conditions, which will be discussed in Section 2.5. Fig. 2.4 illustrates a variety of possible crack propagation orientations. Previous research [22, 28] [8] [4] found that when the crack plane was parallel to that of the tubules, the crack growth resistance and the fracture toughness were much higher (see Fig. 2.4c-d). In contrast, when the crack grew perpendicularly to the tubules orientation, breaking the tubules during propagation (see Fig. 2.4a), the fracture toughness was lowest as the crack path ran parallel to the collagen fibrils. Fig. 2.5 presents the anisotropy of fracture toughness based on different orientations. It is also found the dentin was stiffest in an orientation perpendicular to the axes of the tubules [3, 16, 29]. Fig. 2.6 shows the different morphologies of fracture surface with cracks propagating in different orientations.

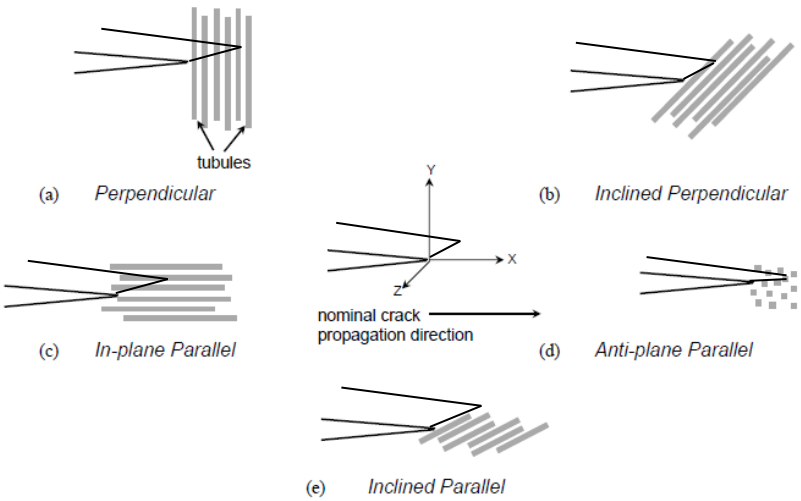

Fig. 2.4 Different crack growth orientations relative to tubules layout [22]. Crack fronts are vertical to the page (z direction).

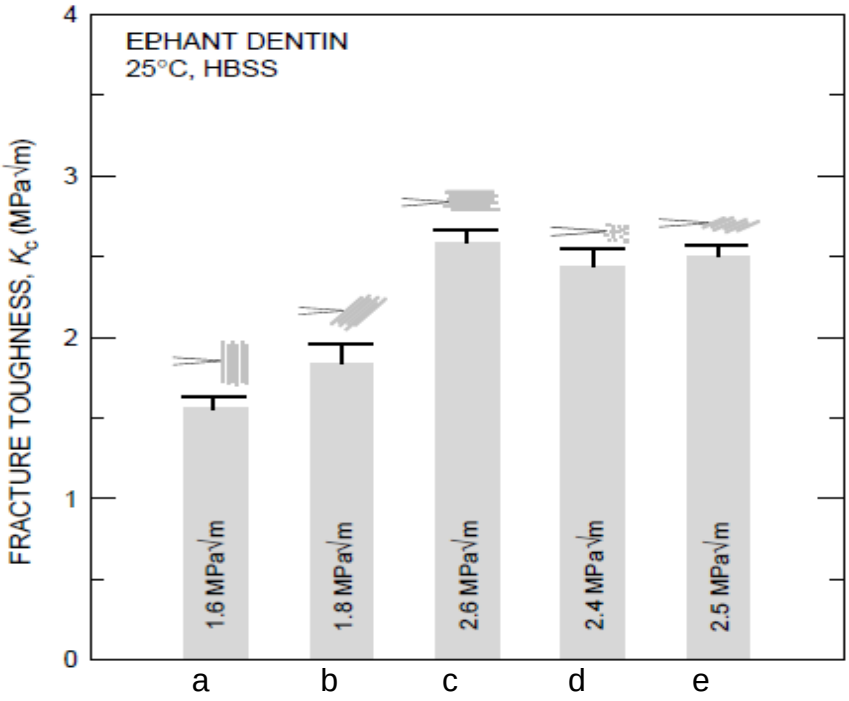

Fig. 2.5 Fracture toughness of five different orientations (Fig. 2.4) studied on hydrated elephant dentin [22].

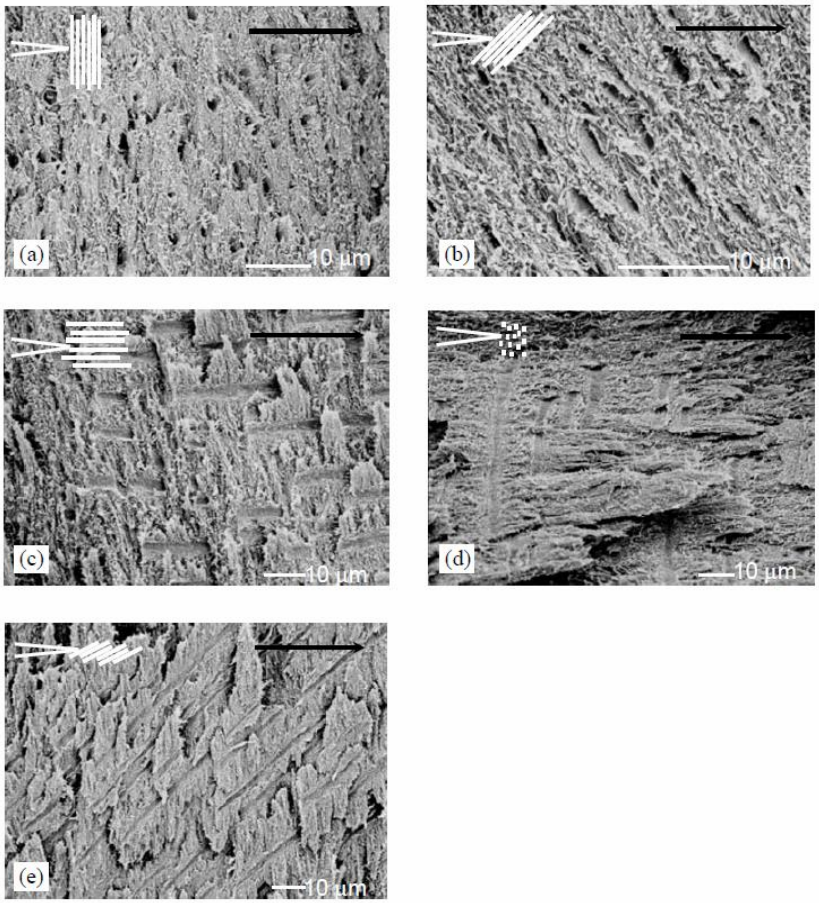

Fig. 2.6 The SEM images showing the fracture surfaces corresponding to cracks growing in different directions (see Fig. 2.4) on hydrated elephant dentin [22].

It has also been found that the orthogonal arrangement of collagen fibrils with respect to tubules renders approximately 10 % anisotropic stiffness of human dentin [30]. Human dentin has a Young's modulus of 15.5 GPa along the tubules versus 18 GPa across the tubules [7].

In addition to the macroscopic mechanical properties, the anisotropy also exists in the length scale as small as single crystal. Fig. 2.7 shows the hydroxyapatite (HAP) crystal has a hexagonal lattice. The HAP crystals are embedded within the collagen fibrils with the c-axis arranging along the long axis of the collagen fibrils (Fig. 2.8). When loaded, the crystals preferentially change its orientation so that the c-axis follows the loading direction. Nano-indentation and micro-indentation were used to study the Young's modulus, hardness and fracture toughness of a single HAP crystal [31].

Table 2.2 demonstrates that the stiffness and hardness were significant higher in c-axis direction which has a propensity to align along loading direction. The fracture toughness was also remarkably anisotropic in the single HAP crystal. The direction along the c-axis (Basal) always demonstrates a higher stiffness and hardness than perpendicular to it (Prism). It is found that HAP crystal is 10 times stiffer than macroscopic dentin, but 2 – 5 times less tough.

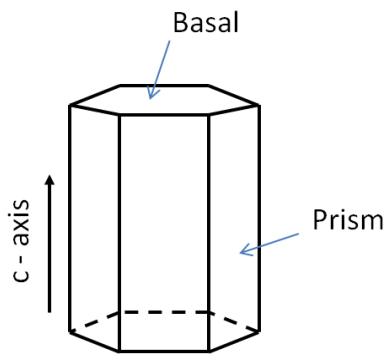

Fig. 2.7 Schematic graph shows the hexagonal geometry of the HAP crystal and the corresponding basal and prism plane. The c-axis is pointed out.

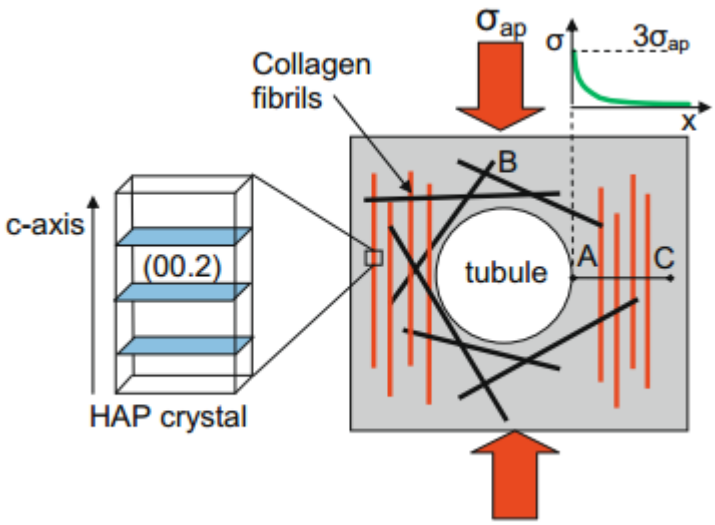

Fig. 2.8 A schematic illustrating the arrangement of the HAP crystal in the dentin. The black and red rods representing the collagen fibrils cross-linked surrounding the tubules [6].

Table 2.2 Mechanical properties of single HAP crystal obtained by nanoindentation [31]

P_{max}	Prism		Basal	
	E (GPa)	H (GPa)	E (GPa)	H (GPa)
2 mN	125.9 ± 1.6	8.8 ± 0.4	135.1 ± 1.3	9.7 ± 0.1
Below pop-in	127.2 ± 10.4	9.5 ± 1.5	162 ± 1.9	14.8 ± 0.1
K_c (MPa $m^{0.5}$)	0.65		0.40	

2.4 Crack-tip Shielding Mechanisms

There are a number of crack tip shielding mechanisms in metallic and ceramic materials, such as crack deflection(twist), contact shielding, zone shielding, combined zone and contact shielding (Fig. 2.9) [32-37]. Basically, the toughening mechanisms can be classified as below: (i) intrinsic toughening mechanisms that operate ahead of the crack tip and act to enhance the material's inherent resistance to microstructural damage and cracking, and (ii) extrinsic toughening mechanisms that operate primarily behind the crack tip by promoting crack-tip shielding, which reduces the local stress intensity actually experienced at the crack tip [32]. Intrinsic mechanisms, such as crack blunting, tend to affect the initiation toughness, while the extrinsic mechanisms, such as crack bridging, zone shielding, promote crack-growth toughness. Since the extrinsic toughening mechanisms function in the crack wake, their effect is dependent on the size of the crack, which in turn can lead to rising R-curve behaviour because after crack extension a more substantial shielding zone can be established in the crack wake [16]. Dentin also possesses a variety of shielding mechanisms to slow down the crack growth rate and increase the crack-growth resistance.

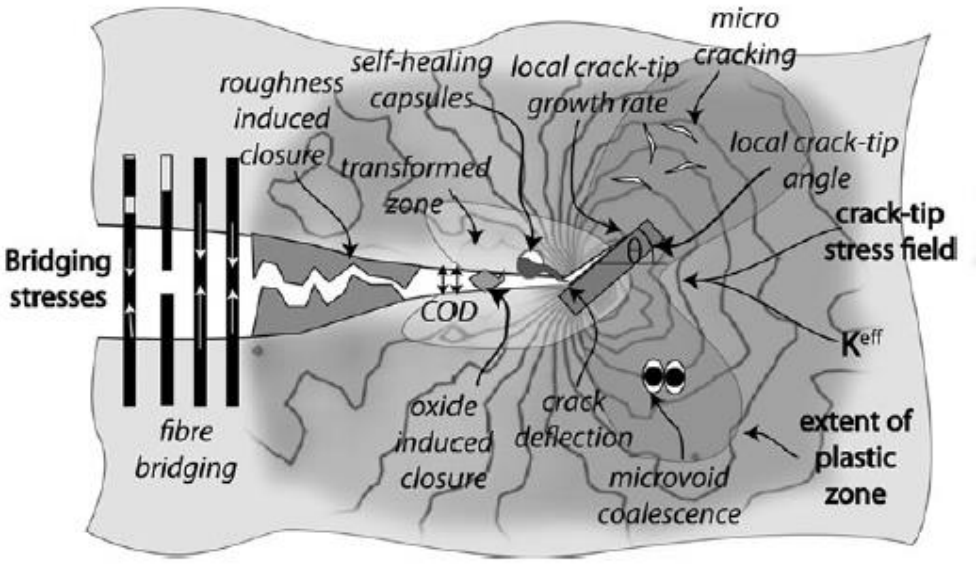

Fig. 2.9 Some of the key microstructural crack-tip shielding and damage mechanisms and fracture mechanics parameters obtainable by X-ray imaging (italics) and diffraction (bold) during a load cycle [38].

2.4.1 Bridging

Crack bridging is a common way of crack-tip shielding, particularly in fibre composites where intact fibres tend to bridge the crack and oppose crack opening [22]. Materials with crack bridging often exhibits an rising R-curve behaviour (i.e. the fracture toughness increases as a function of the crack extension, which will be discussed in later section). Crack-path investigation clearly shows the bridging from collagen fibrils (Fig. 2.10), akin to that proposed for bone [39]. This mechanism is only observed in the parallel orientation in dentin, which is reasonable since the collagen fibres run vertical between tubules. Furthermore, another bridging mechanism also occurs where the dominant crack links with smaller cracks to form uncracked ligaments (Fig. 2.11). Uncracked-ligament bridging makes the crack resistance rise with the propagation of the crack length because of the increase of bridging zone, thus the affected zone keeps increasing and the crack growth resistance becomes higher and higher [16, 40]. After the crack length surpasses a critical value, the ligament at the wake in the far field will break because of the larger and larger crack opening displacement. In front of the crack tip the new uncracked ligament will keep appearing, so it will reach a balanced condition, and the shielding effect from this

mechanism will become stable, leading to a plateau in the R-curve (i.e. the fracture toughness remains constant). Fig. 2.12 illustrates the balanced bridging condition and the bridging stress distribution along the crack path.

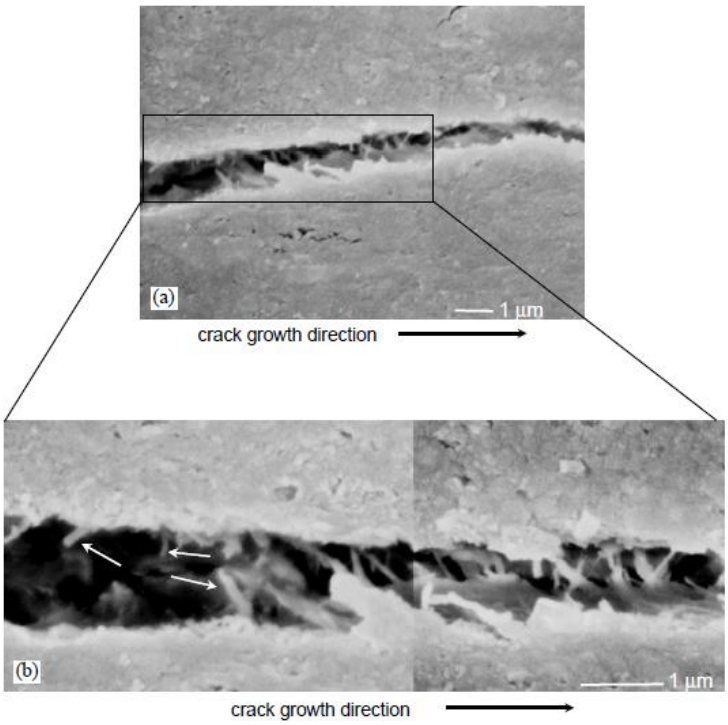

Fig. 2.10 Scanning electron micrographs showing collagen fibres bridging along crack path in anti-plane parallel direction (see Fig. 2.4d) in hydrated elephant dentin [22].

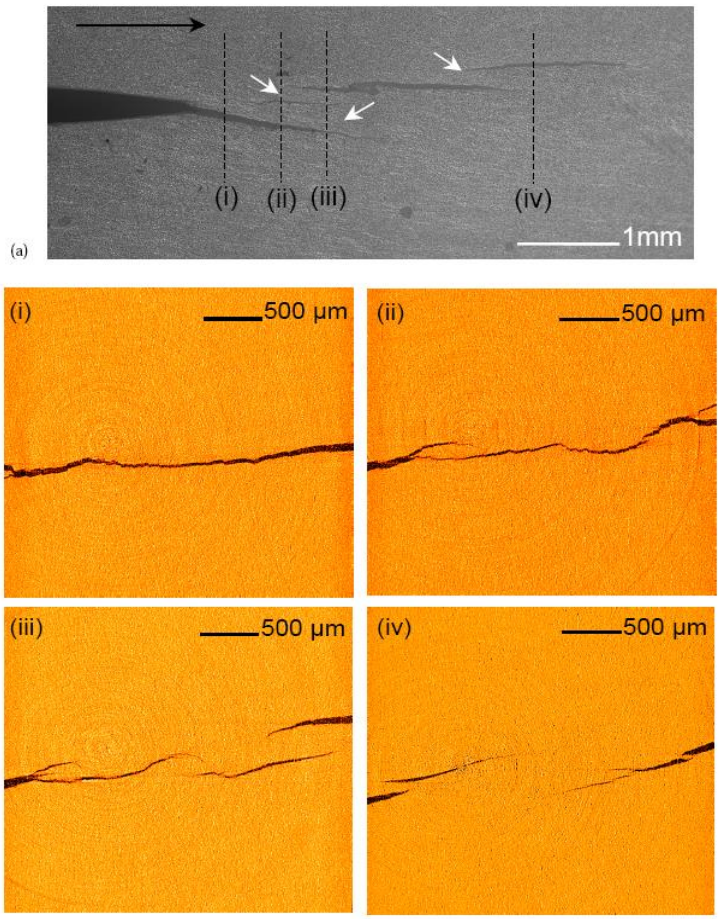

Fig. 2.11 (a) Optical micrograph of a crack in hydrated elephant dentin grown in anti-plane parallel direction (see Fig. 2.4d) showing the formation of uncracked-ligament bridges (indicated by white arrows). The black arrow indicates the direction of nominal crack growth. (b) Reconstructed computed X-ray tomography slices showing the cross-section of the crack front (at positions shown by the dotted lines in (a)) [16].

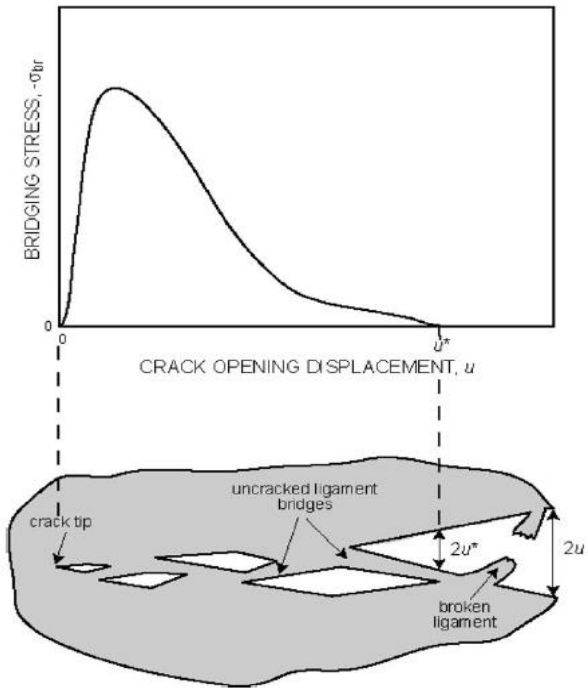

Fig. 2.12 Schematic showing a general phenomenon of uncracked-ligament bridging: a steady-state crack, where bridges are being both created at the crack tip and destroyed in the crack wake beyond the critical crack-opening displacement [16].

These two shielding mechanisms above can contribute to most of the shielding effect among others in dentin. R. Ritchie managed to quantify the shielding effect by comparing the theoretical and the measured gradients of the load *vs* displacement curve, which shows a shielding effect of 0.4 $MPa\sqrt{m}$ for the crack extension Δa less than 1 mm and approximately 1 $MPa\sqrt{m}$ for the extension as long as 5 mm. The methods to calculate the theoretical and measured compliance of the sample can be found in the work [16]. Simple theoretical models for uncracked-ligament bridging can provide comparable estimates. Using a limiting crack-opening displacement approach [41], bridging stress K_{br} can be estimated as

$$K_b = -f_{ul}K_I[(1+l_{ul}/\mathrm{rb})^{1/2}-1]/[1-f_{ul}+f_{ul}(1+l_{ul}/\mathrm{rb})^{1/2}] \qquad (2.1)$$

where f_{ul} is the area fraction of bridging ligaments on the crack plane, l_{ul} is the bridging-zone size, r is a rotational factor (0.195–0.470 [41]) and b is the length of the remaining uncracked region ahead of the crack.

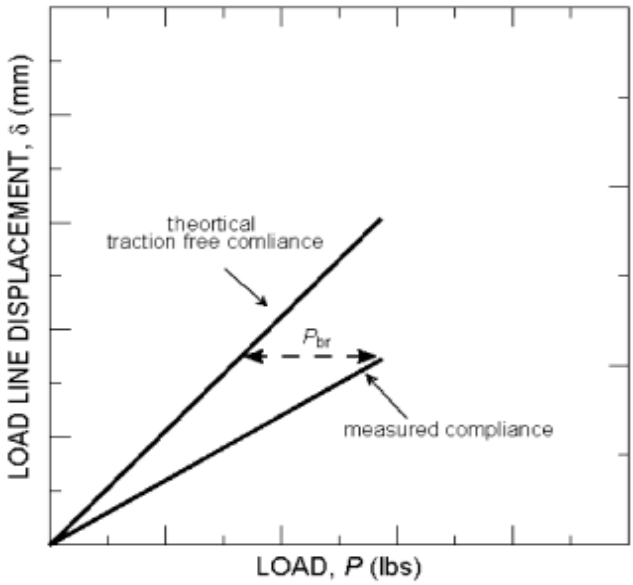

Fig. 2.13 Schematic showing the bridging load by comparing the measured and theoretical compliance. P_{br} is the additional load which must be applied to the bridged crack to achieve the same load-line displacement as the traction free crack.

2.4.2 Deflection/Branching

Generally the crack propagates in the plane of maximum driving force (e.g. maximum tensile stress), but sometimes this is not the case and the crack will deflect away from the highest driving force plane. This is because of microstructural features, such as particles, fibres and dispersed phase. In this case the stress intensity factor at the crack tip will decrease [4, 42-44]. To make the crack continue to grow, higher applied load is needed to reach the critical driving force again and this is the deflection toughening principle. For dentin in the parallel orientation with respect to the tubules, there is no significant crack deflection when the crack propagates in the direction parallel to the tubules. In the perpendicular direction, there is somewhat more crack deflection out-plane of the crack surface away from the maximum driving force plane by the connection of the main crack with the tubules. This reduces the crack tip stress intensity, and because of this the matrix is toughened (Fig. 2.14) [22]. Although this seems to be a quite significant contribution to the toughness in the perpendicular orientation, it should be noted that this toughening effect takes place only at a limited region around the tip and only affects the local stress intensity at the few instances where such crack-path deviations occur [22]; overall, it will not contribute significantly to the globally measured toughness in this orientation in the case that different shielding mechanisms exist concurrently.

However, the deflection in elephant tusk is significantly different. Based on current study, the crack deflection occurs when the crack grows anti-plane parallel to the tubules (see Fig. 2.4d), and it is shown in Fig. 2.15. The crack growth by linking the micro-cracks around the tubule cuffs. No literature has recorded this phenomenon before. This will be discussed later.

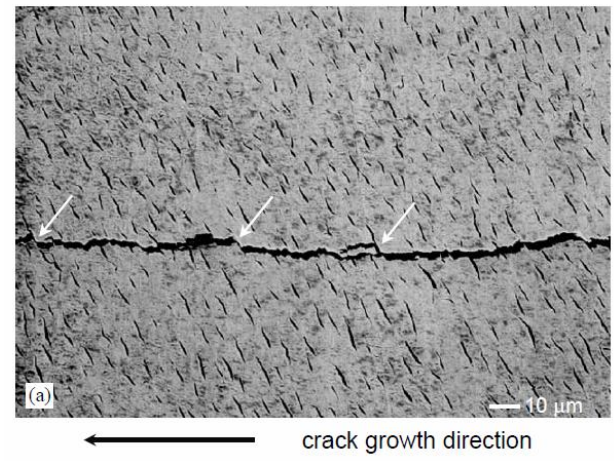

Fig. 2.14 Out of plane deflection of the crack propagating perpendicular to the tubules axes [22].

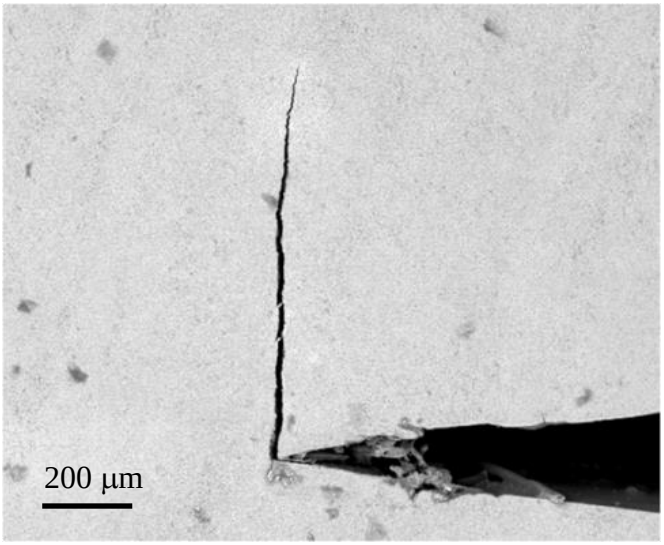

Fig. 2.15 Large angle deflection with the crack growing in anti-plane parallel direction (see Fig. 2.4d) in elephant dentin.

2.4.3 Microcracking

Microcracking at the wake or in front of the crack tip can create a dilation zone (Fig. 2.16) [40]. The occurrence of microcracking can not only release more or less internal energy, but creates a compressive zone because of the constraint by the matrix around the microcracking by which the crack is retarded and shielded [45]. Microcracking phenomenon is found for crack growing both in the perpendicular direction and the parallel direction [40, 46]. Therefore, microcracking cannot be viewed as a reason for the anisotropy of mechanical behaviour. However, it can cause the reduction of the modulus [47]. Micro-cracking has been widely identified as a toughening mechanism in bone [48], and has been reported previously for human dentin [49]. In stable conditions, the toughening effect can be evaluated in terms of the closure stress intensity for such dilatational toughening [50, 51] by

$$K_{mic} = 0.22\varepsilon_m E' f_m l_m^{1/2} + \beta f_m K_c \tag{2.2}$$

where the coefficient (0.22) is an empirical value [22, 52], E' is the plane-strain elastic modulus, ε_m is the residual volumetric strain, f_m is the effective volume fraction of microcracks, l_m is the size (specifically height) of the microcrack zone (estimated to be 15~37 mm, depending on tubule orientation), K_C is the matrix toughness for hydrated human dentin (1.2 ~ 3.08 $MPa\sqrt{m}$) [21, 53] and elephant dentin (1.6 ~ 2.6 $MPa\sqrt{m}$) [22] and b is a parameter dependent on the Poisson's ratio (~1.2) [47]. The toughening effect coming from the microcracking mechanism can be evaluated by a shielding of 0.25 $MPa\sqrt{m}$ in perpendicular direction and 0.3 $MPa\sqrt{m}$ in parallel direction.

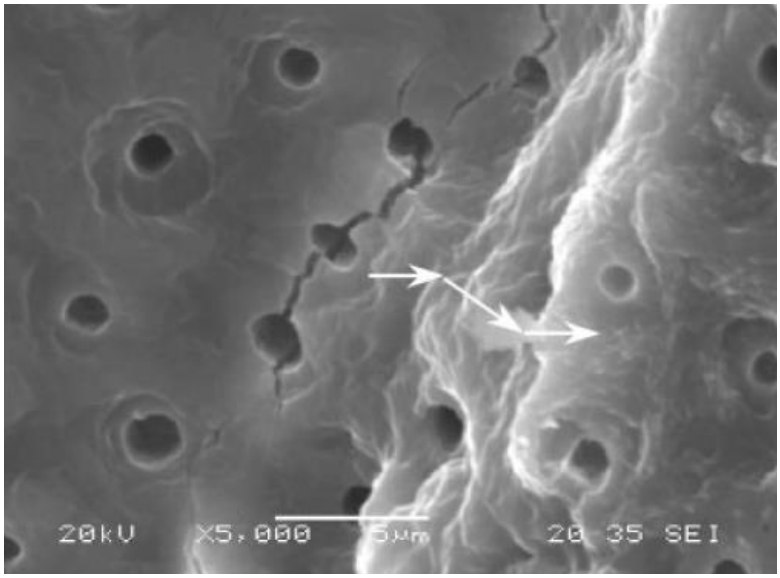

Fig. 2.16 The fracture surface viewed by SEM of a crack growing perpendicularly to the tubule axis in hydrated human dentin. Microcracks induce bifurcation in the vicinity of the main crack (white arrow shows the main growth direction) [40]. Micro-cracks are also observed on the fracture surface of elephant dentin.

2.4.4 Blunting

Blunting is a toughening mechanism relevant to the crack tip plastic deformation, and mostly appears in the hydrated dentin. This is a time-dependent phenomenon [16], and the extent of blunting increased with the time lapse. Viscoplasticity caused the continuous crack opening under the constant load, and the stress-relaxation will also occur if the displacement remain stable (Fig. 2.17). No evidence has shown the tubules can contribute to the crack-tip blunting yet. Generally crack directly grows though the tubules on its path based on our study.

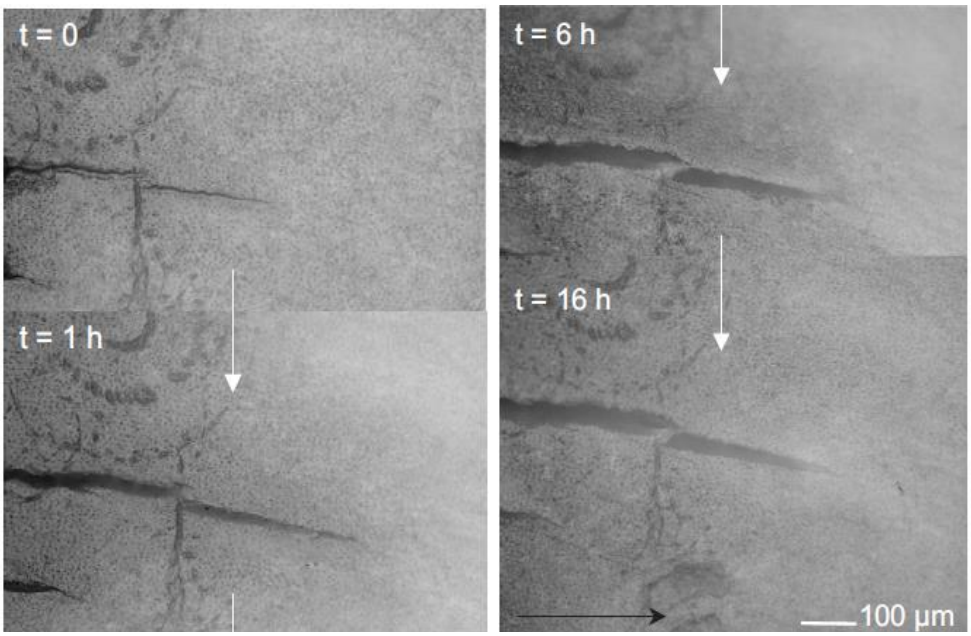

Fig. 2.17 Optical micrographs (at zero load) illustrating the blunting phenomenon in hydrated elephant dentin for a crack growing in anti-plane parallel direction (see Fig. 2.4d) [16]. The blunting is shown in four panels with the time increasing from t = 0 to t= 16 hours.

2.5 Hydrated *vs* Dehydrated Dentin

Hydration plays a critical role in the mechanical properties of dentin. Previous investigations have revealed that hydrated dentin exhibits much higher fracture toughness than the dehydrated ones and crack growth resistance (expressed via an R-curve) when hydrated rather than dehydrated along with enhanced crack-tip blunting [54, 55]. The crack growth rate is much faster in the dehydrated dentin than the hydrated one [12]. Hydration decreases the elastic Young's modulus and hardness by approximately 35% and 30% compared with the dehydrated dentin [23, 26, 56-58]. The moisture benefits the dentin with a 100 % larger magnitude of strain at fracture compared to the dehydrated one [25]. The hydrated tissues exhibited viscoelasticity, demonstrating a good ability to recover the elastic energy stored in the region surrounding the deformed area [59]. More detailed information can be found in Table 2.3.

Table 2.3 Comparisons of the mechanical properties between hydrated and dehydrated human dentin

	Hydrated	Dehydrated
Fracture toughness ($MPa\sqrt{m}$)	3.08 [53]	2.4 ± 0.1 [60]
Young's modulus (GPa)	12 ± 0.3 [23]	13.7 ± 0.29 [23]
Yielding strength (MPa)	~ 60 [22]	153 ± 14 [60]
Strain at fracture %	6.6 ± 0.2 [25]	3.3± 0.3 [25]
Hardness, GPa	0.30 ± 0.05 [26]	0.92 ± 0.12 [26]
Fatigue crack growth exponent ($m/cycle \cdot MPa\sqrt{m}^{-m}$)	13.3 [12]	18.8 [12]

R.O. Ritchie and J.J. Kruzic et al [16] found that hydration-induced blunting could contribute a higher crack initiation toughness (i.e. the original toughness at the beginning of the crack growth, where there is little crack bridging) compared with the dehydrated ones as can be seen by the Fig. 2.18. The dehydrated dentin after rehydrated process will also show a jump in toughness because of the blunting effect. This blunting phenomenon suggested a visco-elastic/plastic behavior, which can dissipate more energy by accommodating larger amount of crack-tip strain.

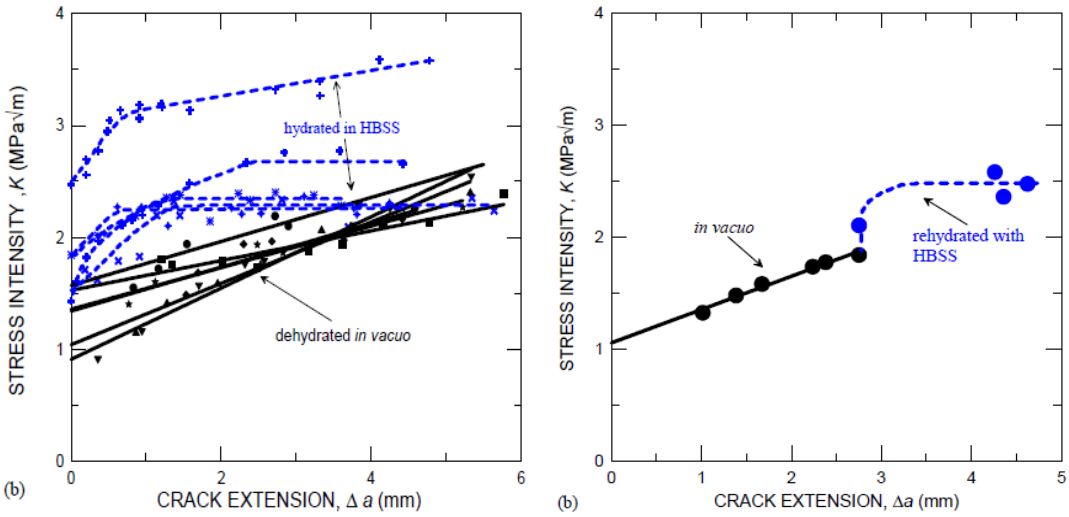

Fig. 2.18 (a) Hydrated elephant dentin samples possess a higher crack initiation threshold because of crack tip blunting compared with dehydrated ones;(b) rehydrated samples present a sudden jump in crack-growth resistance [16]. The crack grew in anti-plane parallel direction (see Fig. 2.4d).

It is concluded that the major differences between the hydrated and dehydrated behaviour are in the development of extensive crack bridging behind the crack tip [55], more pronounced micro-cracking zone and crack-tip blunting (i.e. visco elastic/plastic zone) (summarised in Fig. 2.19). Micro-cracking leads to a stress shielding mechanism similar to a plastic zone [61]. The lynchpin for this problem is *water and collagen*. Water plays an important role in forming the structure of collagen molecules since it helps to form hydrogen bonds which inter-links the triple helices of the collagen molecule, along the peptide chains [62-65]. The hydration layer also forms the hydrogen-bonded ”bridges”, which strengthen the structure of collagen by forming intra- and interchain links within collagen molecules and between neighbouring molecules. Water may act as a plasticizer of collagen [66].

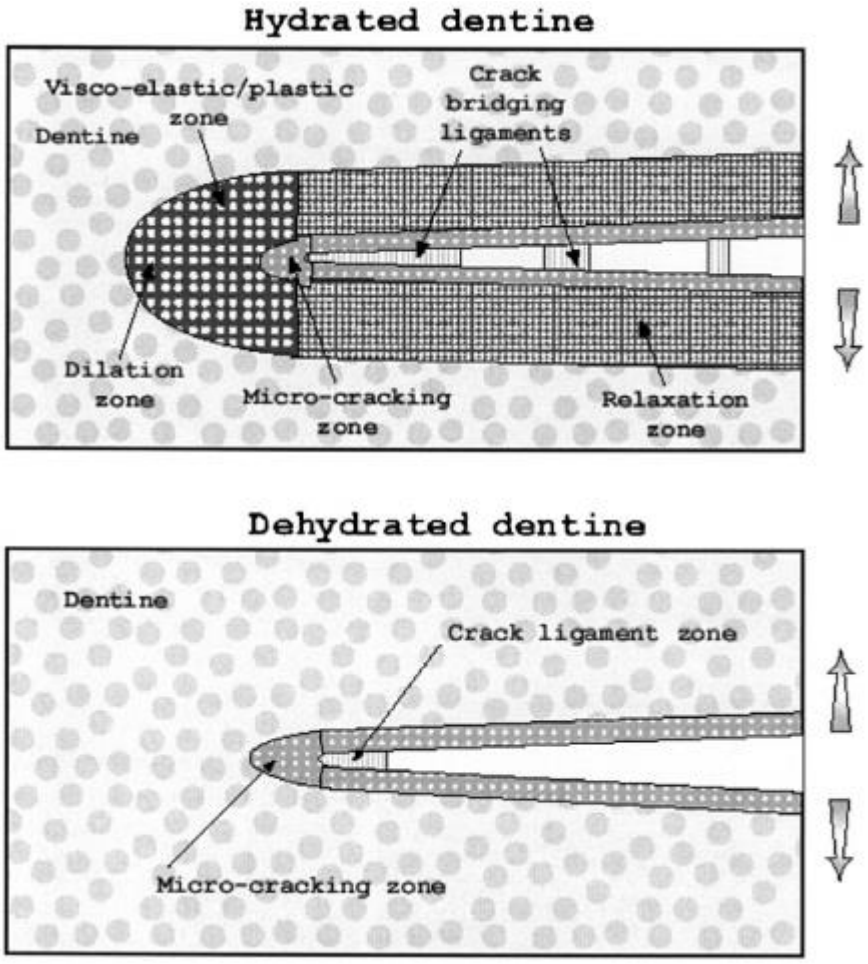

Fig. 2.19 Schematic illustration of the toughening mechanisms operating during the fracture of (a) hydrated and (b) dehydrated dentin [67].

Another explanation is that, the hydroxyapatite crystallites have been suggested to form a granular medium that binds to the organic matrix via hydrophilic interactions or mineral – matrix binding proteins under hydration environment [22]. A dehydrated test-piece has low capability to undergo crack-tip strain compared with the hydrated test-piece is caused by the efficiency of the collagen-based intrinsic shielding. A decrease in moisture content can actually cause the reduction in the strain to fracture [55, 68, 69].

2.6 Fracture Mechanics

2.6.1 Linear Elastic Fracture Mechanics(LEFM)

Linear-elastic fracture mechanics are widely used to study the fracture problems assuming that any inelastic (e.g. yielding) behaviour is limited to a small near-tip region, i.e., where the extent of local (crack-tip) inelasticity is small compared with the size of the test sample. Therefore this method is geometry and size dependent and cannot accurately take the contribution of plastic deformation and energy dissipation into account. To meet the requirement, the specimen should be viewed in plane-strain conditions, in which the Young's Modulus is $E' = E / (1 - v^2)$, where v is Poisson's ratio. Thus, the thickness of the sample should be

$$B \geq 2.5\left(\frac{K_c}{\sigma_{ys}}\right)^2 \tag{2.3}$$

where K_c is the critical fracture toughness, σ_{ys} is the yield strength of the material. There are three ways to enable the crack to propagate under applied load: opening mode (Mode I), in-plane shear mode (Mode II) and out-of-plane shear mode (Mode III) (Fig. 2.20).

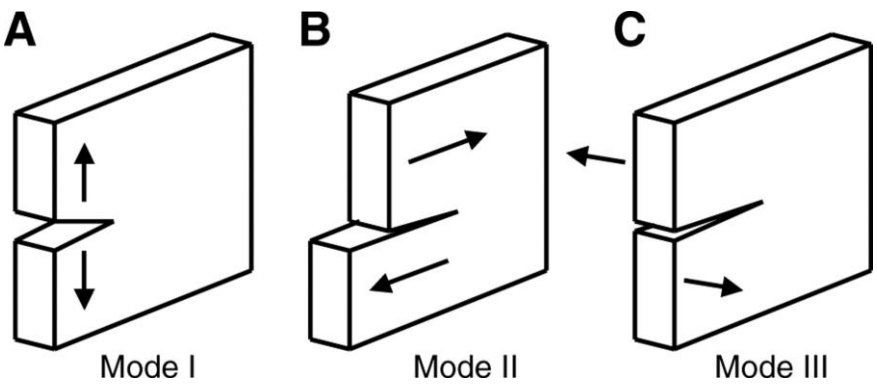

Fig. 2.20 Three different fracture modes.

Linear-elastic fracture mechanics (LEFM) has been widely used to assess the fracture toughness of brittle materials, such as dentin, bone and ceramics. The schematic of crack-tip elastic stress is shown in Fig. 2.21.

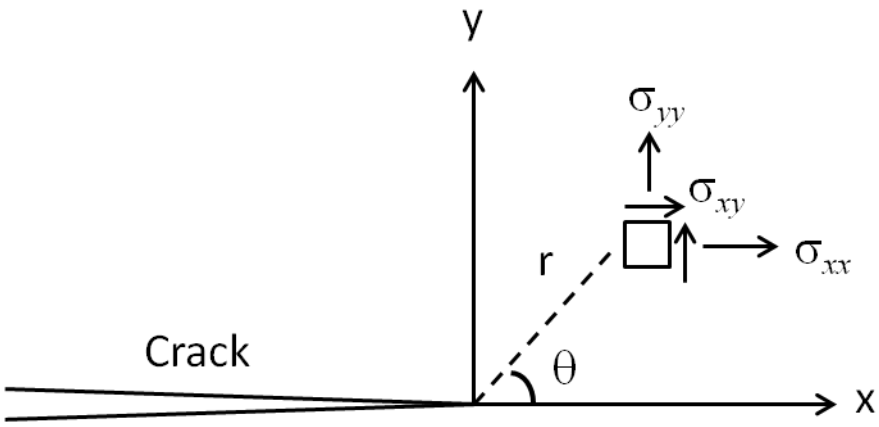

Fig. 2.21 Crack-tip stress component. The crack front is vertical to the page (z-axis).

Under Mode I loading conditions, the elastic stress solution around the crack tip is given by [70]

$$\sigma_{xx}(r,\theta)=\frac{K_I}{\sqrt{2\pi r}}\left[1-\sin\frac{\theta}{2}\sin\frac{3\theta}{2}\right]\cos\frac{\theta}{2}$$

$$\sigma_{yy}(r,\theta)=\frac{K_I}{\sqrt{2\pi r}}\left[1+\sin\frac{\theta}{2}\sin\frac{3\theta}{2}\right]\cos\frac{\theta}{2} \tag{2.4}$$

$$\sigma_{xy}(r,\theta)=\frac{K_I}{\sqrt{2\pi r}}\sin\frac{\theta}{2}\cos\frac{\theta}{2}\cos\frac{3\theta}{2}$$

$$\sigma_{zz}(r,\theta)=\begin{cases}0, & \text{plane stress}\\ \nu(\sigma_{xx}+\sigma_{yy}), & \text{plane strain}\end{cases}$$

Since $\sigma_{yz} = \sigma_{xz} = 0$, $\sigma_{zz} = \sigma_3$ is a principal stress. The other two principal stresses in the crack plane are given by [70]

$$\left.\begin{matrix}\sigma_1(r,\theta)\\ \sigma_2(r,\theta)\end{matrix}\right\}=\frac{1}{2}(\sigma_{xx}+\sigma_{yy})\pm\sqrt{\frac{1}{4}(\sigma_{xx}-\sigma_{yy})^2+\sigma_{xy}^2} \tag{2.5}$$

One of the fundamentals of the LEFM is that, under the conditions of Mode I fracture, one variable is sufficient to describe the stress and strain field at the tip of a crack, and also to predict the onset of unstable crack propagation. This variable is the so-called stress intensity factor, K, and is the function of the crack length a, the component geometry Y_c and the applied loading σ, seen in Eq. (2.6). Stress intensity factor, K, is a significant parameter since it is used in fracture mechanics to predict stress state around the crack tip caused by external load and provide the failure criterion for brittle materials.

$$K=\sigma Y_c\sqrt{\pi a} \tag{2.6}$$

The local stress intensities of the out of plane kinked or deviated crack tip can be evaluated using crack deflection mechanics (Fig. 2.22). Assuming the crack tip deviates from the original growth plane by an angle α, then the local mode I and mode II stress intensities k_1 and k_2 at the deflected crack tip will be represented as Eq. (2.7) [71].

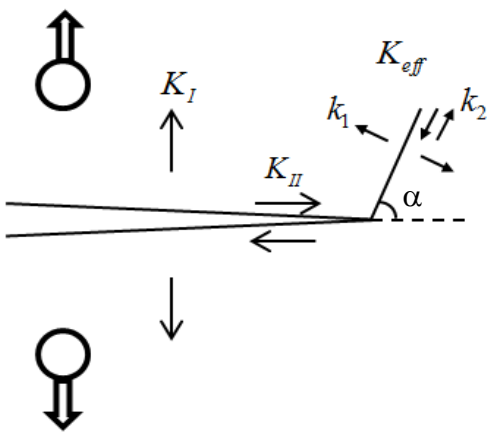

Fig. 2.22 Schematic diagram of global K_I and K_{II} and local k_1, k_2 at the crack-tip in the loaded compact tension test-piece

$$k_1(\alpha) = c_{11}(\alpha)K_I + c_{12}(\alpha)K_{II}\ ,\ k_2(\alpha) = c_{21}(\alpha)K_I + c_{22}(\alpha)K_{II} \tag{2.7}$$

where K_I and K_{II} are the applied mode I (opening) and mode II (shearing) stress intensity factors respectively. The coefficients C_{11}, C_{12}, C_{21}, C_{22} are expressed as following,

$$\begin{aligned} C_{11} &= \frac{1}{4}(3\cos\alpha/2 + \cos 3\alpha/2) \\ C_{12} &= -\frac{3}{4}(\sin\alpha/2 + \sin 3\alpha/2) \\ C_{21} &= \frac{1}{4}(\sin\alpha/2 + \sin 3\alpha/2) \\ C_{22} &= \frac{1}{4}(\cos\alpha/2 + 3\cos 3\alpha/2) \end{aligned} \tag{2.8}$$

The effective stress intensity at the tip of the deflected crack tip, K_{eff} can then be calculated by the mode I and mode II contributions in terms of the strain energy release rate [71],

$$K_{eff} = 0.5k_1 + 0.5\sqrt{k_1^{\ 2} + 6k_2^2} \tag{2.9}$$

a. R-curve

Extrinsic toughening, which is relevant for brittle materials (including dentin and bone), invariably results in resistance-curve (R-curve) behaviour, i.e. the need for a progressively increasing applied driving force to sustain crack extension [72, 73]. The R-curve provides an assessment of the fracture toughness in the presence of subcritical crack growth (Fig. 2.23). It involves measurements of the crack-driving force as a function of crack extension. The value of the driving force at ($\Delta a \rightarrow 0$) provides a measure of the crack-initiation toughness, whereas the slope (or maximum value) of the R-curve can be used to characterize the crack-growth toughness [39, 44, 74-76].

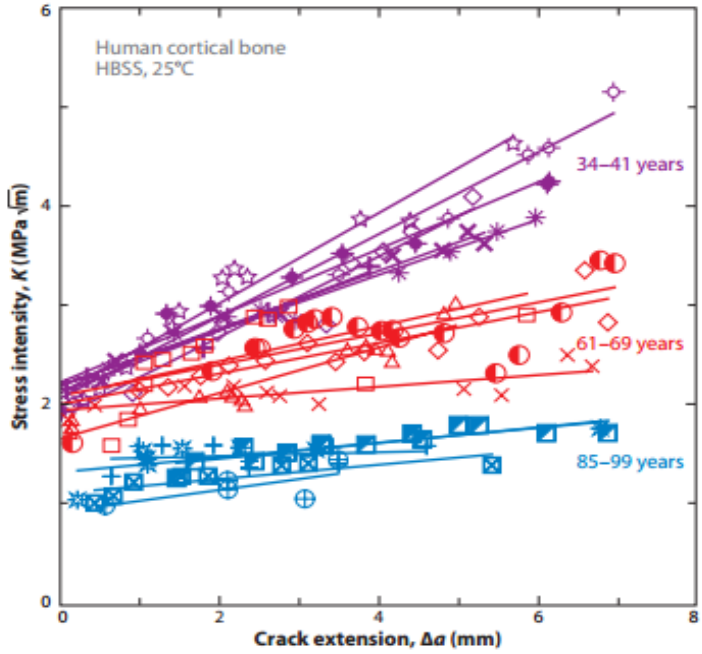

Fig. 2.23 Crack-resistance curves (R-curves) for stable ex vivo crack extension in human cortical bone as a function of age ranging from 34–41 years to 85–99 years, tested in Hanks' Balanced Salt Solution (HBSS) at 25˚C. The crack-initiation toughness, K_0, is indicated by the intercept of the R-curve on the stress intensity axis at $\Delta a \rightarrow 0$. The crack-growth toughness is given by the slope of the R-curve [72].

To evaluate the toughness of the material which is subjected to large plastic deformation, an R-curve approach based on a nonlinear-elastic fracture mechanics approach (i.e. plastic-elastic fracture mechanics) is essential to provide a more reliable assessment of the crack-tip stress and also valuable to capture the toughening contribution from the energy consumed in plastic deformation prior to and during fracture [4]. The best approach appears to be the use of the J-integral as the crack-driving force, where J is the nonlinear strain energy release as mentioned before and this will be introduced in detail in Section 2.6.2.

b. Fatigue crack growth

Different from the characterisation of the crack growth under monotonic load using R-curve, sub-critical crack growth under cyclic load much lower than the critical load is another option to assess the crack growth and fracture resistance [12]. Since the stress intensity factor K provides a reliable parameter for the crack driving force, Paris introduced a new method to assess the crack growth rate under cyclic loading condition [77]; that the crack growth rate (i.e. propagation distance per cycle) can be determined by stress intensity

range, $\Delta K = K_{max} - K_{min}$. K_{max} and K_{min} are the stress intensity factor corresponding to the maximum and minimum applied load. The relationship between these parameters can be expressed as

$$\frac{da}{dN} = C(\Delta K)^m \tag{2.10}$$

This equation is called Paris Law, which is widely used as the fracture mechanics theory for crack growth under fatigue conditions. There exists a threshold value of ΔK below which fatigue cracks will not propagate. ΔK_{th} is the threshold of stress intensity range that is defined as the driving force to make the crack growth rate reach 1×10^{-6} mm per cycle. Generally, the fatigue crack growth process consists of three stages, as seen the typical curve in Fig. 2.24. That is (I) the initiation region; (II) subcritical propagation region and (III) calamitous fracture region. In region I, the crack growth is shear driven, and the growth rate increases very slowly. This is because in this stage the crack interacts with the microstructures, beginning to spread from local position to the neighbouring grains, which includes crack deflection when passing through the grain boundaries and for the very short cracks, the energy required to get through is high. Region II is called the linearly propagation stage, which can be fitted by the Paris law. If region II includes the dominating part of the fatigue life, the fatigue life can be directly estimated by integrating Paris' Law. The crack is insensitive to microstructure and, if it is tensile stress driven, stably grows with the increasing driving force (Fig. 2.25) until region III, the failure stage. During failure stage crack growth rate increases dramatically and quickly propagates all the way through as it approaches the static critical stress intensity factor K_{IC}.

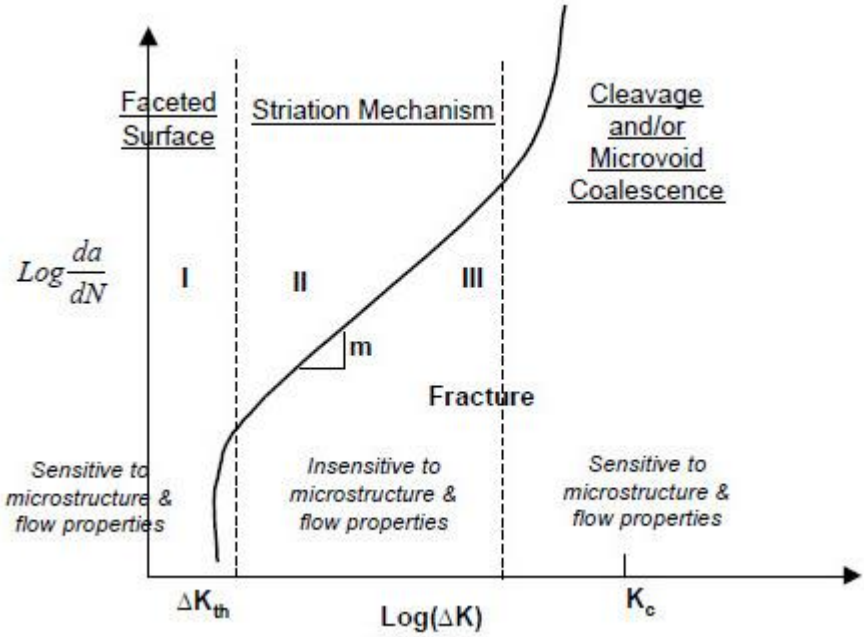

Fig. 2.24 Plotting log-log curve of fatigue crack growth rate versus stress intensity range [78].

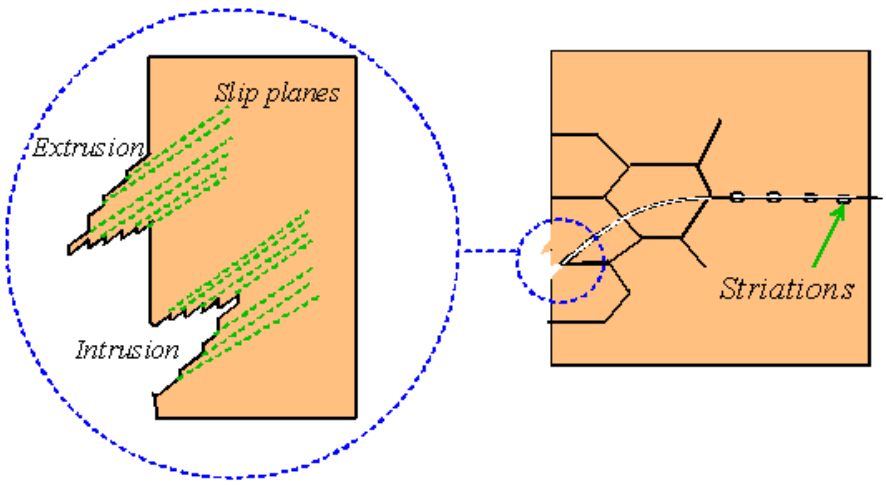

Fig. 2.25 The schematic of fatigue crack growth during the first two stages. In the first stage the crack growth is primarily caused by the shear of the slip planes whereas in the second stage the crack growth is subjected to the tension perpendicular to the crack plane, leaving striations at the wake of the crack-tip [79].

The parameters *C* and *m* values depend on the frequency, loading environment, loading history, and stress ratio [80] used. For the bone and dentin samples the crack growth rate is also related to the depth the crack reaches to in the sample [45], the ages of the animal or human that the teeth come from, the orientation the crack propagates relative

to the tubules [9], the hydration status of the sample [12] and even the irradiation [43]. However, the Paris Law doesn't take mean stress (R-ratio) into account from the equation, nor the history effects. It works well only for long cracks, under LEFM theory, and uni-axial loading. Currently some more problems need to be explored such as the retardation mechanism of overload, the crack closure effect, short crack theory and multi-axial loading condition.

It is generally thought that tooth failure results either from catastrophic impacts caused by high occlusal stresses or, more likely, by cyclic fatigue-induced subcritical crack growth. For this reason, a large range of studies have investigated the effect of prolonged fatigue cycling on human dentin [12, 80-84], as such research outcomes are important for the development of replacement materials for restorative dentistry. The crack growth mechanism in dentin in cyclic load environment is shown in (Fig. 2.26) [83]. Fatigue-static -fatigue experiments show that alternating blunting and resharpening are the main mechanisms for crack propagation and that static loading has little effect on crack growth. Blunting of the crack during the loading portion of the cycle is due to permanent plastic deformation. With such plastic deformation limited to the vicinity of the crack tip, upon unloading the surrounding linear elastic material compresses the deformed near-tip region resulting in resharpening of the crack tip, with the new crack area contributing to crack advance.

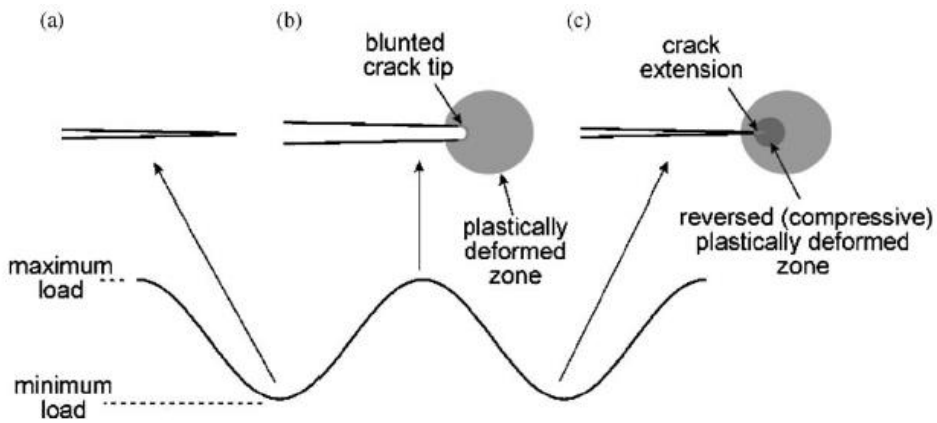

Fig. 2.26 Schematic illustration of the proposed mechanism of alternating crack-tip blunting and resharpening for fatigue-crack growth in dentin. (a) the crack at the beginning of the loading cycle, (b) the blunted crack at the peak of the loading cycle, and (c) the resharpened, extended crack after unloading [83].

Previous dentin research presented the point that the blunting of the crack tip is time-dependent, with the blunting increasing with a longer holding time. This implies that if the cycling frequency is low, longer time will be spent at the peak load of each cycle, more blunting will occur, resulting in more crack advance per cycle than with higher frequencies, i.e. consistent with the results in Fig. 2.27 [83].

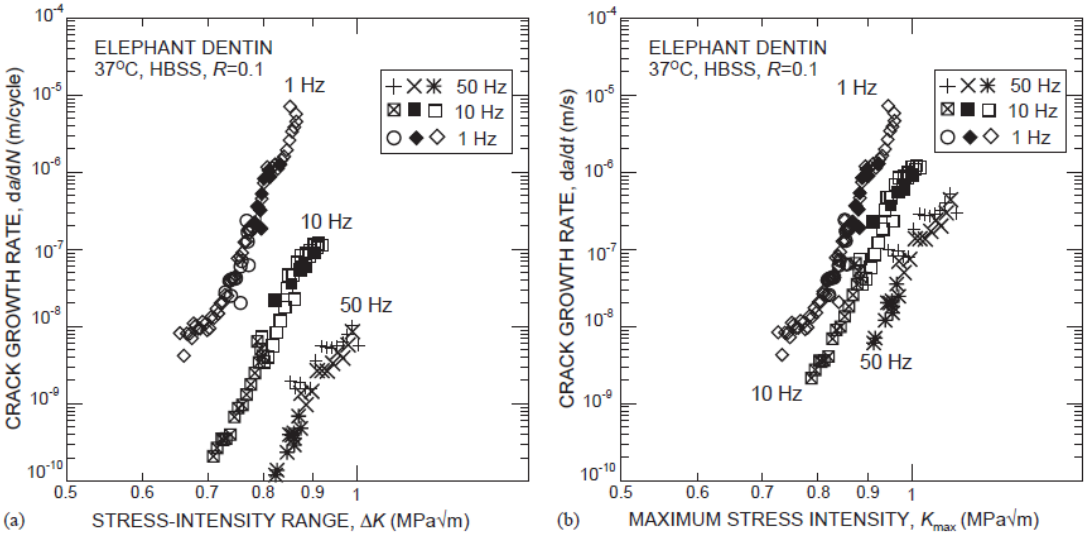

Fig. 2.27 Comparison of different cycling frequencies effect on crack growth rate of hydrated elephant dentin samples. The nominal crack growth direction is vertical to the tubule long axis, and the crack plane is parallel to the tubules [83].

The parameters of Paris law ($\frac{da}{dN}=C(\Delta K)^m$) under different frequencies are showed in table below [83]. It is shown that the constant C is lower with the increase of frequency, and the exponent m is higher at low frequency, which may show sensitivity to the stress intensity factor range.

Table 2.4 Constants in the Paris law for fatigue-crack growth in hydrated elephant dentin with the crack growing in anti-plane parallel direction (see Fig. 2.4d) [83].

Test frequency (Hz)	Constant *C* (m/cycle · (MPa√m)$^{-m}$)	Exponent *m*	Coefficient of determination (R^2)
1	1.8×10^{-4}	26.5	0.96
1	5.1×10^{-4}	32.1	0.65
1	6.4×10^{-4}	32.1	0.70
10	3.0×10^{-6}	28.5	0.94
10	1.8×10^{-6}	26.5	0.91
10	4.7×10^{-7}	16.7	0.87
50	9.6×10^{-9}	12.1	0.81
50	8.6×10^{-9}	15.2	0.91
50	1.1×10^{-8}	22.0	0.60

Moreover, the fatigue crack growth rate is related to the stress ratio (R value), which is defined as the ratio of minimum and maximum load during fatigue process:

$$R = \frac{P_{\min}}{P_{\max}} \tag{2.11}$$

In unrestored teeth, the natural cyclic stress ratio is estimated to be R = 0. However, some changes at the restored teeth material such as shrinkage in volume, residual stress etc, will induce either a tension-tension environment or a tension-compression environment [80]. It is shown that when R > 0.1, with the increase of R crack growth rate will increase drastically but when R < 0.1 there is no significant variation trend for the crack growth (Fig. 2.28). The stress intensity threshold ΔK_{th}, the minimum stress intensity range to initiate a short crack in fatigue loading condition, of the dentin decreased with an increase in *R*. The ΔK_{th} for R < 0.5 is approximately 1.0 $MPa\sqrt{m}$, decreasing to nearly 0.4 $MPa\sqrt{m}$ at a stress ratio of 0.50. Thus the R ratio will accelerate crack growth rate if it is larger than 0.1 and lower the crack initiation stress intensity threshold if it is larger than 0.5.

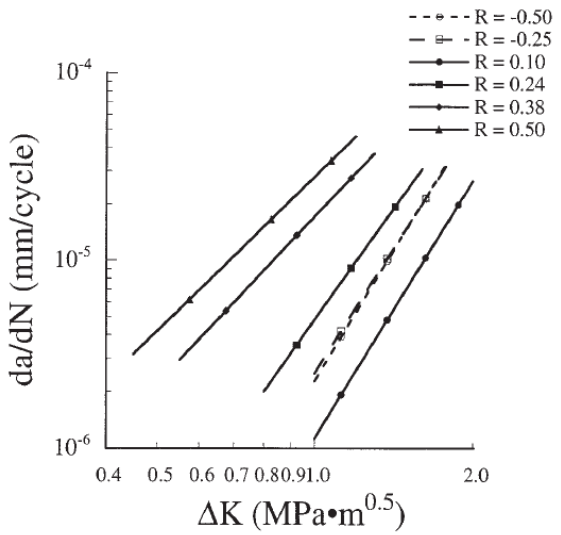

Fig. 2.28 Cycling crack growth rates over the range of different stress ratios in hydrated bovine dentin. The crack growth direction is 45 ° to the tubule long axis and the crack plane was parallel to the tubules [80].

In cases where the crack growth plane is perpendicular to the tubules under cyclic loading striations can be seen, which are caused by the repeated blunting and resharpening process during loading and unloading. It is several cycles rather than every single cycle that causes a obvious striation (Fig. 2.29) [40].

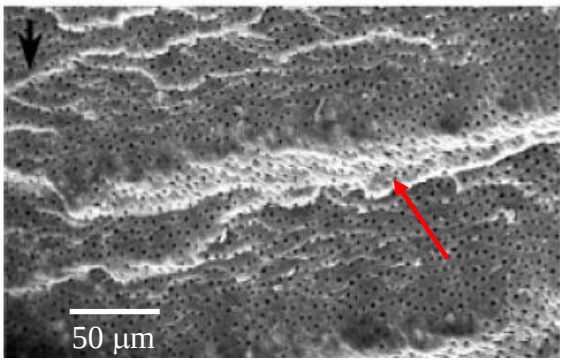

Fig. 2.29 Striations (pointed out by red arrows) created by cycling load on fracture surface of hydrated human dentin with the crack growing perpendicular to the tubules [40]. The black arrow indicates the crack growth direction.

c. Crack Opening Displacement

Crack opening displacement (COD) is a parameter describing the near-tip crack profile and predicting the fracture because the crack profile near the tip reflects the overall severity of the plastic deformation [70].

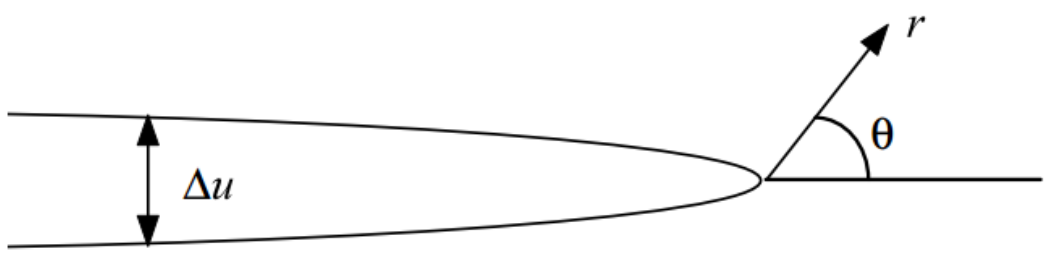

Fig. 2.30 Definition of the crack opening displacement

COD is defined as the relative opening movement of the upper and lower crack flanks (Fig. 2.30):

$$\Delta u(r) = u_y(r, \theta = \pi) - u_y(r, \theta = -\pi) \tag{2.12}$$

where $\Delta u(r)$ is the crack opening displacement, r is the distance from the crack-tip, y is the direction perpendicular to the crack plane. The displacement field around the crack-tip is given as [85]

$$\begin{Bmatrix} u_x \\ u_y \end{Bmatrix} = \frac{K_I}{2E}\left(\frac{r}{2\pi}\right)^{1/2} \begin{Bmatrix} (1+\nu)[(2k-1)\cos(\theta/2) - \cos(3\theta/2)] \\ (1+\nu)[(2k-1)\sin(\theta/2) - \sin(3\theta/2)] \end{Bmatrix} \tag{2.13}$$

Replace u_y in Eq. (2.12) using Eq. (2.13),

$$\Delta u(r) = 2\frac{K_I}{E}\sqrt{\frac{r}{2\pi}}(1+\nu)(k+1) \tag{2.14}$$

where

$$k = \begin{cases} 3-4\nu & \text{plane strain} \\ \dfrac{3-\nu}{1+\nu} & \text{plane stress} \end{cases} \tag{2.15}$$

substituting for *k*, the above can be rewritten as

$$\Delta u(r) = 8\frac{K_I}{E'}\sqrt{\frac{r}{2\pi}} \tag{2.16}$$

where

$$E' = \begin{cases} \dfrac{E}{1-\nu^2} & \text{plane strain} \\ E & \text{plane stress} \end{cases} \tag{2.17}$$

Eq. (2.16) predicts a parabolic dependence of $\Delta u(r)$ with distance *r*. COD is a useful measure of the effective stress intensity K_I^{eff} , thus the difference between K_I^{eff} and K_I^{app} indicates the extent of crack shielding. It is also possible to measure the crack opening load [86-88].

2.6.2 Elastic Plastic Fracture Mechanics (EPFM)

Linear elastic fracture mechanics (LEFM) is valid only as long as nonlinear material deformation is confined to a small region surrounding the crack tip. If the plastic deformation zone is significant compared with the crack length and sample size, it is virtually impossible to characterize the fracture behaviour with LEFM, and alternative fracture mechanics model is required.

Elastic-plastic fracture mechanics applies to materials that demonstrates nonlinear behaviour (i.e. plastic deformation). The main elastic-plastic parameters being widely used is *J contour integral*, regardless of the sample size, under the circumstances of large crack-tip plasticity.

The J contour integral, a parameter based on elastic-plastic fracture mechanics (EPFM), is used to evaluate the materials toughness under which the toughening effect of

plastic deformation around the crack tip and its energy relaxation contribution is taken into account [16, 28, 89, 90]. Yan et al compared the results of J-integral using EPFM with K_c determined using LEFM on dentin samples [4] (Table 2.5) which shows that the fracture toughness (K_{Jc}) estimated using EPFM is found to be 32.5% greater than the critical stress intensity factor (K_c). In addition, the J integral of anti-plane parallel specimens is significantly greater than that of in-plane parallel specimens.

Table 2.5 Comparison of the dehydrated human dentin fracture toughness evaluated by K and J based parameters [4]. In-plane and anti-plane parallel directions are shown in Fig. 2.4c and d respectively.

	In-plane parallel dentin	Anti-plane parallel dentin
E (GPa) ($n = 3$)	15.0±0.5	15.4±0.4
σ_{ys} (MPa) ($n = 3$)	153.2±13.5	165.3±10.7
K_c (MPa m$^{1/2}$) ($n = 10$)	2.4±0.2	2.5±0.2
J_{el} (kPa m) ($n = 10$)	0.39±0.06	0.41±0.06
J_{pl} (kPa m) ($n = 10$)	0.20±0.09	0.30±0.11
J_{total} (kPa m) ($n = 10$)	0.59±0.11	0.71±0.12
K_{Jc} (MPa m$^{1/2}$) ($n = 10$)	3.1±0.3	3.4±0.3
Water (%) ($n = 5$)	9.7±0.4	9.5±0.3
Organics (%) ($n = 5$)	22.7±0.3	22.6±0.5
Minerals (%) ($n = 5$)	67.6±0.3	67.9±0.6

Thus, the direct application of LEFM to dentin is questionable since the aforementioned toughening mechanisms and collagen can alter crack propagation and increase the plasticity in dentin [91]. It has been shown that the J integral can be used to better describe the fracture behaviour of materials with moderate yielding of bone and dentin than K_c does. The J-integral consists of two parts, the elastic deformation part of J-integral (J_{el}) and the plastic deformation part (J_{pl}), as follows [4]:

$$J_{total} = J_{el} + J_{pl}\ ,\ J_{el} = \frac{K_c^2}{E'},\ \ J_{pl} = \frac{1.9A_{PL}}{Bb_0} \tag{2.18}$$

where $E' = E$ for plane-stress conditions and $E' = E / (1 - \nu^2)$ for plane strain condition (E is elastic modulus, ν is Poisson's ratio), B is the specimen thickness, $b_0 = W - a_0$ is the height of the uncracked ligament (W is the specimen height, a_0 is the notch depth). A_{PL} is the area of plastic deformation (Fig. 2.31) [92]. The toughness is generally tested by load-

displacement experiments where the displacement rate is controlled under a constant value and then the load-displacement or strain-stress curve is generated. Fig. 2.32 illustrates the contribution of two components (J_{pl} and J_{el}) to the fracture toughness of dentin evaluated by EPFM. From panel B it is clearly showed that the A_{PL} component is larger than A_{EL}, which can explain why the J integral of anti-plane parallel specimens is significantly greater than that of in-plane parallel specimens.

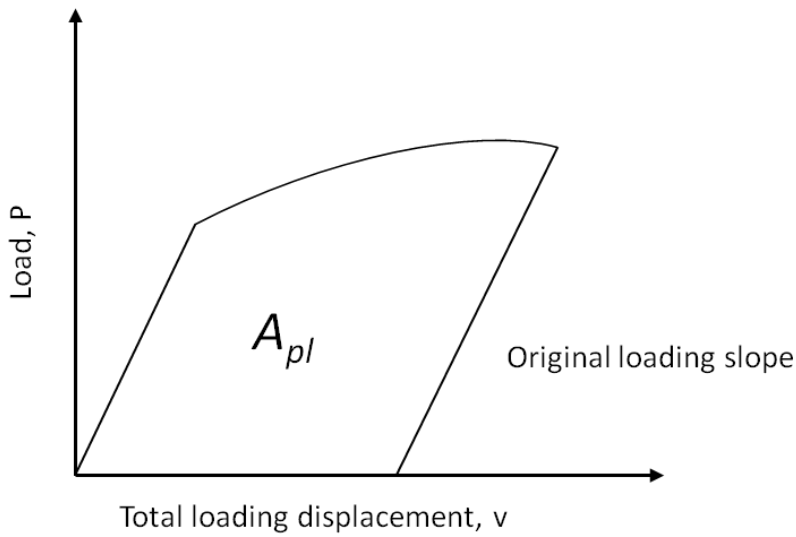

Fig. 2.31 The definition of the area of plastic deformation (A_{PL}) for J-integral calculation.

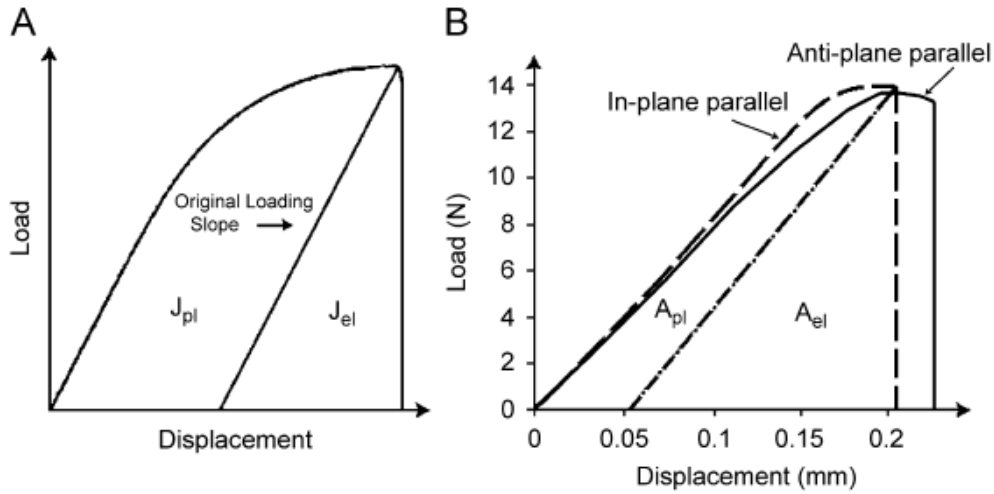

Fig. 2.32 Load – displacement diagrams of J integral measurements. (A) An illustrative diagram showing what J_{pl} and J_{el} represent. (B) Real load – displacement curves of one in-plane parallel and one anti-plane parallel specimens. The dotted-dashed line divides the in-plane parallel curve into area of the plastic deformation (A_{pl}) and area of elastic deformation (A_{el}) [4].

It is important to note that the measurement above is for the single-value fracture toughness evaluation, which is different from that evaluated by resistance curve under the process of subcritical crack growth. Similar to *K* based R-curve, it is also achievable to measure the J based R-curve, J-R curve. The form for the continuing measurement of J-curve is as follows,

$$J_{(i)} = \frac{K_{(i)}^{2}}{E'} + J_{pl(i)} \tag{2.19}$$

Where *i* stands for the a consecutive measuring points in order (i.e. 1,2,...N). Every single measuring point correspond to the $J_{(i)}$, $K_{(i)}$, and $J_{pl(i)}$ based on the different crack length. Plotting all the $J_{(i)}$ values versus the different crack lengths will create the J-R curve figure [92].

It should be pointed out that the measured plastic zone size for dentin in this study is less than 0.05 of the crack length in the hydrated dentin, accordingly in this case LEFM is reasonably chosen for the research of fracture problem.

2.7 Cohesive Zone Model of Crack Bridging

Crack bridging is closely related to the anisotropic fracture toughness of elephant dentin. However, it can be challenging to quantify the bridging effect directly from the mechanical measurement. Cohesive zone model provides with a promising measure to simulate the physical process of crack growth in the fracture process zone by establishing the model based on mechanical test. This will help us to link the anisotropic fracture with the crack performance in the fracture process zone. Its predictive capability of R-curve, damage energy dissipation via crack growth simulations can give more insights into understanding the extrinsic shielding induced fracture anisotropy.

In linear elastic fracture mechanics (LEFM), the stresses at the crack tip are infinitely large assuming the existence of the perfect sharp crack. In practical, there is a critical stress at the crack tip causing the failure of the material. Great effort has been done trying to remove the stress singularity at the crack tip in LEFM, such as Irwin's and Dugdale's [93] theory. However, these work mostly used the parameters obtained from LEFM theory to solve the problem of crack tip singularity. Barenblatt [94] proposed a cohesive zone model to illustrate the fracture of the material avoiding the crack tip stress singularity. Based on his method, a zero-thickness band zone ahead of the crack tip is introduced to mimic the crack growth behaviour. The cohesive zone is assumed as two cohesive surfaces held close by a internal force, which is known as cohesive traction (Fig. 2.33). This traction can be viewed as the atomic bonding forces holding the two atomic layers together. Under load, the cohesive surfaces begin to separate relating a function describing the relationship between the displacement of the surfaces and the applied load. Physical crack tip growth can be defined as a critical value of the damage of the cohesive zone ahead of the crack tip.

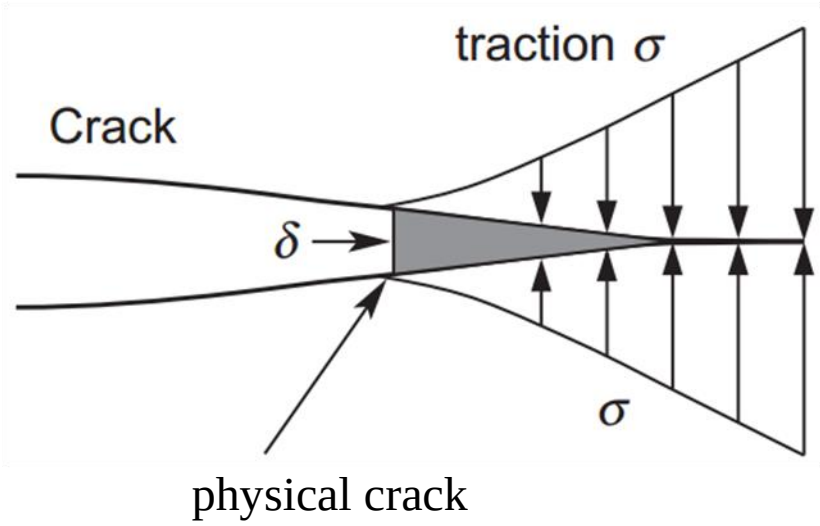

Fig. 2.33 The concept of cohesive zone ahead of the crack tip [95].

There are three basic hypotheses of the cohesive zone model, based on Barenblatt's theory: (1) The magnitude of the cohesive traction is on the order of the theoretical strength of the solid with the cohesive zone size much smaller than the crack length. (2) The size of the cohesive zone, the magnitude and the distribution of the cohesive traction the initiation of the crack growth are independent of the crack geometries and the applied loads. (3) There is no stress singularity at the crack tip and surrounding the crack tip. It should be noted that in the Barenblatt model, the position of the cohesive zone is within a small area just behind the crack tip. However, currently prevailing applications of cohesive zone assume it works ahead of the crack tip, imitating the physical fracture process. Fig. 2.34 demonstrates the role of the cohesive zone at different stages of the crack growth behaviour.

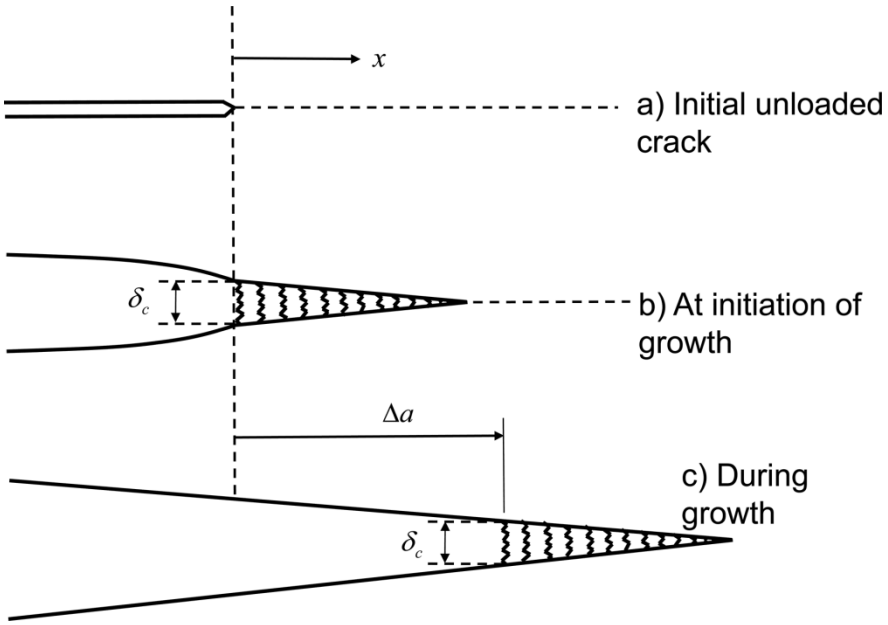

Fig. 2.34 The role of the cohesive zone at different stages of the crack growth behaviour [95].

Apart from eliminating the crack tip stress singularity, using cohesive zone model, it is also possible to represent the complex cracking processes, such as void nucleation, coalescence, microcracking and so on (Fig. 2.35) [96]. If the fracture occurs within a very thin band with little crack opening, the cohesive zone can be treated as a representation of the physical performance in the fracture process zone. However, for those cases in which there are complicated microstructure interactions, this method can be viewed as a hypothesis or approximation of the failure in the fracture process zone.

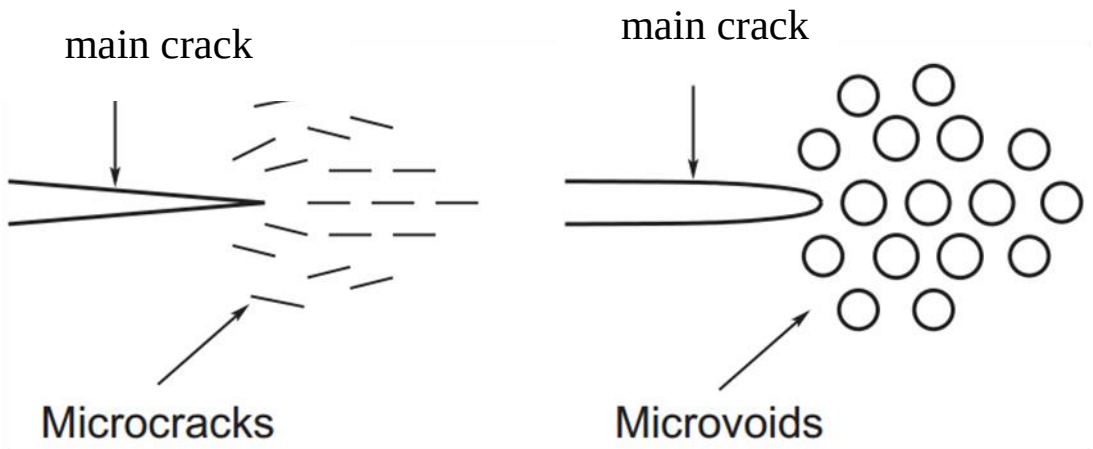

Fig. 2.35 Different microstructures ahead of the crack tip may introduce complex fracture process zone, which can be simulated by cohesive zone model [96].

The function describing the relationship between cohesive separation and traction is called cohesive law. A general form of the cohesive law is shown in Fig. 2.36. σc is the maximum traction before the degradation of the cohesive zone. δc depicts the critical separation of the cohesive zone, representing the complete failure. The area under the curve is cohesive energy density, which indicates the work of separating per unit area of the cohesive surfaces. If the fracture of the material occurs in a narrow deformation band, the cohesive law may be developed by considering the stress and deformation states in the narrow band [97]. Otherwise, a phenomenological cohesive law is often adopted and the parameters such as the maximum traction and the cohesive energy density need to be determined by experiment. Most researchers consider the work of separation per unit area of interface and the strength of the interface as the most two important parameters [98, 99]. Results indicate that the shape parameters have a relatively small influence. However, It is pointed out that a specific shape of the cohesive zone model can essentially affect numerical simulation of the fracture process [100], which suggests that it's not enough to simulate interface fracture process by only considering the strength and separation work. There are different cohesive traction-separation shape functions [101-104]. Above all the elementary functions used in cohesive zone models they can be classified as four main types [100]: (1) Linear, (2) trapezoidal, (3) parabolic, and (4) exponential (Fig. 2.37).

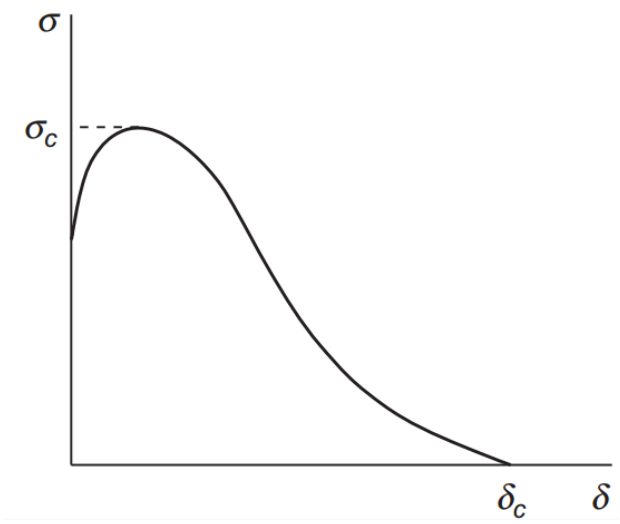

Fig. 2.36 A basic cohesive law illustrating the relationship between separation traction and separation displacement [96].

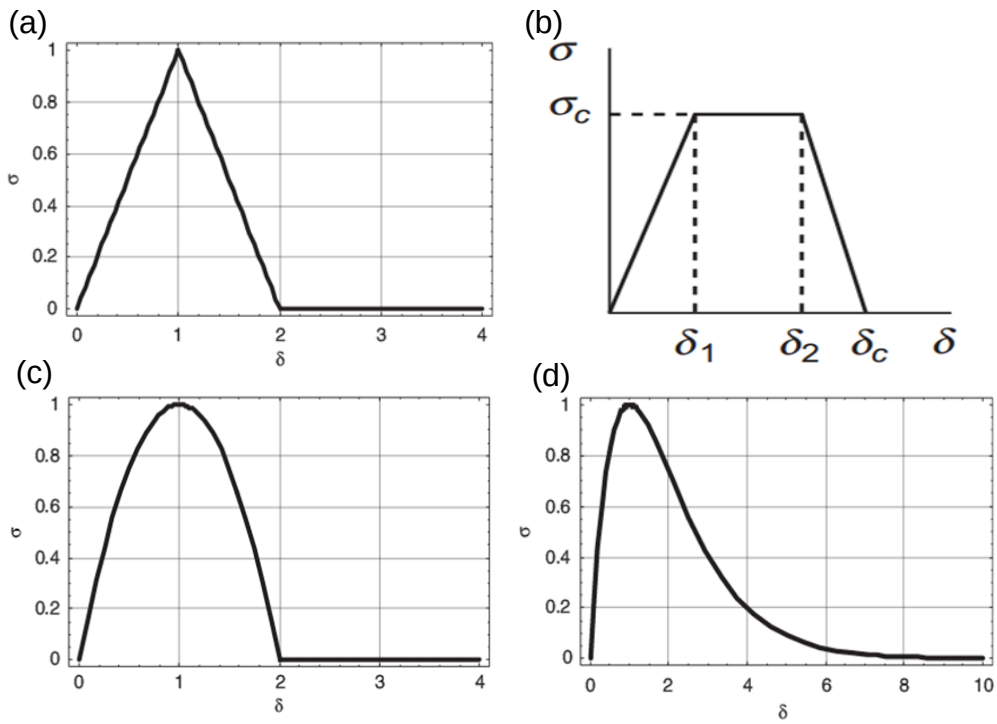

Fig. 2.37 Cohesive zone models of different shape function. (a) Linear softening (b) trapezoidal (c) parabolic and (d) exponential [100].

The cohesive zone model has become a popular tool for simulating the crack-tip toughening effect in the fracture process zone in the vicinity of the crack-tip for a variety of materials [105-113] especially those with an extensive damage zone, for example to

describe aspects of shielding in bone as a function of age [107], its anisotropic fracture behaviour [114] and its R-curve response [115]. The model can also be used to predict the stress distribution at the crack-tip of different extension length [115].The critical point of the application of cohesive zone model is how to establish the constitutive traction-separation law and validate it. To author's knowledge, most of the previous researchers established the model based on the indirect mechanical test result, e.g. displacement *vs* load curve. The best case scenario is to establish the model from the measured data of the crack itself, e.g. COD. This will be discussed in details in Chapter 7.

2.8 X-Ray Computed Tomography

High resolution X-ray computed tomography (CT) is a non-destructive technique that can be used to obtain images of the interior of micro-heterogeneous materials such as metal matrix composites, ceramics and biomaterials. Different from optical microscopy and scanning electron microscopy, X-ray CT enables to inspect the microstructure of the material underneath the sample surface, which is especially useful to observe the crack morphologies in the materials with extrinsic shielding mechanisms. In present study, the X-ray CT technique has been used to study the in-situ crack growth and crack opening in a self-designed loading rig.

2.8.1 Basic Principles

X-ray computed tomography is a transmission-based technique in which X-rays from a source pass through the material, and the photons transmitted are recorded by a CCD detector. A scintillator is used to convert the transmitted radiation into visible light to protect the CCD from the radiation (Fig. 2.38). Tomographic imaging consists of directing X-rays at an object from multiple orientations and measuring the decrease in intensity along a series of linear paths because of attenuation (Fig. 2.39). This decrease is characterized by Beer's Law Eq. (2.20) [116-120], which describes intensity reduction as a function path length and material linear attenuation coefficient. The attenuation coefficient of the material is dependent on wavelength, the density of the material and the atomic number, thus the total attenuation suffered by one beam of X-rays as it travels in a straight line (x,y_1) through an object can be represented by a line integral. Rather than taking just one 2D X-ray picture, known as a radiograph, hundreds or even thousands of radiographs

are taken of the object as it is rotated through 360°. The series of 2D radiographs are then reconstructed into a 3D image using specialized algorithm to reconstruct the distribution of X-ray attenuation in the volume being imaged. The sophisticated software packages coupled with powerful computers will enhance the structure visualization. The real advantage of CT lies in the fact that a virtual replica is created where one can slice through the layers of the object to reveal its internal structure, akin to peeling an onion. Further, in some cases one can then follow its structure as it changes over time.

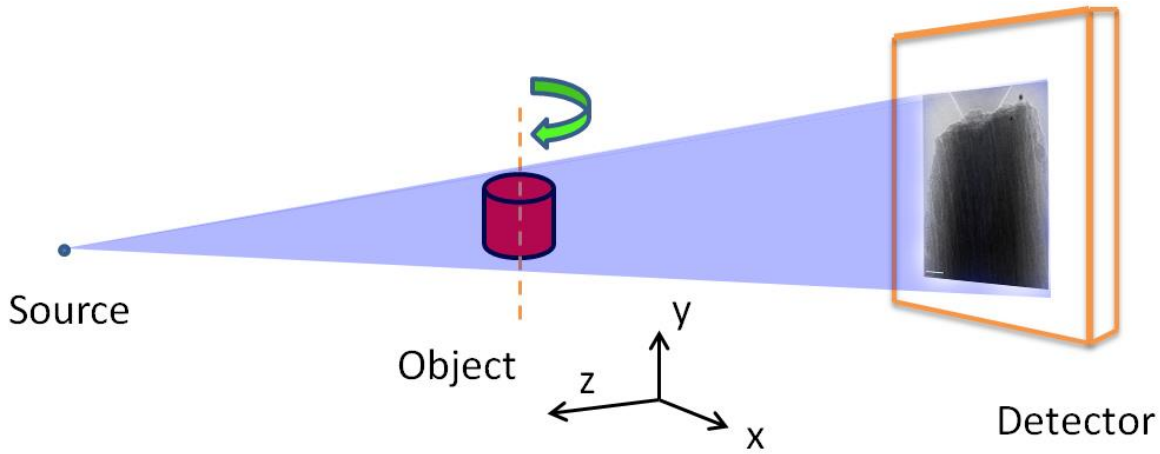

Fig. 2.38 A schematic illustration of the x-ray cone beam tomography setup

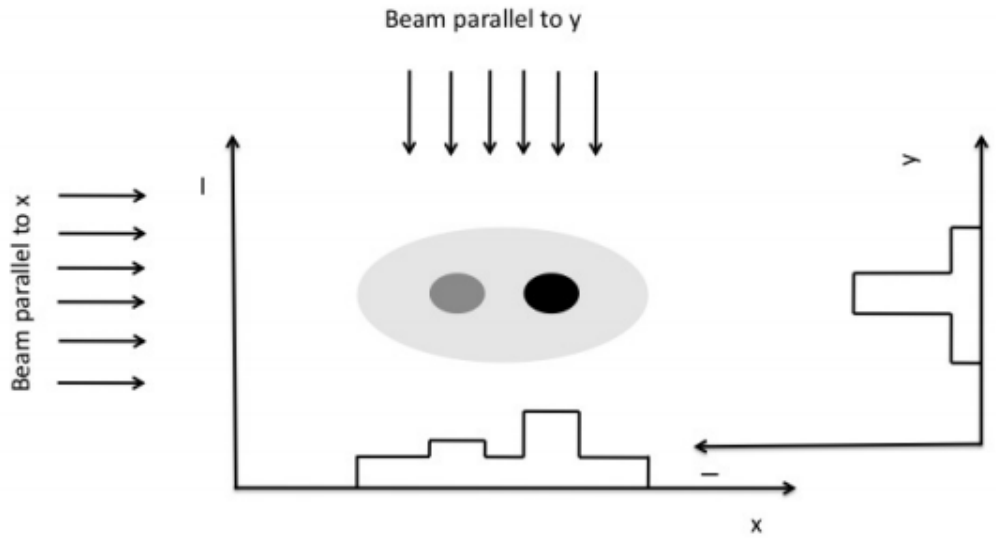

Fig. 2.39 Projection intensities from perpendicular directions of a component with three different linear attenuation coefficients.

$$I = I_0 e^{-\int \mu(\mathrm{x},\mathrm{y}_1)\mathrm{dx}}$$

$$\ln \frac{I_0}{I} = \int \mu(\mathrm{x}, \mathrm{y}_1)\,\mathrm{dx} \tag{2.20}$$

2.8.2 Reconstruction Methods

There are a number of the different reconstruction algorithms used for different cases. The most widely used reconstruction method is *Filtered Back Projection*. In this method, a projection is formed by combining a set of line integrals. For a complete scan, a collection of projections at different rotation angles of the object are recorded (Fig. 2.40). The received projections at each angles are then backprojected to reconstruct the object [121-123].

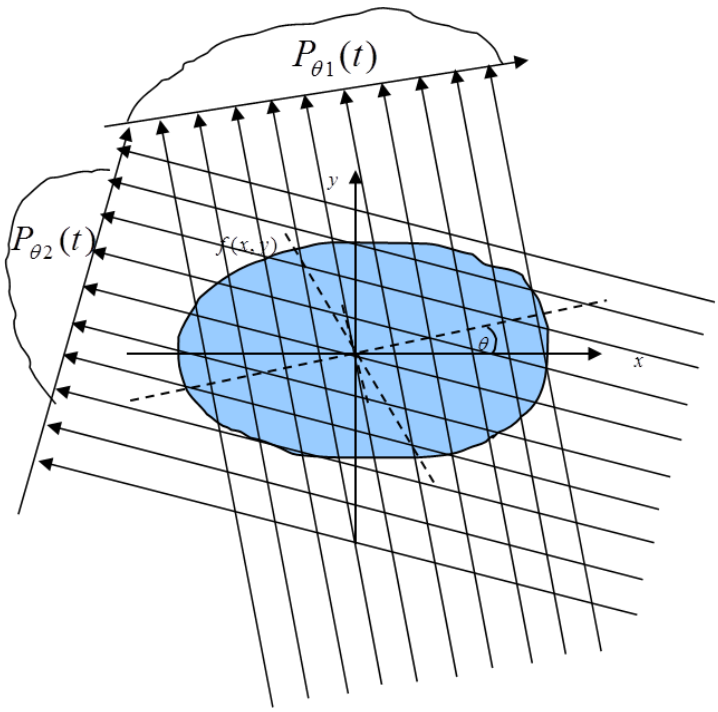

Fig. 2.40 Projections taken at a number of angles of the same slice using the parallel beam [124].

It is found that the image is back projected by setting the same values for all the pixels along the integral path and the final image is obtained by the summation of all the back projected rays [125, 126], as in seen in Fig. 2.41. However, in practice, the back projection method cannot correctly present the actual image since it is very blurry at the edges of the feature (Fig. 2.41b). This occurs because a single point in the true image is reconstructed as a circular region that decreases in intensity away from the centre. In order to reduce the effect of this blurred edge, a weighted filter (Fig. 2.42) can be applied to the 1-D projection before back projection (Fig. 2.43).

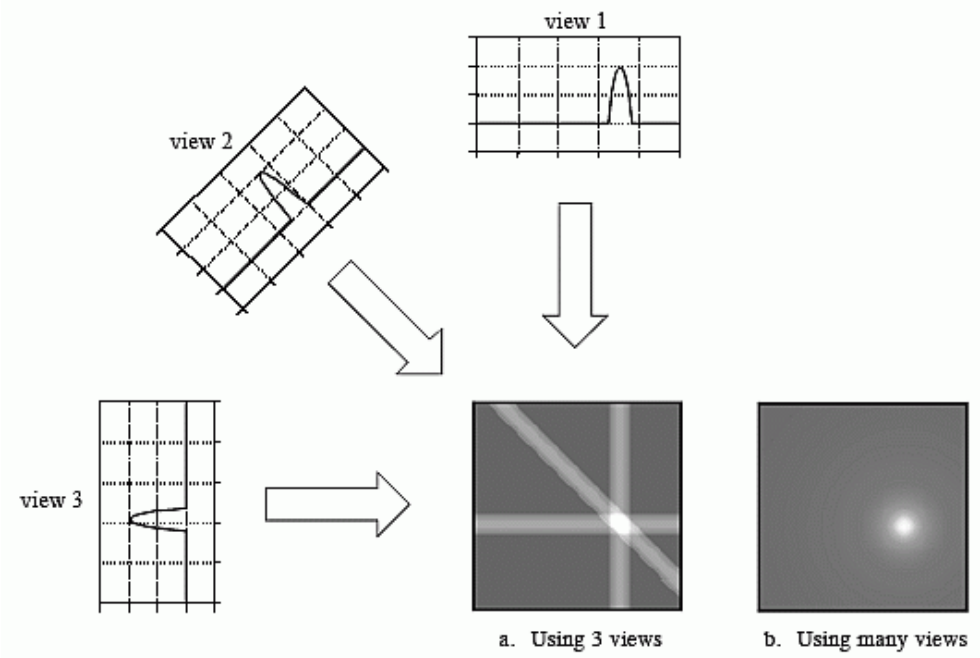

Fig. 2.41 Back projection reconstruction. This method simply smears back the image based on the projections of the attenuation coefficient at different angles along the integral path with the same value, which consequently makes the final image blurry [127].

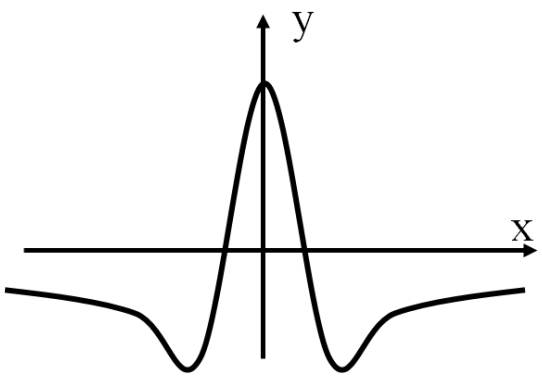

Fig. 2.42 1-D filter used for the spectrum obtained by Randon transformation to deblurr the image.

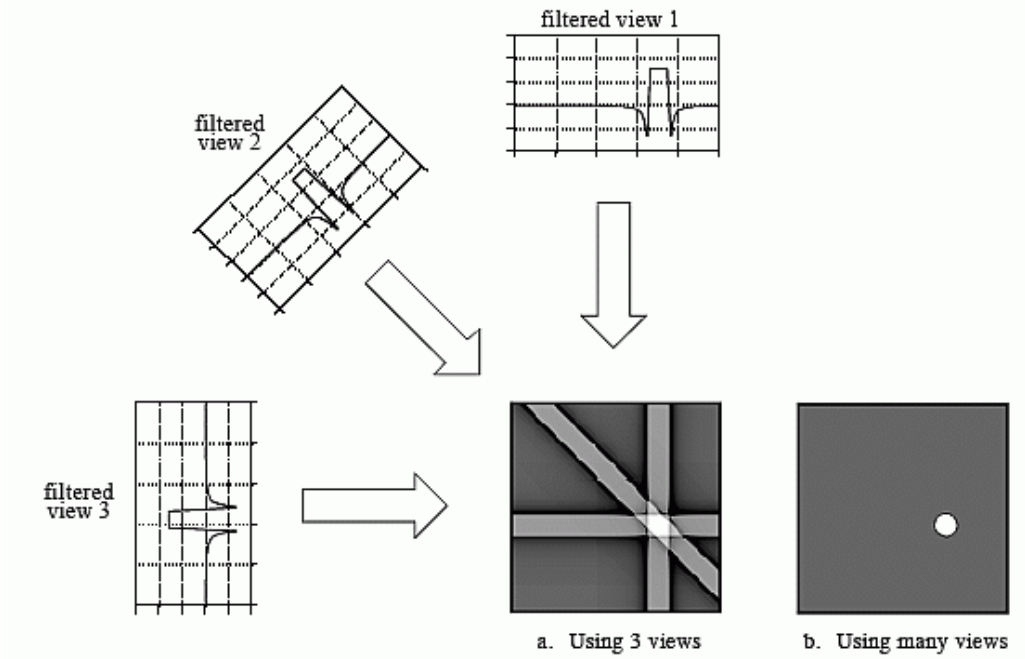

Fig. 2.43 Filtered back projection using a filter kernel to filter the 1-D projection before back projection to remove the blurry [127].

Filtered back projection is a technique to correct the blurring generated in simple back projection [128, 129]. As is demonstrated in Fig. 2.43, each 1-D projection is filtered before the back projection by means of one-dimensional convolution with a filter kernel. These filtered 1-D projections are then back projected to provide the reconstructed image, which is more close to the actual image. By increasing the number of projections, and with more pixels in the reconstructed image, the reconstructed image will be more coincidence with the real image. The angular increment of each projection should be small enough to allow adequate sampling of features in the object. Early work on CT reconstructions demonstrated that the ideal number of projections lies between $q\pi/4$ and $q\pi/2$, where q is the maximum width of the object in pixels [130]. For example, an object filling the field of view on a 2000-pixel wide detector would require between 3142 and 1570 projections.

However, in some cases the fast scan and low dose radiation conditions are required, as a result, the angular increment has to be sacrificed. Reconstruction using FBP is no longer suitable for these cases, instead, a more advanced reconstruction algorithm called *Iterative Reconstruction* (IR) is developed. While analytical algorithms such as the commonly used FBP are based on only a single reconstruction, IR uses multiple repetitions in which the current solution converges towards a better solution.

The basic process of IR can be shown in Fig. 2.44. The iteration process begins with a forward projection of an empty image estimate or a standard FBP reconstruction. Generally, the better the prior images match the final images, the faster the process converges towards a stable solution. In a second step, the forward projected data are compared to the real measured raw data in order to compute a corrected data. The iterative process is finished when either a fixed number of iterations is reached, or the update for the current data estimate is considered small enough or when a predefined quality criterion in the image estimate is fulfilled. Otherwise, the corrected data is back projected onto the volumetric object estimate and then forward projected to start step 1 again.

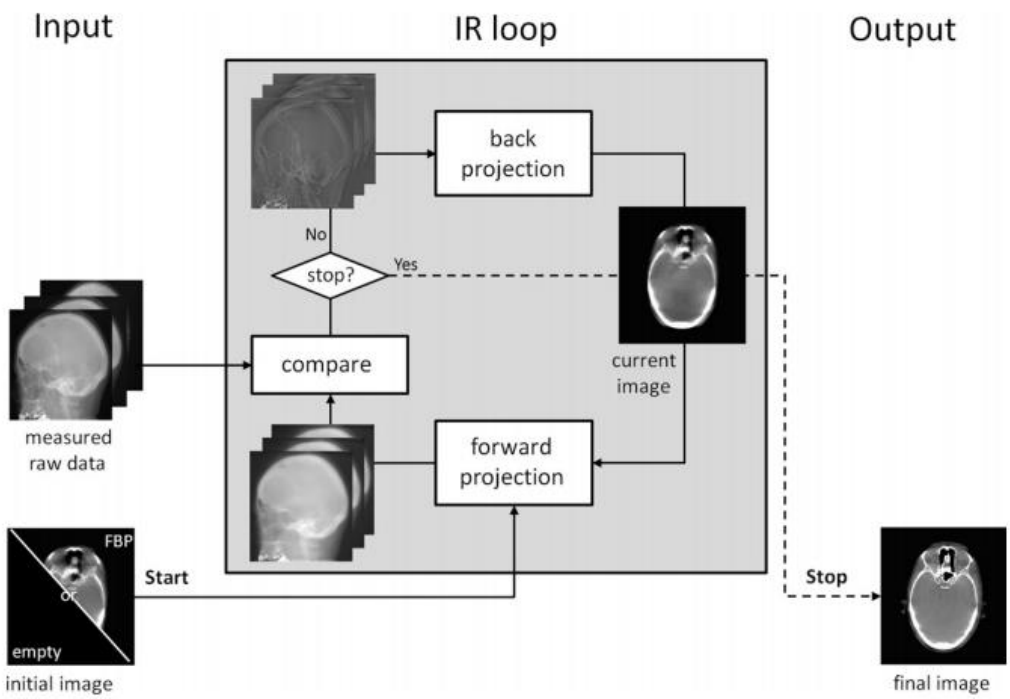

Fig. 2.44 The general procedure of the IR reconstruction [131].

2.8.3 Phase-Contrast Imaging

Absorption contrast imaging is suitable to inspect a material which has several components with distinct attenuation coefficients. However, for materials that are weakly absorbing or the different phases in the material are quite similar in the absorption capability, such as Al / SiC composite [132, 133], or biological soft tissue [134-136], the conventional absorption contrast imaging cannot provide sufficient details of the scanned object due to the low contrast. Phase-contrast imaging, which can be divided into in-line

phase-contrast and Zernike phase-contrast imaging, exploiting the Fresnel diffraction and dubbed phase-contrast imaging method [137, 138], is a significant improvement of the conventional attenuation-based imaging technique in certain cases.

a. In-line Phase Contrast

It is based on the principle that the phase of the x-ray wavefront changes when passing through the sample with variation in thickness and x-ray refractive index, and consequently leads to a phase difference φ when reaching the detector (Fig. 2.45) [139]. It is seen from the figure, that when the detector is close to the object, a conventional absorption contrast imaging is obtained. With the detector moving far away from the object, the visualization based on the phase change due to the refractive index variation is more obvious. However, this doesn't mean that it is the best to move the detector as far away as possible. The quality of the phase-contrast imaging is closely related to the spatial or lateral coherence of the beam L_{coh} [140], which can be expressed as

$$d = \frac{\lambda l}{D_s} = \frac{\lambda}{\gamma} \tag{2.21}$$

where l is the source-object distance, D_s is the source size, λ is the wavelength and γ is the angular width of the source seen from the signal detection point. Accordingly, a very small spot size or large source-object distance enhance the contrast of the image. The parameter R_2 should be selected carefully. Too large R_2 can lead to the blurring of the image, which is defined as sR_2/R_1 [141], here s is the spot size. An example of the dependence of phase-contrast quality on R_2 is shown in Fig. 2.46. It is found that when R_2 is small, only the features absorb the x-ray a lot can be seen. With R_2 increase, the phase-contrast feature can also be seen. There is an optimum R_2 that can make the contrast and the feature magnification most idea, as is seen in panel (c). If R_2 is too large, all the features will be blurred. Apart from the advantages of inspecting light materials, phase-contrast imaging can reduce the dose that the object suffered during the scan because the degradation of the contrast with the rise of x-ray energy of phase-contrast imaging is less rapidly compared with the absorption contrast imaging. This is quite important for some clinical applications [136].

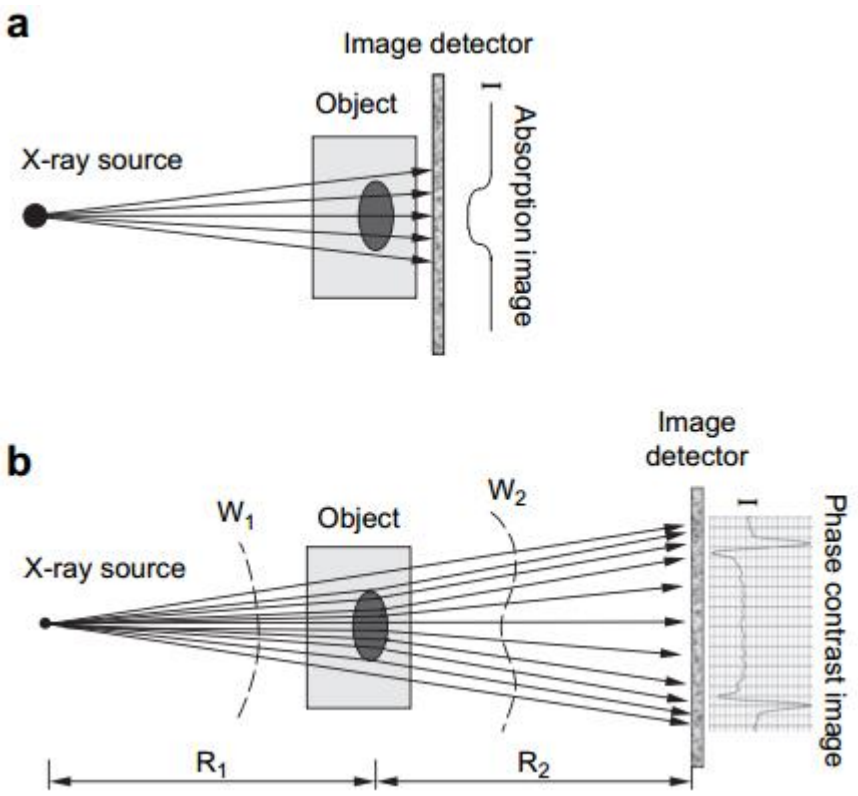

Fig. 2.45 Schematic illustration of the (b) phase-contrast imaging using a microfocus source and the comparison with the (a) absorption-contrast imaging. The spherical wave front W1 emanating from the point source becomes distorted to W2 on passing through the object O. R_1 and R_2 are the source-object and object-detector distance [139].

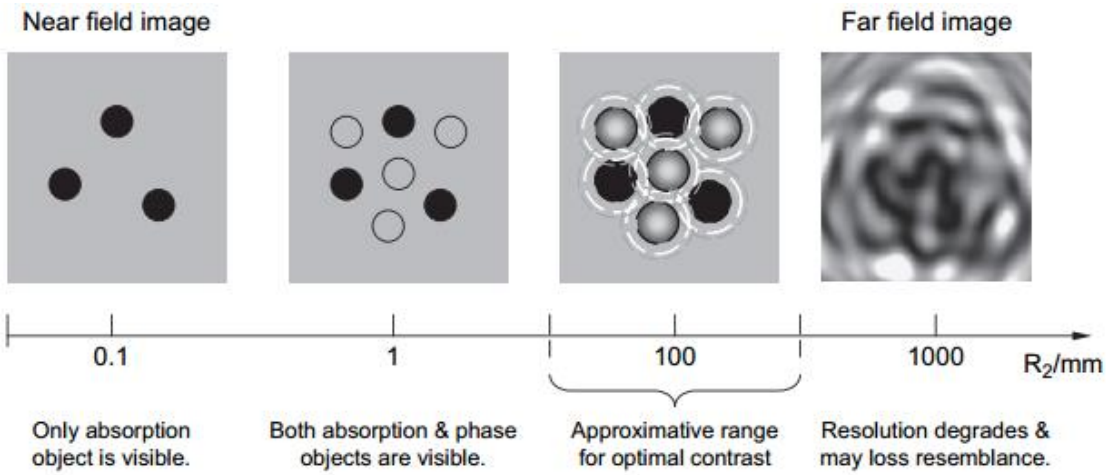

Fig. 2.46 Dependence of the phase-contrast imaging on the detector-object distance [139].

Fig. 2.47 demonstrates the effect of phase-contrast imaging on the carbon-fibre reinforced polymer at different R_2 = 180 mm (left) and 486 mm (right) respectively [142].

Obvious enhancement of the visibility of the feature details is achieved when R_2 = 486 mm, as illustrated in Fig. 37 where the edges are sharper compared with the left panel.

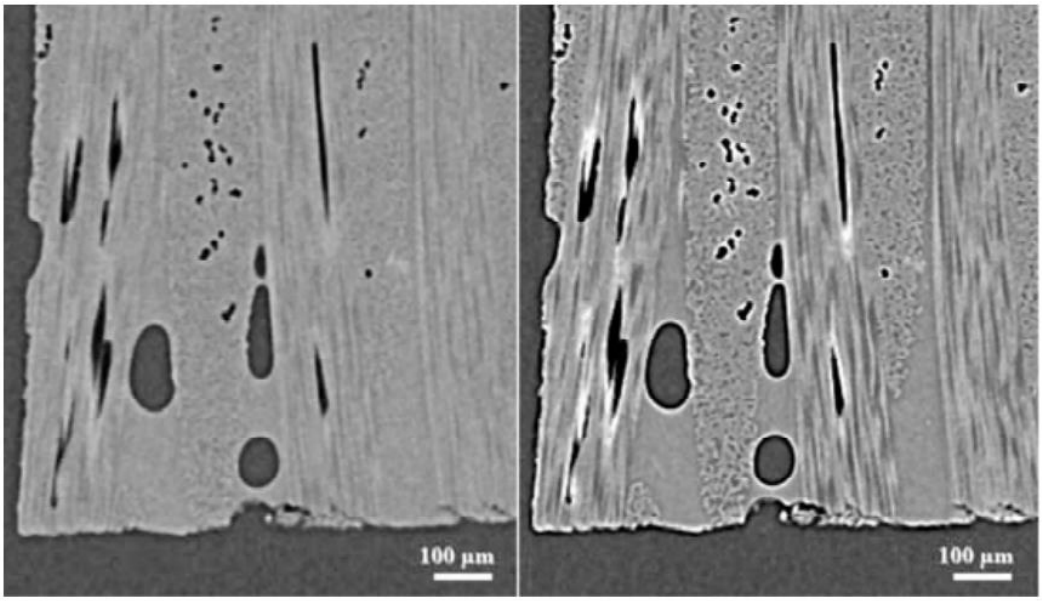

Fig. 2.47 Comparison of the in-line phase-contrast imaging on a carbon fibre reinforced polymer sample with R_2 set at (left) 180mm and (right) 486 mm. Images were acquired on Phoenix Nanotom 180NF CT desktop device. The voxel size is 2.75 μm^3 [142].

b. Zernike Phase Contrast

In contrast to in-line phase contrast imaging, which doesn't require any X-ray optics to be positioned between sample and detector, Zernike phase contrast is achieved by insertion of a phase ring. Zernike phase contrast imaging is well established for the lab source X-ray microscope, e.g. Xradia Ultra-810: the unique architecture of the Xradia instrument utilizes a capillary condenser lens to focus the incident X-ray beam and a Fresnel zone plate objective lens for post transmission focusing, providing sub-100 nm imaging resolution across a fixed field of view from 15 × 15 to 65 × 65 μm^2.

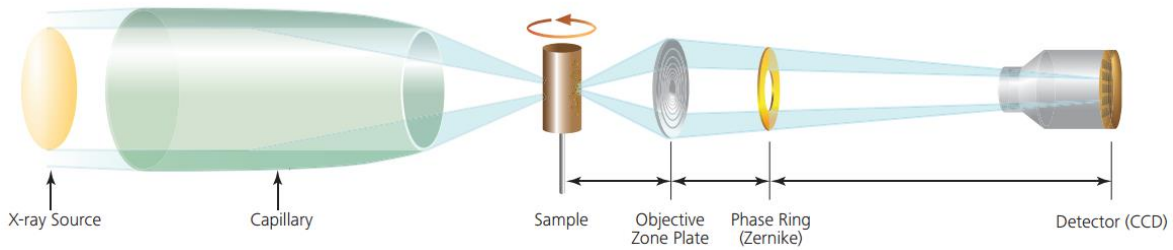

Fig. 2.48 Schematic figure illustrating the optics configuration of a lab-source Zernike phase contrast [143]. Without the phase ring, a conventional attenuation contrast image is obtained.

The basic principle of Zernike phase contrast is that: according to Abbe's theory [144], the light illuminating the object is divided into an undiffracted part and a diffracted part carrying the structure information of the sample structure. Separation of these two components is achieved by the phase ring, aligned at the back-focal plane of the objective lens, imparting a phase shift onto the undiffracted part (Fig. 2.49). The phase contrast image is formed by the interference of the phase-shifted undiffracted component with the undisturbed diffracted component [145].

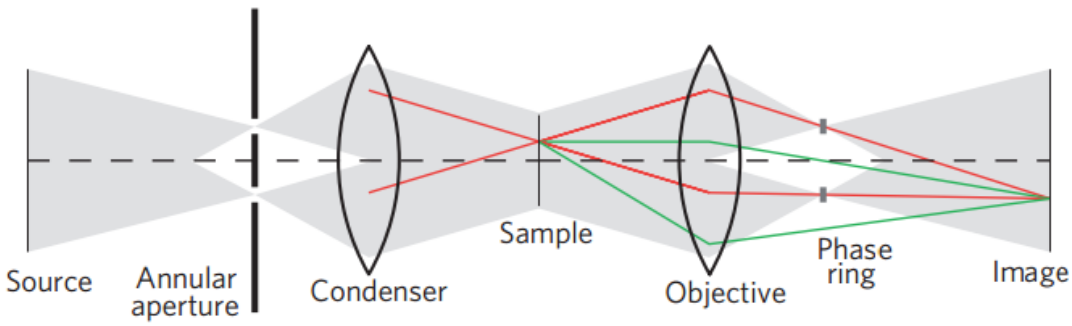

Fig. 2.49 Principle of Zernike phase contrast. Phase ring shifts the undiffracted incident beam (red) at the back-focal plane of the objective, and this shifted beam interferes with the diffracted light (green) to generate the intensity contrast [145].

2.8.4 Applications of X-ray CT Imaging to Biomaterials

Structure investigations of biomaterials have much to benefit from 3D-nondestructive x-ray imaging. Due to the low absorption, x-ray with the energy ranging from 20 – 50 keV is often used for biomaterials imaging [146]. S. Zabler [147, 148] managed to resolve the dentinal tubules that are between 1– 2 μm using phase-contrast imaging. The ring artifacts

and the random noise in the dentin matrix can be reduced by taking sequential scans repeatedly (Fig. 2.50). In order to improve the understanding of the fracture behaviour of dentin, crack morphologies were also observed in 3D using x-ray CT [116]. In the field of crack growth investigation, X-ray imaging is the optimal illustration method because it can show crack growth in 3D volume (Fig. 2.51) [43, 149] below the surface, which will contribute a deeper understanding of the shielding behaviour. The contrast of the crack can be enhanced using straining techniques (Fig. 2.52) [150]. R. Ritchie [16, 151] reported the crack bridging phenomenon previously in the dentin (Fig. 2.53).

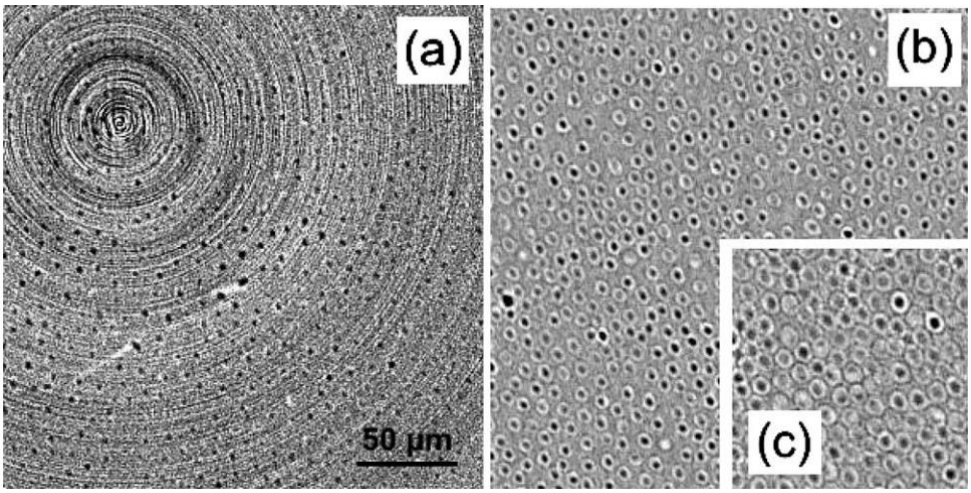

Fig. 2.50 Microstructural detail in dentin (a) conventional radiographs showing the human dentinal tubules, associated with strong ring artifacts. (b) Improved reconstructed images, produced from three sequential scans, result in high-quality virtual microscopy images of interference rings corresponding to wet 1μm thick tubules (D=100 mm). Images obtained for larger propagation distances (c) (D=180 mm) show enlarged tubules, yet the centre-to-centre distances 8–10 μm remain constant [147].

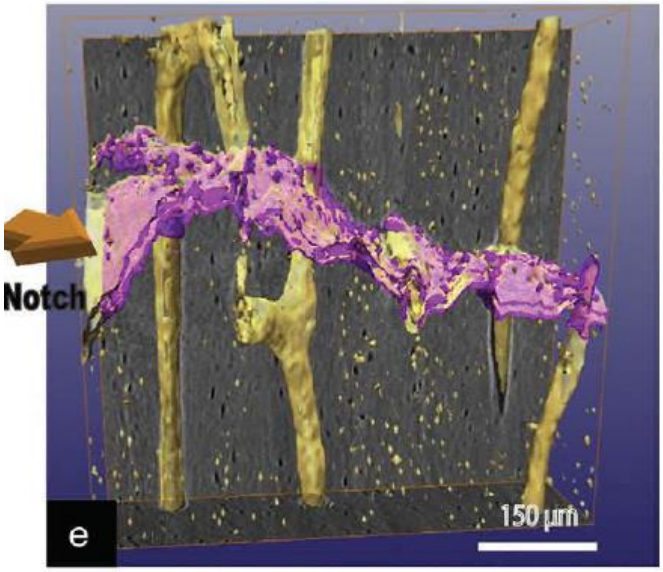

Fig. 2.51 Crack propagation path in human cortical bone demonstrated by 3D x-ray imaging [43, 149].

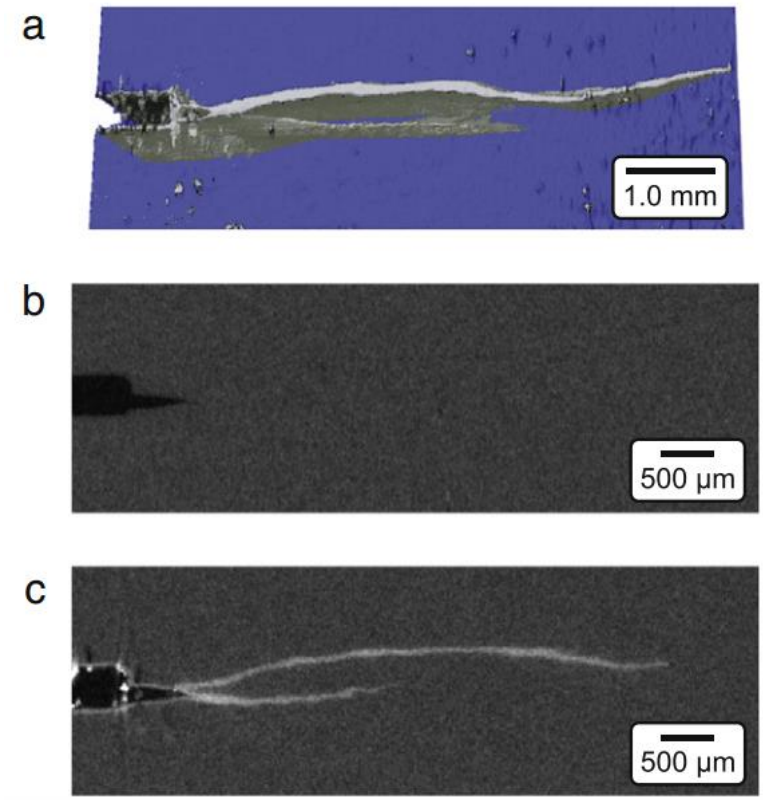

Fig. 2.52 A branched crack that propagated from a notch (left) in a compact tension specimen of dehydrated elephant dentin was imaged by micro-CT before and after staining by $BaSO_4$ precipitation. The crack grew in the direction perpendicular to the tubule axis and was in the plane of the tubules. (a) A segmented, three-dimensional micro-CT reconstruction showed crack surfaces stained with $BaSO_4$. Cross-sectional grayscale micro-CT images at the same depth approximately midway through the specimen thickness

(b) before and (c) after staining by $BaSO_4$ precipitation showed it was not possible to detect the crack at this location without the use of the contrast agent [150].

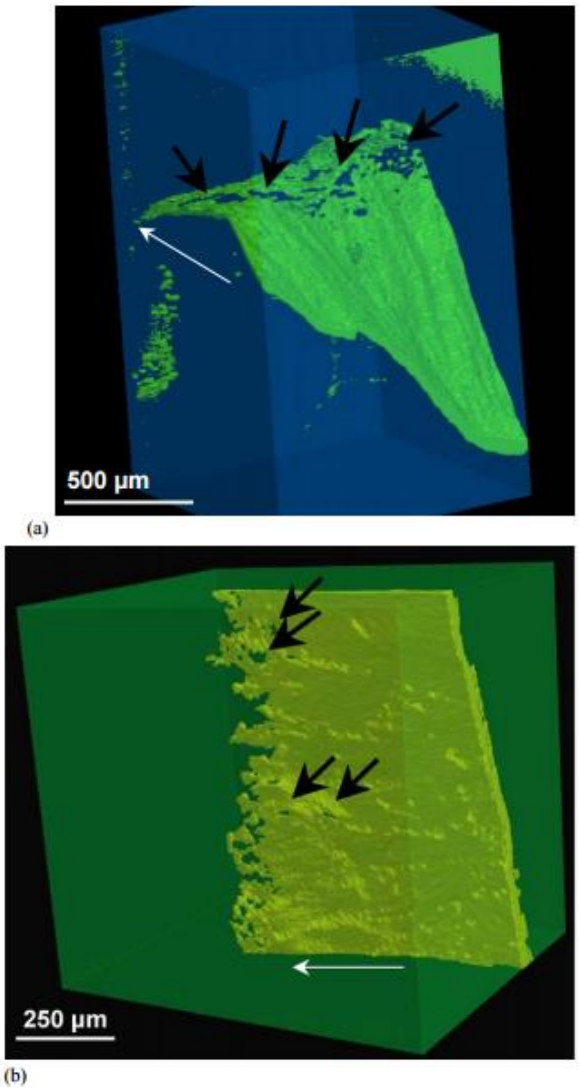

Fig. 2.53 Three-dimensional X-ray tomographic reconstructions of fatigue cracks in (a) normal human dentin, and (b) sclerotic dentin. Uncracked ligaments are pointed out using black arrows in the wake of the crack and the white arrow in each case indicates the direction of nominal fatigue-crack growth [151].

In summary, X-ray CT has a number of advantages over traditional materials analysis techniques such as Scanning Electron Microscopy (SEM) or 3D laser scanning. These include: 1) Non-destructive testing of specimens – so that the sample is undamaged. 2) Hidden internal complex features or faults such as cracks or voids can be precisely measured without cutting the sample up. 3) Specimens can be analysed either stress-free or under the influence of an applied load or temperature in-situ, so as to replicate actual

working conditions. 4) Time-lapse studies can be undertaken, e.g. fluid flow, corrosion cracking. With the high-speed development of the technology for resolution improvement, the structure with scales ranging from nanometers to hundreds of micrometers can be resolved clearly.

In present study, the X-ray CT technique has been used to measure the crack opening displacement (COD) and crack morphologies in 3D to characterise the anisotropic fracture performance and the extrinsic shielding mechanism (Chapter 4).

2.9 Digital Image Correlation

Digital image correlation (DIC) technique has been widely accepted and used as a powerful and flexible tool for surface deformation measurements. Full-field displacements and strains can be obtained by comparing the digital images of the sample surface in the un-deformed (or reference) and deformed states respectively. This technique is especially suitable for the materials possessing high contrast speckle patterns on the surface, e.g. tubule cuffs in dentin. In present study, digital image correlation technique has been used to measure the crack-tip displacement and strain for a deeper understanding of the anisotropic fracture properties in terms of effective stress intensity and strain to failure.

2.9.1 Basic Principle and Correlation Methods

Digital image correlation is an emerging strain-mapping technique that allows full-field surface strain mapping by comparing the images of the same region before, during and after deformation. It was first developed by M. Sutton from University of South Carolina in the 1980s [152-155]. Subset-based digital image correlation procedures are widely used in the research. Fundamentally, the technique compares pixels from two different images and tries to match them. It is assumed that if the intensities from pixels in one image correlate with those in a different image of the same object, the pixels in two images represent the same feature. If the region in the two images is offset by simple translation or rotation, by performing the correlation to all pixels, the relative offset can be quantified as a displacement vector according to the highest correlation result. On the surface of a strained sample, however, the relative displacement of two images (of the same region but obtained at different strains) varies with position. Therefore a map covers the offsets over the whole surface for individual regions are required. The solution is that the two images (unloaded and loaded) are divided into smaller subsets (i.e. interrogation

window), which are individually correlated. Subsets must contain enough features in order to generate reliable correlation result with the same subsets in the next image. The difference of the subset centre in the reference image and the deformed image yields the displacement vector joining the subset centre of the reference and deformed image (Fig. 2.54). This procedure allows the relative displacement to be determined for each region, thereby creating a displacement map for the entire image (Fig. 2.55).

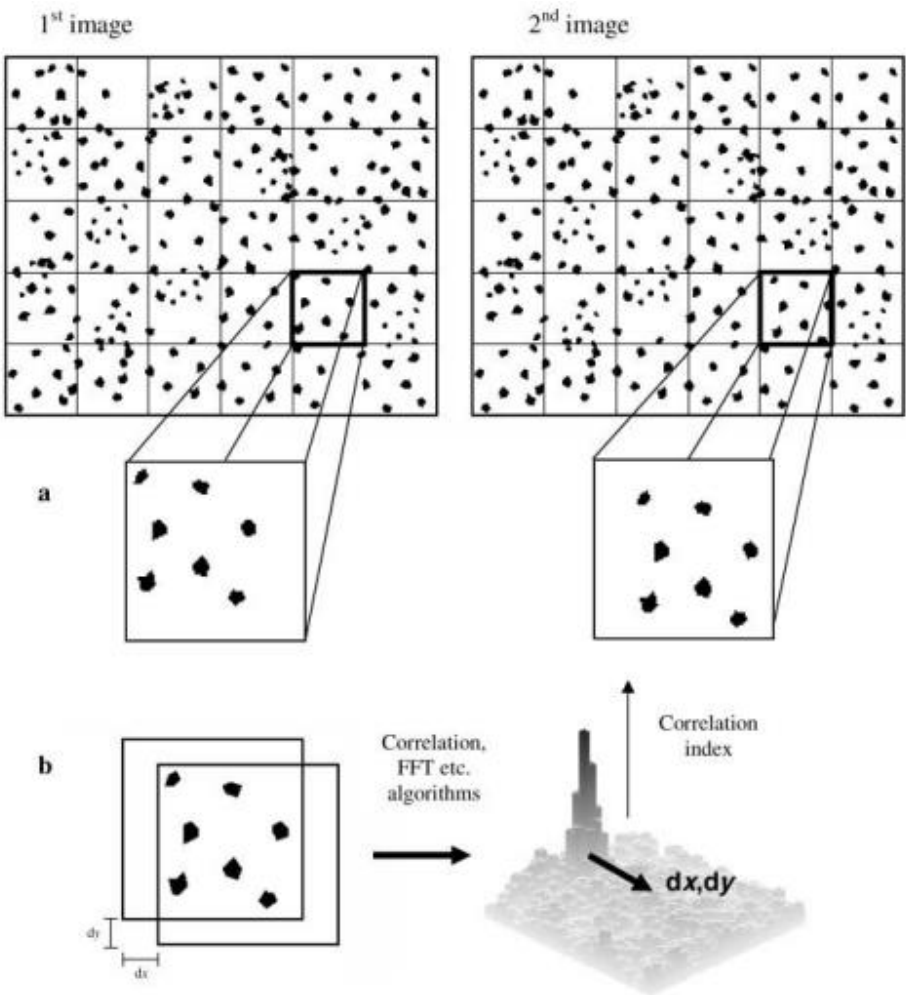

Fig. 2.54 Subsets are mapped to their deformed locations to determine the displacement at each correlation point [156, 157].

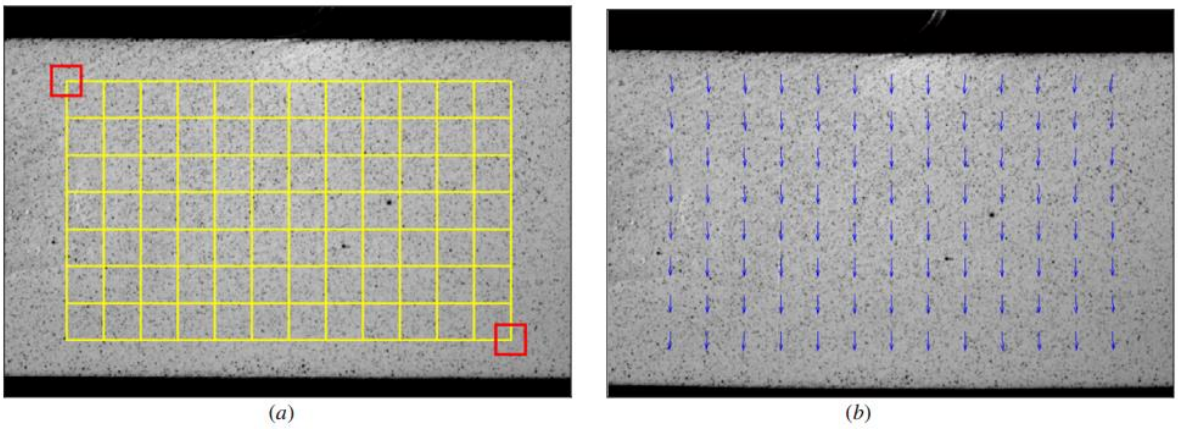

Fig. 2.55 (a) The reference image is superimposed by the yellow grid, at the intersection points of which the displacement vector is calculated using the subset (red); (b) the resultant calculated displacement vector at each intersection point of the grid [156].

In order to track the movement of the subset with high accuracy, considering the translation, rotation and shear, and therefore improving the correlation, different shape functions (mapping functions) may be used. Normally the reference subset is mapped to the target subset by a second-order mapping function [158, 159]:

$$x_i^{'} = x_i + \bar{u} = x_i + u + u_x \Delta x + u_y \Delta y + u_{xy} \Delta x \Delta y + u_{xx} \Delta x^2 + u_{yy} \Delta y^2$$

$$y_i^{'} = y_i + \bar{v} = y_i + v + v_x \Delta x + v_y \Delta y + v_{xy} \Delta x \Delta y + v_{xx} \Delta x^2 + v_{yy} \Delta y^2 \qquad (2.22)$$

where x_i and y_i are the coordinates of the pixel in the reference subset. $x_i^{'}$, $y_i^{'}$ denotes the new coordinates in the deformed image. u and v are the displacement components of the reference subset centre in x and y direction. u_x and u_y are the first order displacement gradient and u_{xx}, v_{yy}, u_{xy}, v_{xy} are the second order displacement gradients of the reference subset. Second order displacement shape function has 12 parameters defining the movement of each subset, which is much more than first order function (6 parameters) [160].

To evaluate the similarity degree between the reference and deformed subsets, a correlation criterion should be defined in advance before correlation analysis. There are a great number of criteria that can be found in the literature. These correlation criteria can be categorized into two groups, namely CC (cross-correlation) criteria and SSD (sum of squared differences) correlation criteria [156, 161]. These correlation methods are all built

in the commercial DIC software Lavision Davis V8.0. In present study, CC criteria was used as the tracking algorithm. The displacement of each subset is tracked by matching all the pixels in the subset of the reference image to the corresponding one in the deformed image. The solution of the 12 displacement parameters in Eq. (2.22) will be determined once obtaining the optimum correlation coefficient.

Actually, the displacement in the accuracy of sub-pixel can be achieved although the images contain only integer information. Sub-pixel interpolation is necessary after a very good first guess of the displacement using the correlation algorithm based on integer pixels. In order to obtain the gray intensity level at the sub-pixel positions, there are various of sub-pixel interpolation methods available [162]. A high-order interpolation method is recommended due to the higher registration accuracy and better convergence than the simple interpolation methods, especially when the subset size is quite large.

The definition of strain calculated based on the displacement field in Software Davis is as follows

$$E_{\mathrm{ij}} = \frac{dV_i}{dr_j} \qquad \text{with } i,j=x,y,z \tag{2.23}$$

where V_i stands for the displacement vector components in x(V_x), y(V_y), z(V_z) directions, r_j means the distance in *x*, *y* or *z* direction. For example, $E_{xx}=dV_x/dr_x$. The strain is computed using a central difference scheme: at each individual grid centre (m, n), the displacement vector in *x* or *y* direction is divided by the distance between those neighbouring vectors (2x grid spacing), which is described in Eq. (2.24). *g* is the grid spacing. For example, for a 32 × 32 interrogation window size with 50 % overlap, the grid spacing is 16 pixels. This is equivalent of averaging the simple forward difference to the side and the other side only.

$$E_{xx}(m,n) = ((V_x(m+1,n) - V_x(m,n)) + (V_x(m,n) - V_x(m-1,n)))/2*g \tag{2.24}$$

$$= (V_x(m+1,n) - V_x(m-1,n))/2*g$$

2.9.2 Error, Precision and Accuracy of DIC Measurement

The precision of the DIC measurement is the reproducibility of the measurement and gives the statistical error, while accuracy is a systematic error of the evaluated results (Fig. 2.56). The accuracy of the displacement vectors mainly depends on the size of the interrogation window: the larger the interrogation window size, the more accurate correlation peak will be found due to more texture information and contrast. The relation between the interrogation window and the consequent vector accuracies is listed in Table 2.6. The absolute accuracy of the vectors in length scale depending on the zoom factor of the camera used for the study, i.e. pixel/mm. However, choosing a large interrogation window size will sacrifice the spatial strain resolution. Thus it is a trade-off between the expected strain gauge and the required accuracy. The effect of feature size on accuracy is dealt with in detail in [163]. Theoretically, the sampling frequency should be at least twice that of the signal, i.e. each feature should be at least 2 × 2 pixels. In practice, owing to noise in the CCD and the fact that each pixel is separated by a finite gap, a 3 × 3 pixel feature size is the minimum required.

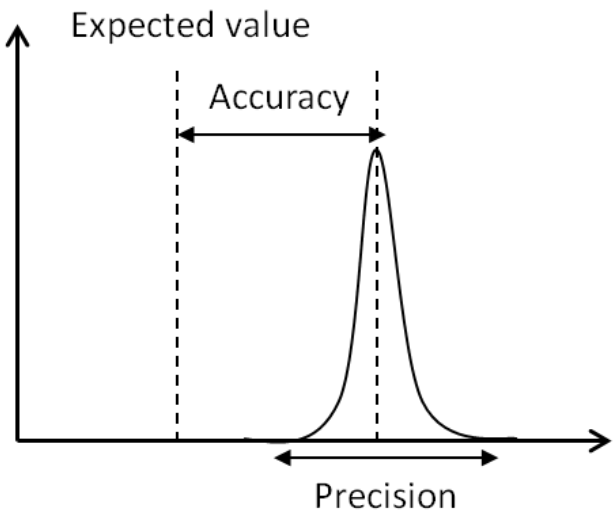

Fig. 2.56 The precision and accuracy for a DIC measurement.

Table 2.6 The relationship between the size of interrogation window and measured 2D displacement vectors tested on both artificial and real images with known results [164].

Size of the interrogation window (pixels)	Accuracy of the 2D vectors (pixels)
128 × 128	0.005
64 × 64	0.01
32 × 32	0.025
16 × 16	0.05

The accuracy of the strain measurement can be deduced from the error propagation of the displacement vector. The total error composes of the error from the vector displacement σ_v and the calibration function σ_{cal}, i.e. the offset when pinpointing the next vector position at a distance of g pixels away [164]. Based on the error propagation theory,

$$\sigma_{total} = \sqrt{(\sqrt{2}\sigma_v / E_{xx} \cdot 2g)^2 + 0.0001^2} \tag{2.25}$$

The relative error of the calibration function is in the order of 0.0001 pixel/pixel [164]. Considering the strain shown in Eq. (2.24). If the vector displacement error σ_d is the same for the two vectors, i.e. $V_x(m+1,n)$, $V_x(m-1,n)$, the propagated error is

$$\sigma_v = \sqrt{\sigma_{v1}^2 + \sigma_{v2}^2} = \sqrt{2}\sigma_d \tag{2.26}$$

the relative propagated error to the strain is $\sqrt{2}\sigma_d/(E_{xx} \cdot 2g)$, then Eq. (2.25) becomes,

$$\sigma_{total}^{re} = \sqrt{(\sqrt{2}\sigma_v / E_{xx} \cdot 2g)^2 + 0.0001^2} \tag{2.27}$$

the absolute error is

$$\sigma_{total}^{ab} = E_{xx} \cdot \sqrt{(\sqrt{2}\sigma_v / E_{xx} \cdot 2g)^2 + 0.0001^2}$$

$$= \sqrt{0.5(\sigma_v / g)^2 + (0.0001 \cdot E_{xx})^2} \tag{2.28}$$

From the above expression it is found that the error of the measured strain is determined by the interrogation size, which determines the displacement error; the spacing of the grid; the strain magnitude (Table 2.7).

Table 2.7 The consequent strain accuracy under the predefined interrogation window size and grid spacing. These also depend on the quality of the contrast pattern (size, spacing etc) [164].

Interrogation window size (pixel)	Grid spacing (pixel)	Strain accuracy (μs)
128 × 128, 0 %	128	40
128 × 128, 50 %	64	60
64 × 64, 0 %	64	115
64 × 64, 50 %	32	220
32 × 32, 0 %	32	440
32 × 32, 50 %	16	880
16 × 16, 0 %	16	2200
16 × 16, 50 %	8	4400

2.9.1 Applications of DIC to Study Fracture Problems

In the study of fracture mechanics, the displacement field obtained by DIC measurement can be directly used to extract the stress intensity factor by fitting it with the analytical displacement field solutions defined in LEFM [165-167]. The stress intensity factor obtained by this method is known as the effective stress, K_{eff}, which is generally

lower than the nominally applied load K_{app} [168, 169]. By comparing these two, the effect of extrinsic shielding can be assessed. Fig. 2.57 shows a example of the displacement field and fitting on a compact tension sample. The material is aluminium 2024-T351 alloy [170].

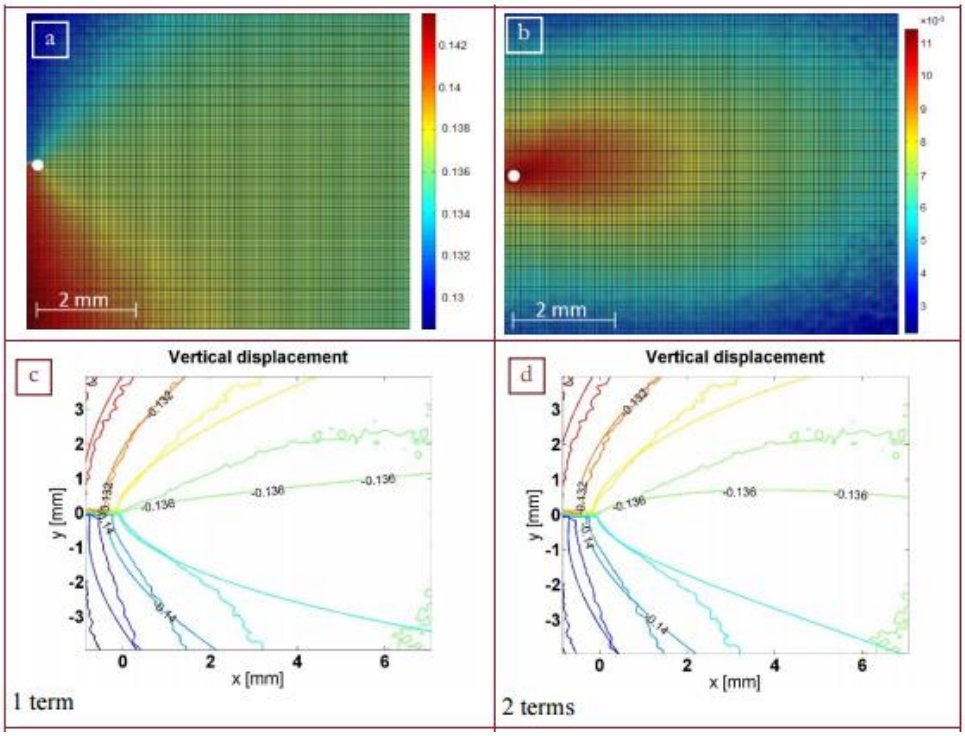

Fig. 2.57 The displacement field of the loaded compact tension sample of aluminium 2024-T351 alloy. (a) and (b) demonstrate the vertical and horizontal displacement fields respectively. (c) and (d) compare the difference of the displacement field being fitted by William's solution using term 1 and term 2 to extract stress intensity factor [170].

Another important application of DIC technique is to measure the crack-tip strain [171-174]. Fig. 2.58 shows different strain components at the crack-tip measured by DIC on a cylindrical pipe which is subjected to the internal pressure. This experimental results is tused to demonstrate the crack development tendency in defect materials and the stress concentration zone under fluid flow condition.

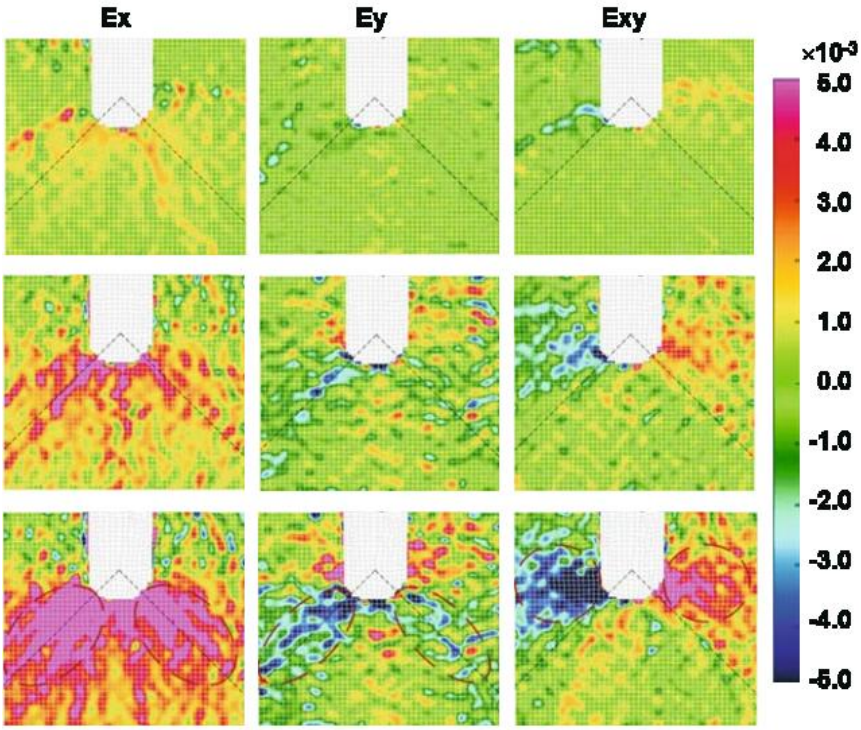

Fig. 2.58 Different crack-tip strain components measured by DIC in the cylindrical pipe made of Type 304 N stainless steel [175].

2.10 Summary

The anisotropic fracture toughness of dentin has been well studied in terms of stress intensity factor *K*, and R-curve under both hydrated and dehydrated conditions. The crack-tip shielding mechanisms are also recorded based on 2-D inspections. However, few study has focused on the quantitative assessment of the shielding mechanisms. The strain ability at the crack-tip with different cracking directions, at either hydrated or dehydrated conditions, has never been measured before. This is critical in terms of characterising the moisture effect on intrinsic shielding mechanisms in dentin. Although some researchers tried to simulate the crack-tip shielding effect, using either spring element, or cohesive element models, none of them established the model based on the crack self-performance (e.g. crack opening displacement), which can produce more realistic and accurate results simulating the physical process ahead of the crack-tip. In this thesis, the anisotropic fracture behaviour has been evaluated by crack opening displacement both in 2-D and 3-D for the first time. Crack-tip shielding mechanisms have been characterised both quantitatively and qualitatively, using optical method and X-ray computed tomography technique. Crack-tip strain mapping has been achieved for the first time in dentin materials

using digital image correlation technique. This provides a new insight into understanding the fracture anisotropy of dentin other than stress intensity *K*. The plastic zones for hydrated and dehydrated samples are also measured, which evidences the effect of moisture in toughing the dentin. In order to simulate the crack growth process, the crack opening displacement measured optically is used to establish the cohesive constitutive law, which enables us to predict the crack bridging distance, R-curve, energy dissipation and crack-tip strain fields.

References

[1] Gher ME, Dunlap RM, Anderson MH, Kuhl LV. Clinical survey of fractured teeth. The Journal of the American Dental Association 1987;114:174-7.
[2] Cameron CE. The cracked tooth syndrome: additional findings. The Journal of the American Dental Association 1976;93:971-5.
[3] Kinney JH, Balooch M, Marshall GM, Marshall SJ. A micromechanics model of the elastic properties of human dentine. Archives of Oral Biology 1999;44:813-22.
[4] Yan J, Taskonak B, Platt JA, Mecholsky JJ, Jr. Evaluation of fracture toughness of human dentin using elastic-plastic fracture mechanics. Journal of Biomechanics 2008;41:1253-9.
[5] Nalla RK, Imbeni V, Kinney JH, Staninec M, Marshall SJ, Ritchie RO. In vitro fatigue behavior of human dentin with implications for life prediction. Journal of Biomedical Materials Research Part A 2003;66A:10-20.
[6] Deymier-Black A, Almer J, Stock S, Haeffner D, Dunand D. Synchrotron X-ray diffraction study of load partitioning during elastic deformation of bovine dentin. Acta biomaterialia 2010;6:2172-80.
[7] Arola DD, Reprogel RK. Tubule orientation and the fatigue strength of human dentin. Biomaterials 2006;27:2131-40.
[8] Iwamoto N, Ruse ND. Fracture toughness of human dentin. Journal of Biomedical Materials Research Part A 2003;66A:507-12.
[9] Arola DD, Rouland JA. The effects of tubule orientation on fatigue crack growth in dentin. Journal of Biomedical Materials Research Part A 2003;67A:78-86.
[10] Marshall GW, Marshall SJ, Kinney JH, Balooch M. The dentin substrate: structure and properties related to bonding. Journal of Dentistry 1997;25:441-58.
[11] Deymier-Black AC, Almer JD, Stock SR, Haeffner DR, Dunand DC. Synchrotron X-ray diffraction study of load partitioning during elastic deformation of bovine dentin. Acta Biomaterialia 2010;6:2172-80.
[12] Bajaj D, Sundaram N, Nazari A, Arola D. Age, dehydration and fatigue crack growth in dentin. Biomaterials 2006;27:2507-17.
[13] Marshall GW, Inai N, Magidi ICW, Ballouch M, Kinney JH, Tagami J, et al. Dentin demineralisation: effects of dentin depth, pH and different acids (vol 13, pg 338, 1997). Dental Materials 1998;14:383-.
[14] Gallegos R. Maintain Dentin Bond Strength Over Time. Daily Digest http://wwwspeareducationcom/spear-review/tag/dentin/page/3/ 08. 03. 2015.
[15] Heuer AH, Fink DJ, Laraia VJ, Arias JL, Calvert PD, Kendall K, et al. Innovative Materials Processing Strategies - a Biomimetic Approach. Science 1992;255:1098-105.
[16] Kruzic J, Nalla RK, Kinney JH, Ritchie RO. Crack blunting, crack bridging and resistance-curve fracture mechanics in dentin: effect of hydration. Biomaterials 2003;24:5209-21.
[17] Lees S, Prostak K. The Locus of Mineral Crystallites in Bone. Connect Tissue Res 1988;18:41-54.
[18] Lees S, Prostak KS, Ingle VK, Kjoller K. The Loci of Mineral in Turkey Leg Tendon as Seen by Atomic-Force Microscope and Electron-Microscopy. Calcified Tissue Int 1994;55:180-9.
[19] Raubenheimer EJ, Dauth J, Dreyer MJ, Smith PD, Turner ML. Structure and Composition of Ivory of the African Elephant (Loxodonta-Africana). S Afr J Sci 1990;86:192-3.
[20] Locke M. Structure of ivory. J Morphol 2008;269:423-50.
[21] Iwamoto N, Ruse ND. Fracture toughness of human dentin. Journal of Biomedical Materials Research Part A 2003;66:507-12.

[22] Nalla RK, Kinney JH, Ritchie RO. Effect of orientation on the in vitro fracture toughness of dentin: the role of toughening mechanisms. Biomaterials 2003;24:3955-68.
[23] Huang T-JG, Schilder H, Nathanson D. Effects of moisture content and endodontic treatment on some mechanical properties of human dentin. Journal of Endodontics 1992;18:209-15.
[24] Giannini M, Soares CJ, de Carvalho RM. Ultimate tensile strength of tooth structures. Dental Materials 2004;20:322-9.
[25] Jameson M, Hood J, Tidmarsh B. The effects of dehydration and rehydration on some mechanical properties of human dentine. Journal of Biomechanics 1993;26:1055-65.
[26] Guidoni G, Denkmayr J, Schöberl T, Jäger I. Nanoindentation in teeth: influence of experimental conditions on local mechanical properties. Philosophical Magazine 2006;86:5705-14.
[27] Chen P-Y, Lin A, Lin Y-S, Seki Y, Stokes A, Peyras J, et al. Structure and mechanical properties of selected biological materials. Journal of the Mechanical Behavior of Biomedical Materials 2008;1:208-26.
[28] Imbeni V, Nalla RK, Bosi C, Kinney JH, Ritchie RO. In vitro fracture toughness of human dentin. Journal of Biomedical Materials Research Part A 2003;66A:1-9.
[29] Currey JD, Brear K, Zioupos P. DEPENDENCE OF MECHANICAL-PROPERTIES ON FIBER ANGLE IN NARWHAL TUSK, A HIGHLY ORIENTED BIOLOGICAL COMPOSITE. Journal of Biomechanics 1994;27:885-&.
[30] Kinney J, Marshall S, Marshall G. The mechanical properties of human dentin: a critical review and re-evaluation of the dental literature. Critical Reviews in Oral Biology & Medicine 2003;14:13-29.
[31] Viswanath B, Raghavan R, Ramamurty U, Ravishankar N. Mechanical properties and anisotropy in hydroxyapatite single crystals. Scr Mater 2007;57:361-4.
[32] Ritchie RO. Mechanisms of Fatigue Crack-Propagation in Metals, Ceramics and Composites - Role of Crack Tip Shielding. Mat Sci Eng a-Struct 1988;103:15-28.
[33] Colombo C, Vergani L. A numerical and experimental study of crack tip shielding in presence of overloads. Engineering Fracture Mechanics 2010;77:1644-55.
[34] Pezzotti G, Nishida T, Sakai M. Crack-wake shielding and small-scale crack-tip yielding as potential mechanisms for improving the delayed-failure resistance of silicon nitride at elevated temperatures. Ceramics International 1996;22:521-5.
[35] Weertman J. Dislocation crack tip shielding and the Paris exponent. Materials Science and Engineering a-Structural Materials Properties Microstructure and Processing 2007;468:59-63.
[36] Kotoul M, Vrbka J. Crack bridging and trapping mechanisms used to toughen brittle matrix composite. Theoretical and Applied Fracture Mechanics 2003;40:23-44.
[37] Ritchie RO. Mechanisms of fatigue-crack propagation in ductile and brittle solids. International Journal of Fracture 1999;100:55-83.
[38] Withers PJ. 3D Crack-tip Microscopy: Illuminating Micro-Scale Effects on Crack-Tip Behavior. Advanced Engineering Materials 2011;13:1096-100.
[39] Launey ME, Buehler MJ, Ritchie RO. On the Mechanistic Origins of Toughness in Bone. In: Clarke DRRMZF, editor. Annual Review of Materials Research, Vol 402010. p. 25-53.
[40] Bajaj D, Sundaram N, Arola D. An examination of fatigue striations in human dentin: In vitro and In vivo. Journal of Biomedical Materials Research Part B-Applied Biomaterials 2008;85B:149-59.
[41] Shang JK, Ritchie R. Crack bridging by uncracked ligaments during fatigue-crack growth in SiC-reinforced aluminum-alloy composites. Metallurgical Transactions A 1989;20:897-908.

[42] Burke-Veliz A, Reed PAS, Syngellakis S. A numerical study of crack shielding and deflection under extensive plasticity. Engineering Fracture Mechanics 2009;76:1345-56.
[43] Barth HD, Launey ME, MacDowell AA, Ager JW, III, Ritchie RO. On the effect of X-ray irradiation on the deformation and fracture behavior of human cortical bone. Bone 2010;46:1475-85.
[44] Koester KJ, Ager JW, III, Ritchie RO. The true toughness of human cortical bone measured with realistically short cracks. Nature Materials 2008;7:672-7.
[45] Ivancik J, Neerchal NK, Romberg E, Arola D. The Reduction in Fatigue Crack Growth Resistance of Dentin with Depth. Journal of Dental Research 2011;90:1031-6.
[46] Eltit F, Ebacher V, Wang R. Inelastic deformation and microcracking process in human dentin. Journal of Structural Biology 2013;183:141-8.
[47] Sigl LS. Microcrack toughening in brittle materials containing weak and strong interfaces. Acta Materialia 1996;44:3599-609.
[48] Vashishth D, Tanner KE, Bonfield W. Contribution, development and morphology of microcracking in cortical bone during crack propagation. Journal of Biomechanics 2000;33:1169-74.
[49] Nalla RK, Kinney JH, Ritchie RO. On the fracture of human dentin: Is it stress- or strain-controlled? Journal of Biomedical Materials Research Part A 2003;67A:484-95.
[50] Fu Y, Evans AG. SOME EFFECTS OF MICROCRACKS ON THE MECHANICAL-PROPERTIES OF BRITTLE SOLIDS .1. STRESS, STRAIN RELATIONS. Acta Metallurgica 1985;33:1515-23.
[51] Liu G, Zhu D, Shang JK. ENHANCED FATIGUE-CRACK GROWTH RESISTANCE AT ELEVATED-TEMPERATURE IN TIC/TI-6AL-4V COMPOSITE - MICROCRACK-INDUCED CRACK CLOSURE. Metallurgical and Materials Transactions a-Physical Metallurgy and Materials Science 1995;26:159-66.
[52] Evans AG. Perspective on the development of high-toughness ceramics. Journal of the American Ceramic Society 1990;73:187-206.
[53] El Mowafy O, Watts D. Fracture toughness of human dentin. Journal of dental research 1986;65:677-81.
[54] Kruzic JJ, Nalla RK, Kinney JH, Ritchie RO. Crack blunting, crack bridging and resistance-curve fracture mechanics in dentin: effect of hydration. Biomaterials 2003;24:5209-21.
[55] Kahler B, Swain MV, Moule A. Fracture-toughening mechanisms responsible for differences in work to fracture of hydrated and dehydrated dentine. Journal of biomechanics 2003;36:229-37.
[56] Pugach MK, Strother J, Darling CL, Fried D, Gansky SA, Marshall SJ, et al. Dentin caries zones: mineral, structure, and properties. Journal of dental research 2009;88:71-6.
[57] Bertassoni LE, Habelitz S, Kinney JH, Marshall SJ, Marshall GW, Jr. Biomechanical Perspective on the Remineralization of Dentin. Caries Research 2009;43:70-7.
[58] Nalla R, Balooch M, Ager J, Kruzic J, Kinney J, Ritchie R. Effects of polar solvents on the fracture resistance of dentin: role of water hydration. Acta biomaterialia 2005;1:31-43.
[59] Bertassoni LE, Swain MV. Influence of hydration on nanoindentation induced energy expenditure of dentin. Journal of biomechanics 2012;45:1679-83.
[60] Yan J, Taskonak B, Platt JA, Mecholsky JJ. Evaluation of fracture toughness of human dentin using elastic–plastic fracture mechanics. Journal of Biomechanics 2008;41:1253-9.
[61] Vashishth D, Behiri J, Bonfield W. Crack growth resistance in cortical bone: concept of microcrack toughening. Journal of Biomechanics 1997;30:763-9.

[62] Chapman GE, Danyluk SS, McLauchl.Ka. MODEL FOR COLLAGEN HYDRATION. Proceedings of the Royal Society Series B-Biological Sciences 1971;178:465-+.
[63] Chapman GE, McLaughl Ka. THE HYDRATION STRUCTURE OF COLLAGEN. Proceedings of the Royal Society Series B-Biological Sciences 1969;173:223-+.
[64] Lazarev YA, Grishkovsky BA, Khromova TB. AMIDE-I BAND OF IR-SPECTRUM AND STRUCTURE OF COLLAGEN AND RELATED POLYPEPTIDES. Biopolymers 1985;24:1449-78.
[65] Lazarev YA, Grishkovsky BA, Khromova TB, Lazareva AV, Grechishko VS. BOUND WATER IN THE COLLAGEN-LIKE TRIPLE-HELICAL STRUCTURE. Biopolymers 1992;32:189-95.
[66] Saito H, Yokoi M. A 13C NMR study on collagens in the solid state: hydration/dehydration-induced conformational change of collagen and detection of internal motion. Journal of Biochemistry 1992;111:376-82.
[67] Braidotti P, Branca F, Stagni L. Scanning electron microscopy of human cortical bone failure surfaces. Journal of Biomechanics 1997;30:155-62.
[68] Jameson MW, Hood JAA, Tidmarsh BG. The effects of dehydration and rehydration on some mechanical properties of human dentine. Journal of biomechanics 1993;26:1055-65.
[69] Arola D, Zheng W. Hydration and dynamic fatigue of dentin. Journal of Biomedical Materials Research Part A 2006;77:148-59.
[70] Kanninen M. Advanced Fracture Mechanics. Oxford University Press 1985.
[71] Cotterell B, Rice JR. SLIGHTLY CURVED OR KINKED CRACKS. International Journal of Fracture 1980;16:155-69.
[72] Launey ME, Buehler MJ, Ritchie RO. On the mechanistic origins of toughness in bone. Annual review of materials research 2010;40:25-53.
[73] Koester KJ, Ager J, Ritchie R. The true toughness of human cortical bone measured with realistically short cracks. Nature materials 2008;7:672-7.
[74] Fett T, Munz D, Geraghty RD, White KW. Bridging stress determination by evaluation of the R-curve. Journal of the European Ceramic Society 2000;20:2143-8.
[75] Koester KJ, Barth HD, Ritchie RO. Effect of aging on the transverse toughness of human cortical bone: Evaluation by R-curves. Journal of the Mechanical Behavior of Biomedical Materials 2011;4:1504-13.
[76] Fuenfschilling S, Fett T, Oberacker R, Hoffmann MJ, Oezcoban H, Jelitto H, et al. R Curves from Compliance and Optical Crack-Length Measurements. Journal of the American Ceramic Society 2010;93:2814-21.
[77] Paris. The growth of fatigue cracks due to variations in load. PhD thesis 1962;Lehigh University.
[78] Linear Elastic Fracture Mechanics (LEFM): Part Two. http://wwwtotalmateriacom/pageaspx?ID=CheckArticle&site=kts&LN=EN&NM=299 18. 12. 2014.
[79] Fracture Mechanics. Mechanics of Solids, Division of Engineering, Brown Univseristy.
[80] Arola D, Zheng W, Sundaram N, Rouland JA. Stress ratio contributes to fatigue crack growth in dentin. Journal of Biomedical Materials Research Part A 2005;73A:201-12.
[81] Soappman MJ, Nazari A, Porter JA, Arola D. A comparison of fatigue crack growth in resin composite, dentin and the interface. Dental Materials 2007;23:608-14.
[82] Arola D, Rouland JA, Zhang D. Fatigue and fracture of bovine dentin. Experimental Mechanics 2002;42:380-8.
[83] Kruzic JJ, Nalla RK, Kinney JH, Ritchie RO. Mechanistic aspects of in vitro fatigue-crack growth in dentin. Biomaterials 2005;26:1195-204.

[84] J.R.Rice. Mechanics of Crack Tip Deformation and Extension by Fatigue. Fatigue Crack Propagation 1967;ASTM STP 415.
[85] O'Dowd N. Advanced Fracture Mechanics: Lectures on Fundamentals of Elastic, Elastic-Plastic and Creep Fracture. Imperial College London 2002.
[86] Ridell WT, Piascik RS. Determine fatigue crack openging loads from near-crack-tip displacement measurement and analysis. Advances in fatigue crack closure 1999;Second Volume:17.
[87] McEVILY AJ. On the cyclic crack-tip opening displacement. Fatigue Fract Engng Mater Struct 2009;32:2.
[88] Lopez-Crespo P, Withers PJ, Yusof F, Dai H, Steuwer A, Kelleher JF, et al. Overload effects on fatigue crack-tip fields under plane stress conditions: surface and bulk analysis. Fatigue Fract Eng M 2013;36:75-84.
[89] Ipina JEP, Yawny A, Oliver CG. On the applicability of elastic-plastic fracture mechanics to discontinuously reinforced aluminum composites. Journal of Composite Materials 2003;37:2001-10.
[90] Rice JR. A path independent integral and the approximate analysis of strain concentration by notches and cracks. Journal of Applied Mechanics 1968;35:379-86.
[91] Grellmann W. New developments in toughness evaluation of polymers and compounds by fracture mechanics. In: Grellmann, W, Seidler, S (Eds), Deformation and Fracture Behaviour of Polymers 2001;Springer, New York:3-26.
[92] ASTM. Standard Test Method for Measurement of Fracture Toughness. American Society for Testing Materials, West Conshohocken 2002;E1820-01.
[93] Wang G, Blom A. A strip model for fatigue crack growth predictions under general load conditions. Engineering Fracture Mechanics 1991;40:507-33.
[94] Barenblatt GI. The mathematical theory of equilibrium cracks in brittle fracture. Advances in applied mechanics 1962;7:104.
[95] Sun CT, Jin ZH. Chapter 9 - Cohesive Zone Model. In: Jin CTSH, editor. Fracture Mechanics. Boston: Academic Press; 2012. p. 227-46.
[96] Chin-Teh Sun ZJ. Fracture mechanics. Elsevier Inc 2012.
[97] Jin Z-H, Sun C. Cohesive fracture model based on necking. International journal of fracture 2005;134:91-108.
[98] Tvergaard V, Hutchinson JW. The relation between crack growth resistance and fracture process parameters in elastic-plastic solids. Journal of the Mechanics and Physics of Solids 1992;40:1377-97.
[99] Wei Y, Hutchinson JW. Interface strength, work of adhesion and plasticity in the peel test: Springer; 1998.
[100] Volokh KY. Comparison between cohesive zone models. Communications in Numerical Methods in Engineering 2004;20:845-56.
[101] Needleman A. An analysis of tensile decohesion along an interface. Journal of the Mechanics and Physics of Solids 1990;38:289-324.
[102] Ortiz M, Pandolfi A. Finite-deformation irreversible cohesive elements for three-dimensional crack-propagation analysis. International Journal for Numerical Methods in Engineering 1999;44:1267-82.
[103] Tvergaard V, Hutchinson JW. The influence of plasticity on mixed mode interface toughness. Journal of the Mechanics and Physics of Solids 1993;41:1119-35.
[104] Geubelle PH, Baylor JS. Impact-induced delamination of composites: a 2D simulation. Composites Part B: Engineering 1998;29:589-602.
[105] Jin Z-H, Sun C. Cohesive zone modeling of interface fracture in elastic bi-materials. Engineering fracture mechanics 2005;72:1805-17.

[106] Gálvez J, Planas J, Sancho J, Reyes E, Cendón D, Casati M. An embedded cohesive crack model for finite element analysis of quasi-brittle materials. Engineering fracture mechanics 2012.
[107] Ural A, Vashishth D. Cohesive finite element modeling of age-related toughness loss in human cortical bone. Journal of Biomechanics 2006;39:2974-82.
[108] Su X, Yang Z, Liu G. Finite Element Modelling of Complex 3D Static and Dynamic Crack Propagation by Embedding Cohesive Elements in Abaqus. Acta Mechanica Solida Sinica 2010;23:271-82.
[109] Campilho R, De Moura M, Domingues J. Using a cohesive damage model to predict the tensile behaviour of CFRP single-strap repairs. International Journal of Solids and Structures 2008;45:1497-512.
[110] De Moura M, Campilho R, Goncalves J. Mixed-Mode Cohesive Damage Model Applied to the Simulation of the Mechanical Behaviour of Laminated Composite Adhesive Joints. Journal of Adhesion Science and Technology 2009;23:1477-91.
[111] Ren W, Yang Z, Sharma R, Zhang C, Withers PJ. Two-dimensional X-ray CT image based meso-scale fracture modelling of concrete. Engineering Fracture Mechanics 2015;133:24-39.
[112] Ren W, Yang Z, Withers P. Meso-scale fracture modelling of concrete based on X-ray computed tomography images. The 5th Asia-Pacific congress on computational mechanics (APCOM) Singapore2013.
[113] Guinea G, Planas J, Elices M. A general bilinear fit for the softening curve of concrete. Materials and Structures 1994;27:99-105.
[114] Ural A, Vashishth D. Anisotropy of age-related toughness loss in human cortical bone: A finite element study. Journal of biomechanics 2007;40:1606-14.
[115] Yang Q, Cox BN, Nalla RK, Ritchie R. Fracture length scales in human cortical bone: the necessity of nonlinear fracture models. Biomaterials 2006;27:2095-113.
[116] Baruchel J, Buffiere J-Y, Maire E. X-ray tomography in material science. 2000.
[117] Hsieh J. Computed tomography: principles, design, artifacts, and recent advances. SPIE Bellingham, WA; 2009.
[118] Banhart J. Advanced tomographic methods in materials research and engineering. 2008.
[119] Farber L, Tardos G, Michaels JN. Use of X-ray tomography to study the porosity and morphology of granules. Powder Technology 2003;132:57-63.
[120] Wellington S, Vinegar H. X-ray computerized tomography. J Pet Technol;(United States) 1987;39.
[121] Dove EL. Notes on computerized tomography. Bioimaging Fundamentals 2001.
[122] Kak AC, Slaney M. Principles of computerized tomographic imaging: Siam; 1988.
[123] Feldkamp L, Davis L, Kress J. Practical cone-beam algorithm. JOSA A 1984;1:612-9.
[124] School of Engineering TUoW. Tomographic lecture. wwwengwarwickacuk/~espbc/courses//tomographic%20lectureppt 05. 02. 2014.
[125] Xu M, Wang LV. Universal back-projection algorithm for photoacoustic computed tomography. Biomedical Optics 2005: International Society for Optics and Photonics; 2005. p. 251-4.
[126] Goitein M, Abrams M, Rowell D, Pollari H, Wiles J. Multi-dimensional treatment planning: II. Beam's eye-view, back projection, and projection through CT sections. International Journal of Radiation Oncology* Biology* Physics 1983;9:789-97.
[127] Smith S. Computed Tomography. The Scientist and Engineer's Guide to Digital Signal Processing 1998;Special Imaging Techniques:Chapter 25

[128] Lauritsch G, Härer WH. Theoretical framework for filtered back projection in tomosynthesis. Medical Imaging'98: International Society for Optics and Photonics; 1998. p. 1127-37.
[129] Sagara Y, Hara AK, Pavlicek W, Silva AC, Paden RG, Wu Q. Abdominal CT: comparison of low-dose CT with adaptive statistical iterative reconstruction and routine-dose CT with filtered back projection in 53 patients. American Journal of Roentgenology 2010;195:713-9.
[130] Kak AC, Slaney M. Principles of computerized tomographic imaging: Society for Industrial and Applied Mathematics; 2001.
[131] Beister M, Kolditz D, Kalender WA. Iterative reconstruction methods in X-ray CT. Physica medica 2012;28:94-108.
[132] Buffiere J-Y, Maire E, Cloetens P, Lormand G, Fougeres R. Characterization of internal damage in a MMC p using X-ray synchrotron phase contrast microtomography. Acta materialia 1999;47:1613-25.
[133] Cloetens P, Pateyron-Salomé M, Buffiere J, Peix G, Baruchel J, Peyrin F, et al. Observation of microstructure and damage in materials by phase sensitive radiography and tomography. Journal of Applied Physics 1997;81:5878-86.
[134] Momose A, Takeda T, Itai Y, Hirano K. Phase-contrast X-ray computed tomography for observing biological soft tissues. Nature medicine 1996:473-5.
[135] Wu X, Liu H. Clinical implementation of x-ray phase-contrast imaging: Theoretical foundations and design considerations. Medical physics 2003;30:2169-79.
[136] Arfelli F, Assante M, Bonvicini V, Bravin A, Cantatore G, Castelli E, et al. Low-dose phase contrast x-ray medical imaging. Physics in medicine and biology 1998;43:2845.
[137] Snigirev A, Snigireva I, Kohn V, Kuznetsov S, Schelokov I. On the possibilities of x ‐ ray phase contrast microimaging by coherent high ‐ energy synchrotron radiation. Review of Scientific Instruments 1995;66:5486-92.
[138] Wilkins S, Gureyev T, Gao D, Pogany A, Stevenson A. Phase-contrast imaging using polychromatic hard X-rays. Nature 1996;384:335-8.
[139] Zhou S-A, Brahme A. Development of phase-contrast X-ray imaging techniques and potential medical applications. Physica Medica 2008;24:129-48.
[140] Gabor D. A new microscopic principle. Nature 1948;161:777-8.
[141] Kotre C, Birch I. Phase contrast enhancement of x-ray mammography: a design study. Physics in medicine and biology 1999;44:2853.
[142] Kastner J, Plank B, Kottler C, Revol V. Comparison of phase contrast X-ray computed tomography methods for non-destructive testing of materials. Conference Proceedings of the world conference on non-destructive testing2012.
[143] Microscopy CZ. Zeiss Xradia 810 Ultra Nanoscale X-ray Imaging at the Speed of Science. 2013.
[144] Goodman JW. Introduction to Fourier optics: Roberts and Company Publishers; 2005.
[145] Holzner C, Feser M, Vogt S, Hornberger B, Baines SB, Jacobsen C. Zernike phase contrast in scanning microscopy with X-rays. Nature physics 2010;6:883-7.
[146] HAYAKAWA T, MISHIMA H, YOKOTA I, SAKAE T, KOZAWA Y, NEMOTO K. Application of high resolution microfocus X-ray CT for the observation of human tooth. Dental materials journal 2000;19:87-95.
[147] Zabler S, Cloetens P, Zaslansky P. Fresnel-propagated submicrometer x-ray imaging of water-immersed tooth dentin. Optics letters 2007;32:2987-9.
[148] Zaslansky P, Zabler S, Fratzl P. 3D variations in human crown dentin tubule orientation: A phase-contrast microtomography study. Dental Materials 2010;26:e1-e10.

[149] Khor KH, Buffiere JY, Ludwig W, Toda H, Ubhi HS, Gregson PJ, et al. In situ high resolution synchrotron x-ray tomography of fatigue crack closure micromechanisms. Journal of Physics-Condensed Matter 2004;16:S3511-S5.
[150] Landrigan MD, Flatley JC, Turnbull TL, Kruzic JJ, Ferracane JL, Hilton TJ, et al. Detection of dentinal cracks using contrast-enhanced micro-computed tomography. Journal of the Mechanical Behavior of Biomedical Materials 2010;3:223-7.
[151] Kinney JH, Nalla RK, Pople JA, Breunig TM, Ritchie RO. Age-related transparent root dentin: mineral concentration, crystallite size, and mechanical properties. Biomaterials 2005;26:3363-76.
[152] Peters W, Ranson W. Digital imaging techniques in experimental stress analysis. Optical Engineering 1982;21:213427--.
[153] Chu T, Ranson W, Sutton M. Applications of digital-image-correlation techniques to experimental mechanics. Experimental mechanics 1985;25:232-44.
[154] Sutton M, Mingqi C, Peters W, Chao Y, McNeill S. Application of an optimized digital correlation method to planar deformation analysis. Image and Vision Computing 1986;4:143-50.
[155] Sutton MA, McNeill SR, Helm JD, Chao YJ. Advances in two-dimensional and three-dimensional computer vision. Photomechanics: Springer; 2000. p. 323-72.
[156] Pan B, Qian K, Xie H, Asundi A. Two-dimensional digital image correlation for in-plane displacement and strain measurement: a review. Measurement science and technology 2009;20:062001.
[157] Quinta da Fonseca J, Mummery P, Withers P. Full‐field strain mapping by optical correlation of micrographs acquired during deformation. Journal of microscopy 2005;218:9-21.
[158] Lu H, Cary P. Deformation measurements by digital image correlation: implementation of a second-order displacement gradient. Experimental mechanics 2000;40:393-400.
[159] Carroll J. Relating fatigue crack growth to microstructure via multiscale digital image correlation: Air Force Research Laboratory; 2011.
[160] Schreier HW, Sutton MA. Systematic errors in digital image correlation due to undermatched subset shape functions. Experimental mechanics 2002;42:303-10.
[161] Giachetti A. Matching techniques to compute image motion. Image and Vision Computing 2000;18:247-60.
[162] Schreier HW, Braasch JR, Sutton MA. Systematic errors in digital image correlation caused by intensity interpolation. Optical Engineering 2000;39:2915-21.
[163] Zhou P, Goodson KE. Subpixel displacement and deformation gradient measurement using digital image/speckle correlation (DISC). Optical Engineering 2001;40:1613-20.
[164] Davis StrainMaster 2D Software. Product-Manual for Davis 72 2010.
[165] Lopez-Crespo P, Shterenlikht A, Patterson E, Yates J, Withers P. The stress intensity of mixed mode cracks determined by digital image correlation. The Journal of Strain Analysis for Engineering Design 2008;43:769-80.
[166] Eftis J, Subramonian N, Liebowitz H. Crack border stress and displacement equations revisited. Engineering Fracture Mechanics 1977;9:189-210.
[167] Evans W, Luxmoore A. Limitations of the Westergaard equations for experimental evaluations of stress intensity factors. The Journal of Strain Analysis for Engineering Design 1976;11:177-85.
[168] Zhang R, He LF, Li CR. The Stress Intensity Factor of Opening Mode Determined by Digital Image Correlation. Applied Mechanics and Materials: Trans Tech Publ; 2011. p. 54-9.
[169] Zhang R, He L. Measurement of mixed-mode stress intensity factors using digital image correlation method. Optics and Lasers in Engineering 2012;50:1001-7.

[170] Mokhtari M, Lopez-Crespo P, Moreno B, Zanganeh M. Some experimental observations of crack-tip mechanics with displacement data. Fracture and Structural Integrity 2015:143-50.
[171] Marciniak T, Lutowski Z, Bujnowski S, Boronski D, Giesko T. Application of Digital image Correlation in Fatigue Crack Analysis. In: Skibicki D, editor. Fatigue Failure and Fracture Mechanics2012. p. 218-21.
[172] Mathieu F, Hild F, Roux S. Identification of a crack propagation law by digital image correlation. International Journal of Fatigue 2012;36:146-54.
[173] Mauroux T, Benboudjema F, Turcry P, Ait-Mokhtar A, Deves O. Study of cracking due to drying in coating mortars by digital image correlation. Cement and Concrete Research 2012;42:1014-23.
[174] Nowell D, Kartal ME, De Matos PFP. Digital image correlation measurement of near-tip fatigue crack displacement fields: constant amplitude loading and load history effects. Fatigue & Fracture of Engineering Materials & Structures 2013;36:3-13.
[175] Tung S-H, Sui C-H. Application of digital-image-correlation techniques in analysing cracked cylindrical pipes. Sadhana 2010;35:557-67.

Chapter 3

Experimental Methods

3.1 Materials and Sample preparation

For the present study we chose elephant dentin, which is often used as a structural analogue for human dentin due to the similarities in microstructure and chemical composition [1]. Despite the similarities, tubules in elephant dentin are more elliptical in shape and slightly bigger [2], and the peritubular dentin is comparatively smaller. The fracture toughness of human dentin is slightly lower than elephant dentin (1.13 ~2.02 [3] *vs* 1.6 ~2.6 $MPa\sqrt{m}$ [4], depending on cracking orientation). The larger size of elephant tusk favours the study in terms of more convenient sample preparation, less size restrictions and stable crack propagation in a longer distance.

A cross-sectional slice from a tusk of African elephant ivory was used in this study. Fracture toughness test-pieces with three different orientations relative to the tubules alignment were extracted as shown in Fig. 3.1a and a compact tension test-piece (9×8×2 mm^3) (Fig. 3.1b) was designed based on ASTM E1820 [5]. In Fig. 3.1a, three types of test-pieces were prepared: HAH (crack in hoop-axial plane of the tusk, grow in hoop direction), RAR (crack in radial-axial plane, grow in radial direction) and HRH (crack in hoop-radial plane, grow in hoop direction). The different alignments of the collagen fibrils and dentinal tubules relative to crack growth direction in three cases are shown in Fig. 3.1c (HAH), d (RAR) and e (HRH) respectively. The collagen fibrils are drawn as cross linked red lamella. Before cutting, the test-pieces were stored in distilled water at 4℃ for more than two weeks to keep hydrated. A 1 cm thick plate was sliced off from the top of the whole tusk, followed by numerically controlled slicing of test-pieces under water-based coolant with diamond abrasive cutting wheels. Subsequently, the plates were cut into

rectangular bars and further into compact tension test-pieces with a 0.3 mm thick cutting wheel. A razor blade was used to sharpen the notch tip. Finally, the test-pieces were ground with SiC papers from grit 600 up to grit 2400 finish, then polished in an alumina slurry (up to 0.25 μm) to remove the surface defects (e.g. scratches, dimples and dust).

All of the test-pieces were pre-cracked under static load at the displacement rate of 0.001 μm/s on an Instron 3344 machine. A travelling microscope was placed close to the sample surface to monitor the crack growth process and record the length. The average pre-crack length was 3.260 mm.

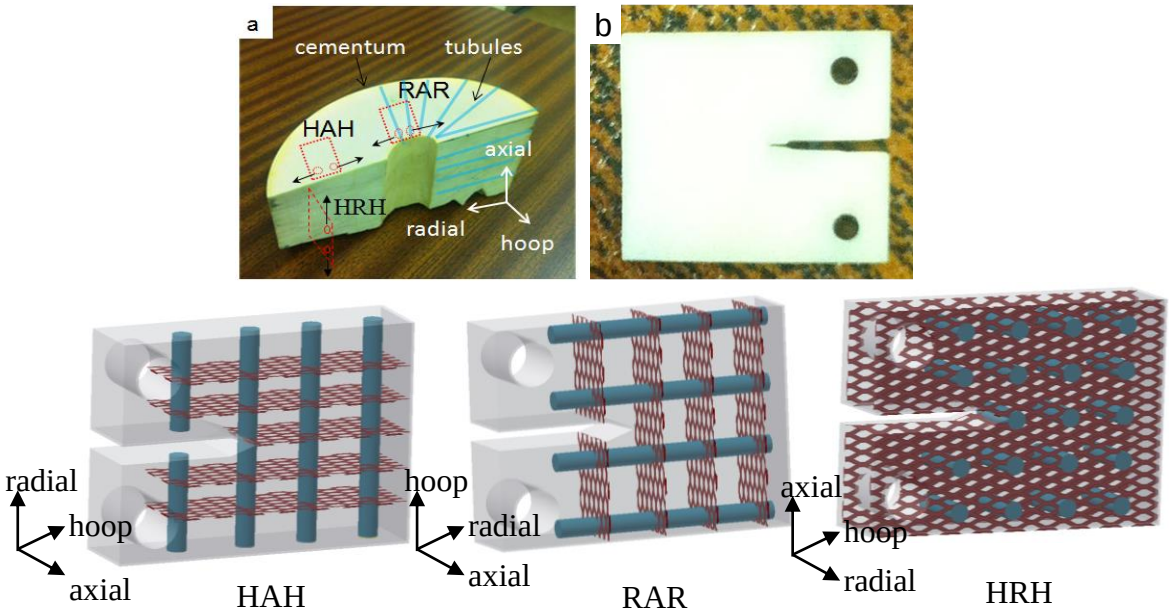

Fig. 3.1. (a) Schematic illustration showing the locations where three CT test-pieces were extracted;(b) compact tension test-piece (c) test-piece 1, d) test-piece 2 and e) test-piece 3 in each case showing the crack growth direction relative to the alignment of the tubules (blue) and collagen fibrils (red) in the dentin.

3.2 X-ray CT Configuration

Non destructive high resolution X-ray computed tomography (CT) was used to elucidate the crack opening displacement and morphologies in 3-D. This was achieved using the

Xradia Versa XRM-500 laboratory X-ray microscope at the Manchester X-ray Imaging Facility. This system utilizes a novel geometry employing high detector resolution rather than relying on the traditional geometric magnification. A self-designed screw-driven loading rig was used to incrementally load the compact tension test-pieces in-situ (Fig. 3.2). Considering the CODs were measured across the sample thickness direction, two rectangular windows were cut at the front and back side of the supporting Perspex tube so as to reduce the reconstruction artefacts caused by the tube. In this study, the source operated at 80 kV with a source - test-piece distance of 30 mm and test-piece - detector distance of 60 mm (Fig. 3.3). Under this configuration, the consequent voxel size was 1.12 μm and field of view was 2.4 mm. A sequence of 1301 2000 × 2000 16-bit transmission radiographs were collected over 6.5 hours. The exposure time was 18 second per projection. A filtered-back projection algorithm was used for the reconstruction and the 3D volume was visualised using Avizo V7.0 software.

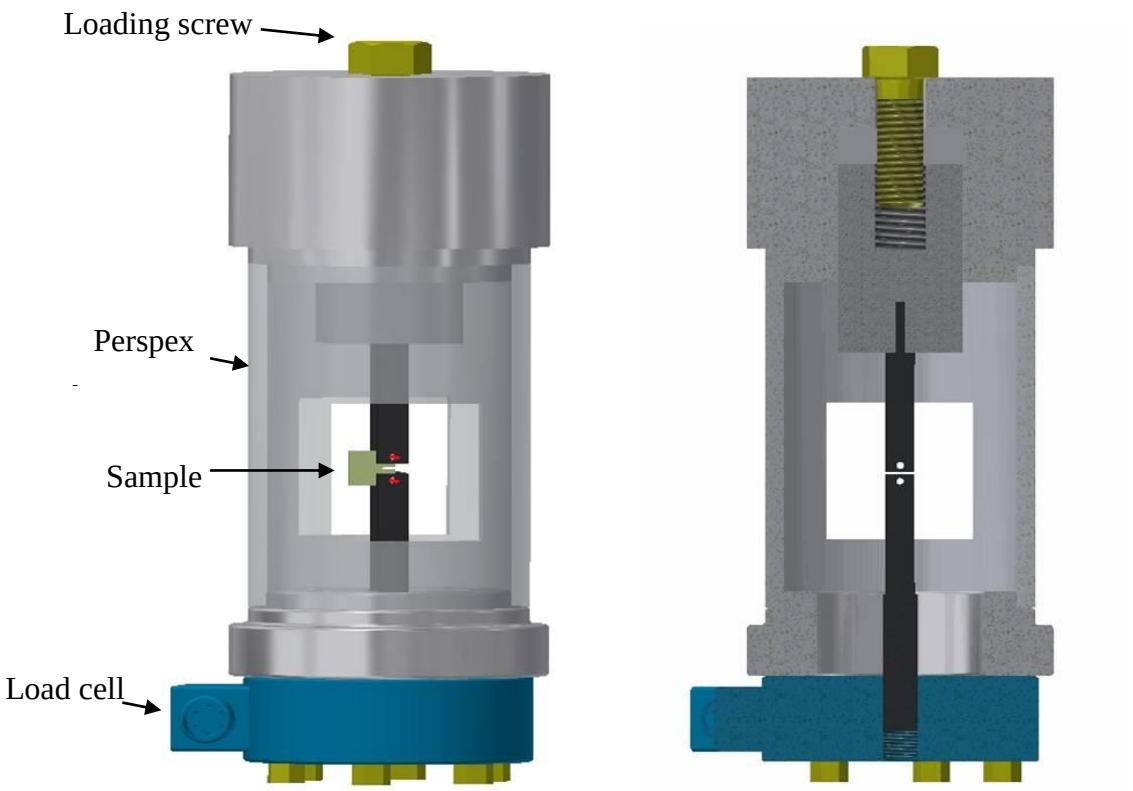

Fig. 3.2 Self-designed loading rig for the in-situ X-ray tomography experiment.

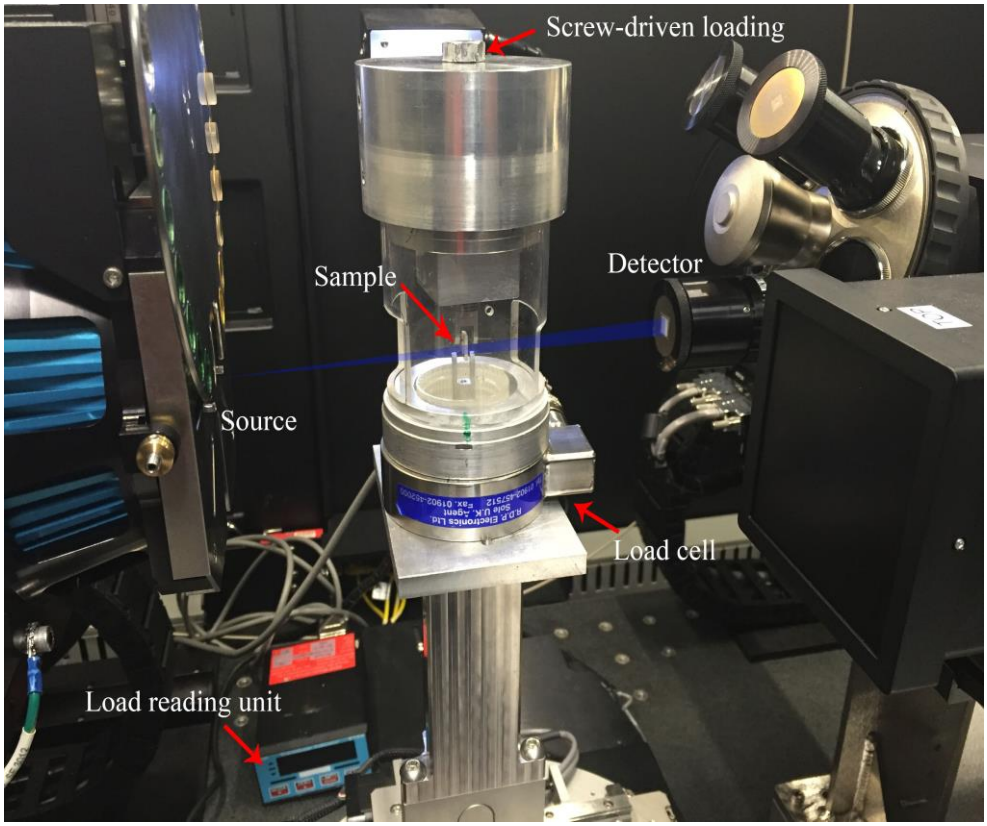

Fig. 3.3 X-ray computed tomography experiment configuration.

3.3 Crack Opening Displacement Measurement

Both the optical microscopic images and the reconstructed tomographic volumes were used to calculate the COD in 2-D and 3-D respectively. In both cases, the contrast of the images were enhanced using Matlab R2012a (Fig. 3.4a). The speckle patterns surrounding the crack path were masked out before using an interactive thresholding tool to segment the cracked region (Fig. 3.4b). By doing this, a binary image was produced where the crack body was characterized by intensity 1 and the rest (background) was assigned 0. In each column of the segmented image, the crack opening displacement was calculated by summing up the foreground pixels vertically using Matlab. For the volume COD measurement, the same procedure discussed above would be applied to all the slices throughout the crack width so as to create a 3-D COD map.

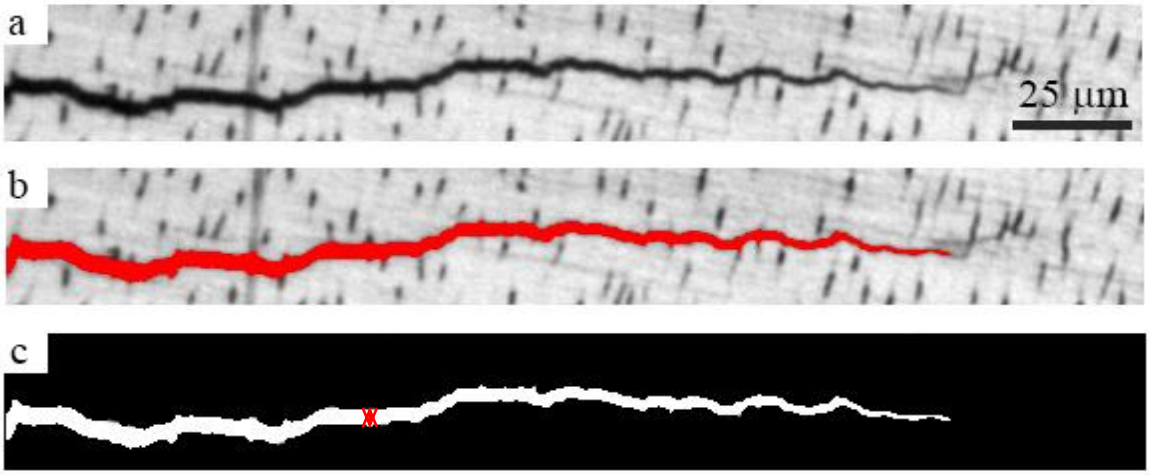

Fig. 3.4 The determination of the crack opening displacement: (a) optical images showing the region of crack, the contrast was enhanced using Matlab; (b) crack identified by interactive thresholding; (c) segmentation of the crack with intensities 0 and 1 assigned to the crack and background respectively.

References

[1] Kruzic J, Nalla RK, Kinney JH, Ritchie RO. Crack blunting, crack bridging and resistance-curve fracture mechanics in dentin: effect of hydration. Biomaterials 2003;24:5209-21.
[2] Raubenheimer EJ, Dauth J, Dreyer MJ, Smith PD, Turner ML. Structure and Composition of Ivory of the African Elephant (Loxodonta-Africana). S Afr J Sci 1990;86:192-3.
[3] Iwamoto N, Ruse ND. Fracture toughness of human dentin. Journal of Biomedical Materials Research Part A 2003;66:507-12.
[4] Nalla RK, Kinney JH, Ritchie RO. Effect of orientation on the in vitro fracture toughness of dentin: the role of toughening mechanisms. Biomaterials 2003;24:3955-68.
[5] E1820-08a A. Standard Test Method for Measurement of Fracture Toughness. American Society for Testing and Materials (ASTM) International, West Conshohocken, PA, USA 2008.

Paper 1: Characterisation of Anisotropic Fracture Toughness in Elephant Dentin Using 2-D and 3-D Methods

Contributions:

X. Lu: Principal investigator to conduct the experiment, analyse and interpret all the results, write up the paper

Dr. J.N. Walsh: Language corrections, structure organisation

Prof. P.J. Withers: Comments on the results discussion and interpretation

Chapter 4

Characterisation of Anisotropic Fracture Toughness in Elephant Dentin using 2-D and 3-D Methods

X. Lu[a], J.N. Walsh[b], P.J. Withers[a,b*]

[a]*School of Materials, University of Manchester, Grosvenor Street, Manchester M1 7HS, UK*

[b]*The Research Complex at Harwell, Rutherford Appleton Laboratory, Didcot, Oxfordshire OX11 0FA, UK*

Abstract

It is well known that elephant dentin exhibits orientation-dependent fracture toughness, until now, anisotropic fracture have only been characterised in terms of the parameter *K* or R-curve, and the effect of crack-tip shielding has never been characterised in 3-D neither qualitatively nor quantitatively. This paper presents the first quantitative measurements of the in-situ crack opening displacement, in 2-D and 3-D (X-ray computed tomography), along with R-curve measurements, and effective *K* values in 3 cracking directions, to inspect the microstructure-dependent crack growth mechanisms and characterise the bridging effect. Examination of 2-D crack path morphology, fracture surfaces, and 3-D crack plane morphology has led to identification of the active toughening mechanisms. Results showed that for crack growth parallel to tubule axes, remarkable extrinsic shielding,

* Corresponding author, School of Materials, University of Manchester, Grosvenor Street, Manchester M13 9PL, UK

Email address: p.j.withers@manchester.ac.uk, +44 (0)161 306 4282

e.g. collagen bridging and uncracked-ligament bridging, have been observed by both optical and 3-D X-ray tomography techniques, and they effectively reduced the crack opening locally. The bridging distance was observed as large as 400 mm. These shielding effect was also confirmed by the much lower effective K. Perpendicular to the tubule axis, in the hoop-axial plane of the tusk, crack paths exhibit large deflections and the highest critical stress intensity factors KIC. These discoveries confirm the strong dependence of the anisotropic fracture behaviour on the arrangement of the collagen fibrils, which contribute significantly to the crack retardation process.

Key words: Severe crack kink, crack growth resistance, mixed-mode *K*, crack opening displacement fitting, 3D crack bridging, extrinsic toughening, collagen orientation, bridging length

4.1 Introduction

This paper aims to improve our mechanistic understanding of the anisotropic fracture of dentin. This is important from the perspective of developing a framework for failure prediction in clinical research, to develop biomimetic restorative materials or oral treatments, and to understand the effect of the wide variety of restorative or aesthetical dental procedures [1]. Human dentin consists of enamel; a peripheral component the cementum, which is continuous with but structurally different from enamel; and a central pulp cavity of dentin. The cementum layer is softer than the dentin [2]. The dentinal tubules are the predominant microstructural feature in the main dentin, running from the central pulp to the periphery of the dentin. These tubules are embedded in a mineralized collagen matrix, which consists of Type I collagen fibrils and Mg containing hydroxyapatite [2-7]: the highly mineralized hydroxyapatite (HAP) improves the stiffness of teeth, while collagen provides toughness [8]. For the present study we chose elephant dentin, which is often used as a structural analogue for human dentin due to the similarities in microstructure and chemical composition, in order to avoid test-piece size restrictions given the larger size of ivory than human teeth. In comparison to human dentin, elephant dentin tubules are more elliptical in shape [7]. The tubules stack one above the other axially to form microlaminae, most commonly in the radial/axial plane (Fig. 4.1B–J) [2]. Around these tubules, collagen fibrils are distributed radially in planes perpendicular to the long axis of the tubules [5]. They form a mesh and crosslink around the tubules to provide the desirable mechanical properties of teeth [7, 9].

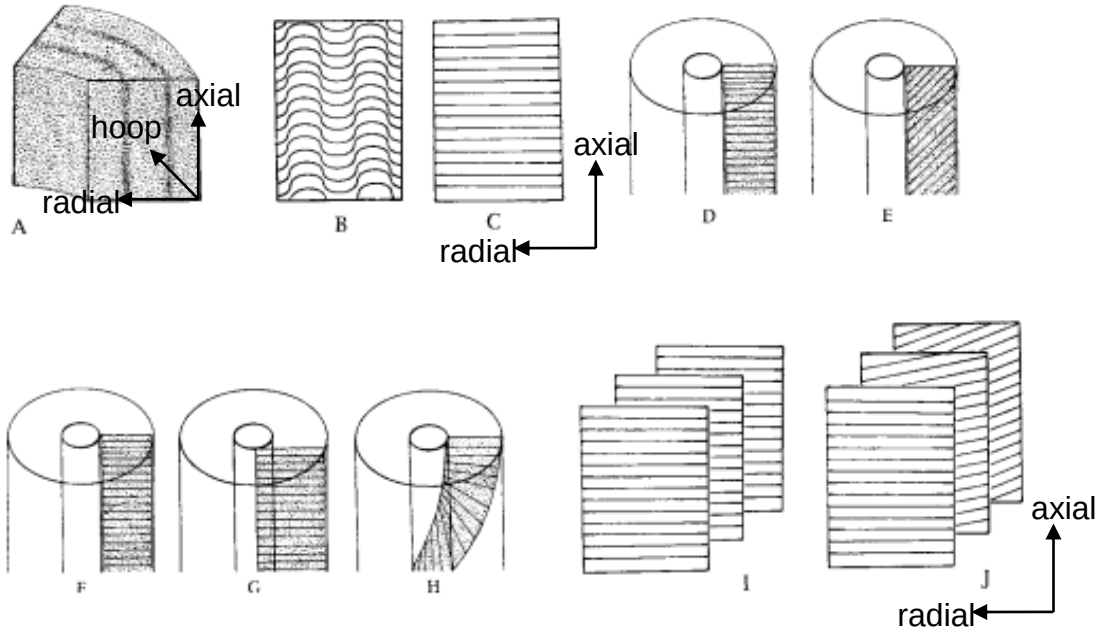

Fig. 4.1 Overview of ivory structure. (A) Macroscopic view of the ivory. The black lines correspond to the growth layers, the spotty pattern represents the radial tubules; (B) curled tubules into waves; (C) straight tubules. (B) and (C) are radial profiles. (D) and (E) show the microlaminae that are made of different oriented tubules. (F-H) indicate that the microlaminae can be radial/axial (F), axial but angled to the forming face (G), or radial but helical(H). Different microlaminae can have the identical orientations (I), or varying orientations to get the helicoidal pattern(J) [2].

Much work has been done on the fracture mechanics of dentin [10-13], typically in elephant and bovine dentin. The length-scales over which cracks can propagate are much smaller in human dentin because of the limited test-piece size which makes it difficult to achieve stable crack growth. This is disadvantageous for work concentrating on the fracture toughness which property has been shown to increase with crack length , due to activation of extrinsic toughening mechanisms similar to those in cortical bone [14]. Fracture toughness is often quantified in terms of the parameters: *K*, the stress intensity factor for a particular mode of linear-elastic fracture; *J*, the elastic-plastic fracture toughness – a measure of the energy required to grow a crack; and COD, the crack opening displacement. Toughness in linear-elastic fracture can be measured in the R-curve format, where the extent of crack growth is measured as a function of applied stress intensity factor, *K*, or as a point value, using a range of different geometries and test methods, such as three or four-point bending, compact tension, and nanoindentation. In the present study, the fracture toughness is assessed in terms of *K* in single point and R-curve format.

Although when studying dentin it needs to be borne in mind that hydrated samples exhibit much higher fracture toughness than dehydrated ones [15, 16], previous work has revealed that for most kinds of dentin (e.g. human, bovine and ivory dentin), the critical fracture toughness K_c is 55–65% higher for cracks propagating parallel to the long axis of the dentinal tubules compared to crack propagation perpendicular to the tubules [12, 17-19]. Fracture toughness has unsurprisingly also been found to be affected by microstructure variation [20] and age [15, 21]. Several toughening mechanisms in dentin, particularly for the case when a crack propagates parallel to the tubules, have been proposed such as crack blunting [19, 21], crack-tip bridging [17, 19, 21, 22], and micro-cracking [17, 22].

Until now, no one has looked at extrinsic shielding (e.g. bridging) quantified in terms of R-curve behaviour and crack opening displacement (COD) either using 2-D or 3-D methods. The aim of this paper is to undertake such a study to correlate crack growth in different directions with the corresponding microstructure and the shielding mechanisms in order to assess the degree of anisotropy.

4.2 Materials and experimental methods

4.2.1 Materials preparation and methods

A cross-sectional slice from a tusk of African elephant ivory was used in this study. Fracture toughness test-pieces with three different orientations relative to the tubules alignment were extracted as shown in Fig. 4.2a and a compact tension test-piece (9×8×2 mm^3) (Fig. 4.2b) was designed based on ASTM E1820 [23]. In Fig. 4.2a, depending on the orientation of the tubules, three different types of test-pieces were prepared for this study: HAH (crack in hoop-axial plane, growing in hoop direction), RAR (crack in radial-axial plane, growing in radial direction). HRH (crack in hoop-radial plane, growing in hoop direction). The different alignments of the collagen fibrils and dentinal tubules relative to crack growth direction in three cases are shown in Fig. 4.2c (HAH), d (RAR) and e (HRH) respectively. The collagen fibrils are drawn as cross linked red lamella. Before cutting, the test-pieces were stored in distilled water at 4℃ for more than two weeks to keep hydrated. A 1 cm thick plate was sliced off from the top of the whole tusk, followed by numerically controlled slicing of test-pieces under water-based coolant with

diamond abrasive cutting wheels. Subsequently, the plates were cut into rectangular bars and further into compact tension test-pieces with a 0.3 mm thick cutting wheel.

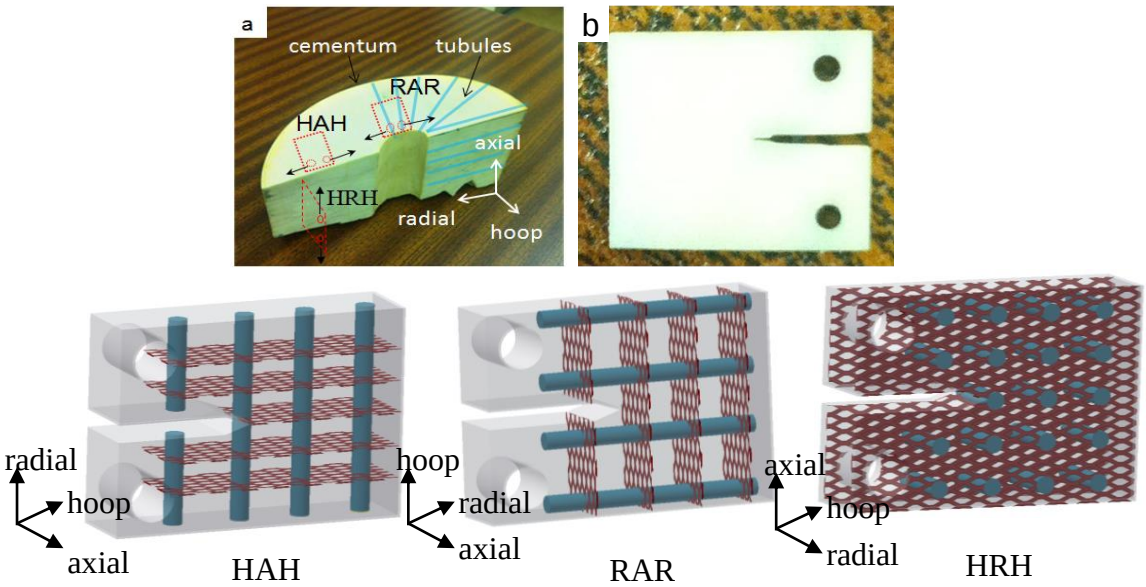

Fig. 4.2. (a) Schematic illustration showing the locations where three CT test-pieces were extracted;(b) compact tension test-piece (c) test-piece 1, (d) test-piece 2 and (e) test-piece 3 in each case showing the crack growth direction relative to the alignment of the tubules (blue) and collagen fibrils (red) in the dentin.

Finally, the test-pieces were ground with SiC papers from grit 600 up to grit 2400 finish, then polished in an alumina slurry (up to 0.25 μm) to remove the surface defects (e.g. scratches, dimples and dust). All the test-pieces used in the work are listed in the table below:

Table 4.1 Test-pieces and the related test in present study

Test-piece type	Direction of crack wrt tubules	R-curve	COD	Fracture surface
HAH1	perpendicular	Yes	Yes	Yes
HAH2	perpendicular	Yes	No	No
RAR1	0° parallel	Yes	Yes	Yes
RAR2	0° parallel	Yes	No	No
HRH1	90° parallel	Yes	Yes	Yes
HRH2	90° parallel	Yes	No	Yes
HRH3	90° parallel	Yes	No	No

For HAH1, RAR1 and HRH1, R-curve measurement was conducted immediately after the COD measurement when the crack had initiated to grow.

4.2.2 Resistance-curve measurement

An Instron-3344 was used for all the R-curve tests. After the test-piece was cracked, the displacement rate was changed to 0.001 μm/s for the rest of the test. A travelling microscope with 60x objective lens and reticule was used to observe the crack extension. The equipment was backlit with a lamp to enhance the contrast of the crack and test-piece matrix.

Despite the anisotropic fracture toughness, the elastic properties in elephant dentin are more isotropic, thus it is reasonable to use stress intensity factor K to characterise the crack-tip stress state. In cases where the crack path deflects from the maximum driving force plane (due to a preferred growth trajectory, for instance) local mixed-loading conditions occur at the crack tip. The loading has contributions from tensile opening (K_I) and shear (K_{II}) modes. To deduce the stress at the crack tip for a deflection at a constant angle from the maximum tensile stress plane, the following equations [17, 22, 24] are used:

$$\mathrm{k}_1 = c_{11}(\alpha)K_{\mathrm{I}} + c_{12}(\alpha)K_{\mathrm{II}}$$

$$\mathrm{k}_2 = c_{21}(\alpha)K_{\mathrm{I}} + c_{22}(\alpha)K_{\mathrm{II}} \tag{4.1}$$

where $c_{ij}(\alpha)$ are the mathematical expressions dependent on the deflection angle [24]. K_I and K_{II} are the global mode I and mode II stress intensities respectively. For compact tension test-piece K_{II} = 0. According to the ASTM standard [25], the expression for the nominal mode I stress intensity factor for compact tension test-piece is as

$$K_{\mathrm{I}} = \frac{P}{B\sqrt{W}} \frac{(2+\alpha)}{(1-\alpha)^{3/2}} (0.886 + 4.64\alpha - 13.32\alpha^2 + 14.72\alpha^3 - 5.6\alpha^4) \tag{4.2}$$

where P is the applied load, B is the test-piece thickness, W is the test-piece width, α is the ratio which is equal to length, a, divided by width: a/W. The effective stress intensity at the tip of the deflected crack tip, K_{eq} can then be calculated by the mode I and mode II contributions,

$$K_{eq} = \frac{k_1}{2} + \frac{1}{2}\sqrt{k_1^{\,2} + 6k_2^2} \tag{4.3}$$

4.2.3 Crack opening displacement

Crack opening displacement (COD) is defined as the relative opening movement of the upper and lower crack flanks:

$$\Delta u(r) = u_y^{top}(r) - u_y^{bot}(r) \tag{4.4}$$

where $\Delta u(r)$ is the crack opening displacement, r is the distance from the crack-tip, y is the direction perpendicular to the crack plane, $u(r)$ is the crack flank displacement at position r. COD is a useful measure of the effective stress intensity K_I^{eff}, thus the difference between K_I^{eff} and K_I^{app} indicates the extent of crack shielding. It is also possible to measure the crack opening load [26-28]. A camera-attached optical microscope, with 100x magnification was set up to acquire images of the crack-tip. To determine the COD the raw images recorded by the camera were imported into ImageJ v1.46. The crack was identified using intensity thresholding, converted to a binary image and the crack opening displacement along the crack wake was calculated using Matlab 2012a.

The mode-I stress intensity factor K_I can be inferred from the ΔCOD measurement [29, 30]:

$$\Delta u(r) = 8\frac{K_I^{eff}}{E'}\sqrt{\frac{r}{2\pi}} \tag{4.5}$$

where E' is equal to E under plane stress conditions and $E / (1-\nu^2)$ under plane strain conditions. $\Delta u(r)$ is the net (i.e. after background subtraction) COD at distance r away from the crack tip. This equation predicts a parabolic dependence of $\Delta u(r)$ with distance r.

4.2.4 Fracture surface inspection (SEM)

Fractographic features often provide important information about the crack growth process. A Philips XL30 scanning electron microscope was used to compare the fracture surfaces for crack growth perpendicular and parallel to the tubule orientation. Prior to imaging the fractured surfaces were gold coated to enhance the conductivity.

4.2.5 3D crack morphology observation by X-ray tomography

Non destructive high resolution X-ray computed tomography (CT) was undertaken on the Xradia Versa XRM 500 X-ray microscope at the Manchester X-ray Imaging Facility. The experiment setup is shown in Fig. 4.3. It is a lab-source cone beam system and was operated at 80 kV with a source – test-piece distance of 30 mm and test-piece – detector distance of 60 mm. A radiograph (projection) was taken every 0.18° and 2001 frames in total were taken in a full scan. The exposure time was 18 second per projection. A filtered-back projection algorithm [31, 32] was used for the reconstruction and the 3D volume was visualised using Avizo V8.0 software. A region-of-interest scan was conducted with a final voxel size of 1.12 μm.

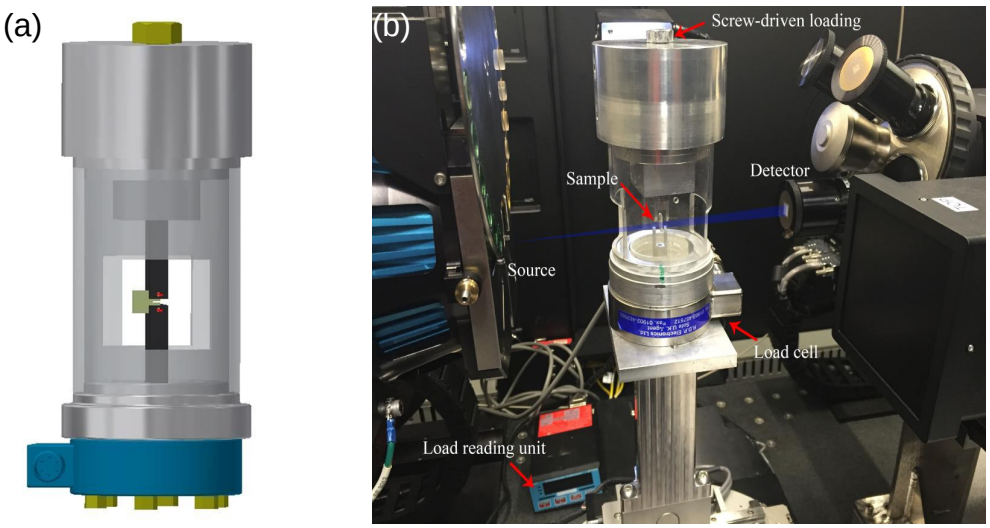

Fig. 4.3 (a) The schematic of the loading rig used in X-ray CT scan and (b) the experiment setup.

4.3 Results

4.3.1 2D Crack morphologies

The crack path and the microstructure for three test-pieces are shown in Fig. 4.4. It is found that the tubule pattern changes from lines to speckles with a periodicity of 250 μm based on Fig. 4.4a and b. Crack deflection is significant (72°) in Fig. 4.4c. In order to maintain the test-piece in plane strain condition, the test-piece thickness should be no less than 1.12 mm [33]. Similar crack deflection was previously found in bone [34] under four point bending.

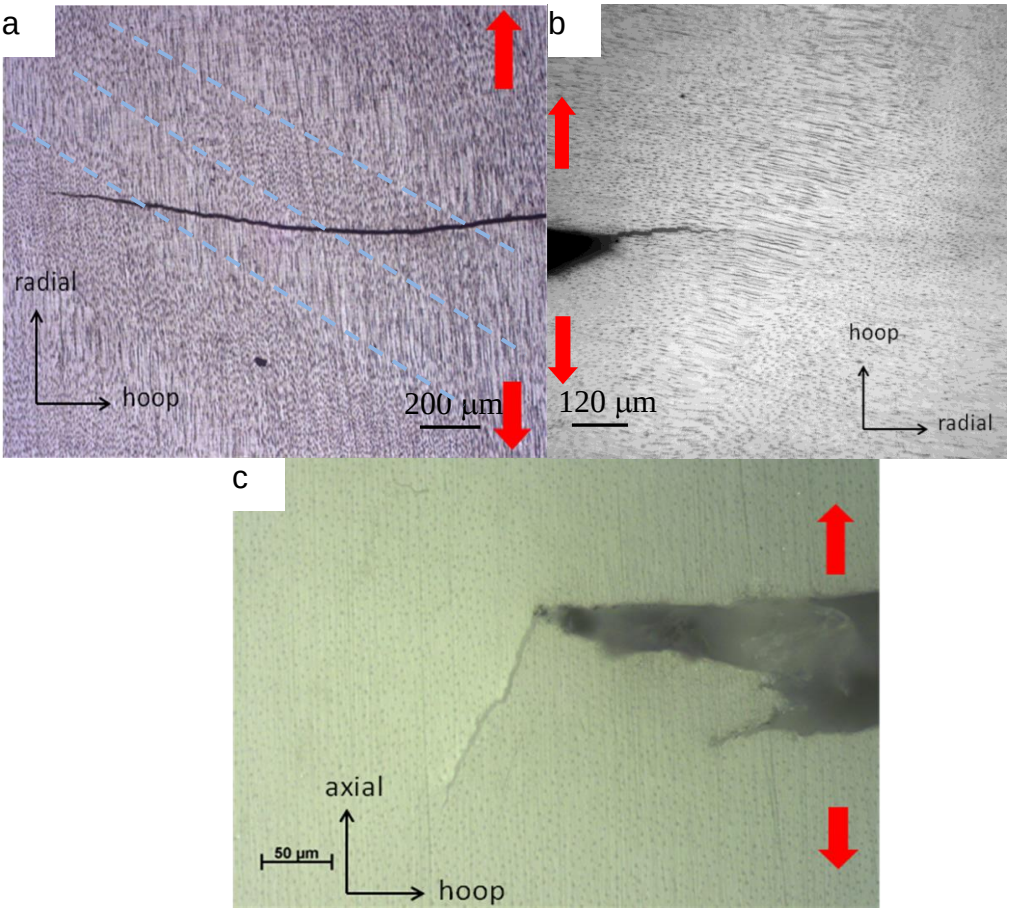

Fig. 4.4 Optical microscopic images showing the crack paths and the surrounding microstructure for three test-pieces of different cracking directions for a) HAH1;b) RAR1 and c) HRH1. The red arrows indicate the loading direction. The dashed lines indicate the periodicity of the tubule patterns.

Crack toughening mechanisms are closely related to the microstructures. Ductile metals usually rely on intrinsic toughening mechanisms (e.g. plasticity) ahead of the crack-tip whereas biomaterials such as dentin, bone, and cuticle tend to rely on extrinsic toughening mechanisms (e.g. bridging) behind the crack-tip [12, 14, 16, 19, 35]. Understanding the interaction between the crack and the microstructure can help identify the active toughening mechanisms.

Micro-cracks were noticed at the cross-section of the tubules (hoop-axial plane) (Fig. 4.5) on uncracked test-piece. The micro-cracks not only appear at the boundary of the matrix and the carbonated apatite, pointed out by arrow A (the white substance in the tubules), but also penetrate the tubules (arrow B). These micro-cracks may be the real feature of the test-piece since no load had been applied, but it is still possible that they were introduced during the sample preparation stage (e.g. cutting, polishing) even though special care was taken to avoid this.

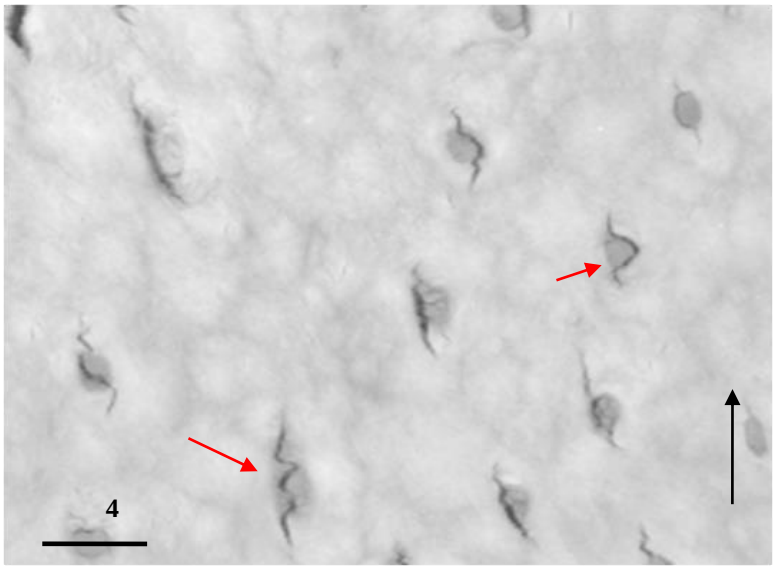

Fig. 4.5 Pre-existing micro-cracks in elephant dentin test-piece. (A) shows a micro-crack penetrate a tubule with deflection. (B) display the micro-crack bypasses a tubule. The black arrow means the crack growth direction.

Fig. 4.6 presents the crack morphology of HAH test-pieces under scanning electron microscopy (SEM). In Fig. 4.6a, the crack propagates straight to the end from the notch tip. Magnified images show crack-tip deflections at the tubules. Fig. 4.6c shows a clear, wide crack with little evidence of toughening mechanisms. It is noticed that the carbonated apatite in almost all the tubules are cracked along the tubule axis direction, which are the same seen from Fig. 4.5.

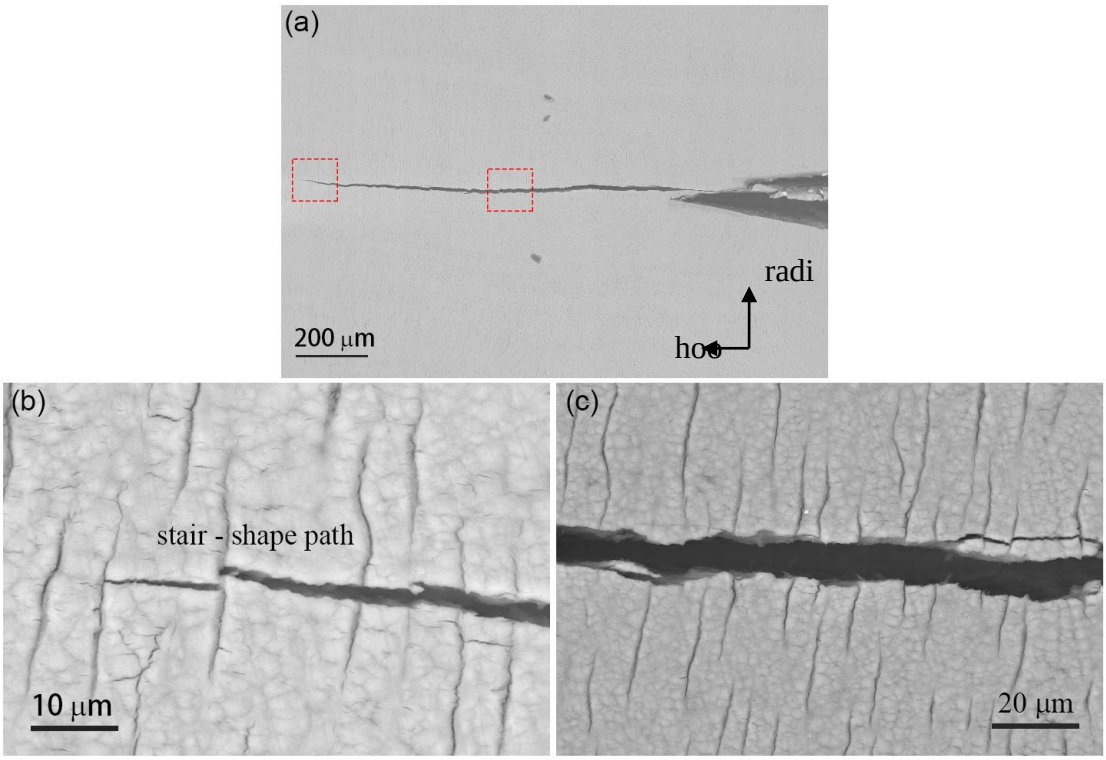

Fig. 4.6 SEM images of crack morphology of HAH test-piece. (a) macroscopic crack morphology; (b)magnified crack tip of the red square zone in panel (a); (c) magnified crack wake of the red square zone in panel (a).

Fig. 4.7 shows the significantly deflected crack path for HRH test-piece. Several potential toughening mechanisms are in action: uncracked-ligament bridgingcan be seen, as well as the meandering of the crack-tip along the tubule cuffs. Collagen fibrils bridging is visible in Fig. 4.7d.

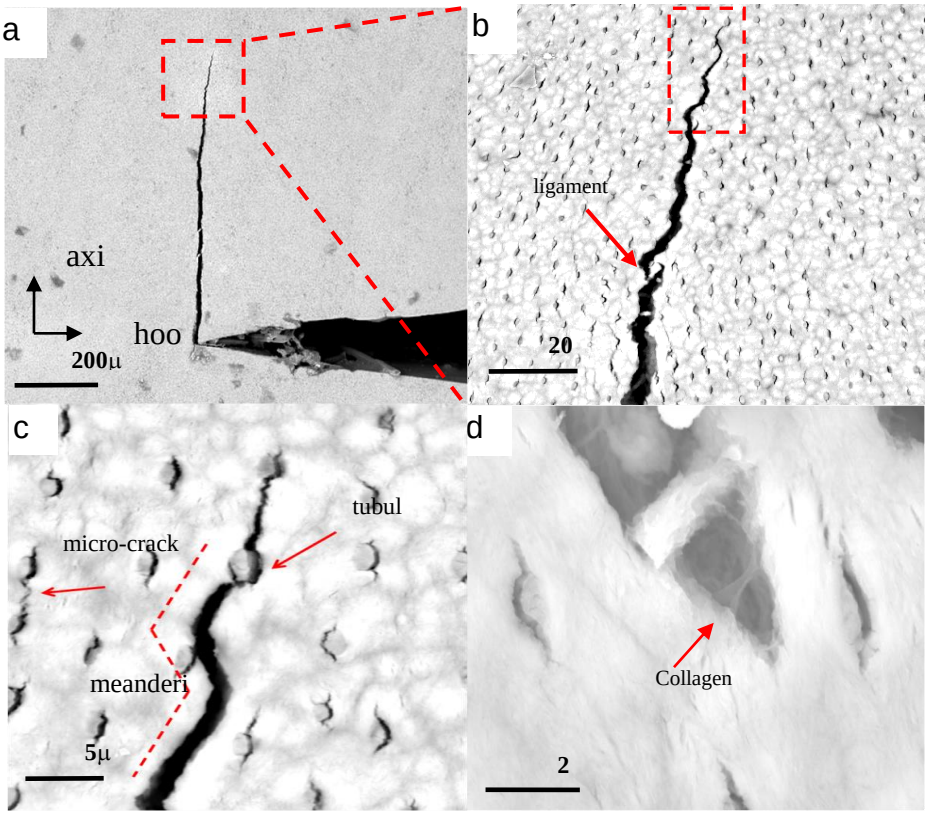

Fig. 4.7 Crack morphology observations of HRH with increasing magnifications.(a) Macroscopic crack path, revealing the 90° deflection phenomenon; (b) is the magnified image of the red square in (a). Tubules, crack bridging and meandering were noticed; (c) Crack tip stair-shape path and micro-cracks linking; (d) local fibrils bridging.

Fig. 4.8 demonstrates the crack bridging phenomenon for RAR test-piece. When the main crack approaches the area where the linear tubules are it propagates through the tubules by intercepting them at an ~ 45° angle. Remarkable crack bridging is seen during this progress. As the applied load increases, the bridging effect degrades as small pieces of the crack open wider and merge. While the crack continues to grow into the area with tubule speckles, the crack path reverts to a horizontal direction and bridging appears when a small crack initiates at the tubule cuffs out of the crack plane (black arrow in Fig. 4.8c).

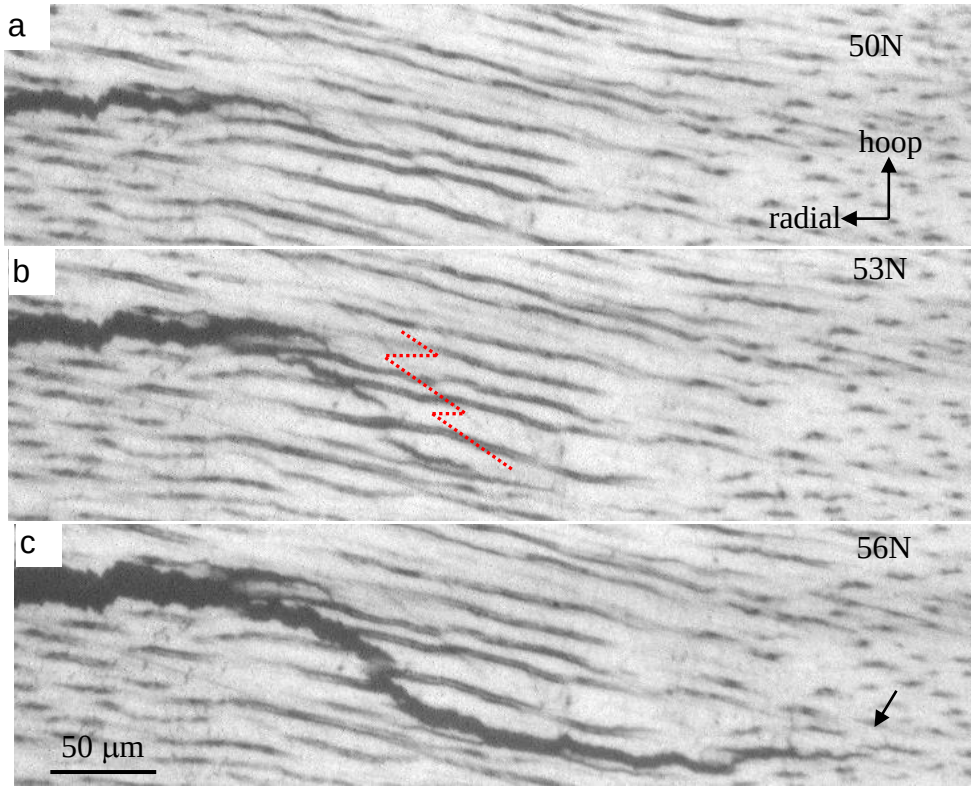

Fig. 4.8 Optical microscope images showing crack growth process of RAR test-piece at (a) 50 N (b) 53 N and (c) 56 N. The red dashed lines means the " Z " shape crack path and the black arrow indicates the uncracked-ligament bridging.

4.3.2 3D crack morphologies

X-ray computed tomography technique was used to image the crack plane and pick out shielding mechanisms in 3D, non-destructively. Fig. 4.9 presents the morphologies of the crack plane for the three directions obtained from X-ray CT data. It is clearly seen that HAH (Fig. 4.9a) test-pieces produce a flat crack plane with uniformly straight crack front and constant crack width; RAR test-pieces exhibit a quite different crack morphology compared with the previous two: distinct uncracked-ligament bridging is seen across the crack width. Fig. 4.9c is a colour coded map of the crack plane where a different colour indicates the different pieces of crack separated by uncracked-ligaments. The bridging distance is 400 μm in average. The crack front for RAR is no longer continuous but stepped, which evidences the ligament bridging. It is noticeable that the extent of bridging, seen from Fig. 4.9e, is much less on one side of the test-piece. The blue arrow points out the same ligament corresponding to that in Fig. 4.9c. HRH test-pieces exhibit a meandering and bumpy crack front where no ligament bridging can be seen.

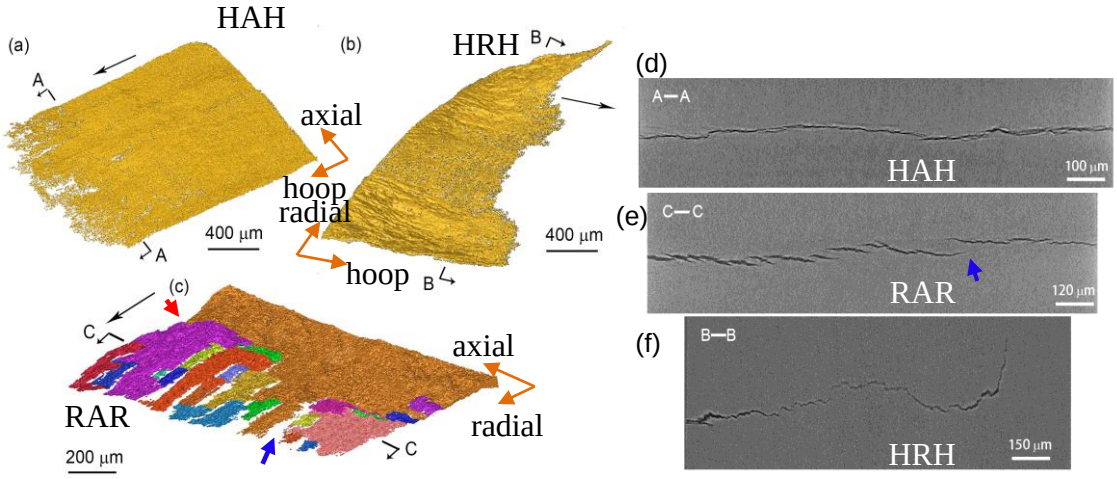

Fig. 4.9 The morphology segmentations of the crack plane for (a) HAH (b) HRH and (c) RAR test pieces from X-ray CT data. The cracks labelled by different colours of RAR test-piece stand for the discontinuity of the crack plane, forming the uncracked-ligament. The black arrows indicate the crack growth direction; the cross-sections of the crack front for three types of test-pieces are shown in (d)-(f). The blue arrow in (c) represents the bridging in (e).

4.3.3 Fracture surface

Fig. 4.10 shows the fracture surface of HAH test-piece under SEM. The blue arrows point in the crack growth direction. Fig. 4.10a displays clearly the exposed dentinal tubule cuffs. The red arrows show micro-cracks around the cuffs, which coincides with the micro-cracks observed from HRH test-piece surface in terms of shape and size (Fig. 4.7c). Collagen fibrils are also observed (the white fluffy microstructure). Fig. 4.10b is another area of the fracture surface, from which the collagen fibrils are more clearly seen. The surface is flat and the collagen fibrils are arranged roughly in one direction.

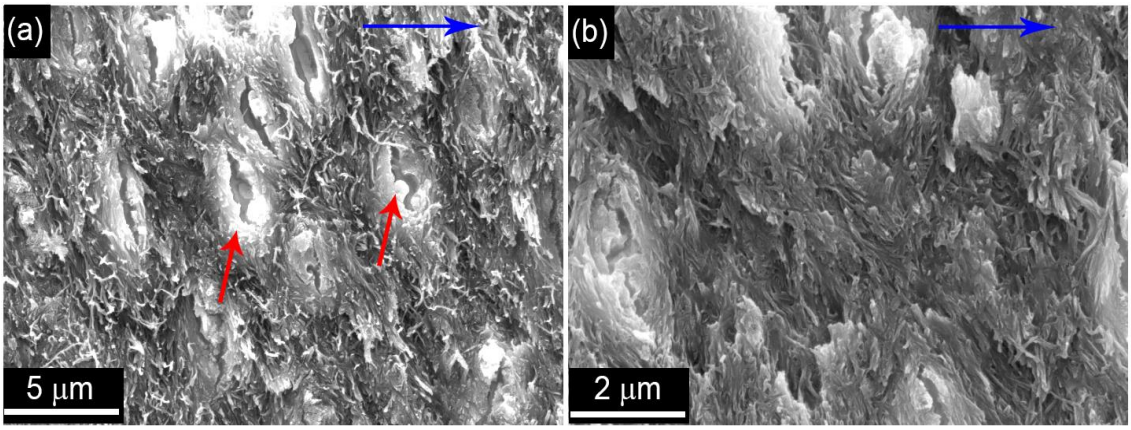

Fig. 4.10 Fracture surface of HAH test-piece by SEM under different magnifications. White arrows point in the crack growth direction and the red arrows indicate the micro-cracks around the tubule cuffs.

Fig. 4.11 show the SEM morphologies of fracture surface of RAR test-piece under increasingly greater magnifications. The white arrows point in the crack growth direction. Fig. 4.11a shows the macroscopic fracture surface under 100x magnification. Tubule patterns are visible along the crack growth direction. The dashed red line indicates the curved shape of the tubules arrayed in the dentin matrix. Compared with the fracture surface seen in Fig. 4.10, RAR specimens have a much rougher fracture surface. Fig. 4.11b is a magnified image from Fig. 4.11a: the tubules can be clearly seen aligned horizontally, they are indicated by blue arrows. Perpendicular to the tubule traces, a great many pieces of “leaf-shaped” microstructures are observed, which appear across the entire fracture surface. Fig. 4.11c is the magnified image of one of these “leaf-shapes” from the red square zone in Fig. 4.11b. Snapped edges of collagen fibrils are visible.

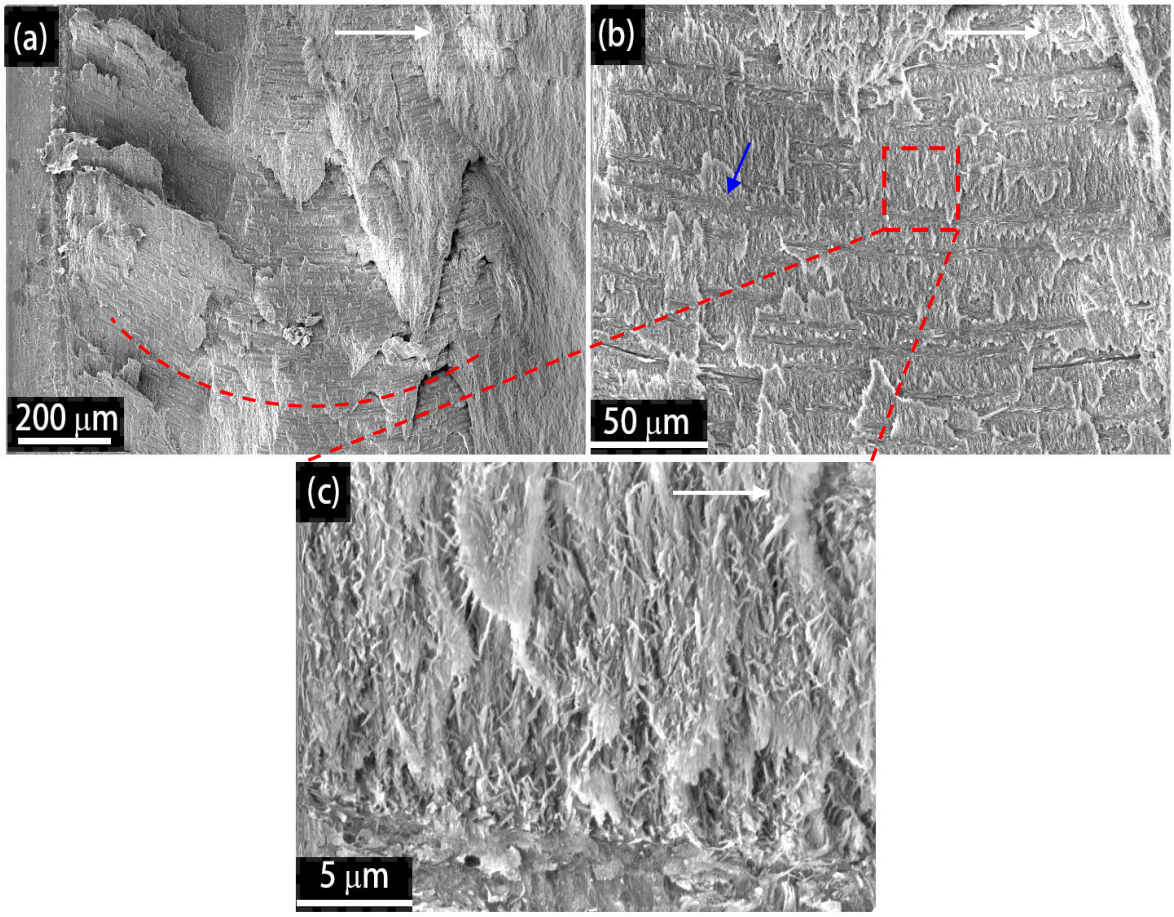

Fig. 4.11 Fracture surface of RAR test-piece by SEM under different magnifications. White arrows indicate the crack growth direction. (c) is the magnified image of the red square area in (b)

The fracture surface of HRH test-piece manifests similar "leaf-shaped" microstructures to RAR, as shown in Fig. 4.12a. Tubules and the surrounding collagen fibrils are clearly visible in Fig. 4.12b. It is found that some of the tubules are filled with carbonated apatite, which is common in elephant dentin but not in other types of dentin (e.g. bovine and human dentin). Fig. 4.12c magnifies the red dashed square zone in panel (a). As before, snapped ends of collagen fibrils are observed at the edge of the leaf-shaped pattern.

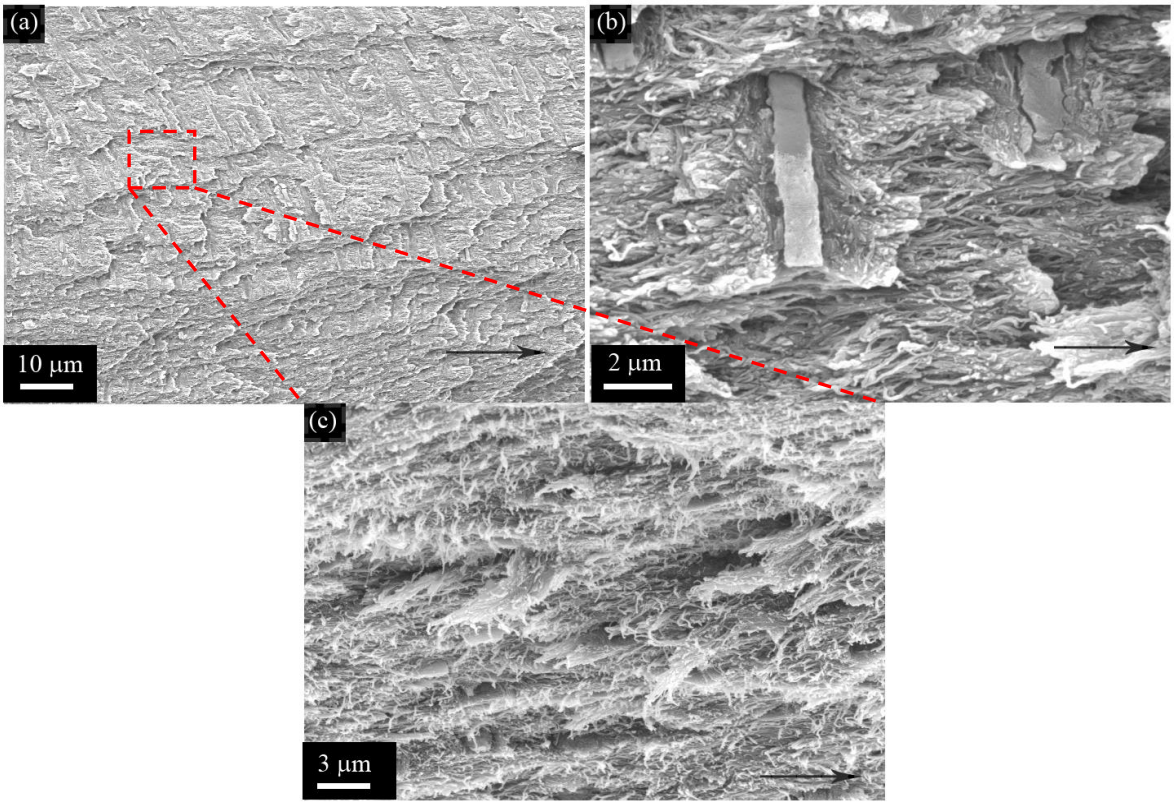

Fig. 4.12 Fracture surface of HRH test-piece under different magnifications (a) macroscopic fracture surface (b) magnified tubules and surrounding collagen fibrils; (c) magnified image of the leave-shape pattern in (a), and it clearly shows the fluffy collagen fibrils. The black arrows indicate the crack growth direction.

4.3.4 R-curve measurement

From the measurement of the resistance curve during subcritical crack growth (Fig. 4.13a) it can be seen that, for all directions of crack growth measured, fracture resistance increases with the crack extension. In each direction the R-curve does not show a smooth increase, rather the initial gradient is steep but after a point it flattens off. In RAR the steep gradient persists over a much greater crack extension length (0.4 mm) compared with the other two directions, for instance in HRH the rapid rise ceases after only 0.1 mm. Despite this, HRH test-piece has the highest critical fracture toughness K_{IC} at end of crack extension out of all the three types of test-pieces. HAH test-piece is the least tough, with K_{IC} = 0.6 – 1 $MPa\sqrt{m}$, compared with 1.25 – 1.5 $MPa\sqrt{m}$ for RAR and 2 – 2.5 $MPa\sqrt{m}$ for HRH test-piece. The results are shown in Table 4.2. Fig. 4.13b shows that after the crack extension Δa of 0.4 mm, the bridging distance has reached the maximum, which is about 100 μm. This agrees well with the R-curve performance for RAR. Both 2-D and 3-D

measurement exhibit that the bridging effect saturates at Δa = 0.4 mm, but the surface measurement shows a much smaller bridging distance (i.e. the region including all the bridging length ahead of the mother crack-tip) than the 3-D measurement (100 μm vs 400 μm).

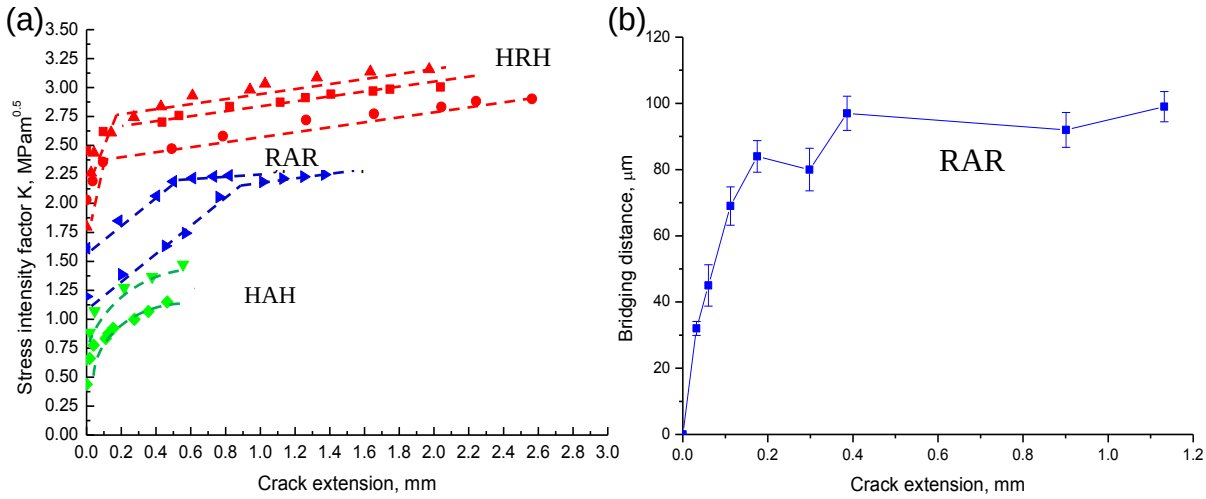

Fig. 4.13 (a) R-curve measurements for three type test-piece; (b) bridging distance for RAR test-pieces.

Table 4.2 R-curve measurements comparison for three type test-pieces

	K_s ($MPa\sqrt{m}$)	K_c ($MPa\sqrt{m}$)
HAH	0.77 ± 0.16	1.18 ± 0.21
RAR	1.62 ± 0.33	2.21 ± 0.04
HRH	2.35 ± 0.23	2.94 ± 0.13

4.3.5 Crack opening displacement

The ΔCOD vs √r curve was plotted based on Eq. (4.5) for three types of test-pieces, and the corresponding morphologies of the crack were attached underneath each figure. Since the plasticity at the crack-tip is little, it is assumed that the COD at the crack-tip x=0 is zero, except that at the critical loads for HAH and HRH, in which crack-tip blunting were observed and represented as an interception at x=0. There are three main observations from these data: (1) The distributions of ΔCOD are consistently linear with √r as a function of incremental applied load for all three types of test-piece; (2) RAR test-piece

shows lower gradients (0.034) at low load (< 6 N) compared with those for HAH (0.71) and HRH (0.62) test-pieces; (3) the crack width for RAR test-piece is smaller than the other two, observed from the morphologies. Moreover, for RAR test-piece, there is a sharp transition along the crack path, which indicates less crack opening within the distance from 0 to 50 μm to the crack tip.

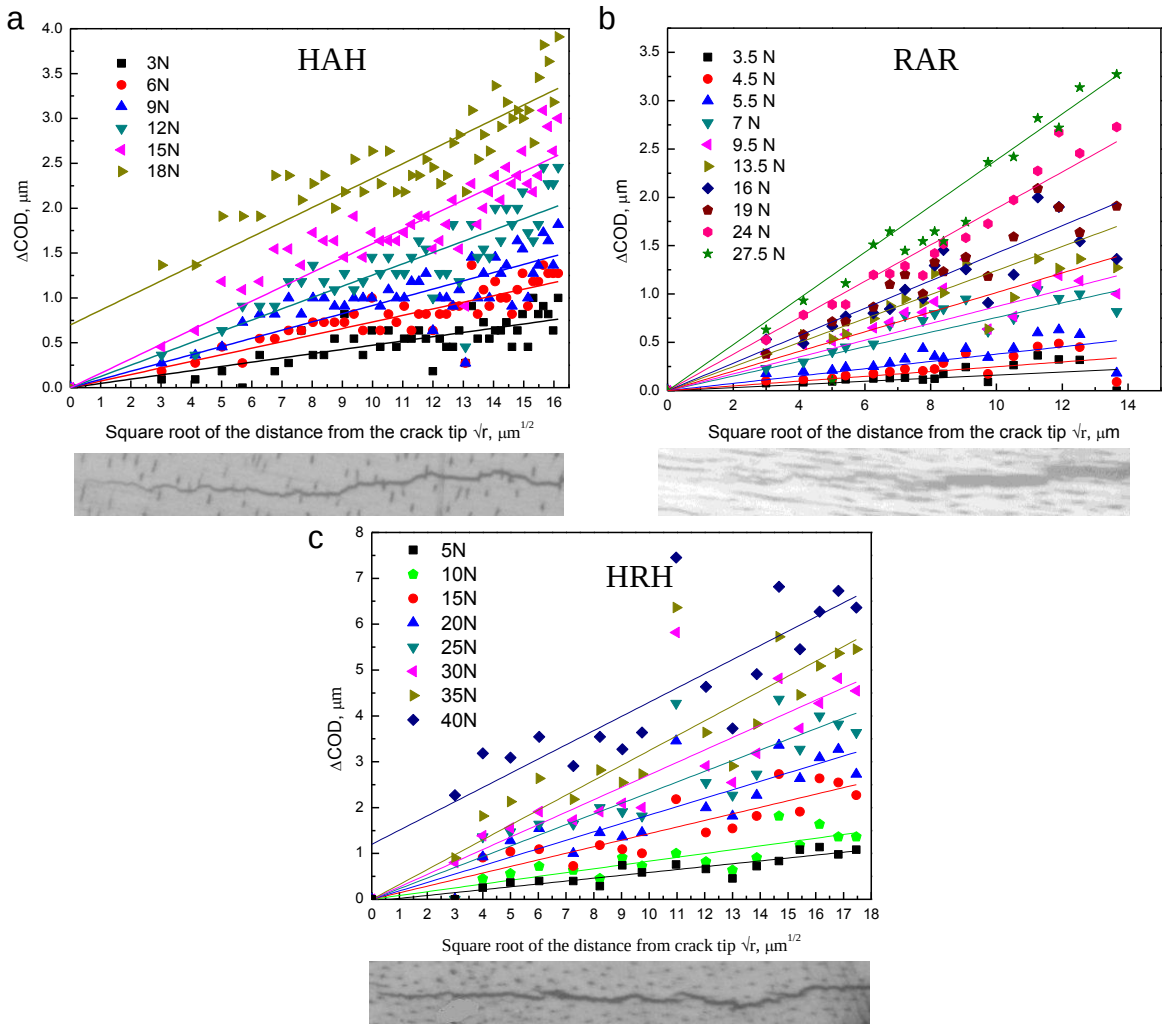

Fig. 4.14 ΔCOD plotted against the square root of the distance from crack tip (√r) for (a) HAH test-piece, (b) RAR test-piece and (c) HRH test-piece. The plots are then fitted with the straight lines. The crack morphologies observed by optical microscope were attached underneath corresponding test-pieces.

The fitted gradients were converted to plots of K_I^{eff} *vs* applied load (solid lines) and the results are shown in Fig. 4.15 alongside calculations of K_I^{appl} calculated using equation

(2) (dashed lines). It is clearly seen that for the measured K_I^{eff} the gradients for all test-pieces are identical with the corresponding nominal curve K_I^{appl}, except that at low load (less than 6 N), RAR test-piece exhibits a much lower rate of increase. The gradient of RAR test-piece rises significantly at 6 N, which can be attributed to the sudden widening of the crack path when the load is high, this phenomenon is not observed for the other two test-pieces. Fig. 4.15 also shows that the fracture toughness of HAH test-piece at failure (18 N load) is 0.89 $MPa\sqrt{m}$, and this value is lower compared with those for RAR (1.28 $MPa\sqrt{m}$ at 27.5 N) and HRH (1.67 $MPa\sqrt{m}$ at 40 N) test-pieces.

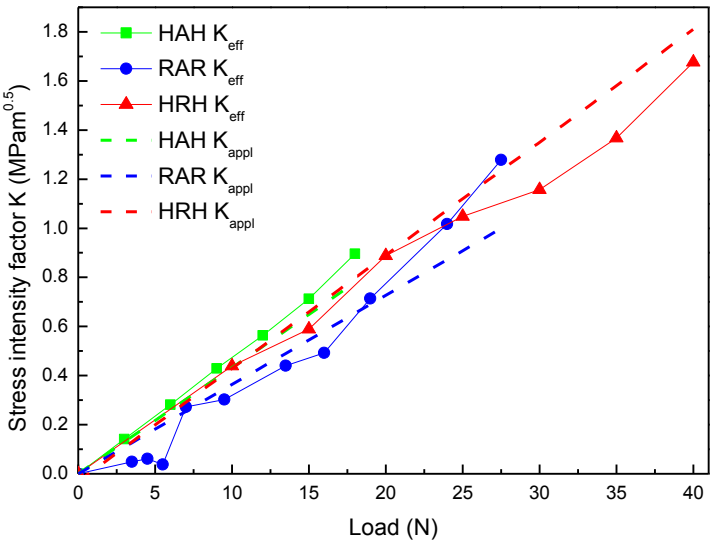

Fig. 4.15 Comparisons of the applied load K_I^{appl} and the effective load K_I^{eff} for three types of test-pieces.

4.3.6 Crack-tip shielding based on 3D measurement

In order to understand the how the uncracked-ligament bridging shields the crack-tip, the crack opening displacement (COD) was measured along the cross-section at C - C' plane for RAR test-pice (Fig. 4.16). The result depicts a non-uniform crack opening along the crack line: the magnitude of the opening decreases monotonically from front face at x = 0 μm to the back face x = 1400 μm. Also, and more importantly, from K = 0 to $K = 0.4K_{IC}$ the ΔCODs (i.e. subtracting the COD at K = 0 from the loaded ones) is smaller compared with that at $K = 0.8\ K_{IC}$, which indicates a disproportional crack opening with the load.

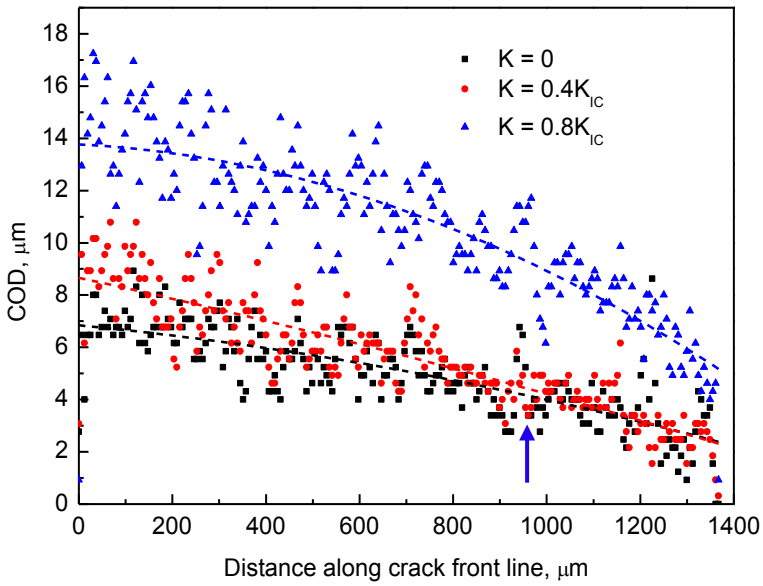

Fig. 4.16 The crack opening displacement of RAR test-piece along C-C' plane in Fig. 4.9c under incremental loads. x = 0 and 1400 mm cover the crack front from left to right edge in Fig. 4.9c and e. The blue arrows here and in Fig. 4.9 correspond to the same location.

The 3D COD map can clearly delineate the variance of the COD as a function of the distance along the crack-tip as well as across the crack front (Fig. 4.17). It is seen that crack opens evenly along its crack length until at y = 200 (i.e. pointed by red arrow in Fig. 4.9c), where uncracked-ligament bridging starts to become apparent. Crack growth and opening decrease with distance from the left surface, i.e. $x = 0$. From $K = 0$ to $K = 0.4K_{IC}$, the volume ΔCOD is smaller compared to that from $K = 0.4$ to $K = 0.8K_{IC}$, in agreement with the 2-D cross-section COD measurement. It is noticed that the area within the black dashed square opens much less than other areas across the crack plane at the same y position. This non-uniform crack-tip and COD could be a result of the crack bridging.

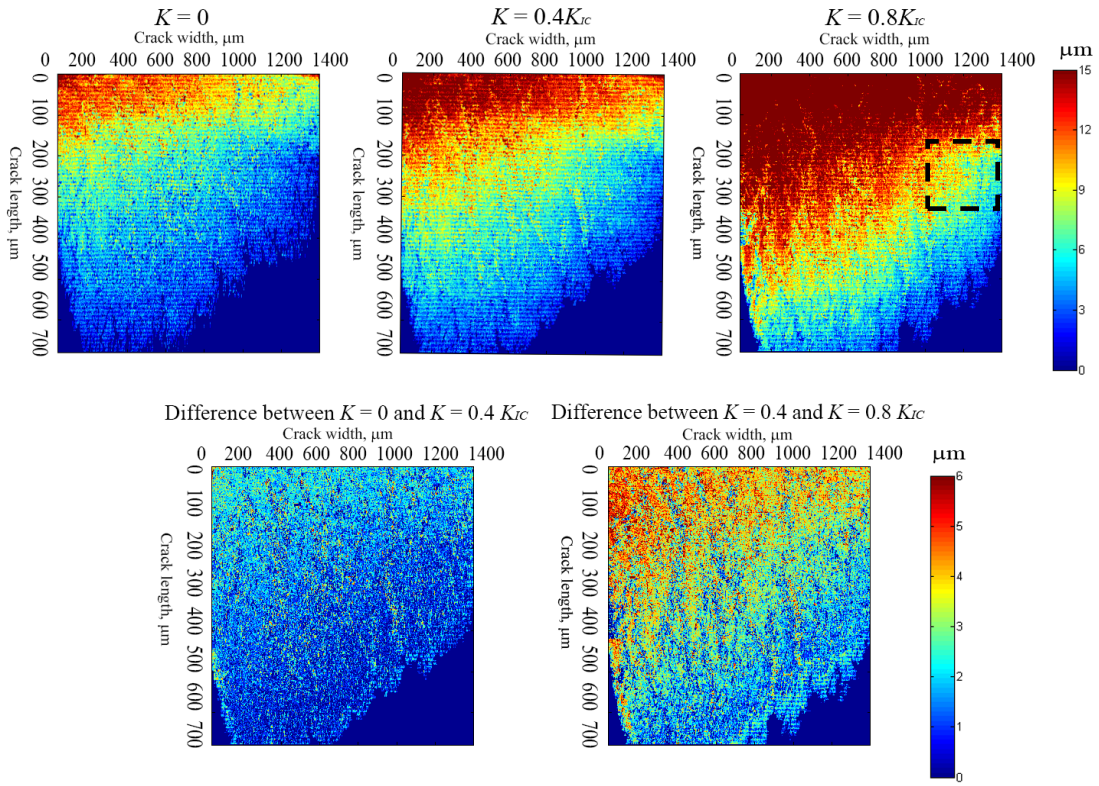

Fig. 4.17 The volume COD measurement for RAR test-piece and the ΔCOD comparison between K = 0 to K = 0.4K_{IC} and K = 0.4 to K = 0.8K_{IC}. The region in the black dashed box corresponds to that from x = 1000 to 1400 in Fig. 4.16.

4.4 Discussion

4.4.1 R-curve measurement

The anisotropy of the fracture toughness is clearly revealed in the different K_{IC} at failure for each type of test piece. HRH test-piece display the highest initial fracture toughness K_s and critical fracture toughness K_{IC} among all three types of test-pieces. HAH test-piece shows the lowest initial and critical fracture toughness (Table 4.2). The R-curve of RAR test-piece can be divided into two linear stages, where in the first stage the amount of bridging by uncracked-ligaments and collagen fibrils monotonically increases and afterwards, the crack propagation enters into a relatively steady stage when bridging reaches saturation[19, 36, 37]. The bridging distance as a function of the crack extension is coincident with the gradient change in the R-curve. In contrast, both HAH and HRH test-pieces showed monotonically increasing R-curve. The high fracture toughness for HRH test-piece arises from the strong deflection of the crack path, which significantly reduces the mode I stress and creates a mixed-mode driving force for crack extension [14, 38].

4.4.2 Crack opening displacements and effective K extraction

The non-linear extracted K_I^{eff} confirms the crack-tip shielding effect for RAR test-piece. However, this non-linear behaviour only seemed to occur at low load (<7N). This is due to the degradation of the extrinsic toughening mechanisms, i.e. uncracked-ligament bridging, with increasing crack width [36]. The maximum bridging load stress intensity factor, $K_I^{br} = K_I^{app} - K_I^{eff}$, is approximately 0.2 $MPa\sqrt{m}$ (20% of K_{IC}) for RAR test-piece.

Bridging phenomena are more clear from 3-D COD measurement - the variable crack opening for RAR test-pieces seen in 2-D images (Fig. 4.16) is in accordance with 3D tomography results (Fig. 4.17). Both images show non-uniform crack opening at the position where the ligament bridging is significant. By correlating the 2-D and 3-D CODs with the associated crack morphologies, it is concluded that crack bridging effectively retards the crack growth by reducing stress at the crack-tip, and thus contributing to a smaller crack opening displacement.

4.4.3 2-D and 3-D crack paths observation

2D crack path observations by SEM show that crack growth mechanisms are significantly different for each type of test piece. The straight and smooth crack path for HAH test-piece, similar to the cleavage planes seen in brittle materials, is related to the parallel alignment of the collagen fibrils and the crack plane. Large angle deflection in HRH test-piece always aligns with the orientation of the micro-cracks around the dentinal tubules. This indicates the crack growth resistance in the middle plane is much higher than deviation.

Although it has been suggested that micro-cracks only form around unfilled tubules [21, 22], this study shows clearly that micro-cracks form around virtually all of the tubules, prior to any load being applied. The tubules, filled or not, are not the key factor that determines the micro-cracks behaviour, in contrast to the conclusion made in [22]. These micro-cracks can penetrate the carbonated apatite or bypass it. Micro-cracks facilitate crack-tip shielding by promoting the formation of un-cracked ligament bridges and enable

dissipation of energy stored in the region of the crack tip [39, 40] thus reducing the stress and enhancing the fracture resistance [19, 37, 41, 42]. The apparent crack tip meandering (i.e. local deflection) occurs due to the linking of micro-cracks ahead of the crack tip.

The crack-tip toughening mechanisms for RAR test-piece is a combination of HAH and HRH, as indicated by a tortuous crack-tip at the spotty pattern area and crack re-initiation at the line pattern area (Fig. 4.8). Remarkable crack bridging is seen along the crack path, especially in the line pattern area. This mechanism is a critical crack retarding mechanism in bone [34, 40] arising from re-initiation of cracking at different points away from the main crack path. No such bridging was observed in HAH test-piece.

3-D crack plane observation is a good complementary technique to inspect the crack path through the volume. Strong crack bridging is observed across the crack line for RAR test-piece, but not for HAH and HRH test-piece.

4.4.4 Fracture surface observation

In respect of fracture surface observation, HAH test-piece exhibits more flat and smooth surface than that of RAR and HAH test-pieces. No evidence of snapped collagen fibrils is seen, which is in direct contrast with RAR and HAH test-pieces, from which the leaf-shaped microstructures and the collagen fibrils are seen pulled out from the plane, standing at the edge of them. This indicates that the low fracture toughness of HAH test-piece is caused by the absence of the collagen fibrils strengthening the material along the crack growth path. The difference between RAR and HRH test-piece is that, since there is significant uncracked-ligament bridging in RAR test-piece, the localised fracture plane is more rough and bumpy than HRH test-piece, as is shown in Fig. 4.11a.

4.5 Conclusion

After the study of the elephant dentin test-pieces with the crack growth in three different directions, the following conclusions can be made:

1. Elephant dentin exhibits anisotropic fracture toughness in three different cracking directions by R-curve measurement. HAH test-piece (crack in hoop-radial plane, growth in hoop direction) exhibits lowest toughness (1.18 ± 0.21 $MPa\sqrt{m}$) over the stable crack extension of 0.55 mm, and HRH (crack in hoop-axial plane, growth in hoop direction) is the toughest test-piece (2.94 ± 0.13 $MPa\sqrt{m}$) over the crack extension of 2.2 mm.

2. Crack tip shielding is achieved by bridging in RAR test pieces, evidenced by phenomena: (1) a coincidence of the gradient change between the measured bridging distance and R-curve, and the bridging distance was measured as large as 400 μm; (2) smaller crack opening displacement, and non-linear behaviour at low loads where there is effective bridging. This does not occur in HAH and HRH test pieces; (3) significant uncracked-ligament bridging observed both in 2-D and 3-D crack morphology images, and 20 % of K_{IC} was reduced by bridging; (4) wide distribution of the snapped collagen fibrils on fracture surface, but also found in HRH.

3. Crack growth mechanisms are significantly different in three test-pieces. HRH demonstrates large angle crack deflection, which always follows the direction of the pre-existing micro-cracks, forming a meandering crack growth path; crack in HAH test-piece is fairly straight, perpendicularly intersecting each tubules in the path; crack growth in RAR is more complex: it varies from intersecting the tubules long axis to follow the tubule micro-cracks periodically according to the line and speckle pattern of the tubules.

References

[1] Kinney JH, Balooch M, Marshall GM, Marshall SJ. A micromechanics model of the elastic properties of human dentine. Archives of Oral Biology 1999;44:813-22.
[2] Locke M. Structure of ivory. J Morphol 2008;269:423-50.
[3] Nalla RK, Imbeni V, Kinney JH, Staninec M, Marshall SJ, Ritchie RO. In vitro fatigue behavior of human dentin with implications for life prediction. Journal of Biomedical Materials Research Part A 2003;66A:10-20.
[4] Moyes AB, Doidge DW. COMPOSITION OF THE MINERAL PHASE OF DENTIN IN SOUTHERN ELEPHANT SEAL AND ANTARCTIC FUR-SEAL TEETH. British Antarctic Survey Bulletin 1984:81-4.
[5] Povar ML. Miles,Aew - Structural and Chemical Organization of Teeth. J Am Vet Med Assoc 1967;151:1211-&.
[6] Miles AEW, Boyde A. Observations on Structure of Elephant Ivory. J Anat 1961;95:450-&.
[7] Raubenheimer EJ, Dauth J, Dreyer MJ, Smith PD, Turner ML. Structure and Composition of Ivory of the African Elephant (Loxodonta-Africana). S Afr J Sci 1990;86:192-3.
[8] Marshall GW, Inai N, Magidi ICW, Ballouch M, Kinney JH, Tagami J, et al. Dentin demineralisation: effects of dentin depth, pH and different acids (vol 13, pg 338, 1997). Dental Materials 1998;14:383-.
[9] Su XW, Cui FZ. Hierarchical structure of ivory: from nanometer to centimeter. Mat Sci Eng C-Bio S 1999;7:19-29.
[10] Arola D, Rouland JA, Zhang D. Fatigue and fracture of bovine dentin. Experimental Mechanics 2002;42:380-8.
[11] Ivancik J, Neerchal NK, Romberg E, Arola D. The Reduction in Fatigue Crack Growth Resistance of Dentin with Depth. Journal of Dental Research 2011;90:1031-6.
[12] Iwamoto N, Ruse ND. Fracture toughness of human dentin. Journal of Biomedical Materials Research Part A 2003;66A:507-12.
[13] Bonfield W, Li CH. Deformation and Fracture of Ivory. J Appl Phys 1965;36:3181-&.
[14] Koester KJ, Barth HD, Ritchie RO. Effect of aging on the transverse toughness of human cortical bone: Evaluation by R-curves. Journal of the Mechanical Behavior of Biomedical Materials 2011;4:1504-13.
[15] Bajaj D, Sundaram N, Nazari A, Arola D. Age, dehydration and fatigue crack growth in dentin. Biomaterials 2006;27:2507-17.
[16] Kruzic JJ, Nalla RK, Kinney JH, Ritchie RO. Crack blunting, crack bridging and resistance-curve fracture mechanics in dentin: effect of hydration. Biomaterials 2003;24:5209-21.
[17] Nalla RK, Kinney JH, Ritchie RO. Effect of orientation on the in vitro fracture toughness of dentin: the role of toughening mechanisms. Biomaterials 2003;24:3955-68.
[18] Watanabe LG, Marshall GW, Marshall SJ. Dentin shear strength: Effects of tubule orientation and intratooth location. Dent Mater 1996;12:109-15.
[19] Kruzic J, Nalla RK, Kinney JH, Ritchie RO. Crack blunting, crack bridging and resistance-curve fracture mechanics in dentin: effect of hydration. Biomaterials 2003;24:5209-21.
[20] Ivancik J, Arola DD. The importance of microstructural variations on the fracture toughness of human dentin. Biomaterials 2013;34:864-74.
[21] Arola D, Reprogel RK. Effects of aging on the mechanical behavior of human dentin. Biomaterials 2005;26:4051-61.
[22] Koester KJ, Ager Iii JW, Ritchie RO. The effect of aging on crack-growth resistance and toughening mechanisms in human dentin. Biomaterials 2008;29:1318-28.

[23] E1820-08a A. Standard Test Method for Measurement of Fracture Toughness. American Society for Testing and Materials (ASTM) International, West Conshohocken, PA, USA 2008.
[24] Cotterell B, Rice JR. SLIGHTLY CURVED OR KINKED CRACKS. International Journal of Fracture 1980;16:155-69.
[25] ASTM. Standard Test Method for Measurement of Fracture Toughness. American Society for Testing Materials, West Conshohocken 2002;E1820-01.
[26] Ridell WT, Piascik RS. Determine fatigue crack openging loads from near-crack-tip displacement measurement and analysis. Advances in fatigue crack closure 1999;Second Volume:17.
[27] McEVILY AJ. On the cyclic crack-tip opening displacement. Fatigue Fract Engng Mater Struct 2009;32:2.
[28] Lopez-Crespo P, Withers PJ, Yusof F, Dai H, Steuwer A, Kelleher JF, et al. Overload effects on fatigue crack-tip fields under plane stress conditions: surface and bulk analysis. Fatigue Fract Eng M 2013;36:75-84.
[29] Kanninen M. Advanced Fracture Mechanics. Oxford University Press 1985.
[30] O'Dowd N. Advanced Fracture Mechanics: Lectures on Fundamentals of Elastic, Elastic-Plastic and Creep Fracture. Imperial College London 2002.
[31] Sagara Y, Hara AK, Pavlicek W, Silva AC, Paden RG, Wu Q. Abdominal CT: comparison of low-dose CT with adaptive statistical iterative reconstruction and routine-dose CT with filtered back projection in 53 patients. American Journal of Roentgenology 2010;195:713-9.
[32] Lauritsch G, Härer WH. Theoretical framework for filtered back projection in tomosynthesis. Medical Imaging'98: International Society for Optics and Photonics; 1998. p. 1127-37.
[33] Yan J, Taskonak B, Mecholsky JJ. Fractography and fracture toughness of human dentin. Journal of the Mechanical Behavior of Biomedical Materials 2009;2:478-84.
[34] Zimmermann EA, Launey ME, Ritchie RO. The significance of crack-resistance curves to the mixed-mode fracture toughness of human cortical bone. Biomaterials 2010;31:5297-305.
[35] Imbeni V, Nalla RK, Bosi C, Kinney JH, Ritchie RO. In vitro fracture toughness of human dentin. Journal of Biomedical Materials Research Part A 2003;66A:1-9.
[36] Ritchie RO. Mechanisms of Fatigue Crack-Propagation in Metals, Ceramics and Composites - Role of Crack Tip Shielding. Mat Sci Eng a-Struct 1988;103:15-28.
[37] Ritchie RO. Mechanisms of fatigue-crack propagation in ductile and brittle solids. International Journal of Fracture 1999;100:55-83.
[38] Koester K, Ager J, Ritchie R. How tough is human bone? In situ measurements on realistically short cracks. Nat Mater 2008;7:672-7.
[39] Nalla RK, Kinney JH, Ritchie RO. On the fracture of human dentin: Is it stress- or strain-controlled? Journal of Biomedical Materials Research Part A 2003;67A:484-95.
[40] Vashishth D, Tanner KE, Bonfield W. Contribution, development and morphology of microcracking in cortical bone during crack propagation. Journal of Biomechanics 2000;33:1169-74.
[41] Bajaj D, Sundaram N, Arola D. An examination of fatigue striations in human dentin: In vitro and In vivo. Journal of Biomedical Materials Research Part B-Applied Biomaterials 2008;85B:149-59.
[42] Evans AG, Fu Y. SOME EFFECTS OF MICROCRACKS ON THE MECHANICAL-PROPERTIES OF BRITTLE SOLIDS .2. MICROCRACK TOUGHENING. Acta Metallurgica 1985;33:1525-31.

Paper 2: Anisotropic Fracture Toughness Quantitative Analysis of Elephant Dentin Based on Digital Image Correlation Technique

Contributions:

X. Lu: Principal investigator to conduct the experiment, data analysis and interpretation and write up the paper

Dr. J. Duff: Data analysis software training and advisor

Dr. R.S. Bradley: Language and general corrections

Dr. J.N. Walsh: Language corrections, structure organisation

Prof. P.J. Withers: Comments on the results discussion and interpretation

Chapter 5

Anisotropic Fracture Toughness Quantitative Analysis of Elephant Dentin Based on Digital Image Correlation Technique

X. Lu[a*], J. Duff[b], R.S. Bradley[a], J.N. Walsh[b], P.J. Withers[a]

[a]*School of Materials, University of Manchester, Grosvenor Street, Manchester M1 7HS, UK*

[b]*Materials Performance Centre, University of Manchester, Sackville St,*

Abstract

Anisotropic fracture toughness is characteristic for dentin materials, and has been widely studied in terms of stress intensity factor *K*. Although a variety of shielding mechanisms in dentin were previously proposed, few study has directly assessed the crack-tip shielding effect quantitatively. In this study, we characterised the deformation ability at the crack-tip of elephant dentin in terms of crack-tip sustainable strain for the first time using digital image correlation (DIC), and this provides a new insight into the anisotropic fracture toughness. The effectiveness of the crack-tip shielding was assessed by comparing the effective stress intensity factor K_{eff}, obtained by displacement field fitting, with the nominally applied stress intensity K_{app}. It was found that in HRH test-piece (crack in hoop-radial plane of the tusk, and grow in hoop direction), severe crack deflection (> 72°) from

[*] Corresponding author, School of Materials, University of Manchester, Grosvenor Street, Manchester M13 9PL, UK

Email address: xuekun.lu@postgrad.manchester.ac.uk, +44 (0)7428662326

the mid-plane was observed, consequently introducing mixed-mode K (K_I+K_{II}) at the crack-tip. The maximum sustainable strain for HRH is 4.2 %, which is 250% larger than HAH (crack path in hoop-axial plane of the tusk, and grow in hoop direction) and 120 % larger than RAR test-piece (crack in radial-axial plane of the tusk, and grow in radial direction). The presence of the shielding effect was confirmed by a much lower crack-tip strain at low load in RAR. The mismatch of K_{eff} and K_{app} indicates the maximum shielding stress of 0.36 $MPa\sqrt{m}$ in RAR. No obvious crack-tip shielding was found in HRH and HAH.

Key words: Crack kink, Westergaard's solution, displacement fitting, crack-tip shielding, K extraction, effective stress intensity factor, accumulative strain

5.1 Introduction

Dentin is distinctive among biological materials for its great toughness. Many studies have attempted to reproduce its properties in the development of novel materials [1]. Ivory tusk is often used as a structural analogue for human teeth due to the similarities in microstructure and composition between the two materials and less restrictions on test-piece size, given the larger size of ivory than human teeth [2]. Fig. 5.1 illustrates the structure of human dentin. Dentinal tubules, which are the most characteristic feature in the dentin layer, running from the central pulp to the periphery of the dentin. These tubules are embedded in a mineralized collagen matrix, which consists of Type I collagen fibrils and Mg containing hydroxyapatite [3-8]: the highly mineralized hydroxyapatite (HAP) improves the stiffness of teeth, while collagen provides toughness [9]. Around these tubules, collagen fibrils are distributed radially in planes but perpendicular to the long axis of the tubules [5]. They form a mesh and crosslink around the tubules to provide its desirable mechanical properties [8, 10]. A mechanistic understanding of the mechanical properties of dentin is important from the perspective of developing a framework for failure prediction in clinical research, to develop biomimetic restorative materials or oral treatments, and to understand the effect of the wide variety of restorative or esthetical dental procedures [11].

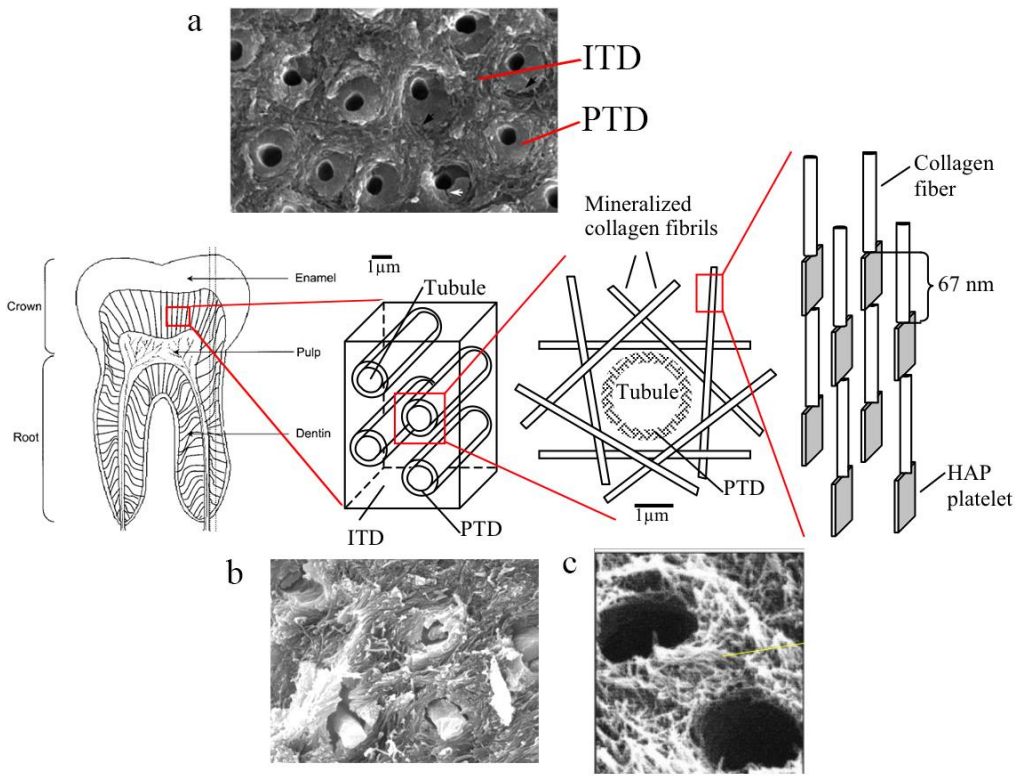

Fig. 5.1 Schematic of the hierarchical structure of teeth starting with the whole tooth molar (far left), which is magnified to show the tubules surrounded by peritubular dentin (PTD) and intertubular dentin (ITD). This ITD is further composed of tangential mineralized collagen fibrils and hydroxyapatite (HAP). Electron microscopic images show (a) the dentinal tubules and the ITD, PTD [12] (b) tubules occlusion by carbonated apatite (c) woven collagen between tubules respectively [13].

In the past years, much work has been done on the fracture mechanics of human, bovine and elephant dentin [14-17]. The length-scales over which cracks can propagate are much smaller in human dentin. This is disadvantageous for work looking at fracture resistance (R-curve) studies of the activation of extrinsic toughening mechanisms, similar to those operating in cortical bone [18].

Dentin is known for its orientation-dependent fracture toughness. Precedent work has revealed that, the fracture toughness K_c is 55–65% higher for cracks propagating parallel to the long axis of the dentinal tubules compared to crack propagation perpendicular to the tubules [2, 16, 19, 20]. The fatigue life is two orders of magnitude longer for cracks in the parallel direction compared to those in the perpendicular direction [3, 21]. Moreover, a hydrated test-piece exhibits much higher fracture toughness than a dehydrated one [22, 23]. Fracture toughness was also found to be affected by microstructure variation [24] and age [22, 25]. Several toughening mechanisms, particularly for the case when a crack

propagates parallel to the tubules, have been proposed such as crack blunting [2, 25], crack-tip bridging [2, 19, 25, 26], and microcracking [19, 26].

Digital Image Correlation (DIC) is a widely adopted technique used to inspect crack-tip displacement fields, surface strain and crack growth problems [27-30]. Recent applications in biological materials include strain measurements on mouse tibia [31] and bones [32, 33]. However, there has been little discussion about the crack-tip strain fields for dentin test-pieces. Moreover, by fitting the crack-tip displacement field using Westergaard's analytical solution [34, 35], the effective stress intensity factor K_{eff} can be extracted [36, 37]. Therefore, the crack-tip shielding effect can be assessed in terms of the disparities between K_{eff} and K_{appl}. The aim of this paper is to apply the DIC technique to elephant dentin for the first time to evaluate the anisotropic fracture toughness of three types of dentin test-pieces in terms of accumulative crack-tip strain and crack-tip shielding.

5.2 Materials and experimental methods

5.2.1 Materials preparation

A large cross-sectional slice from a tusk of African elephant (*Loxodonta africana*) ivory was used in this study, supplied by customs house for scientific purposes only. The test-pieces were extracted from three locations respectively from the ivory tusk (Fig. 5.2a) and named as *RAR*, *HAH*, *HRH*. *H*, *R* and *A* stand for *hoop*, *radial* and *axial* respectively, e.g. *HAH* means the crack is in hoop-axial plane, growing in hoop direction. Blue rods in Fig. 5.2c-e demonstrate the alignment of the dentinal tubules. The test-pieces were made into compact tension geometry (Fig. 5.2b) based on ASTM E1820 [38]. The different alignments of the collagen fibrils relative to crack growth direction in the three cases are illustrated in Fig. 5.2c-e. The collagen fibrils are drawn as cross linked red lamella. Before cutting, the test-pieces were stored in distilled water at 4 ℃ for over two weeks to keep hydrated. A 1 cm thick plate was sliced off from the top first, followed by an automatically controlled slicing under water-based coolant with diamond abrasive slicing wheels. Subsequently, the plates were cut into rectangular bars and further into 10×8×2 mm compact tension test-pieces with a 0.3 mm thick rotary cutting wheels.

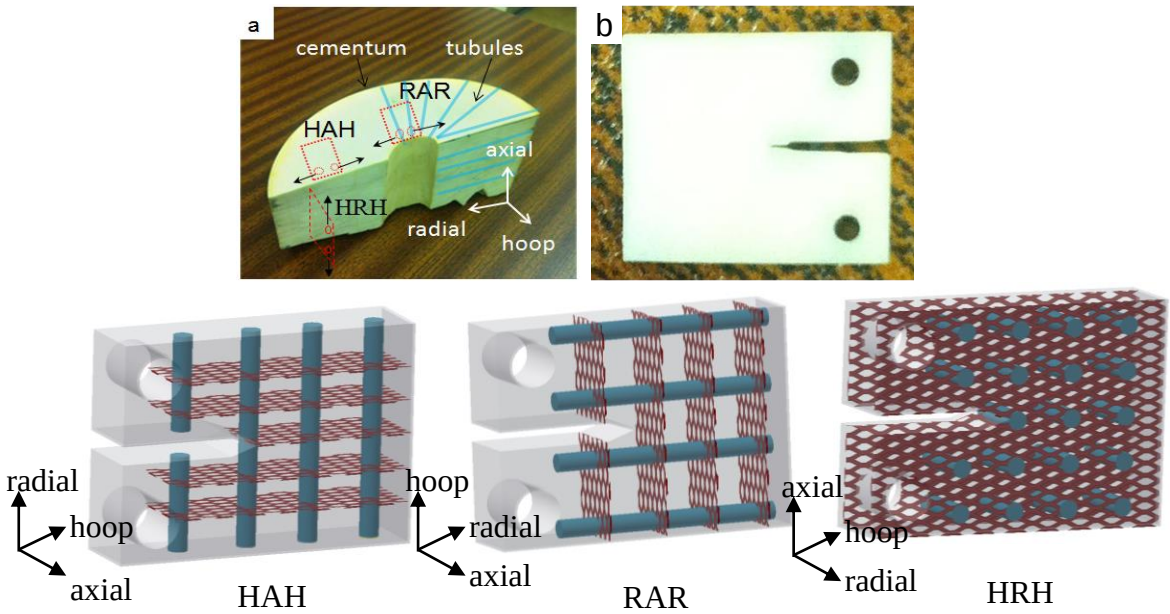

Fig. 5.2. (a) the schematic illustration of the ivory tusk, where the test-pieces were extracted from, and the alignment of the tubules (blue rods) in the tusk.; (b) real compact tension test-piece in 10×8×2 mm; (c)-(e) the crack growth direction relative to the alignment of the tubules (blue) and collagen fibrils (red) in the dentin for three test-pieces respectively.

A notch was introduced in the middle plane of the test-piece using a rotary wheel and sharpened with a razor blade till the radius of the notch tip was equal or below 5 μm. Lastly, the test-pieces were ground with SiC papers from grit 600 up to grit 2400 finish, then polished in an alumina slurry (up to 0.25 μm) to remove the surface defections (e.g. scratches, dimples and sands).

5.2.2 Crack-tip strain field measurement by digital image correlation

Digital image correlation is a well established technique used to trace the movement of surface features during a continuously loading process [39, 40]. The time-lapse crack-tip deformation was recorded by a series of images taken by a high speed camera. The natural patterns on the test-piece surface (e.g. lines and spots) provide ideal contrast for use as tracking references (Fig. 5.3). The crack paths of HAH and RAR are straight but in HRH, the crack path deflected about 72° from the middle plane. In order to extract the strain vertical and parallel to the crack line, the test-piece was rotated by -72° so that the crack plane was horizontally aligned (Fig. 5.3c). The red square zones in the 3 images indicate the region of interest (ROI) in which the displacement fields and consequently the strain

fields were measured using decreasing interrogation window sizes, from 128×128 pixels decreasing to the fine search of 32×32 pixels with 25% subset overlap.

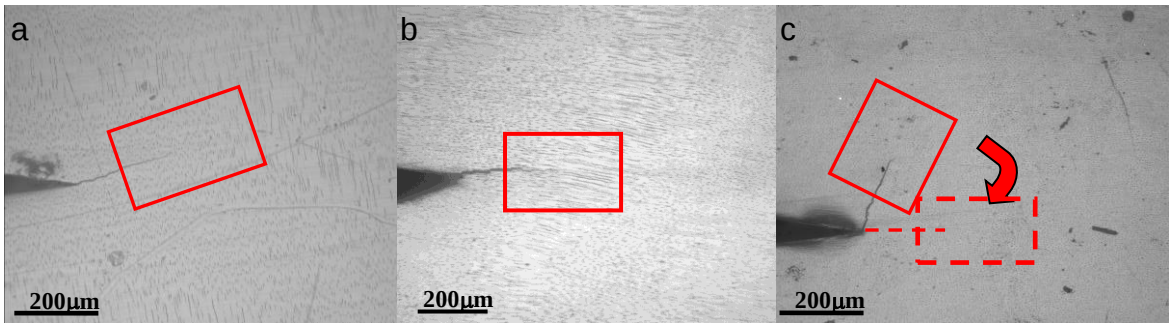

Fig. 5.3 Raw images taken during in-situ digital image correlation experiment. (a), (b) and (c) correspond to HAH, RAR and HRH. The red square zones around the crack-tip in three panels were used to extract the displacement fields information. HRH was rotated to align the crack path in horizontal

The displacements were tracked using LaVision Davis V7.2 Software over an array of 45×37 patches (0.495×0.407 mm^2) for HAH, 36×38 patches (0.381×0.403 mm^2) for RAR and 21×21 patches (0.233×0.233 mm^2) for HRH. ROI measurement can remarkably accelerate the calculation speed and the size of ROI box must be large enough so as to cover all the detectable crack-tip strain with the crack-tip at the centreline. Fig. 5.4 shows the displacement vectors extracted within the ROI, which is then utilized to obtain the strain field. The assessment of the instrument error (i.e. vibrations, exposure variation etc) was carried out by taking 2 reference images at an interval of 1 minutes, as a result of which, the average instrument error was estimated to be 0.046 pixels (maximum 0.12 pixels), corresponding to 0.018 μm in displacement and 1330 μs in strain measurement.

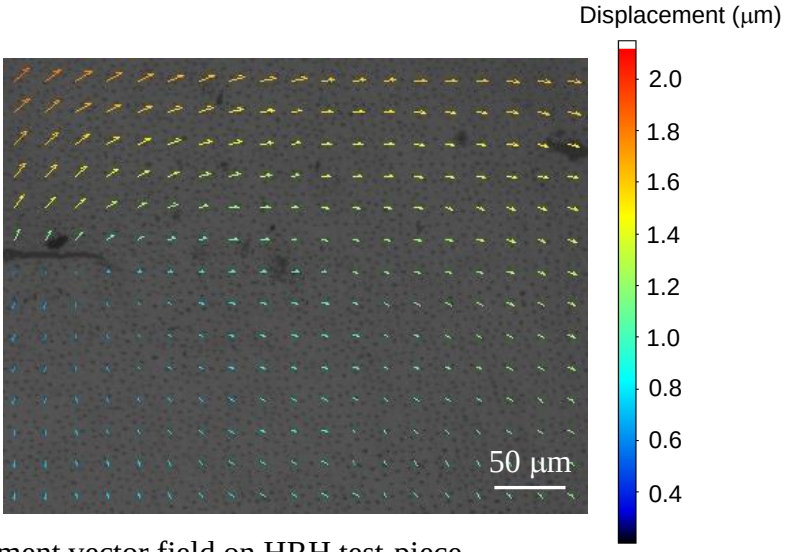

Fig. 5.4 Displacement vector field on HRH test-piece.

5.2.3 Stress intensity factor (SIF) extraction from crack-tip displacement field

Extracting the stress intensity factor from DIC displacement fields is a common procedure that relies on using least squares regression on the DIC crack tip displacement fields [41-44]. For mode I, mode II and mixed-mode cracks in plane stress problems, Westergaard's analytical solutions give the displacement fields around the crack-tip as [41-43, 45-47]:

$$u=\sum_{n=1}^{\infty}\frac{A_n}{2G}r^{n/2}[\chi+\frac{n}{2}+(-1)^n\cos\frac{n}{2}\theta-\frac{n}{2}\cos(\frac{n}{2}-2)\theta)]-\sum_{n=1}^{\infty}\frac{B_n}{2G}r^{n/2}[\chi+\frac{n}{2}-(-1)^n\sin\frac{n}{2}\theta-\frac{n}{2}\sin(\frac{n}{2}-2)\theta)]$$

$$v=\sum_{n=1}^{\infty}\frac{A_n}{2G}r^{n/2}[\chi-\frac{n}{2}-(-1)^n\sin\frac{n}{2}\theta+\frac{n}{2}\sin(\frac{n}{2}-2)\theta)]-\sum_{n=1}^{\infty}\frac{B_n}{2G}r^{n/2}[-\chi+\frac{n}{2}-(-1)^n\cos\frac{n}{2}\theta-\frac{n}{2}\cos(\frac{n}{2}-2)\theta)]$$

(5.1)

where u and v are displacement components parallel and perpendicular to the crack line respectively, G is shear modulus, χ equals (3- γ)/(1+ γ) for plane stress and (3-4 γ) for plane strain. γ is Poisson's ratio. The plane stress assumption was made for this case due to the surface strain observation. The coefficients of the first terms A_1 and B_1 represent the proportional relationship to stress intensity factors, SIFs, as $A_1=\frac{K_I}{\sqrt{2\pi}}$, $B_1=\frac{K_{II}}{\sqrt{2\pi}}$ since

Westergaard's solution is an asymptotic displacement field equation, and K field only dominates close to the crack-tip instead of the whole test-piece. Thus the parameters A_1 and B_1 can be attained by fitting the measured near tip displacement field to Westergaard's solution, which is also known as K regression [48, 49].

In cases where the crack path deflects from the maximum driving force plane (due to a preferred growth trajectory, for instance) local mixed-loading conditions occur at the crack-tip. The loading has contributions from tensile opening (K_I) and shear (K_{II}) modes. To deduce the stress at the crack-tip for a deflection at a constant angle from the maximum tensile stress plane, equations given in [19, 26, 50] are used:

$$k_1 = c_{11}(\alpha)K_{\mathrm{I}} + c_{12}(\alpha)K_{\mathrm{II}}$$

$$k_2 = c_{21}(\alpha)K_{\mathrm{I}} + c_{22}(\alpha)K_{\mathrm{II}} \tag{5.2}$$

where $c_{ij}(\alpha)$ are the mathematical expressions dependent on the deflection angle [50]. K_I and K_{II} are the global mode I and mode II stress intensities, and k_1, k_2 are the local stress intensity factors at the crack-tip. Fig. 5.5 demonstrates the relation between K_I, K_{II} and k_1, k_2.

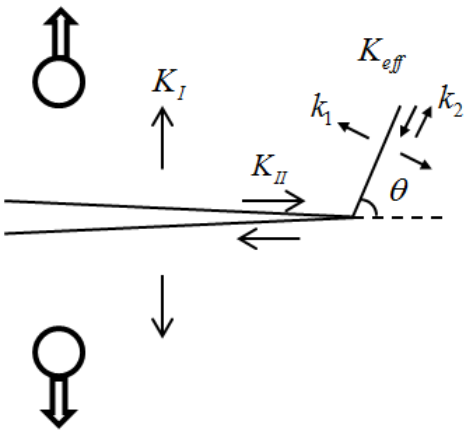

Fig. 5.5 Schematic diagram of global K_I and K_{II} and local k_1, k_2 at the crack-tip in the loaded compact tension test-piece

The equivalent effective stress intensity at the deflected crack-tip, K_{eff} can then be calculated by the mode I and mode II contributions,

$$K_{eff} = 0.5k_1 + 0.5\sqrt{k_1^{\,2} + 6k_2^2} \tag{5.3}$$

Because of the compact tension loading configuration, originally applied K_{II} = 0. According to ASTM standard [51], the expression of the applied mode I stress intensity factor for compact tension test-piece, i.e. C(T) test-piece, is as

$$K_{\mathrm{I}} = \frac{P}{B\sqrt{W}} \frac{(2+\alpha)}{(1-\alpha)^{3/2}} (0.886 + 4.64\alpha - 13.32\alpha^2 + 14.72\alpha^3 - 5.6\alpha^4) \tag{5.4}$$

where P is the applied load, B is the test-piece thickness, W is the test-piece width, α is the ratio of a/W and a is the crack length.

5.3 Results

5.3.1 Strain field around the crack-tip

Strain fields were extracted through the differentiation of the neighbouring displacement vectors. A trade-off between spatial resolution and precision of derived strain values needs to be considered when using discrete data. Improving one leads to degradation in the other. Thus the spatial resolution (i.e. gauge area) for the strain measurement is 11×11 μm^2, as a compromise to resolve strain discontinuities in the strain field. Due to the disparities of the fracture toughness, the maximum loads that can be applied on three types of the test-pieces are different.

Fig. 5.6 demonstrates the accumulative elastic strain around the crack-tip of HAH during in-situ loading process. The crack-tip strain level in vertical direction ε_{yy} (i.e. in radial direction) is fairly low. As the applied load is less than K_{app} = 0.62 $MPa\sqrt{m}$ little strain is observed local to the crack-tip. When the applied load reached K_{IC} = 0.74 $MPa\sqrt{m}$, the maximum strain at the vicinity of the crack-tip reaches 1.2 %. Compared with HAH, the strain field in surface of RAR increased considerably (Fig. 5.7) and the crack-tip strain at K_{IC} = 1.38 $MPa\sqrt{m}$ reaches 1.88 %. Inspection of the HRH reveals that at critical load i.e. K_{app} = 1.61 $MPa\sqrt{m}$, the maximum strain reaches 4.2 % at the crack-tip, forming an asymmetrical lobe-shape pattern. As load increases, the strain pattern significantly enlarges (Fig. 5.8). It is worth mentioning that relatively small strain was found at K_{app} = 0.69 $MPa\sqrt{m}$ (Fig. 5.7a) in RAR compared to those in HAH and HRH, which could be caused by crack-tip bridging. When the applied load rises, the strain level increases remarkably.

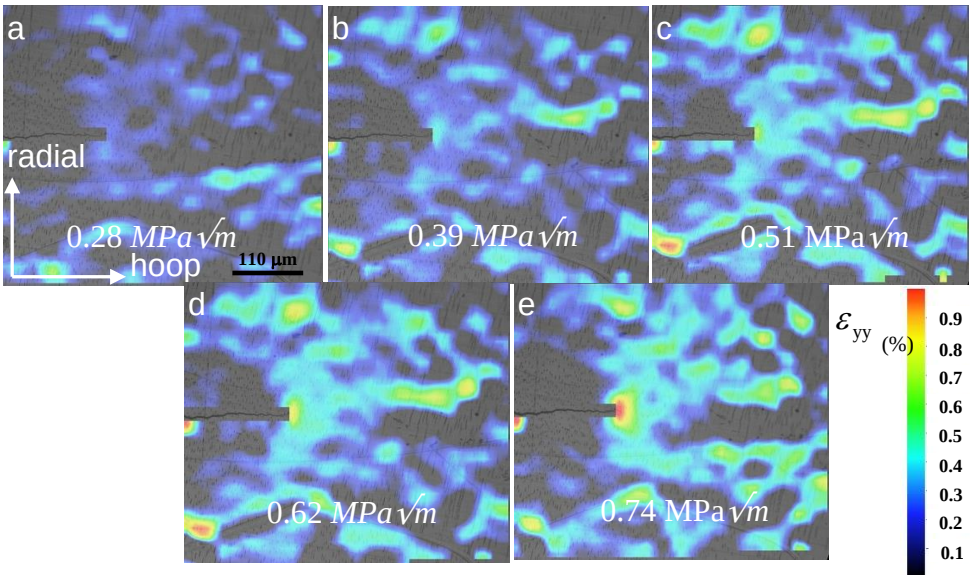

Fig. 5.6 Elastic strain fields in vertical direction (ε_{yy}) of HAH during in-situ loading process. K_{app} = (a) 0.28; (b) 0.39; (c) 0.51; (d) 0.62; (e) 0.74 *MPa√m*. The colour bar at right corner shows the strain level corresponding to the colour in the figure. The crack is in the radial-hoop plane and grows in hoop direction

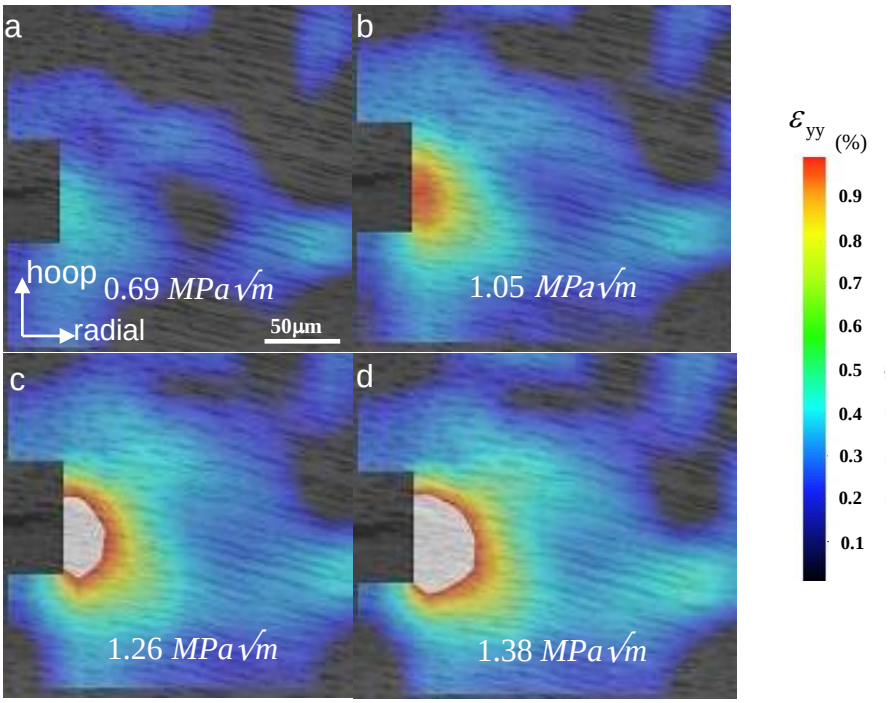

Fig. 5.7 Elastic strain field in vertical direction (ε_{yy}) of RAR at incremental loads of K_{app} = (a) 0.69; (b) 1.05; (c) 1.26 and (d) 1.38 *MPa√m*. The crack is in hoop-radial plane and grows in radial direction. The colour bar at right corner shows the strain level corresponding to the colour in the figure.

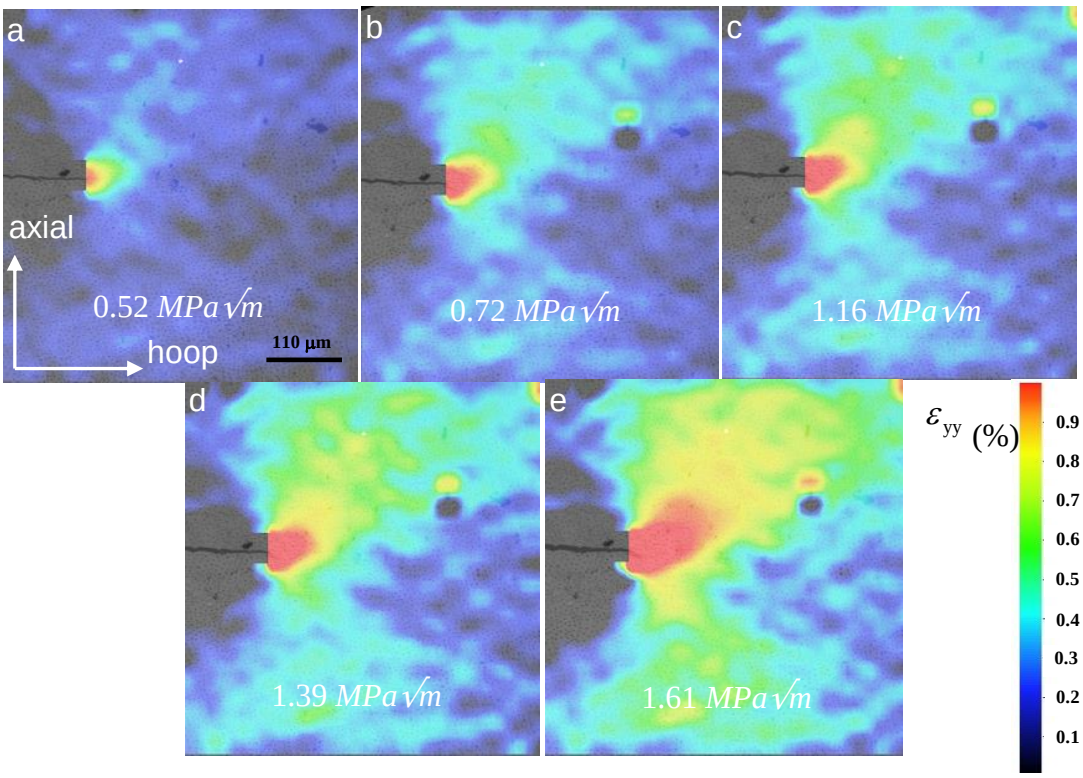

Fig. 5.8 Elastic strain fields in vertical direction (ε_{yy}) of HRH during in-situ loading process. K = (a) 0.09; (b) 0.37; (c) 0.51; (d) 0.75; (e) 1.42. The crack is in axial-hoop plane and grows in hoop direction. The colour bar at right corner shows the strain level corresponding to the colour in the figure.

The normalized strains (by load) *vs* distance from crack-tip on the crack plane is plotted for the three test-pieces under incremental loads (Fig. 5.9). It is found that the curves are very similarly at all loads for HAH and HRH (Fig. 5.9a and c), which indicates linear dependence of the strain on the applied load. However, there are distinct discrepancies of the strain curves in RAR (Fig. 5.9b), in which case the strains vary non-linearly with applied load. Moreover, the increase of the strain from K_{app} = 0.69 $MPa\sqrt{m}$ to K_{app} = 1.05 $MPa\sqrt{m}$ is more pronounced than those at higher loads. This may correspond to the stress reduction caused by bridging at the crack-tip.

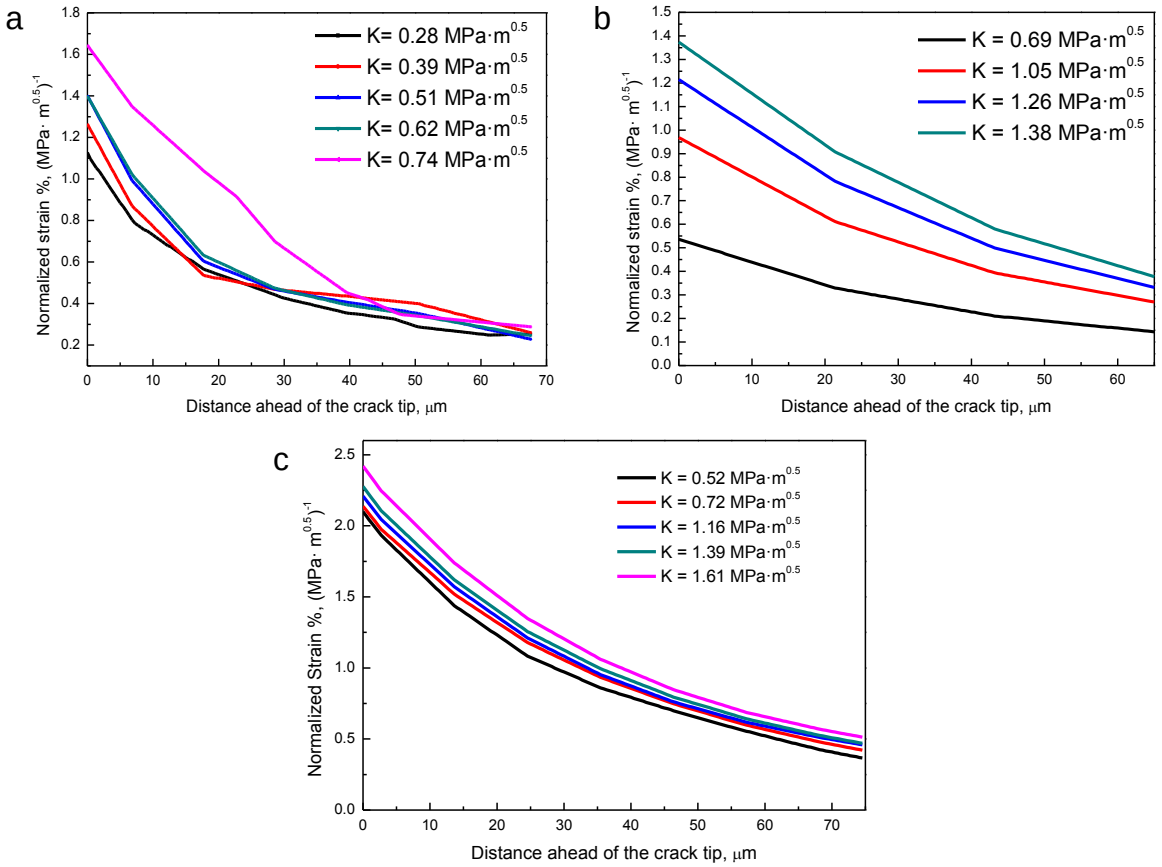

Fig. 5.9 Normalized crack – tip strain (i.e. strain divided by K_{app}) of (a) HAH (b) RAR and (c) HRH at incremental loads. The strains of three types of test-pieces at the same load are plotted in figure (d).

5.3.2 Stress intensity factor (K) extraction

It is shown in Fig. 5.3 that the crack paths in HAH and RAR are relatively straight, whereas there is large angle crack deflection for HRH. Therefore, only mode I (opening) fracture problems are investigated for HAH and RAR here, but mix-mode fracture is considered for HRH. Fig. 5.10 delineates the displacement contour maps for three types of test-pieces. Displacements in vertical direction *v* are plotted for HAH and RAR, whereas two kind of displacement *u* (horizontal) and *v* were utilized for HRH to extract stress intensity *K* by least square regression [41-43]. The displacement data within and close to the edge of the notch were masked out since the displacement information in this area exclusively comes from the crack wall rigid opening and is not representative of the crack-tip displacement fields, and would otherwise contribute to errors and a decrease in the fitting accuracy. It is noticed that the contour maps for HRH are more smooth than the other two, which may be attributable to the absolute strain in HRH being larger, giving a high signal to noise ratio. Another possible reason may be the surface pattern on HRH,

comprising pure tubule speckles, being ideal for displacement tracking, whereas those for RAR and HAH are a combination of periodical lines and speckles which are less robust for correlation. Subsequently, the experimental displacement contour map (Fig. 5.10) were fitted by Westergaard's analytical solution using a least squares regression method (Fig. 5.12).

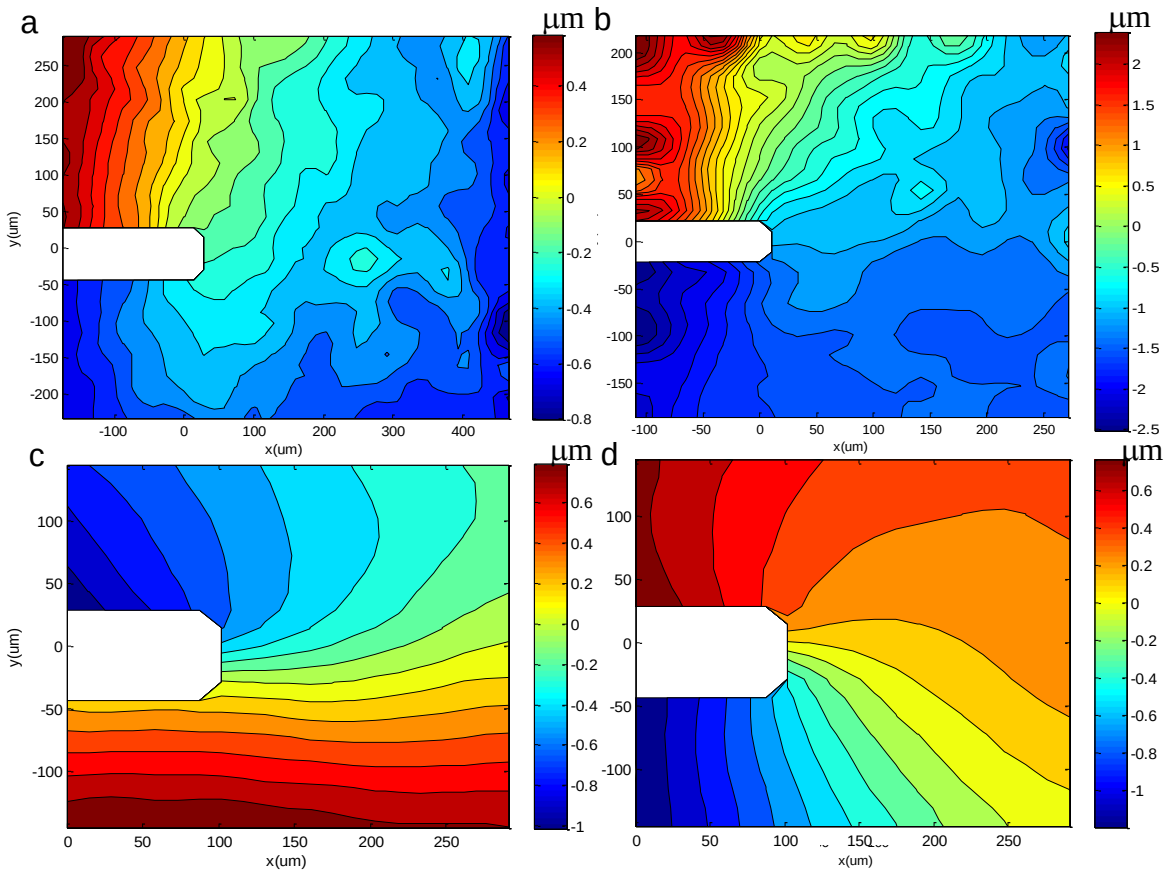

Fig. 5.10 Contour field of the displacements vertical to the crack of (a) HAH (K_{app} = 0.39 $MPa\sqrt{m}$) and (b) RAR (K_{app} = 1.05 $MPa\sqrt{m}$); Displacement field (c) parallel and (d) vertical to the crack for HRH at K_{app} = 0.52 $MPa\sqrt{m}$. The crack boundary areas are masked out as the displacements from these parts are from pure crack opening and will generate errors during fitting.

The fitting errors as a function of the used term (N) of the asymptotic solution (Eq. (5.1)) was assessed for HRH and RAR test-pieces at K_{app} = 0.52 $MPa\sqrt{m}$ and 0.48 $MPa\sqrt{m}$ respectively. It was found that the errors of HRH fitting is much lower than RAR. Fitting of HRH converges within 3 terms, however, for RAR, the fitting curve doesn't converges until N = 5 (Fig. 5.11). Moreover, in both cases, the fitted K_{eff}s increase from N = 1 and converge at a higher term. RAR demonstrates a more dramatic change compared to HRH. It is found that the higher N is, the better the fitting curve would match with the experiment

displacement data further away from the crack-tip, which increase the reliability of the K_{eff} extraction results [49]. Accordingly, term N = 9 in the asymptotic solution was used to make the system converge and minimize the error. The effects of rigid body translation and rotation of the test-pieces has been eliminated according to [43]. It can be seen from Fig. 5.12 that the fitting curves overlapped reasonably well with the experimental contours.

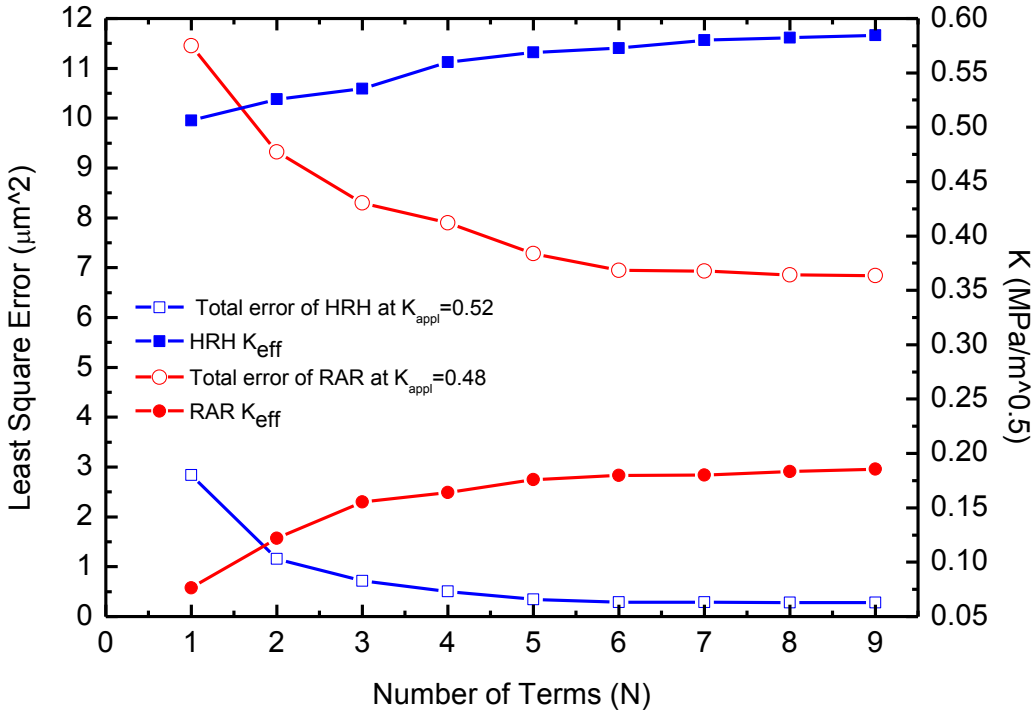

Fig. 5.11 Fitting accuracy and K_{eff} are closely related to the term used in the asymptotic solution for HRH test-piece.

The effective stress intensity factor K_{eff} was then extracted for the corresponding applied load (Fig. 5.13). K_{app} was calculated using Eq. (5.4) (in the case of HAH and RAR) and Eq. (5.2) - (5.3) for HRH. Fig. 5.13(a) presents a comparison of the effective k_1, k_2 and the K_{eff} with the applied k_1, k_2 and K_{app}. It is noticed that the measured K_{eff} is slightly larger than the K_{app}, which may mainly come from the discrepancies of effective and applied k_1: the measured curve stays above the applied one, but for k_2, the difference is negligible. Fig. 5.13b gives the comparison between effective k_2 / k_1 ratio and the applied one. It is found that the effective curve decreases from 0.52 at 10 N, to 0.44 at 40 N. The entire range of the experimentally measured ratio is 18% lower than the applied value. Based on the experimental curve, it is inferred that the mode I stress becomes increasingly dominant in the crack-tip stress field with the increasing load. Fig. 5.13c compares the K_{app} and the K_{eff}

of three types of test-piece. The applied and measured curves match reasonably well for HAH, but for RAR K_{eff} is much lower than the applied one. With respect to HRH, the measured K_{eff} is slightly higher than the applied curve. In addition, the increases of K_{eff} for HAH and HRH are linearly proportional to the applied load, and the gradient of HRH is slightly lower than HAH. Table 5.1 summarizes the key parameters obtained from the fitting results.

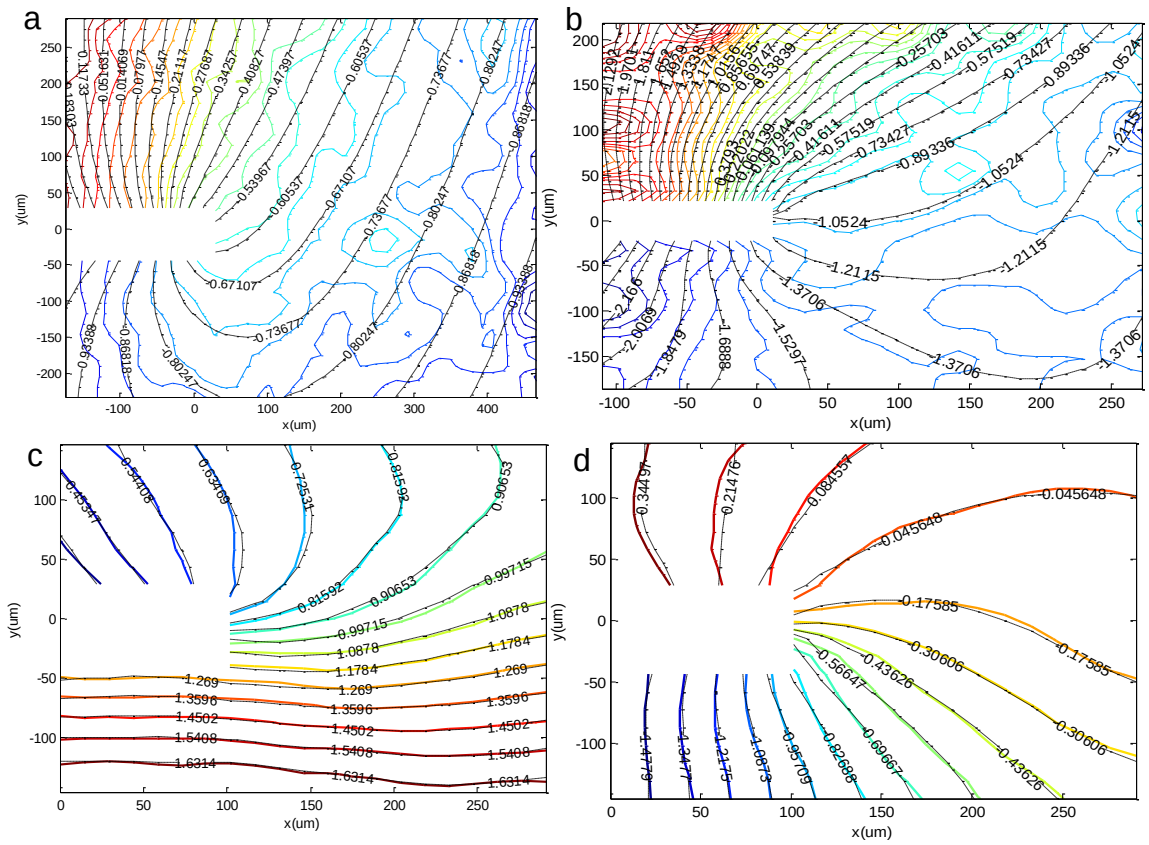

Fig. 5.12 The crack-tip displacement contour fitting using least square regression method for HAH in radial direction (K_{app} = 0.39 $MPa\sqrt{m}$); (b) RAR in hoop direction (K_{app} = 1.05 $MPa\sqrt{m}$) ; HRH in both (c) hoop and (d) axial direction (K_{app} = 0.52 $MPa\sqrt{m}$).

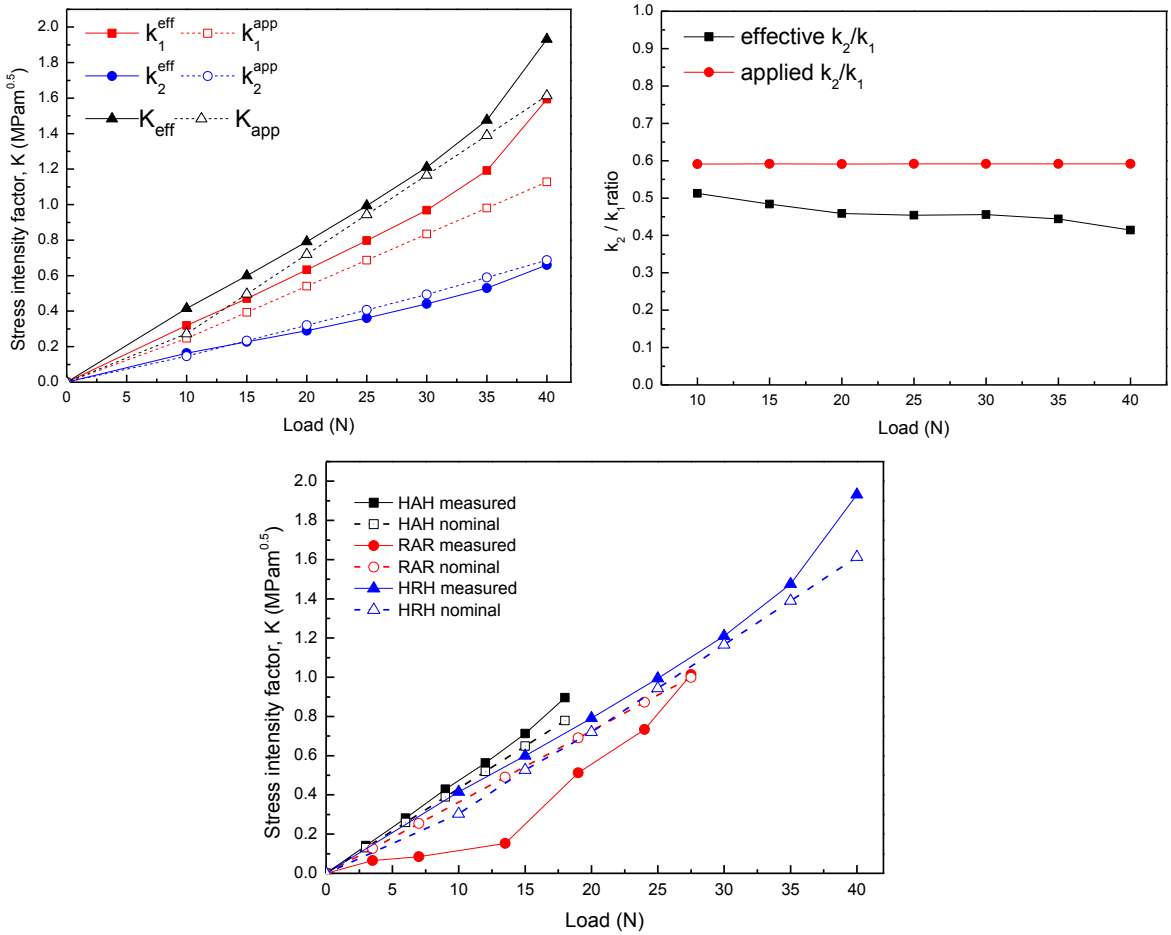

Fig. 5.13 (a) The applied and effective K_I and K_{II} , and the equivalent K_{app} and K_{eff} for HRH; (b) effective K_{II} / K_I with the applied K_{II} / K_I ratio; (c) comparisons of the K_{app} and K_{eff} for all the three types test-pieces.

Table 5.1 List of the key parameters by displacement fitting for three test-pieces

	Gradient	Maximum K_{eff} (MPa√m)	Average displacement fitting error ($\times 10^{-4}$ μm^2)
HAH	0.049	0.889	61
RAR	0.009 ~ 0.066	1.013	49
HRH	0.037	1.931	6.8

4. Discussion

The present study utilized digital image correlation technique to measure the elastic strain field around the crack-tip in elephant dentin test-pieces, which has not been previously reported. Accumulative crack-tip strain was measured under incremental in-situ loading. It was found that HAH (i.e. crack path in hoop-radial plane, grow in hoop direction) exhibit the lowest critical strain at the crack-tip before unstable crack growth; RAR test-piece (i.e. crack path in hoop-radial plane, grow in radial direction) demonstrates minimal strain at the crack-tip when the load is lower than a threshold value (K_{app} = 0.69 $MPa\sqrt{m}$), beyond which strain increases more quickly as a function of the load; HRH test-piece (i.e. crack path in hoop-axial plane, grow in hoop direction) shows the largest strain just before cracking, corresponding to the fracture toughness being the highest among the three test-pieces. This anisotropic strain at failure coincides well with previous reports of anisotropic fracture toughness [2, 21, 52].

The anisotropic cracking deformation in dentin may result from a combination of two factors. (1) The orientation of the collagen fibrils is one of the most important factors. Previous work have proven that collagen fibrils are closely related to the intrinsic (e.g. energy dissipation via uncramping and sliding of collagen molecules) and extrinsic crack-tip shielding mechanisms (e.g. collagen fibrils bridging) [53, 54]. HAH test-piece cannot benefit from any of the collagen induced shielding since the collagen fibrils are aligned parallel to the crack plane; however, RAR and HRH test-piece are toughened by the fibrils in the crack growth direction. (2) The difference of the fracture toughness between RAR and HRH test-pieces arises from the alignment of the dentinal tubules and the pre-existing micro-cracks that generally follow the long axis of the elliptical tubules based on our previous observation. Fig. 5.14a demonstrates the periodic tubules patterns in front of the crack-tip in RAR (see Fig. 5.3b). The orientations of the tubules are more realistic here compared with the one shown in Fig. 4.2, which is a simplification for general tubule orientation. The main crack grows by merging the micro-cracks in the crack plane, and consequently penetrates the tubules in the direction vertical and parallel to the tubule axis (Fig. 5.14b); in contrast, the resistance for the crack propagation in HRH is higher: there is no extended crack growth path forming by the tubules and micro-cracks on the fracture plane. The micro-cracks deviate the crack away from the maximum driving force plane, significantly reducing the mode I stress and generating a mix-mode driving force ($K_I + K_{II}$) for crack extension.

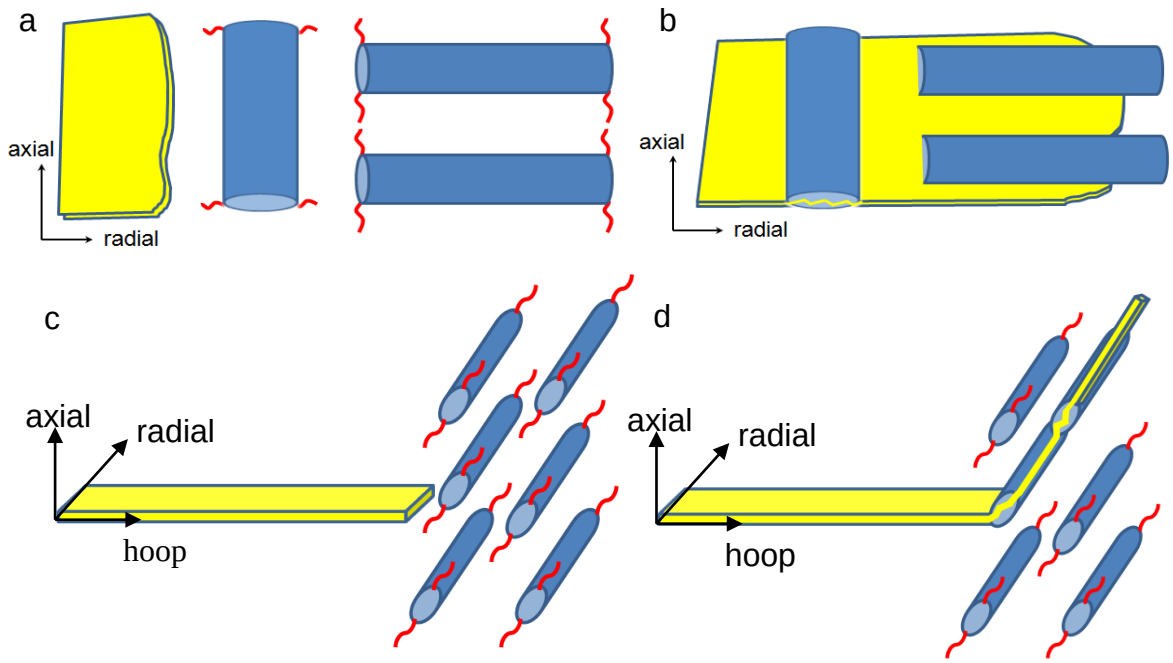

Fig. 5.14 Schematic figure illustrating the different crack growth mechanisms interacting with the microstructures (blue rods representing the tubules and the red curves are micro-cracks) in (a) – (b) RAR and (c) – (d) HRH.

Clear evidence of crack-tip shielding effects are found in RAR test-piece, specifically: (1) normalised strain as a function of the distance ahead of the crack-tip demonstrated that HAH and HRH test-pieces experience linear elastic deformation, whereas non-linear crack-tip strain is noticed in the RAR test-piece; (2) stress intensity extraction shows that the stress is linearly proportional to the applied load for HAH and HRH test-pieces, and slightly higher than the applied value, while RAR test-piece showed a bilinear relation between K_{eff} and applied load, with a turning point of 13 N, and the strain field is much lower than K_{app}.

The reason for a higher fitting error of RAR than HRH is because (1) the displacement contours of RAR (and also HAH) are less smooth than HRH, which could be caused by the surface texture contrast, as can be seen from Fig. 5.4 for HRH and Fig. 5.7 for RAR; (2) The displacement magnitude for HRH is much larger than RAR, which makes the signal to noise ratio higher for HRH. These can explain why K_{eff} for RAR increases more quickly than HRH in the first several terms. Theoretically, fitting with a low term equation mainly counts for the contribution close to the crack-tip and vice versa. Thus in the cases that the crack-tip behaviour is linear elastic, first one or two terms equation can generate converged results. The phenomenon seen from Fig. 5.11 that the K_{eff} increases with the first several

fitting term, especially for RAR, may result from the accuracy defining the crack-tip in the polar coordinate system, and some rigid body translation and rotation, which are challenging to eliminate completely, along with the factor of displacement magnitude.

Extrinsic crack-tip shielding was found in RAR in terms of a lower K_{eff} than the K_{app} at low opening load. This is also supported by the normalised strain at the crack-tip. There is little sign of extrinsic crack-tip shielding for HAH and HRH test-pieces since K_{eff} and K_{app} are very similar. Several well known kinds of toughening mechanisms are reported in dentin materials: crack blunting, uncracked-ligament bridging, collagen fibril bridging, crack branching and microcracking [2, 19, 26, 55, 56]. The sudden change of the slopes in K_{eff} for RAR could be caused by failure of the shielding mechanisms due to the continuously increasing crack opening displacement that exceeds the critical crack opening width beyond which collagen fibril bridging and uncracked-ligament bridging effects collapse [2, 56-59]. The disparities between K_{eff} and K_{app} for HRH mainly come from k_1 contributions (effective k_1 being larger that applied k_1, but effective k_2 being similar to applied k_2). Measured k_2/k_1 ratio proved an increasing mode I stress dominance at the deflected crack-tip with the incremental load. The lower experiment k_2/k_1 ratio than the nominal one could be expected due to the widely distributed micro-cracks along the crack growth direction, which makes the material less stiffer, although dentin is reported as orthotropic elasticity in the plane vertical to the tubule axis [19, 52, 60, 61].

5.4 Conclusions

In present work we managed to measure the crack-tip strain field for three different types of test-pieces using DIC technique, which is the first application on the characterisation of dentin deformation. The displacement field around the crack-tip was then used to extract the effective stress intensity factor to assess the crack bridging effect quantitatively. The results are concluded as follows:

1. Elephant dentin exhibits anisotropic fracture toughness in relation to the axis of the tubules measured by K_{eff} extraction. HRH test-piece (i.e. crack in hoop-radial plane, grow in hoop direction) exhibited the largest fracture toughness (1.93 $MPa\sqrt{m}$), which was 91 % tougher than RAR (i.e. crack in radial-axial plane, grow in radial direction) and 120 % tougher than HAH (i.e. crack in hoop-axial plane, grow in hoop direction).

2. The critical strain fields around the crack-tips for these three types of test-piece are different. The maximum strain at the crack-tip for HAH, RAR and HRH were 1.2 %, 1.88 % and 4.2% respectively. Normalised strains demonstrate linear elastic behaviours for HAH and HRH, but non-linear for RAR.

3. For RAR test-piece, the effective stress and strain increased slowly when the applied load is less than a threshold (~0.6 $MPa\sqrt{m}$), beyond which the shielding degrades rapidly. The maximum bridging stress was measured to be 0.36 $MPa\sqrt{m}$. It was necessary to keep N>8 terms in Westergaard's asymptotic solution to achieve stable extraction of K with minimum error.

4. The difference of the fracture toughness comes from the cracking plane relative to the collagen fibrils, which intrinsically shield the crack-tip by dissipating fracture energy in terms of collagen uncramping and sliding for RAR and HRH, but not for HAH. The micro-cracks in HRH test-piece deviate the crack away from the maximum driving force plane, which makes it tougher than RAR.

References

[1] Heuer AH, Fink DJ, Laraia VJ, Arias JL, Calvert PD, Kendall K, et al. Innovative Materials Processing Strategies - a Biomimetic Approach. Science 1992;255:1098-105.
[2] Kruzic J, Nalla RK, Kinney JH, Ritchie RO. Crack blunting, crack bridging and resistance-curve fracture mechanics in dentin: effect of hydration. Biomaterials 2003;24:5209-21.
[3] Nalla RK, Imbeni V, Kinney JH, Staninec M, Marshall SJ, Ritchie RO. In vitro fatigue behavior of human dentin with implications for life prediction. Journal of Biomedical Materials Research Part A 2003;66A:10-20.
[4] Moyes AB, Doidge DW. COMPOSITION OF THE MINERAL PHASE OF DENTIN IN SOUTHERN ELEPHANT SEAL AND ANTARCTIC FUR-SEAL TEETH. British Antarctic Survey Bulletin 1984:81-4.
[5] Povar ML. Miles,Aew - Structural and Chemical Organization of Teeth. J Am Vet Med Assoc 1967;151:1211-&.
[6] Miles AEW, Boyde A. Observations on Structure of Elephant Ivory. J Anat 1961;95:450-&.
[7] Locke M. Structure of ivory. J Morphol 2008;269:423-50.
[8] Raubenheimer EJ, Dauth J, Dreyer MJ, Smith PD, Turner ML. Structure and Composition of Ivory of the African Elephant (Loxodonta-Africana). S Afr J Sci 1990;86:192-3.
[9] Marshall GW, Inai N, Magidi ICW, Ballouch M, Kinney JH, Tagami J, et al. Dentin demineralisation: effects of dentin depth, pH and different acids (vol 13, pg 338, 1997). Dental Materials 1998;14:383-.
[10] Su XW, Cui FZ. Hierarchical structure of ivory: from nanometer to centimeter. Mat Sci Eng C-Bio S 1999;7:19-29.
[11] Kinney JH, Balooch M, Marshall GM, Marshall SJ. A micromechanics model of the elastic properties of human dentine. Archives of Oral Biology 1999;44:813-22.
[12] Deymier-Black A, Almer J, Stock S, Haeffner D, Dunand D. Synchrotron X-ray diffraction study of load partitioning during elastic deformation of bovine dentin. Acta biomaterialia 2010;6:2172-80.
[13] Gallegos R. Maintain Dentin Bond Strength Over Time. Daily Digest http://wwwspeareducationcom/spear-review/tag/dentin/page/3/ 08. 03. 2015.
[14] Arola D, Rouland JA, Zhang D. Fatigue and fracture of bovine dentin. Experimental Mechanics 2002;42:380-8.
[15] Ivancik J, Neerchal NK, Romberg E, Arola D. The Reduction in Fatigue Crack Growth Resistance of Dentin with Depth. Journal of Dental Research 2011;90:1031-6.
[16] Iwamoto N, Ruse ND. Fracture toughness of human dentin. Journal of Biomedical Materials Research Part A 2003;66A:507-12.
[17] Bonfield W, Li CH. Deformation and Fracture of Ivory. J Appl Phys 1965;36:3181-&.
[18] Koester KJ, Barth HD, Ritchie RO. Effect of aging on the transverse toughness of human cortical bone: Evaluation by R-curves. Journal of the Mechanical Behavior of Biomedical Materials 2011;4:1504-13.
[19] Nalla RK, Kinney JH, Ritchie RO. Effect of orientation on the in vitro fracture toughness of dentin: the role of toughening mechanisms. Biomaterials 2003;24:3955-68.
[20] Watanabe LG, Marshall GW, Marshall SJ. Dentin shear strength: Effects of tubule orientation and intratooth location. Dent Mater 1996;12:109-15.
[21] Arola DD, Reprogel RK. Tubule orientation and the fatigue strength of human dentin. Biomaterials 2006;27:2131-40.
[22] Bajaj D, Sundaram N, Nazari A, Arola D. Age, dehydration and fatigue crack growth in dentin. Biomaterials 2006;27:2507-17.

[23] Kruzic JJ, Nalla RK, Kinney JH, Ritchie RO. Crack blunting, crack bridging and resistance-curve fracture mechanics in dentin: effect of hydration. Biomaterials 2003;24:5209-21.
[24] Ivancik J, Arola DD. The importance of microstructural variations on the fracture toughness of human dentin. Biomaterials 2013;34:864-74.
[25] Arola D, Reprogel RK. Effects of aging on the mechanical behavior of human dentin. Biomaterials 2005;26:4051-61.
[26] Koester KJ, Ager Iii JW, Ritchie RO. The effect of aging on crack-growth resistance and toughening mechanisms in human dentin. Biomaterials 2008;29:1318-28.
[27] Marciniak T, Lutowski Z, Bujnowski S, Boronski D, Giesko T. Application of Digital image Correlation in Fatigue Crack Analysis. In: Skibicki D, editor. Fatigue Failure and Fracture Mechanics2012. p. 218-21.
[28] Mathieu F, Hild F, Roux S. Identification of a crack propagation law by digital image correlation. International Journal of Fatigue 2012;36:146-54.
[29] Mauroux T, Benboudjema F, Turcry P, Ait-Mokhtar A, Deves O. Study of cracking due to drying in coating mortars by digital image correlation. Cement and Concrete Research 2012;42:1014-23.
[30] Nowell D, Kartal ME, De Matos PFP. Digital image correlation measurement of near-tip fatigue crack displacement fields: constant amplitude loading and load history effects. Fatigue & Fracture of Engineering Materials & Structures 2013;36:3-13.
[31] Sztefek P, Vanleene M, Olsson R, Collinson R, Pitsillides AA, Shefelbine S. Using digital image correlation to determine bone surface strains during loading and after adaptation of the mouse tibia. Journal of biomechanics 2010;43:599-605.
[32] Thompson MS, Schell H, Lienau J, Duda GN. Digital image correlation: A technique for determining local mechanical conditions within early bone callus. Medical Engineering & Physics 2007;29:820-3.
[33] Vaananen SP, Amin Yavari S, Weinans H, Zadpoor AA, Jurvelin JS, Isaksson H. Repeatability of digital image correlation for measurement of surface strains in composite long bones. Journal of biomechanics 2013;46:1928-32.
[34] Eftis J, Subramonian N, Liebowitz H. Crack border stress and displacement equations revisited. Engineering Fracture Mechanics 1977;9:189-210.
[35] Evans W, Luxmoore A. Limitations of the Westergaard equations for experimental evaluations of stress intensity factors. The Journal of Strain Analysis for Engineering Design 1976;11:177-85.
[36] Zhang R, He LF, Li CR. The Stress Intensity Factor of Opening Mode Determined by Digital Image Correlation. Applied Mechanics and Materials: Trans Tech Publ; 2011. p. 54-9.
[37] Zhang R, He L. Measurement of mixed-mode stress intensity factors using digital image correlation method. Optics and Lasers in Engineering 2012;50:1001-7.
[38] E1820-08a A. Standard Test Method for Measurement of Fracture Toughness. American Society for Testing and Materials (ASTM) International, West Conshohocken, PA, USA 2008.
[39] Quinta da Fonseca J, Mummery PM, Withers PJ. Full - field strain mapping by optical correlation of micrographs acquired during deformation. Journal of microscopy 2005;218:9-21.
[40] Sutton MA, Orteu JJ, Schreier H. Image correlation for shape, motion and deformation measurements: basic concepts, theory and applications: Springer Science & Business Media; 2009.
[41] He L. The Stress Intensity Factor of Opening Mode Determined by Digital Image Correlation. Applied Mechanics and Materials 2011;83:54-9.

[42] A H. A Methodology for Evaluating Mixed-mode (I + II) SIF, Combining Experimental Data Acquired by ESPI with Westergaard Type Solution. Proceedings of the World Congress on Engineering 2010;2.
[43] Zhang R. Measurement of mixed-mode stress intensity factors using digital image correlation method. Optics and Lasers in Engineering 2012;50:7.
[44] Lopez-Crespo P, Withers PJ. Fatigue crack monitoring using image correlation. Key Engineering Materials 2008;385-387:341-4.
[45] D B. Elementary Engineering Fracture Mechanics. Martinus Nijhoff Publishers 1984.
[46] Yoneyama S, Morimoto Y, Takashi M. Automatic evaluation of mixed-mode stress intensity factors utilizing digital image correlation. Strain 2006;42:21-9.
[47] GR I. Analysis of stresses and strains near the end of a crack traveling a plate. Journal of Applied Mechanics 1957;24:361-4.
[48] Sangid MD, Pataky GJ, Sehitoglu H, Rateick RG, Niendorf T, Maier HJ. Superior fatigue crack growth resistance, irreversibility, and fatigue crack growth–microstructure relationship of nanocrystalline alloys. Acta Materialia 2011;59:7340-55.
[49] Jay C. RELATING FATIGUE CRACK GROWTH TO MICROSTRUCTURE VIA MULTISCALE DIGITAL IMAGE CORRELATION. PhD Dissertion, Mechanical Engineering in the Graduate College of the University of Illinois at Urbana-Champaign 2011.
[50] Cotterell B, Rice JR. SLIGHTLY CURVED OR KINKED CRACKS. International Journal of Fracture 1980;16:155-69.
[51] ASTM. Standard Test Method for Measurement of Fracture Toughness. American Society for Testing Materials, West Conshohocken 2002;E1820-01.
[52] Craig RG, Peyton FA. Elastic and mechanical properties of human dentin. Journal of dental research 1958;37:710-8.
[53] Lees S. Considerations regarding the structure of the mammalian mineralized osteoid from viewpoint of the generalized packing model. Connective tissue research 1987;16:281-303.
[54] Thompson JB, Kindt JH, Drake B, Hansma HG, Morse DE, Hansma PK. Bone indentation recovery time correlates with bond reforming time. Nature 2001;414:773-6.
[55] Arola DD, Rouland JA. The effects of tubule orientation on fatigue crack growth in dentin. Journal of Biomedical Materials Research Part A 2003;67A:78-86.
[56] Fett T, Munz D, Geraghty RD, White KW. Bridging stress determination by evaluation of the R-curve. Journal of the European Ceramic Society 2000;20:2143-8.
[57] Ritchie RO. Mechanisms of fatigue-crack propagation in ductile and brittle solids. International Journal of Fracture 1999;100:55-83.
[58] Kanninen M. Advanced Fracture Mechanics. Oxford University Press 1985.
[59] Ritchie RO. Mechanisms of Fatigue Crack-Propagation in Metals, Ceramics and Composites - Role of Crack Tip Shielding. Mat Sci Eng a-Struct 1988;103:15-28.
[60] Cui FZ, Wen HB, Zhang HB, Li HD, Liu DC. Anisotropic Indentation Morphology and Hardness of Natural Ivory. Mat Sci Eng C-Biomim 1994;2:87-91.
[61] Renson CE, Braden M. EXPERIMENTAL DETERMINATION OF RIGIDITY MODULUS, POISSONS RATIO AND ELASTIC LIMIT IN SHEAR OF HUMAN DENTIN. Archives of Oral Biology 1975;20:43-&.

Paper 3: Hydration Effect on Crack-tip Strain, Plasticity Crack Opening Displacement and Shielding Mechanisms in Elephant Dentin

Contributions:

X. Lu: Principal investigator to conduct the experiment, data analysis and interpretation, write up the paper

Prof. P.J. Withers: Language corrections, comments on the results interpretation and discussion

Chapter 6

Hydration Effect on Crack-tip Strain, Plasticity Crack Opening Displacement and Shielding Mechanisms in Elephant Dentin

X. Lu[a], P. J. Withers[a*]

[a]*School of Materials, University of Manchester, Grosvenor Street, Manchester M13 9PL, UK*

Abstract

Although the effect of hydration on the anisotropic fracture toughness has been widely studied, most of the work focused on the comparison of the fracture toughness KIC and R-curve behaviour, there is pool understanding of the hydration effect, which plays an important role in intrinsic shielding, on crack-tip plasticity, strain and crack opening. This study assesses the crack-tip plasticity for hydrated and dehydrated elephant dentin, with the crack growth perpendicular (HAH) and parallel (RAR) to the tubules using digital image correlation (DIC) to measure the crack-tip strain fields. Crack opening displacement (COD), bridging distance and resistance-curves are also compared for both dehydrated and hydrated test-pieces. Results showed that the hydrated RAR test-piece demonstrated

[*] Corresponding author, School of Materials, University of Manchester, Grosvenor Street, Manchester M13 9PL, UK

Email address: p.j.withers@manchester.ac.uk, +44 (0)161 306 4282

substantial crack-tip plasticity, higher crack-tip strain than HAH test-pieces. The plastic zone measured by experiment agreed well with Dugdale's K-field prediction. Theoretical elastic strain coincided well with the experimentally measured one with the presence of stress redistribution due to crack-tip plasticity. Crack-tip stress were reduced by 52 % and 40 % for hydrated and dehydrated RAR test-pieces due to extrinsic shielding. The bridging distance were 180 and 120 μm for the hydrated and dehydrated RAR test-pieces. Collagen-based intrinsic shielding mechanisms contribute most to the crack tip plasticity and the initial linear part on the R-curve, while the extrinsic shielding mechanisms mainly affect the R-curve behaviour. RAR test-pieces demonstrate longer bridging lengths than HAH test-pieces.

Key words: elephant tusk (ivory), crack-tip plasticity, compact tension, yielding zone, dentin materials, crack-tip toughening, bridging length, hydration, stress redistribution, residual strain

6.1 Introduction

This paper aims to characterise and compare the extent of crack-tip plasticity of dentin under hydrated and dehydrated conditions. This work is important in terms of developing a framework for failure prediction, not only for clinical understanding, but also in developing biomimetic restorative materials that are able to mimic the tissue's mechanical response [1]. Here we focus on elephant tusk (ivory) which is often used as a structural analogue for human teeth due to the similarities in microstructure and composition between the two materials. It has the advantage that tusks are very much larger than human teeth making the test-piece preparation and mechanical testing easier than for human teeth [2]. Ivory tusk is made up of a peripheral component, the cementum, continuous with, but structurally different from, enamel and a main core comprising dentin (see Fig. 6.1a). The cementum layer is softer than the dentin inside [3]. The dentinal tubules, are the predominant feature in the main dentin, running from the central pulp to the periphery of the dentin. These tubules are embedded in a mineralized collagen matrix, which consists of Type I collagen fibrils and Mg-containing hydroxyapatite [3-8]: the highly mineralized hydroxyapatite (HAP) improves the stiffness, while collagen provides toughness [9]. The parallel tubules comprise radial microlaminae. The dentin mainly consists of microlaminae arranged side by side from the pulp cavity to the cementum layer. Around these tubules, collagen fibrils are distributed radially in planes perpendicular to the long axis of the

tubules [10]. They form a mesh and cross-link around the tubules to provide its desirable mechanical properties [8, 11].

In recent years, much work has been done on the fracture mechanics of human, bovine and elephant dentin [12-15]. The length-scales over which cracks can propagate are much smaller in human dentin because of the limited test-piece size which makes it tricky to control the stable crack growth. This is disadvantageous for work looking at fracture resistance (R-curve) studies of the activation of extrinsic toughening mechanisms, similar to those operating in cortical bone [16].

Crack growth is highly anisotropic in relation to the orientation of the tubules. For most kinds of dentin (e.g. human, bovine and ivory dentin), the fracture toughness K_c is 55–65% higher for cracks propagating parallel to the long axis of the dentinal tubules compared to crack propagation perpendicular to the tubules [2, 14, 17, 18]. The fatigue life in human dentin is two orders of magnitude longer for cracks growing parallel to the tubules as opposed to perpendicular to them [4, 19]. Unsurprisingly, fracture toughness has also been found to be affected by hydration level [20] and age [21, 22]. Several toughening mechanisms in dentin, particularly for the case where a crack propagates parallel to the tubules, have been proposed such as crack blunting [2, 22], crack-tip bridging [2, 17, 22, 23], and microcracking [17, 23]..

The resistance-curve (R-curve) is a means of evaluating the build-up of crack retarding effects during subcritical crack propagation (i.e. before unstable fracture occurs). Rising R curve behaviour is particularly important in biomaterials, e.g. teeth, bones and tendons [16, 24-28]. Normally an R-curve is expressed in terms of the crack-driving force (the stress intensity K) as a function of the crack extension, Δa, to quantify the increasing fracture resistance with crack length. Previous investigations have revealed that dentin exhibits much higher fracture toughness and crack growth resistance (expressed via an R-curve) when hydrated rather than dehydrated along with enhanced crack-tip blunting [21, 29, 30]. Hydration decreases the elastic Young's modulus and hardness by approximately 35% and 30% compared with the dehydrated dentin [31-34]. The hydrated tissues exhibited viscoelasticity, demonstrating a good ability to recover the elastic energy stored in the region surrounding the deformed area [35].

There are a number of ways to measure crack tip strain. Some of the techniques have disadvantages, such as the need for photoelastic coatings and issues with high strain rates to ensure adiabatic conditions for thermoelasticity. Digital Image Correlation (DIC) is an

increasingly widely adopted technique used for full field surface strain measurement around cracks [36, 37] requiring no, or very little, preparation and can be applied to awkward biological materials include strain measurements on mouse tibia [38] and bones [39, 40].

Despite the large number of investigations comparing fracture toughness in dentin under wet and dry conditions, the elastic and plastic crack-tip strain fields have received little attention. Here, elastic and plastic crack-tip strains accumulated under incremental loads are measured using the digital image correlation (DIC) technique. The plastic zone size is determined for test-pieces cracked in different orientations under both wet and dry condition. The obtained plastic strain sizes are then compared with predictions made using the measured elastic stress fields with different crack-tip yielding criteria. Finally, the measured plastic zone size is used for the crack length correction to plot the R-curve.

6.2 Materials and experimental methods

6.2.1 Test-piece preparation

A cross-sectional slice from a tusk of African elephant ivory was used in this study. Fig. 6.1 presents the hierarchical microstructure of the elephant dentin obtained with different techniques. It clearly illustrates the orientation of the dentinal tubules in the elephant tusk and the relative alignment of the collagen fibrils to the tubules. Compact tension geometry test-pieces (10×8×2 mm) conforming to plane strain conditions were prepared based on ASTM E1820 [41]. The test-pieces were extracted from the interior of the elephant ivory sample as shown in (Fig. 6.1a). In order to investigate the anisotropic properties, two types of compact tension test-pieces were excised: (1) HAH, in which crack plane is in hoop-axial plane and grow in hoop direction (Fig. 6.1g), (2) RAR, in which crack plane is in radial-axial plane and grow in radial direction (Fig. 6.1h). The 3D alignment of the dentin tubules was observed using a Xradia Versa XRM-500 laboratory X-ray microscope (Fig. 6.1d). These tubules were segmented from the matrix using high resolution Xradia Ultra-810 laboratory X-ray microscope (Fig. 6.1f). Hierarchical SEM images (Fig. 6.1b and e) shows the dentinal tubules and the arrangement of the fine collagen fibrils inside of the tubule walls. Collagen fibrils form a woven scaffold structure around the tubules [42] (Fig. 6.1c).

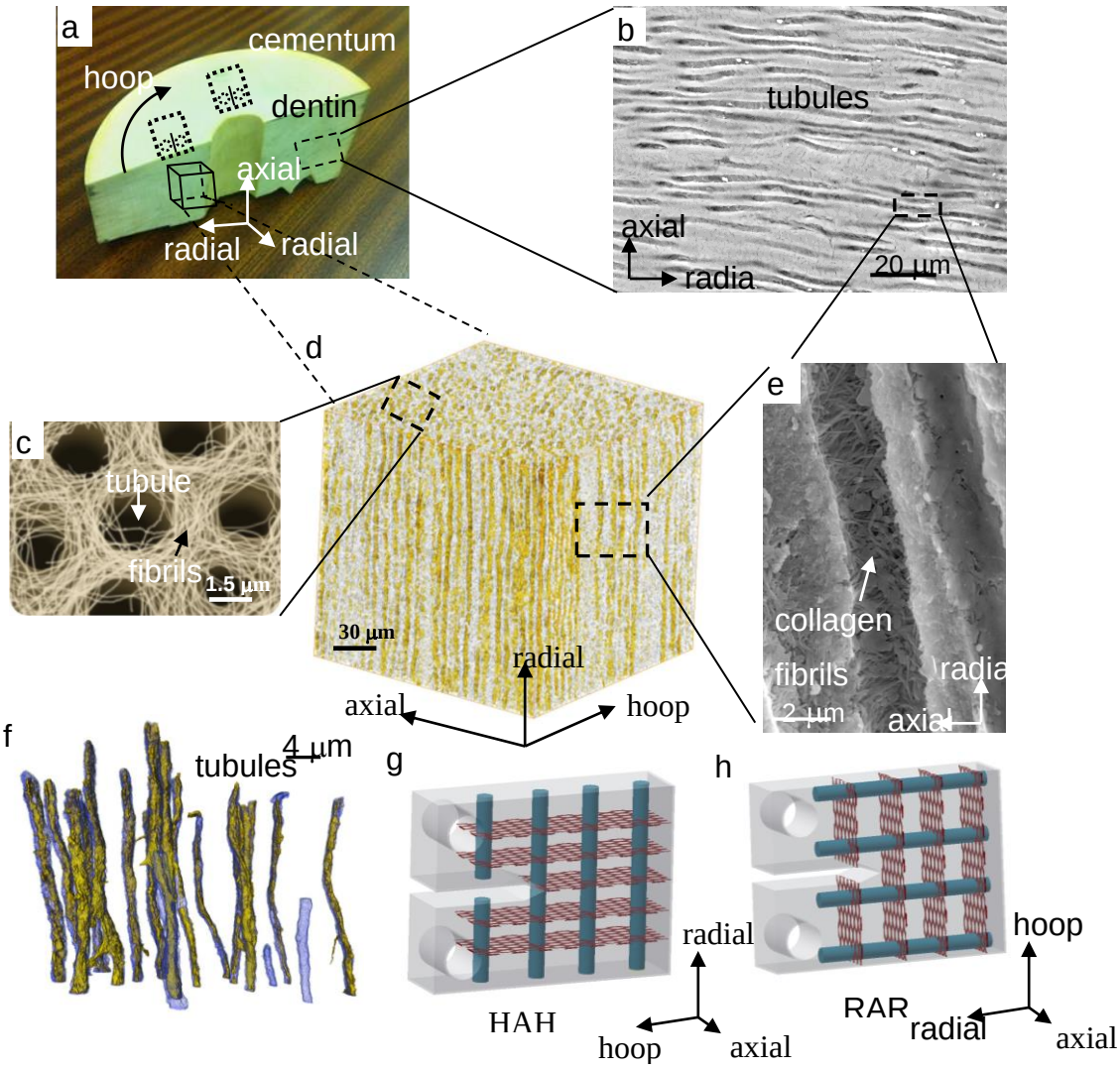

Fig. 6.1 The hierarchical structure of elephant dentin microstructure. (a) photograph of the elephant tusk slice showing the locations of HAH and RAR test-pieces; (b) SEM image showing radial alignment of the tubules; (c) Etched dentin showing collagen fibrils woven around the tubules [42], magnified from (d) x-ray CT representing tubules alignment in the 1 mm cube test-piece in (a); (e) SEM micrograph showing the relative position between the tubules and the collagen fibrils; (f) extracted dentinal tubules in 3D from X-ray CT data; (g)-(h) schematic figure showing the alignment of the tubules and the collagen plane in HAH and RAR test-piece respectively.

Before cutting, the test-pieces were stored in distilled water at 4 ℃ for more than two weeks to keep them hydrated. When preparing the test-pieces a 1cm thick plate was sliced from the top of the ivory sample. Subsequently, the plate were cut into rectangular bars and then into compact tension test-pieces using a 0.3mm thick rotary cutting wheel with water coolant.

6.2.2 Strain measurement by digital image correlation

Digital image correlation (DIC) is a well-established technique used to trace the movement of surface features during the application of loads by continuously taking pictures using a microscope with a camera attached [43, 44]. Only HAH (Fig. 6.2a) and RAR (Fig. 6.2b) were investigated here since the collagen arrangement can effectively reflect the relationship of collagen orientation and deformation capability. The displacements were tracked using LaVision Davis V7.2 Software over an array of 23×26 patches (0.318×0.363 mm^2) for HAH, 25×30 patches (0.363×0.436 mm^2) for RAR (see Fig. 6.2c). Each patch contained 32×32 pixels with 25% overlap with neighbouring patches.

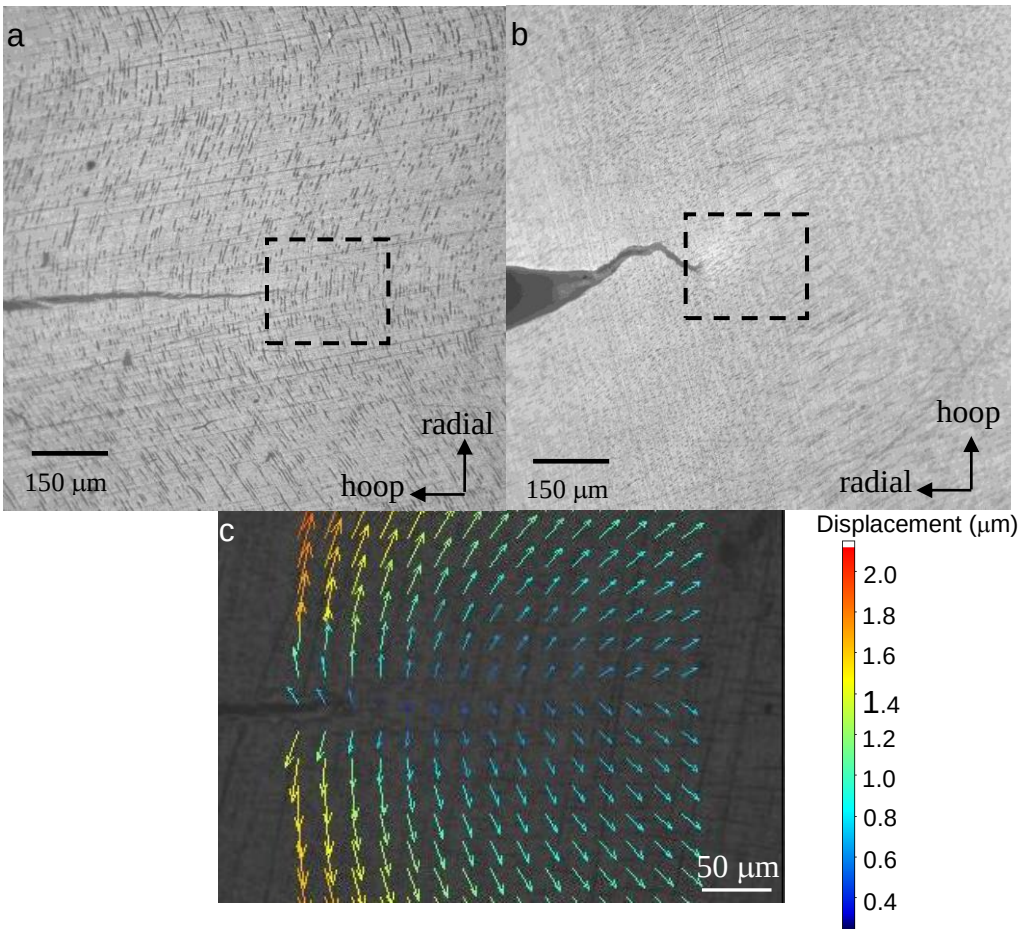

Fig. 6.2 Optical micrographs taken during in-situ digital image correlation experiment for (a) HAH and (b) RAR test-pieces. The dashed square rectangles indicate the region of interest (ROI); (c) displacement vector field on RAR test-piece. The vectors are exaggerated by 20x for vision.

The pre-cracked test-pieces were subject to incremental loading and unloading steps till reaching the critical load using a 500N load cell. The strain field was measured at the peak load and zero load. It is informative to compare the strains at the peak load and zero load for both hydrated and dry test-pieces, in different cracking directions.

The assessment of the error in the DIC measurements was estimated by taking 2 reference images at an interval of 1 minute. In this way it was found that 85% of the displacement vector errors are less than 0.03 μm, and the average instrument error is 0.02 μm, corresponding to 0.18% error in strain measurement. To determine the COD the raw images recorded in the DIC test were imported into ImageJ v1.46. The crack was identified by thresholding selection according to the grey value histogram, converted to a binary image and the crack opening displacement along the crack wake calculated using Matlab 2012a.

6.2.3 Resistance-curve measurement

The pre-cracked C(T) HAH and RAR test-pieces were used to measure the R-curve for the hydrated and dehydrated conditions. A travelling microscope with a 10x objective lens was used to capture the crack extension using a digital camera. According to the ASTM standard [45], the expression for the nominal mode-I stress intensity factor for a compact tension test-piece is given by:

$$K_{\mathrm{I}} = \frac{P}{B\sqrt{W}} \frac{(2+\alpha)}{(1-\alpha)^{3/2}} (0.886 + 4.64\alpha - 13.32\alpha^2 + 14.72\alpha^3 - 5.6\alpha^4) \tag{6.1}$$

where P is the applied load, B is the test-piece thickness, W is the test-piece width, α is the ratio which equals to a/W, a is the effective crack length. A drawback of the experimental set-up is that the hydrated test-piece could not be submerged in the HBSS solution because this hinders the optical strain measurement. Accordingly some low level of drying out may have occurred near-surface during the tests (~7 mins duration).

6.3 Results

6.3.1 Crack-tip strain measurement

RAR Test-piece: crack growth parallel to the tubules

The total crack-tip strain field in the *y* direction ε_{yy}^{tot} (i.e. perpendicular to the crack plane) was measured during the incremental loading and unloading for the RAR test-piece in the hydrated condition (Fig. 6.3). It is evident that upon unloading from K_{appl} = 0.65 $MPa\sqrt{m}$ and 0.83 $MPa\sqrt{m}$ significant residual strains ε_{yy}^{res} had been generated. These residual strains include both plastic strain ε_{yy}^{pl}, resulting from crack-tip plasticity, and elastic strains ε_{yy}^{el} arising from lattice misfits [46]. Unsurprisingly, both ε_{yy}^{tot} (Fig. 6.3b) and ε_{yy}^{res} (Fig. 6.3d) increased significantly with increased loading.

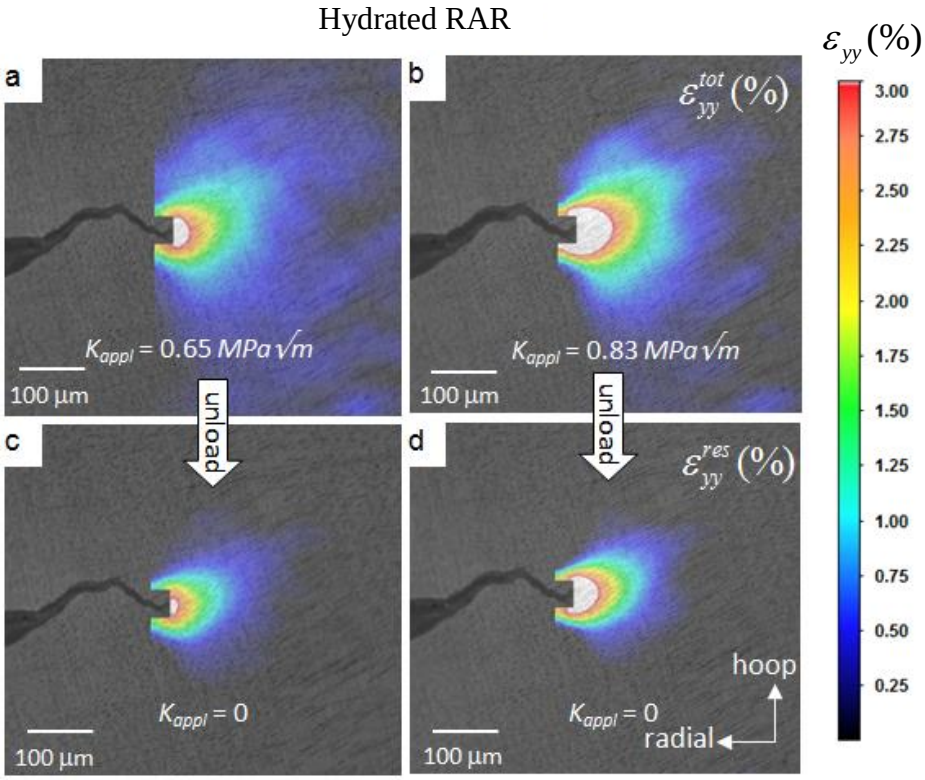

Fig. 6.3 Total crack-tip strain measured by DIC for a RAR test-piece in the hydrated condition. (a) K_{appl} = 0.65 $MPa\sqrt{m}$ (b) K_{appl} = 0.83 $MPa\sqrt{m}$ with loaded (top) and unloaded (bottom).

By contrast no significant ε_{yy}^{pl} was generated at K_{appl} = 0.65 $MPa\sqrt{m}$ in the dehydrated condition as indicated by the very low level ε_{yy}^{res} upon unloading. Even for loads much larger than for the hydrated case (K_{appl} = 1.17 $MPa\sqrt{m}$), much lower ε_{yy}^{res} were evident upon unloading (Fig. 6.4).

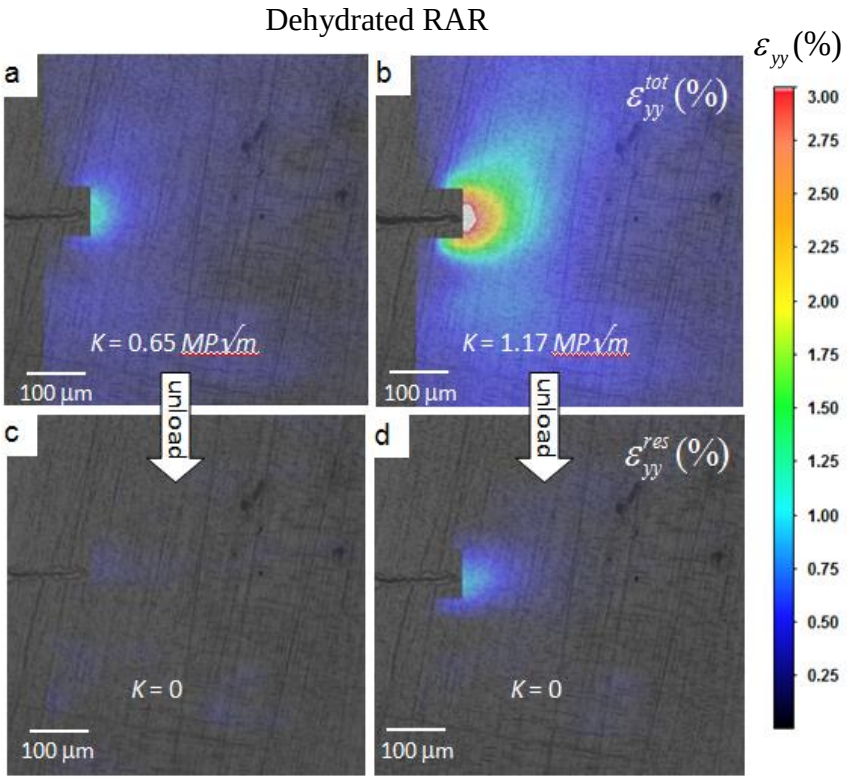

Fig. 6.4 Crack tip strain measured in RAR test-pieces under dehydrated condition. (a) K_{appl} = 0.65 $MPa\sqrt{m}$ (b) K_{appl} = 1.17 $MPa\sqrt{m}$ with loaded (top) and unloaded (bottom).

HAH Test-piece: crack growth parallel to the collagen fibres

The crack-tip strain fields were also measured for HAH test-pieces under dehydrated and hydrated conditions and the results are shown in Fig. 6.5. In the hydrated condition a much lower ε_{yy}^{tot} is observed at K_{appl} = 0.65 $MPa\sqrt{m}$ than for the RAR case (Fig. 6.3a). At the higher load (K_{appl} = 1.2 $MPa\sqrt{m}$), ε_{yy}^{tot} is more extensive but is still characterised by a very small ε_{yy}^{res} (Fig. 6.5d) suggestive of a predominantly elastic crack-tip stress field under load. As for the dehydrated RAR test-piece, very little crack-tip plasticity is observed under dehydrated conditions (Fig. 6.5e, f).

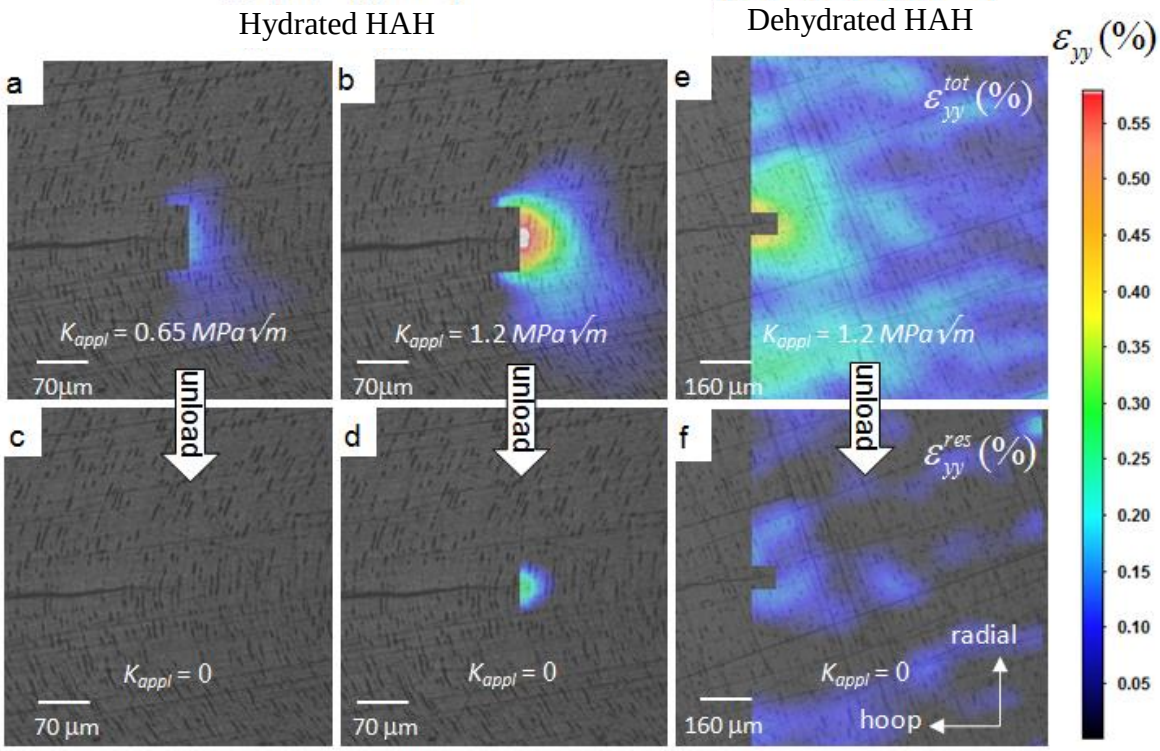

Fig. 6.5 Crack tip strain measured by DIC in HAH test-pieces under (a) – (d) hydrated and (e) – (f) dehydrated conditions. For hydrated HAH test-piece, (a) K_{appl} = 0.65 $MPa\sqrt{m}$ (b) K_{appl} = 1.2 $MPa\sqrt{m}$; for dehydrated HAH test-piece, (c) K_{appl} = 1.2 $MPa\sqrt{m}$ with loaded (top) and unloaded (bottom).

Analysis & discussion

In order to undertake a quantitative analysis of the strain fields, the crack-tip strains ε_{yy}^{tot} along the crack plane have been plotted as a function of distance from the crack-tip for all the tested test-pieces (Fig. 6.6). It is evident that the hydrated test-pieces show much higher strains than the dehydrated ones for similar stress intensities. Furthermore, the hydrated test-pieces also show a much higher ratio of ε_{yy}^{res} to ε_{yy}^{tot}. The elastic strains ε_{yy}^{el} for all the test-pieces (inferred as described above) are normalised by K_{appl} and plotted as a function of the distance ahead of the crack tip in Fig. 6.7. Three main conclusions can be drawn from this; firstly for HAH the curves fall essentially onto a single line suggesting that the unloading is predominantly elastic and the elastic properties in the hydrated and dehydrated cases are similar. Secondly, for RAR the curves agree at distances greater than 60µm from the crack but diverge nearer the crack. This divergence might be caused by the softening in the plastic zone, and will be discussed later. Thirdly, in the elastic far-field

regime the hydrated sample strains more than the dehydrated one, and this indicates a higher Young's modulus of the dehydrated test-piece than the hydrated one in accordance with previous observations [31-34].

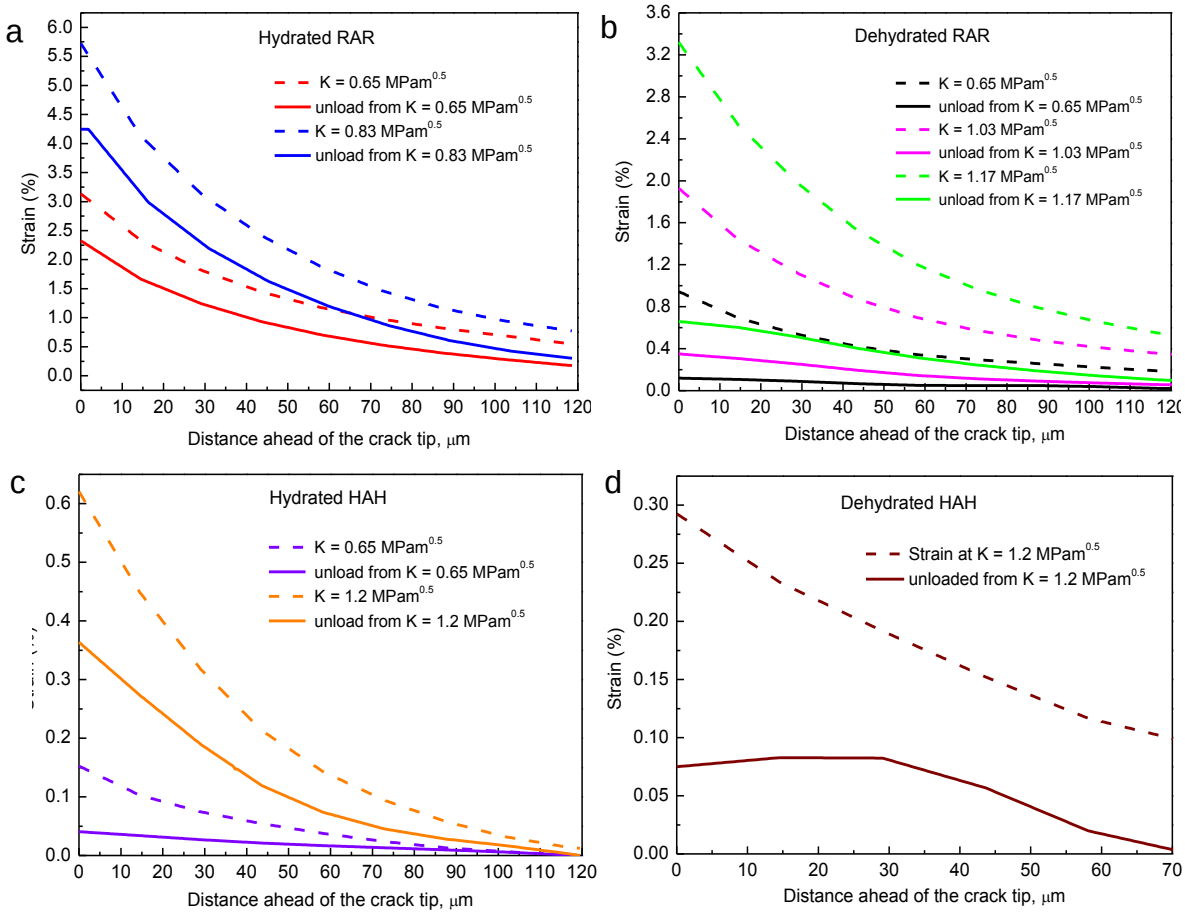

Fig. 6.6 The strain at the crack-plane plotted as a function of distance ahead of the crack tip in the loaded (dashed) and unloaded (solid) conditions for (a) RAR hydrated test-piece (b) RAR dry test-piece (c) HAH hydrated test-piece (d) HAH dry test-piece. Note the very different strain scales.

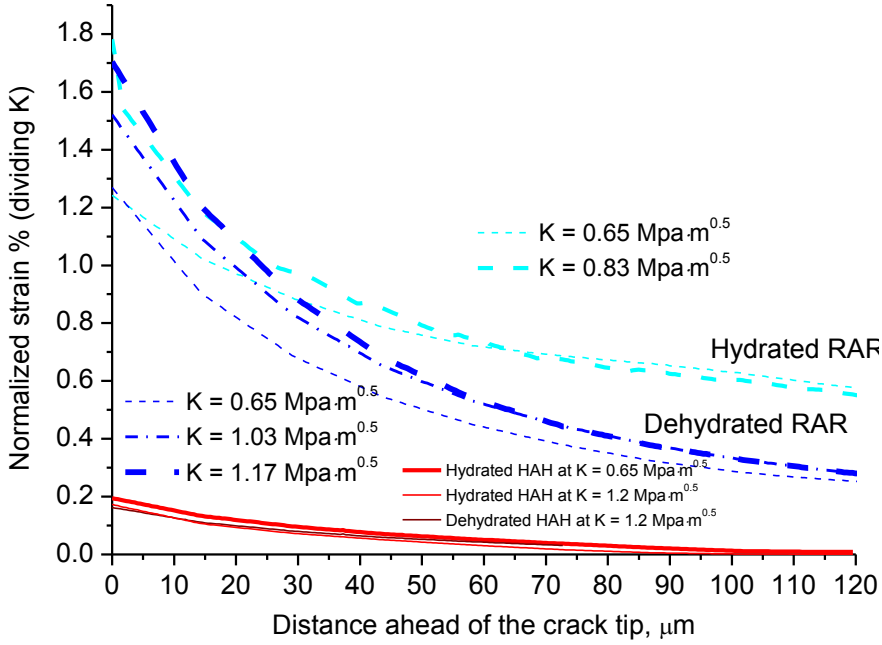

Fig. 6.7 Comparison of the normalized (by K_{appl}) elastic strains for both HAH and RAR test-pieces for different loads under hydrated and dry conditions.

It has been reported that the Young's modulus of the mineral content $E_{hydroxyapatite} \approx 114$ *GPa*, while that for the organic content $E_{collagen} \approx 1.2$ *GPa* under dry [47, 48] and 0.3 *GPa* under hydrated conditions [49]. The Young's modulus for the hydrated RAR test-piece can be inferred by normalizing the elastic strain curves by a factor so that the they overlap with the dehydrated elastic strain curves in the elastic region at each loads. In present study, the Young's modulus for the hydrated test-pieces were inferred by comparing the strain magnitude between the hydrated and dehydrated test-pieces (Fig. 6.8), as the Young's modulus for the dehydrated HAH and RAR test-pieces were measured by nano-indentaiton experiment before hand (It is challenging to conduct nano-indentation test under hydrated condition since the test-piece can quickly dry out during the drift-test stage before the indentation measurement.), which are 13.6 and 15.6 *GPa* respectively, and the results are summarised in Table 6.1. Two noteworthy points are found here: (1) Distinct difference between the hydrated and dehydrated RAR test-piece are seen, but they are identical for HAH test-piece; (2) the Young's modulus for hydrated HAH and RAR test-pieces are different. These evidence indicate that there is distinguished disparity between in hydrated and dehydrated conditions. Moreover, elephant dentin demonstrates anisotropic Young's modulus, especially in hydrated condition. Our results coincide well with the previously reported Young's modulus for the dehydrated elephant dentin (12 ~ 17 *GPa* [2, 17]). To

author's knowledge, there is few study on the Young's modulus measurement of the hydrated elephant dentin. The most relevant work were achieved by Guidoni [31] and Huang [50], who reported the Young's modulus of hydrated human dentin are between 6.5 ~ 10.2 *GPa*.

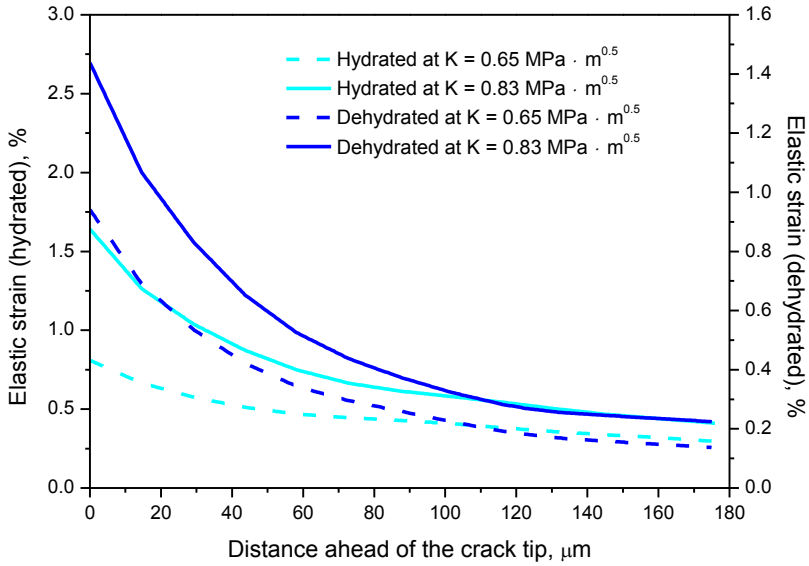

Fig. 6.8 The comparisons of the elastic strain for the hydrated and dehydrated RAR test-pieces, from which it is inferred that the stiffness of the dehydrated test-piece is essentially twice as large as the hydrated one.

Table 6.1 Summary of the inferred Young's modulus by elastic strain comparison based on the DIC strain measurement

	RAR		HAH	
	Hydrated	Dehydrated	Hydrated	Dehydrated
E(GPa)	6.0	13.6	13.8	15.6

6.3.2 Crack opening displacement measurement

The crack opening displacement (COD) provides an alternative measure of the fracture toughness. The effective stress intensity factor K_{eff} can be inferred from the relative COD data (i.e. relative to the opening displacement for zero applied load) [46]:

$$\Delta u(r) = 8\frac{K_{eff}}{E'}\sqrt{\frac{r}{2\pi}} \tag{6.2}$$

where E' is equal to E under plane stress conditions and $E / (1-\nu^2)$ under plane strain conditions. $\Delta u(r)$ is the net (i.e. after background subtraction) COD at distance r away from the crack tip. In theory, this equation predicts a parabolic dependence of $\Delta u(r)$ with distance r.

It is evident from Fig. 6.9a and b that in general the hydrated samples exhibit significantly larger CODs than the dehydrated ones with the RAR test-pieces showing the largest CODs. Moreover, the CODs at Kmin (unloaded) for the hydrated test-pieces are also clearly larger than the dehydrated test-pieces. These results correlate with the residual crack tip strain field ε_{yy}^{res} results in that the cracks which demonstrate the largest plasticity near the tip show the largest COD and crack-tip blunting. The □CODs are identified by subtracting the CODs of the loaded from the unloaded ones, and are shown in Fig. 6.9c and d. The □CODs are then fitted using a least square regression method to extract the gradients. The inferred effective stress intensity factors K_{eff} are compared with the nominally applied ones K_{appl} (Table 6.2), from which it is seen that the shielding effect for RAR hydrated test-piece is slightly better than the dehydrated one, and the bridging effect degrades with the increasing load. In contrast, little shielding effect can be seen for hydrated and dehydrated HAH test-piece. In addition, hydration didn't benefit the HAH test-piece with a higher fracture toughness compared to the dehydrated test-piece.

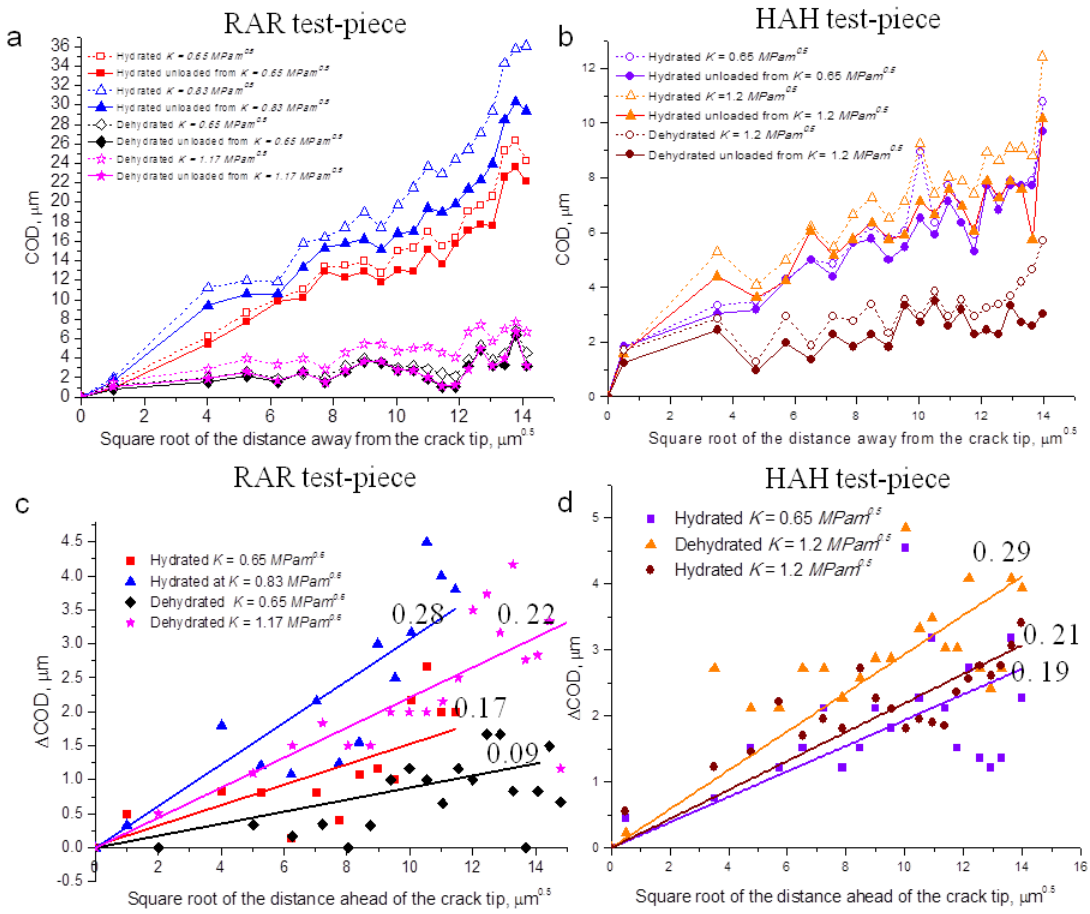

Fig. 6.9 The crack opening displacement (COD) at load (dashed) and after unloading (continuous) for (a) RAR test-piece and (b) HAH test-piece. After subtraction of the unloaded curves from the loaded ones, the elastic ΔCODs were obtained for (c) RAR test-pieces and (d) HAH test-pieces, and fitted by least square regression method. The numbers indicate the gradients.

Table 6.2 The comparison of the inferred K_{eff} and K_{appl}.

	hydrated RAR		dehydrated RAR		hydrated HAH		dehydrated HAH
K_{appl}	0.65	0.83	0.65	1.17	0.65	1.2	1.2
K_{eff}	0.31	0.52	0.37	0.95	0.57	1.02	1.10
K_{eff}/K_{appl}	48%	62%	58%	78%	88%	90%	91%

6.3.3 Plastic zone determination and predictions from models

It is challenging to measure the plastic zone size for brittle materials because of the difficulty identifying the conventional yield strain ε_y. A method described in [51] was used here. The basic idea of this method is: (1) subtracting an released elastic strain field ($\sigma'/E = C/E\sqrt{2\pi r}$) from the loaded curve so as to overlap the subtracted curve with the unloaded curve in the elastic region; (2) in the plastic region, the curve is obtained by subtracting estimated yield strain $\varepsilon_y = \sigma_y/E$ with the released elastic strain from x=0 to the plastic boundary, which varies with σ_y. The curve obtained by (1) in beyond the plastic zone and (2) within the elastic zone together compose of the residual elastic strain field, as are shown as dotted line in Fig. 6.10a and b. If we assume ideal plasticity and elastic unloading we can identify a yield strain ε_y such that the observed total strains at applied K_{max} (dashed line) and K_{min} (solid line) in Fig. 6.10 are consistent with a balance of residual elastic strain at K_{min} (dotted line) [51]. The best-fit ε_y are plotted for the two test-pieces at different loads in Fig. 6.10 where it is evident that despite a subtle variance, the inferred average yield strains are very similar for the hydrated and dehydrated cases (0.9% vs 0.83%). In accordance, the yielding stresses are 54 *MPa* and 109 *MPa* respectively. The hydrated yielding strength coincides with the reported values very well (50 ~ 65 *MPa* [17]), but the dehydrated yield stress is lower than recorded previously (153 $\pm$ 14 *MPa* [52]).

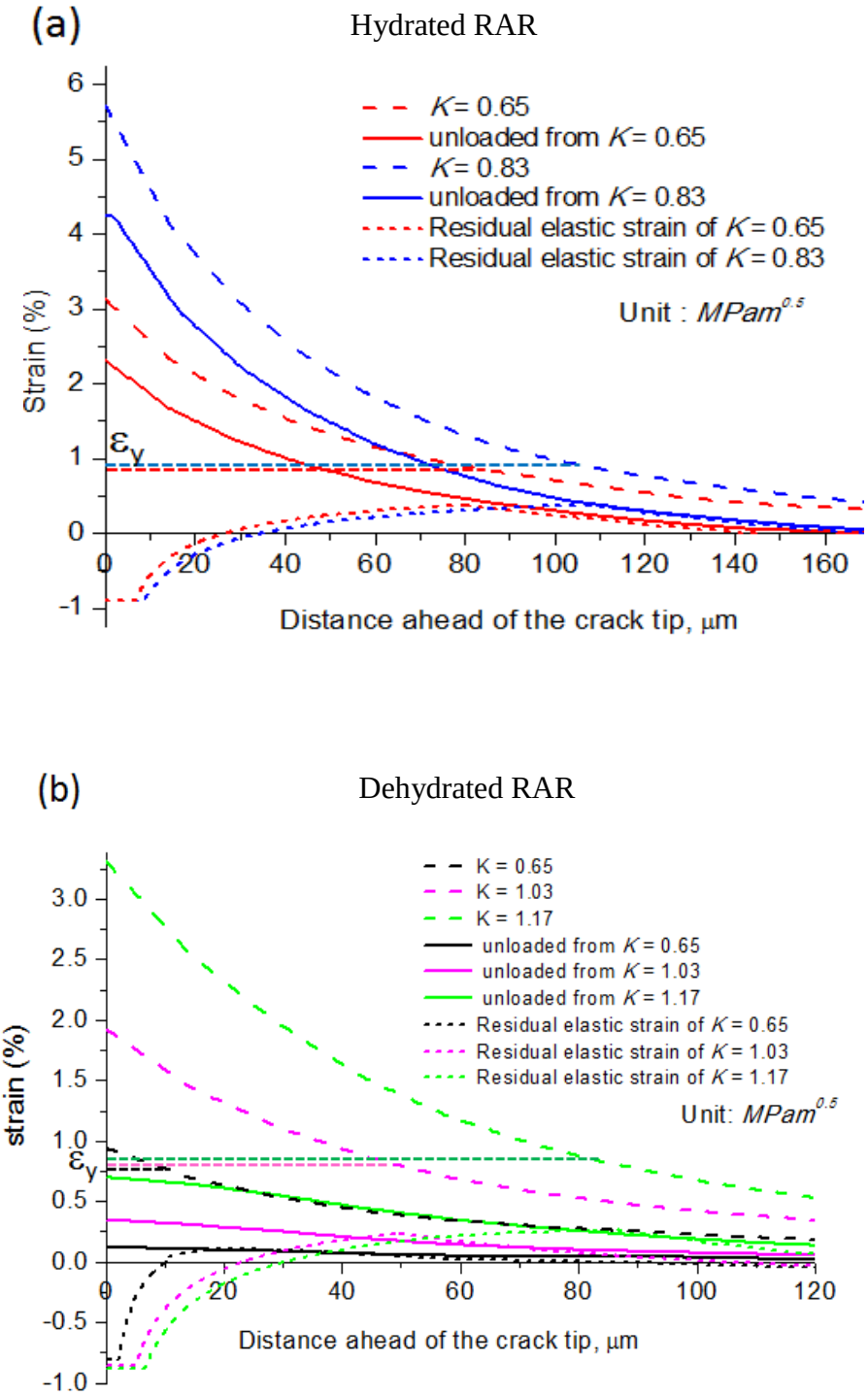

Fig. 6.10 The residual strain and the estimated residual elastic strain at unloaded condition for (a) hydrated and (b) dehydrated RAR test-piece. The estimated elastic strain curves were obtained by defining a yielding strain ε_Y which gives stress balance in the unloaded condition.

Table 6.3 presents the inferred plastic zones for the hydrated and dehydrated test-pieces as well as the predictions by models using the measured yield strains shown above. It is evident that the plastic zone sizes are significantly larger for the hydrated samples relative to the dehydrated ones. Irwin's model gives a smaller plastic zone compared with Dugdale's, which coincides with the measured values better.

Table 6.3 The comparison of the experimentally measured plastic zone and the predictions based on Irwin's and Dugdale's model (μm) for RAR test-piece

	Hydrated ($MPa\sqrt{m}$)		Dehydrated ($MPa\sqrt{m}$)		
	K = 0.65	K = 0.83	K = 0.65	K = 1.07	K = 1.13
Measured	78	107	10	44	84
Irwin	53	87	14	36	48
Dugdale	66	108	18	45	61

Crack-tip plasticity causes the redistribution of stress from that for an idealised linear elastic material. One simple way of accounting for this is to assume that within the plastic zone, the stress equals the yield strength of the material, but for the region outside of the plastic zone, the stress distribution follows the elastic K-field, but with the crack length should be adjusted to account for this [53-55]. To see if the observed crack tip strain field is consistent with such an analysis the crack-tip strain is plotted in Fig. 6.11 as a function of the distance ahead of the crack-tip. The elastic strains measured ahead of the plastic appear to match well with the curves predicted on the basis of stress redistribution using the fictitious crack tip location.

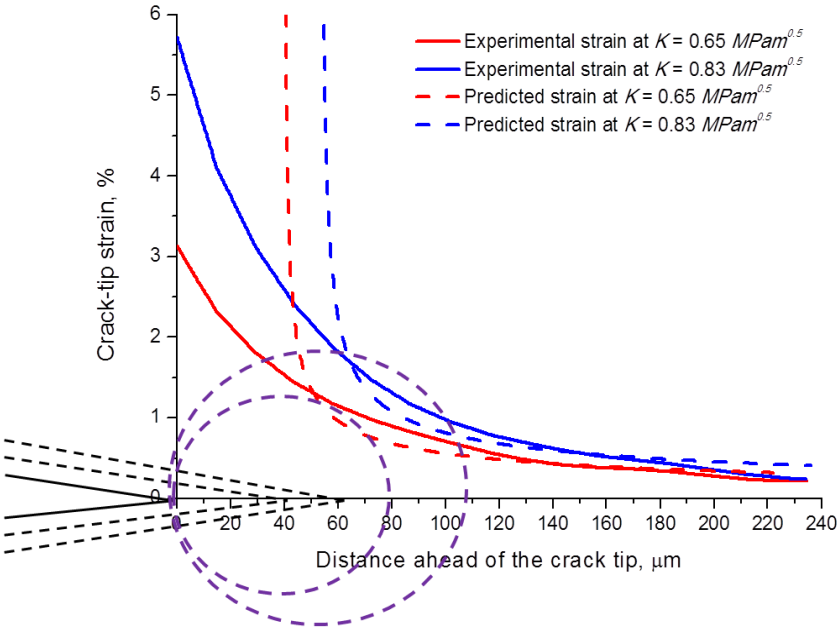

Fig. 6.11 The measured (solid lines) crack tip strain profiles plotted as a function of the distance ahead of the crack tip for the RAR hydrated test-pieces according to Fig. 6.10. The elastic strain field predicted due to the redistribution at the crack-tip because of the plastic zone measured from Fig. 6.10 (dashed lines) is plotted at two loads. The light blue circles and the black dashed lines indicate the plastic zone and the fictitious crack-tip at two loads respectively.

6.3.4 R-curve measurement

R-curves were measured for the two types of test-piece in the hydrated and dehydrated conditions. Unsurprisingly, the results (Fig. 6.12) show clear differences between the RAR and HAH test-pieces. First of all, the cracks in RAR test-pieces experience longer sub-critical growth than those in the HAH test-pieces. In addition, a much higher initial fracture toughness ($\Delta a = 0$) was encountered for the RAR test-pieces ($K_0 \approx 1.2$ $MPa\sqrt{m}$) compared to the HAH test-pieces ($K_0 \approx 0.8$ $MPa\sqrt{m}$). Most of the curves of RAR test-pieces exhibit a K_{IC} around 2.25 $MPa\sqrt{m}$, while for the HAH test-pieces K_{IC} ranges from 1.2 to 1.5 $MPa\sqrt{m}$. Apart from the differences in the fracture toughness, the two test-pieces types also exhibit distinct R-curve behaviours. It is evident that RAR test-pieces demonstrate essentially bilinear curves: initially the fracture toughness increases dramatically with the extension of the crack. After this stage the fracture toughness becomes stable, shown as a plateau on the R-curve. By contrast, the HAH test-pieces show a monotonically increasing

R-curve. It is also meaningful to compare the R-curve response for the hydrated and the dry test-pieces. It is found that for the RAR test-pieces, the hydrated ones are slightly tougher than the dry ones. There is no significant difference in K_0, but for the hydrated test-piece K rises with crack extension more significantly during the first linear part. However, for the HAH test-pieces the dry and hydrated ones behave similarly except that, for the hydrated test-pieces the crack can extend longer than the dry ones.

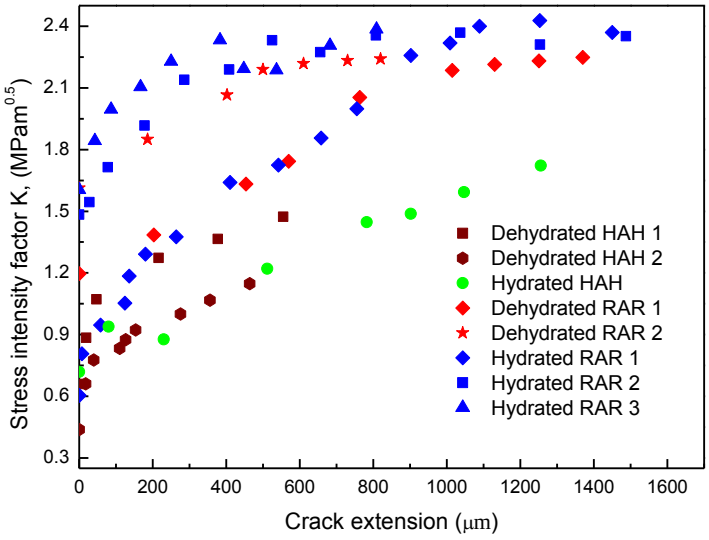

Fig. 6.12 R-curve measurement of two types of test-pieces in hydrated and dry conditions.

6.4 Discussion

6.4.1 Crack-tip strain and the intrinsic shielding mechanism

Effect of crack orientation: Unsurprisingly, our results clearly show marked differences between the different test-pieces under different environments: in both the hydrated and dehydrated conditions the strains ε_{yy}^{tot} in the RAR test-piece (*radial-axial crack plane*) are higher (by as much as 10x) than those for the HAH test-piece (*hoop-axial crack plane*), accompanied by larger crack-tip opening as well (Fig. 6.9a and b). This evidence of higher toughness derives from the microstructure at the crack-tip. Previous studies reveal that the triple-helical domains of collagens comprise three polypeptide chains, and that this triple helix motif has an inherent plasticity in the native collagen molecules [56]. They are not designed to be as rigid and stiff as possible, but rather to

provide some stress relaxation under load. They are made to resist and accommodate deformation [57, 58], that is why RAR test-piece is often found with a blunt tip [2, 17, 21]. Gupta etc [59] also reported that the intrafibrillar plasticity coming from the mineral/collagen sliding is the main reason for the high fracture toughness. This explains why RAR test-pieces always demonstrate higher crack-tip strains and opening than HAH test-pieces, given that the planar collagen fibrils are arranged perpendicular to the crack plane in the RAR test-piece (Fig. 6.1h), but parallel to it in the HAH test-piece (Fig. 6.1g), in which the crack behaves like a cleavage crack. Moreover, as described by Nalla etc [60], microcracks were observed around the tubules in the yielding zone (i.e. fracture process zone) under large strain, which potentially makes the matrix less stiff. This also explains why the normalized strain for RAR test-piece is larger than that for HAH (Fig. 6.7).

In summary, collagen plays a critical role in the intrinsic shielding mechanism for dentin. The strain difference (i.e. total, elastic and plastic strain) between RAR and HAH test-piece lies on the involvement of the collagen-based intrinsic shielding that acts ahead of the crack-tip, reducing the stresses through localized yielding and redistribution [61, 62]. Intrinsic toughening arises from 1) energy required for the collagen molecules to uncrimp and slide; 2) microcracks generated within the collagen fibrils; 3) dissipation of the energy when the bonds within or between the collagen molecules are stretched [63].

Effect of hydration: Unsurprisingly, the hydrated test-pieces exhibited strains ε_{yy}^{tot} twice as large as the dehydrated test-piece, for both types of test-pieces. Substantially larger plastic and elastic strains were observed for the hydrated samples as a result of higher crack tip plasticity and lower elastic modulus. These observations relate to more extensive mineral/collagen sliding in the hydrated condition.

The large plastic strains ε_{yy}^{pl}, high fracture toughness and large elastic strain ε_{yy}^{el} could be the result of the fact that water plays an important role in forming the structure of collagen molecules since it helps to form hydrogen bonds which inter-links the triple helices of the collagen molecule, along the peptide chains [64-67]. The hydration layer also forms the hydrogen-bonded ”bridges”, which strengthen the structure of collagen by forming intra- and interchain links within collagen molecules and between neighbouring molecules. Water may act as a plasticizer of collagen [68]. Another explanation is that, the hydroxyapatite crystallites have been suggested to form a granular medium that binds to

the organic matrix via hydrophilic interactions or mineral – matrix binding proteins under hydration environment [17]. Lees [69] claims that the lateral spacing between the collagen molecules shrinks with decreasing moisture content, consequently there is an increase in the shear stresses between the mineral and the organic matrix because of more extensive interfacial contact of the mineral within the fibrils and interfibrillarly in the collagen network. Dehydrated test-piece has low capability to undergo crack-tip strain compared with the hydrated test-piece is caused by the efficiency of the collagen-based intrinsic shielding. A decrease in moisture content can actually cause the reduction in the strain to fracture [30, 70, 71].

6.4.2 R-curve and the extrinsic shielding

The R-curve of RAR test-pieces showed a more pronounced rise in the fracture toughness K_{IC} vs the crack extension Δa than the HAH test-pieces. Surprisingly, the initial fracture toughness K_0 of the hydrated RAR test-pieces are similar to the dry test-piece, and this may be caused by the microdamage in the yielding zone as mentioned before. But the R-curve rises more steeply initially for the hydrated RAR test-piece, which can be explained by the strengthened intrinsic shielding mechanisms due to hydration effect on the collagen fibrils that improves the extent of bridging. From these phenomena, it is concluded that the initiation of the crack is equally easy in the hydrated and dehydrated test-pieces, but the hydrated test-piece demonstrates increasing crack growth retardation. The rise of the fracture toughness derives from the increasing extent of extrinsic toughening mechanisms, i.e. uncracked-ligament bridging and fibrils bridging at the wake of crack [2, 17, 22, 23]. The plateau in the R-curve of the RAR test-pieces arises because there is a saturation of the bridging effect arising from uncracked ligaments, i.e. after 400 μm of growth as the crack extends. There is a balance between the formation of new bridges and the breaking of existing ones (see Fig. 6.13) which is in accordance with those reported before [2, 54, 72].

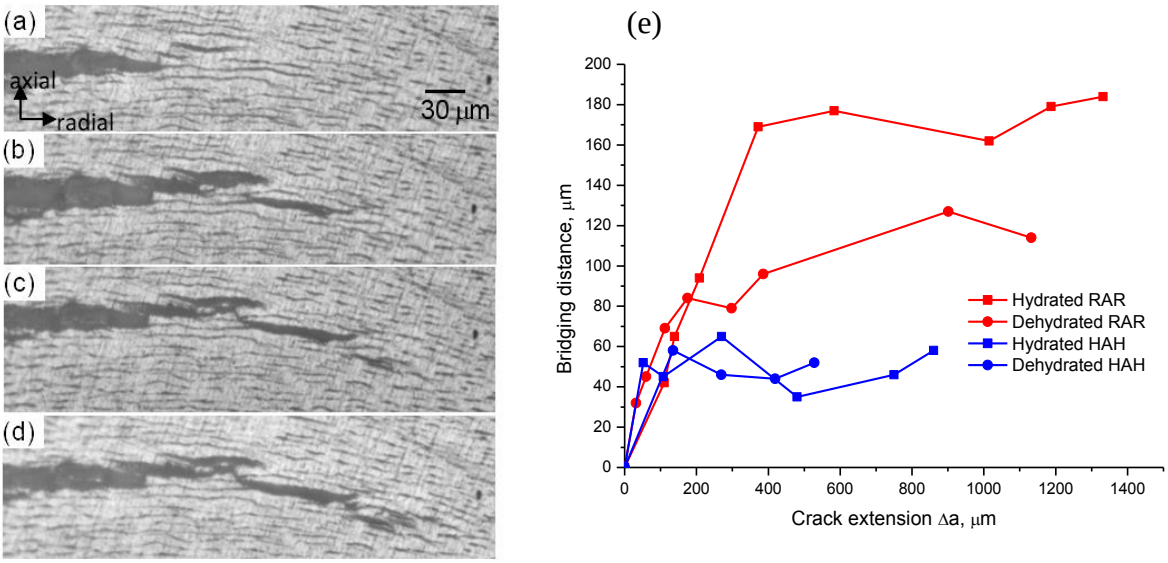

Fig. 6.13 Progressive formation and breaking of bridges in the wake of the crack for RAR hydrated test-piece (a) – (d); (e) crack bridging distance as a function of the crack extension for different types of test-pieces.

6.5 Conclusions

This paper presents the first measurements of the strain fields local to the crack-tip of elephant dentin. The effect of hydration on the intrinsic and extrinsic toughening mechanisms have been assessed in terms of crack-tip plasticity, strain field and R-curve. Several important conclusions are drawn as follows:

1. The maximum strain at the crack-tip of RAR (i.e. crack growth in radial-axial plane, in radial direction) test-piece was 10 times as large as the HAH (i.e. crack growth in hoop-axial plane, in hoop direction) test-pieces, under both hydrated and dry conditions. The strain to failure for the hydrated test-pieces were twice as large as the dehydrated ones. One of the factors contributing these discrepancies is the hydration of the collagen, and the other is the arrangement of the collagen relative to the crack plane.

2. The plastic zones were determined directly from the strain fields. We identified plastic zones of 78 μm at K_{appl} = 0.65 $MPa\sqrt{m}$ and 107 μm at K_{appl} = 0.83 $MPa\sqrt{m}$ in the hydrated and 10 μm at K_{appl} = 0.65 $MPa\sqrt{m}$ and 84 μm at K = 1.17 $MPa\sqrt{m}$ for the dehydrated RAR test-pieces. In contrast the plastic strains for HAH test-pieces were negligible. The measured yielding strength for the hydrated and dehydrated RAR test-piece were 54 and 109 *MPa* respectively. Ahead of the plastic zone, the elastic strains matched well with theoretical expectations. Our results are consistent with Young's moduli of 6.0 and 13.8 *GPa* for the hydrated RAR and HAH test-pieces respectively.

3. The crack-tip stress were shielded by maximum 52 % and 40 % for hydrated and dehydrated RAR test-piece, whereas no significant shielding was found for HAH test-piece. The R-curve response of the RAR test-pieces was much higher than for the HAH test-pieces. While the hydrated and dehydrated samples showed similar initiation toughness K_0 due to the substantial micro-cracks under large strain, former showed a much more significant R-curve response due to more effective intrinsic and extrinsic shielding. The bridging lengths for the hydrated and dehydrated RAR test-piece are 180 and 120 μm respectively, but for HAH test-pieces, the bridging lengths are around 50 μm.

4. Hydrated collagen significantly improves the efficiency of intrinsic shielding mechanisms in terms of larger crack-tip elastic/plastic strain, crack-tip blunting and higher $\Delta K_{IC}/\Delta a$ rate, compared with the dehydrated test-piece. A reduction in moisture content can actually result in the decrease in the strain to fracture. Extrinsic shielding mechanisms (e.g. uncracked-ligament bridging) greatly contribute to the crack retardation in long range crack extension for RAR test-pieces in both hydrated and dehydrated conditions.

References

[1] Kinney JH, Balooch M, Marshall GM, Marshall SJ. A micromechanics model of the elastic properties of human dentine. Archives of Oral Biology 1999;44:813-22.
[2] Kruzic J, Nalla RK, Kinney JH, Ritchie RO. Crack blunting, crack bridging and resistance-curve fracture mechanics in dentin: effect of hydration. Biomaterials 2003;24:5209-21.
[3] Locke M. Structure of ivory. J Morphol 2008;269:423-50.
[4] Nalla RK, Imbeni V, Kinney JH, Staninec M, Marshall SJ, Ritchie RO. In vitro fatigue behavior of human dentin with implications for life prediction. Journal of Biomedical Materials Research Part A 2003;66A:10-20.
[5] Moyes AB, Doidge DW. COMPOSITION OF THE MINERAL PHASE OF DENTIN IN SOUTHERN ELEPHANT SEAL AND ANTARCTIC FUR-SEAL TEETH. British Antarctic Survey Bulletin 1984:81-4.
[6] Mills A. Structural and chemical organization of teeth: Elsevier; 2014.
[7] Miles AEW, Boyde A. Observations on Structure of Elephant Ivory. J Anat 1961;95:450-&.
[8] Raubenheimer EJ, Dauth J, Dreyer MJ, Smith PD, Turner ML. Structure and Composition of Ivory of the African Elephant (Loxodonta-Africana). S Afr J Sci 1990;86:192-3.
[9] Marshall GW, Inai N, Magidi ICW, Ballouch M, Kinney JH, Tagami J, et al. Dentin demineralisation: effects of dentin depth, pH and different acids (vol 13, pg 338, 1997). Dental Materials 1998;14:383-.
[10] Povar ML. The Structural and Chemical Organization of Teeth. J Am Vet Med Assoc 1967;151:1211-&.
[11] Su XW, Cui FZ. Hierarchical structure of ivory: from nanometer to centimeter. Mat Sci Eng C-Bio S 1999;7:19-29.
[12] Arola D, Rouland JA, Zhang D. Fatigue and fracture of bovine dentin. Experimental Mechanics 2002;42:380-8.
[13] Ivancik J, Neerchal NK, Romberg E, Arola D. The Reduction in Fatigue Crack Growth Resistance of Dentin with Depth. Journal of Dental Research 2011;90:1031-6.
[14] Iwamoto N, Ruse ND. Fracture toughness of human dentin. Journal of Biomedical Materials Research Part A 2003;66A:507-12.
[15] Bonfield W, Li CH. Deformation and Fracture of Ivory. J Appl Phys 1965;36:3181-&.
[16] Koester KJ, Barth HD, Ritchie RO. Effect of aging on the transverse toughness of human cortical bone: Evaluation by R-curves. Journal of the Mechanical Behavior of Biomedical Materials 2011;4:1504-13.
[17] Nalla RK, Kinney JH, Ritchie RO. Effect of orientation on the in vitro fracture toughness of dentin: the role of toughening mechanisms. Biomaterials 2003;24:3955-68.
[18] Watanabe LG, Marshall GW, Marshall SJ. Dentin shear strength: Effects of tubule orientation and intratooth location. Dent Mater 1996;12:109-15.
[19] Arola DD, Reprogel RK. Tubule orientation and the fatigue strength of human dentin. Biomaterials 2006;27:2131-40.
[20] Ivancik J, Arola DD. The importance of microstructural variations on the fracture toughness of human dentin. Biomaterials 2013;34:864-74.
[21] Bajaj D, Sundaram N, Nazari A, Arola D. Age, dehydration and fatigue crack growth in dentin. Biomaterials 2006;27:2507-17.
[22] Arola D, Reprogel RK. Effects of aging on the mechanical behavior of human dentin. Biomaterials 2005;26:4051-61.

[23] Koester KJ, Ager Iii JW, Ritchie RO. The effect of aging on crack-growth resistance and toughening mechanisms in human dentin. Biomaterials 2008;29:1318-28.
[24] Foulk JW, III, Cannon RM, Johnson GC, Klein PA, Ritchie RO. A micromechanical basis for partitioning the evolution of grain bridging in brittle materials. Journal of the Mechanics and Physics of Solids 2007;55:719-43.
[25] Kruzic JJ, Satet RL, Hoffmann MJ, Cannon RM, Ritchie RO. The utility of R-curves for understanding fracture toughness-strength relations in bridging ceramics. Journal of the American Ceramic Society 2008;91:1986-94.
[26] Launey ME, Ritchie RO. On the Fracture Toughness of Advanced Materials. Advanced Materials 2009;21:2103-10.
[27] Ritchie RO, Nalla RK, Kruzic JJ, Ager JW, III, Balooch G, Kinney JH. Fracture and ageing in bone: Toughness and structural characterization. Strain 2006;42:225-32.
[28] Zimmermann EA, Launey ME, Ritchie RO. The significance of crack-resistance curves to the mixed-mode fracture toughness of human cortical bone. Biomaterials 2010;31:5297-305.
[29] Kruzic JJ, Nalla RK, Kinney JH, Ritchie RO. Crack blunting, crack bridging and resistance-curve fracture mechanics in dentin: effect of hydration. Biomaterials 2003;24:5209-21.
[30] Kahler B, Swain MV, Moule A. Fracture-toughening mechanisms responsible for differences in work to fracture of hydrated and dehydrated dentine. Journal of biomechanics 2003;36:229-37.
[31] Guidoni G, Denkmayr J, Schöberl T, Jäger I. Nanoindentation in teeth: influence of experimental conditions on local mechanical properties. Philosophical Magazine 2006;86:5705-14.
[32] Pugach MK, Strother J, Darling CL, Fried D, Gansky SA, Marshall SJ, et al. Dentin caries zones: mineral, structure, and properties. Journal of dental research 2009;88:71-6.
[33] Bertassoni LE, Habelitz S, Kinney JH, Marshall SJ, Marshall GW, Jr. Biomechanical Perspective on the Remineralization of Dentin. Caries Research 2009;43:70-7.
[34] Huang T-JG, Schilder H, Nathanson D. Effects of moisture content and endodontic treatment on some mechanical properties of human dentin. Journal of Endodontics 1992;18:209-15.
[35] Bertassoni LE, Swain MV. Influence of hydration on nanoindentation induced energy expenditure of dentin. Journal of biomechanics 2012;45:1679-83.
[36] Lopez-Crespo P, Shterenlikht A, Patterson E, Yates J, Withers P. The stress intensity of mixed mode cracks determined by digital image correlation. The Journal of Strain Analysis for Engineering Design 2008;43:769-80.
[37] Withers PJ. Strain measurement by digital image correlation. Strain 2008;44:421-2.
[38] Sztefek P, Vanleene M, Olsson R, Collinson R, Pitsillides AA, Shefelbine S. Using digital image correlation to determine bone surface strains during loading and after adaptation of the mouse tibia. Journal of biomechanics 2010;43:599-605.
[39] Thompson MS, Schell H, Lienau J, Duda GN. Digital image correlation: A technique for determining local mechanical conditions within early bone callus. Medical Engineering & Physics 2007;29:820-3.
[40] Vaananen SP, Amin Yavari S, Weinans H, Zadpoor AA, Jurvelin JS, Isaksson H. Repeatability of digital image correlation for measurement of surface strains in composite long bones. Journal of biomechanics 2013;46:1928-32.
[41] ASTM Standard E1820-08a. "Standard Test Method for Measurement of Fracture Toughness". ASTM International, West Conshohocken, PA, USA, 2008.
[42] Robert Gallegos, 2012. Maintain Dentin Bond Strength Over Time. Daily Digest;http://www.speareducation.com/spear-review/tag/dentin/page/3/.

[43] Quinta da Fonseca J, Mummery PM, Withers PJ. Full ‐ field strain mapping by optical correlation of micrographs acquired during deformation. Journal of microscopy 2005;218:9-21.
[44] Sutton MA, Orteu JJ, Schreier H. Image correlation for shape, motion and deformation measurements: basic concepts, theory and applications: Springer Science & Business Media; 2009.
[45] ASTM Standard E1820-01. "Standard Test Method for Measurement of Fracture Toughness". ASTM International, West Conshohocken, PA, USA, 2002.
[46] Withers PJ. Residual stress and its role in failure. Reports on progress in physics 2007;70:2211-64.
[47] Gilmore RS, Katz JL. Elastic properties of apatites. Journal of Materials Science 1982;17:1131-41.
[48] Deymier-Black AC, Yuan F, Singhal A, Almer JD, Brinson LC, Dunand DC. Evolution of load transfer between hydroxyapatite and collagen during creep deformation of bone. Acta biomaterialia 2012;8:253-61.
[49] Nalla RK, Balooch M, Ager JW, Kruzic JJ, Kinney JH, Ritchie RO. Effects of polar solvents on the fracture resistance of dentin: role of water hydration. Acta biomaterialia 2005;1:31-43.
[50] Huang TG, Schilder H, Nathanson D. Effects of moisture content and endodontic treatment on some mechanical properties of human dentin. Journal of Endodontics 1992;18:209-15.
[51] Lopez-Crespo P, Steuwer A, Buslaps T, Tai YH, Lopez-Moreno A, Yates JR, et al. Measuring overload effects during fatigue crack growth in bainitic steel by synchrotron X-ray diffraction. International Journal of Fatigue 2015;71:11-6.
[52] Yan J, Taskonak B, Platt JA, Mecholsky JJ. Evaluation of fracture toughness of human dentin using elastic–plastic fracture mechanics. Journal of Biomechanics 2008;41:1253-9.
[53] Broek D. Elementary Engineering Fracture Mechanics. Martinus Nijhoff Publishers 1984.
[54] Kanninen M. Advanced Fracture Mechanics. Oxford University Press 1985.
[55] O'Dowd N. Advanced Fracture Mechanics: Lectures on Fundamentals of Elastic, Elastic-Plastic and Creep Fracture. Imperial College London 2002.
[56] Ricard-Blum S. The collagen family. Cold Spring Harbor perspectives in biology 2011;3:a004978.
[57] Weiss IM, Kirchner HO. Plasticity of two structural proteins: alpha-collagen and beta-keratin. Journal of the Mechanical Behavior of Biomedical Materials 2011;4:733-43.
[58] Gupta HS, Fratzl P, Kerschnitzki M, Benecke G, Wagermaier W, Kirchner HO. Evidence for an elementary process in bone plasticity with an activation enthalpy of 1 eV. Journal of the Royal Society Interface 2007;4:277-82.
[59] Gupta HS, Krauss S, Kerschnitzki M, Karunaratne A, Dunlop JWC, Barber AH, et al. Intrafibrillar plasticity through mineral/collagen sliding is the dominant mechanism for the extreme toughness of antler bone. Journal of the Mechanical Behavior of Biomedical Materials 2013;28:366-82.
[60] Nalla RK, Kinney JH, Ritchie RO. On the fracture of human dentin: Is it stress ‐ or strain ‐ controlled? Journal of Biomedical Materials Research Part A 2003;67:484-95.
[61] Vashishth D, Behiri JC, Bonfield W. Crack growth resistance in cortical bone: concept of microcrack toughening. Journal of biomechanics 1997;30:763-9.
[62] Vashishth D, Koontz J, Qiu SJ, Lundin-Cannon D, Yeni YN, Schaffler MB, et al. In vivo diffuse damage in human vertebral trabecular bone. Bone 2000;26:147-52.
[63] Thompson JB, Kindt JH, Drake B, Hansma HG, Morse DE, Hansma PK. Bone indentation recovery time correlates with bond reforming time. Nature 2001;414:773-6.

[64] Chapman GE, Danyluk SS, McLauchl.Ka. MODEL FOR COLLAGEN HYDRATION. Proceedings of the Royal Society Series B-Biological Sciences 1971;178:465-+.
[65] Chapman GE, McLaughl Ka. THE HYDRATION STRUCTURE OF COLLAGEN. Proceedings of the Royal Society Series B-Biological Sciences 1969;173:223-+.
[66] Lazarev YA, Grishkovsky BA, Khromova TB. AMIDE-I BAND OF IR-SPECTRUM AND STRUCTURE OF COLLAGEN AND RELATED POLYPEPTIDES. Biopolymers 1985;24:1449-78.
[67] Lazarev YA, Grishkovsky BA, Khromova TB, Lazareva AV, Grechishko VS. BOUND WATER IN THE COLLAGEN-LIKE TRIPLE-HELICAL STRUCTURE. Biopolymers 1992;32:189-95.
[68] Saito H, Yokoi M. A 13C NMR study on collagens in the solid state: hydration/dehydration-induced conformational change of collagen and detection of internal motion. Journal of Biochemistry 1992;111:376-82.
[69] Lees S. Considerations regarding the structure of the mammalian mineralized osteoid from viewpoint of the generalized packing model. Connective tissue research 1987;16:281-303.
[70] Jameson MW, Hood JAA, Tidmarsh BG. The effects of dehydration and rehydration on some mechanical properties of human dentine. Journal of biomechanics 1993;26:1055-65.
[71] Arola D, Zheng W. Hydration and dynamic fatigue of dentin. Journal of Biomedical Materials Research Part A 2006;77:148-59.
[72] Raddatz O, Schneider GA, Claussen N. Modelling of R-curve behaviour in ceramic/metal composites. Acta Materialia 1998;46:6381-95.

Paper 4: The Cohesive Zone Constitutive Law from Experimentally Measured Crack Opening Displacement for the Anisotropic Fracture of Elephant Dentin

Contributions:

X. Lu: Principal investigator to conduct the experiment, analyse the results and write up the paper

W. Ren: Abaqus software advisor and statement corrections

Prof. P.J. Withers: language corrections, comments on the results interpretation and discussion

Chapter 7

The Cohesive Zone Constitutive Law From Experimentally Measured Crack Opening Displacement for the Anisotropic Fracture of Elephant Dentin

X. Lu[a], W. Ren[b], P. J. Withers[a*]

[a]*School of Materials, University of Manchester, Manchester M13 9PL, UK*

[b]*School of Mechanical, Aerospace and Civil Engineering, University of Manchester, M13 9PL, UK.*

Abstract

Crack-tip shielding mechanisms can play a significant role in hindering of crack propagation, causing fracture toughness to rise with crack length especially for bio-materials such as bone, and dentin. It is challenging to measure the shielding effect quantitatively by experiment, moreover, few study has reported the application of simulating the bridging effect by cohesive zone model. In this paper we modelled the crack propagation behaviour in elephant dentin using a newly proposed cohesive zone constitutive law to simulate the physical process of crack-tip shielding. The model was established using a multi-linear separation-traction law based on experimentally measured crack opening displacements (COD). The simulation results demonstrate that the bridging in RAR (i.e. crack is in radial-axial plane, growing in radial direction) can dissipate 160 % more energy than HAH test-piece (i.e. crack is in hoop-axial plane, growing in hoop

[*] Corresponding author, School of Materials, University of Manchester, Grosvenor Street, Manchester M13 9PL, UK

Email address: p.j.withers@manchester.ac.uk, +44 (0)161 306 4282

direction). The bridging distance was also measured as large as 400 μm, which agreed with the 3-D observation very well. The model was further verified by experimental R-curve and crack-tip strain fields obtained digital image correlation (DIC).

Key words: Cohesive zone model, multi-linear traction-separation law, crack-tip strain, crack bridging, R-curve, crack-tip shielding, fracture, damage dissipation

7.1 Introduction

Crack tip shielding is an important mechanism in the toughening of hard, hierarchically structured biomaterials such as dentin. In this paper we focus on modelling the crack-tip shielding behaviour of dentin in order to obtain describe the shielding effects via a cohesive zone constitutive law. Elephant dentin is often viewed as a structural analogue for human dentin due to the similarities in microstructure and composition between the two materials. The larger size of tusk makes the sample preparation and fracture testing easier than human teeth [1]. Ivory tusk is made up of cementum, dentin and pulp cavity, from outer layer towards the centre. The cementum layer is softer than the dentin [2]. The dentinal tubules are the predominant feature in the main dentin and run from the central pulp to the periphery of the dentin. These tubules are embedded in a mineralized collagen matrix, which consists of Type I collagen fibrils and Mg containing hydroxyapatite [2-7]: the highly mineralized hydroxyapatite (HAP) improves the stiffness of teeth, while collagen provides toughness [8]. Fig. 7.1 presents the microstructure of the hierarchical elephant dentin with different techniques. It clearly illustrates the orientation of the dentinal tubules in the elephant tusk and the relative alignment of the collagen fibrils to the tubules. In order to investigate the anisotropy in response two sample orientations were used in this study. Based on the crack plane and the crack growth direction, they were named HAH (i.e. crack is in hoop-axial plane, growing in hoop direction) and RAR (i.e. crack is in radial-axial plane, growing in radial direction).

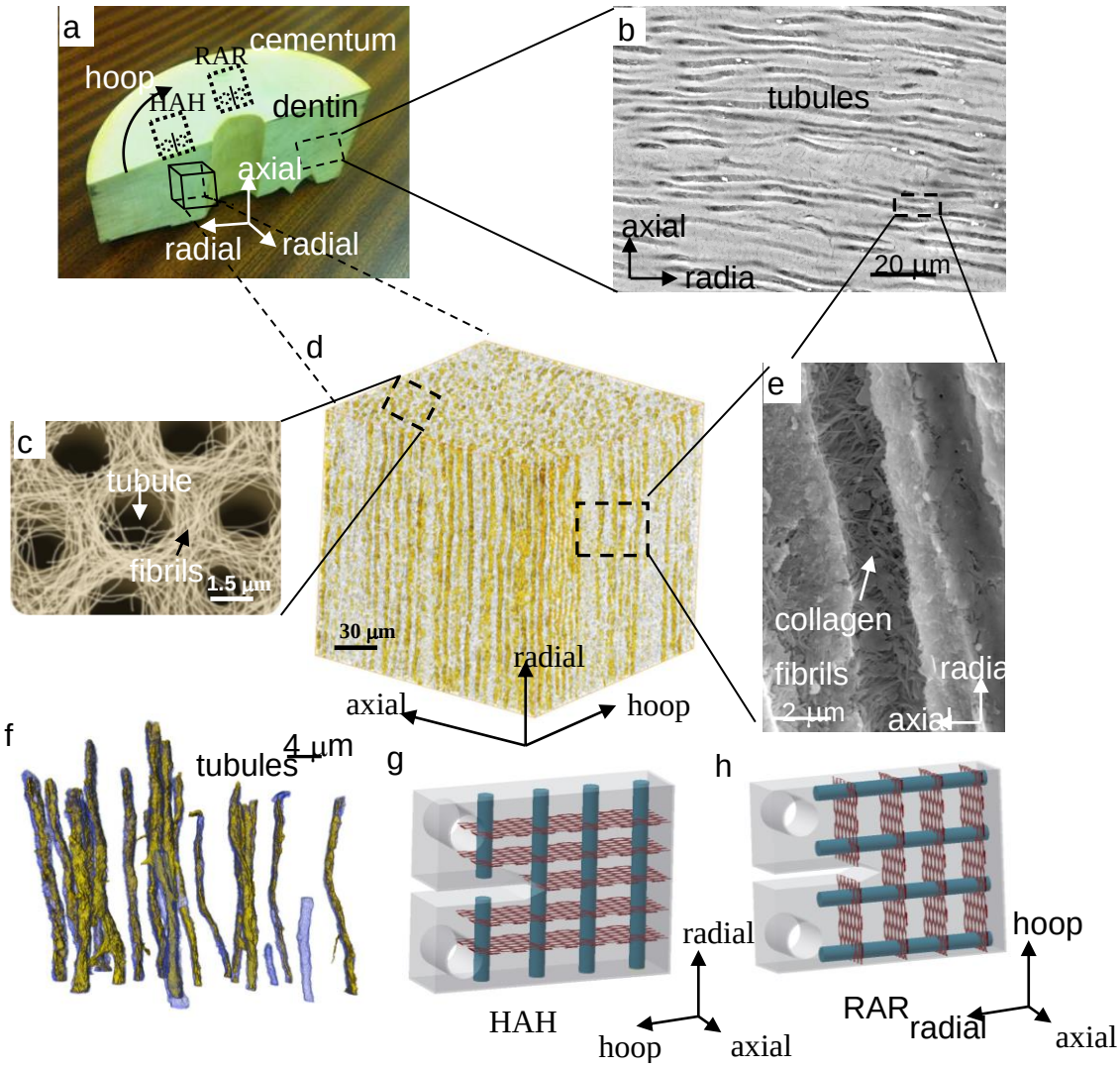

Fig. 7.1 The hierarchical structure of elephant dentin microstructure. (a) photograph of the elephant tusk slice showing the locations of HAH and RAR sample; (b) SEM image showing radial alignment of the tubules; (c) Etched dentin showing collagen fibrils woven around the tubules [9], magnified from (d) x-ray CT representing tubules alignment in the 1 mm cube sample in (a); (e) SEM micrograph showing the relative position between the tubules and the collagen fibrils; (f) extracted dentinal tubules in 3D from X-ray CT data; (g)-(h) schematic figure showing the alignment of the tubules and the collagen plane in HAH and RAR respectively.

To date, most of the investigations of the fracture of dentin materials have been based around linear elastic fracture mechanics (LEFM), assuming the nonlinear zone ahead of the crack-tip to be negligible and the fracture behaviour is regarded as a point process [10-13]. Under such assumptions, the stress at the crack-tip is singular and infinite. However, for some biomaterials such as bone and dentin crack-tip shielding reduces the crack-tip stress, by mechanisms such as uncracked-ligament and collagen fibrils bridging [1, 14-17], crack meandering [18], crack-tip blunting [1, 15], and microcracks [14, 16]. As a result the fracture toughness rises with crack length as these mechanisms come into play causing a

rising crack resistance curve (R-curve) with crack extension [1, 16, 19-21]. Such nonlinear process can be well simulated by inserting cohesive elements behind the crack-tip to represent the bridging zone which can carry load across the crack faces. The fracture process zone in dentin is approximately 2 mm [22], which represents the potential bridging zone length. Therefore, it is necessary to consider the contribution to toughening from bridging K_{br}, which depends on the crack length [23-25].

The typical crack-tip shielding mechanisms observed in dentin are uncracked-ligament bridging (Fig. 7.2a) and collagen fibril bridging (Fig. 7.2b). Fig. 7.3 illustrates how bridging works: the microcracks are generated in front of the main crack, which is traction free, by linking the neighbouring dentinal tubules. Fig. 7.3b is the idealized crack with cohesive zone exerting traction to simulate bridging effect. The traction σ_n varies along the crack direction. The different colours at the crack-tip imply the different magnitudes of softening or damage of the cohesive elements as a function of the distance from the crack-tip. The uncracked-ligament bridging effect span the whole fracture process zone [13], but collagen fibrils bridging effect is only confined to the crack-tip area and within a limited crack-tip opening [26-28]. Based on the observation, it is found that the shielding features were dominant in RAR, but not in HAH.

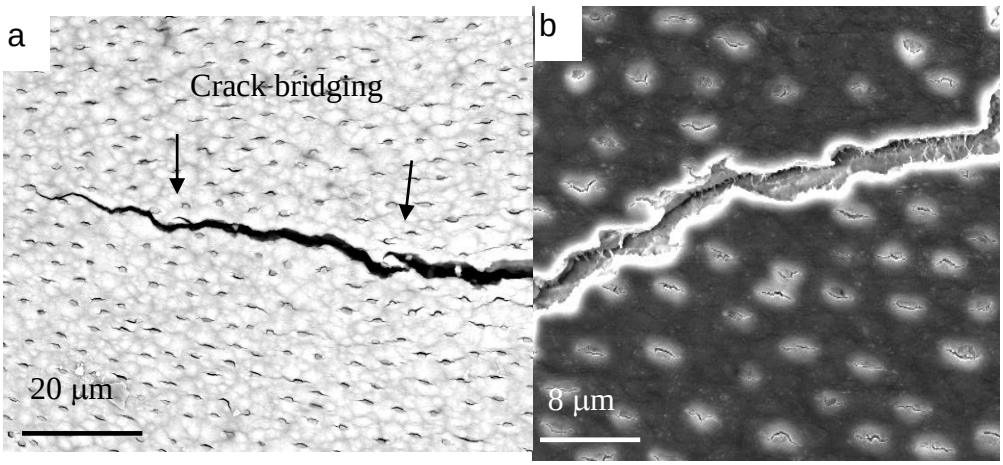

Fig. 7.2 SEM evidence of (a) uncracked-ligament crack bridging (back scatter electron) and (b) collagen bridging (secondary electron) in elephant dentin.

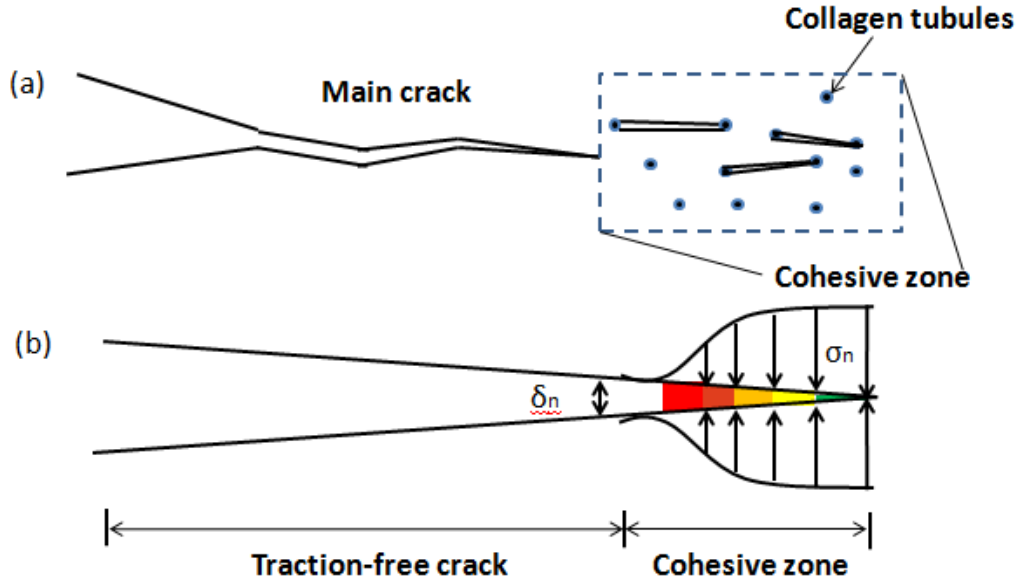

Fig. 7.3 Schematic showing (a) uncracked-ligament crack bridging initiation from the main crack formed by linking dentinal tubules; (b) idealized crack with a cohesive zone exerting crack-face traction to simulate the bridging effect. The traction σ_n varies along the crack direction as a function of the separation δ_n.

The cohesive zone model has become a popular tool for simulating the crack-tip toughening effect in the fracture process zone in the vicinity of the crack-tip for a variety of materials [29-37] especially those with an extensive damage zone, for example to describe aspects of shielding in bone as a function of age [31], its anisotropic fracture behaviour [38] and its R-curve response [13]. To the authors' knowledge, the cohesive model has not been applied to dentin materials. To date the cohesive law has normally been inferred from mechanical behaviours such as the load-displacement curve rather than exploring the cohesive law directly in terms of the behaviour of the crack. Here, for the first time, we infer a multi-linear constitutive cohesive law (traction-separation curve) based on optical in-situ measurements of the crack opening displacement (COD). The R-curve and crack-tip strain field predictions obtained from this model have been validated by the experimentally measured crack-tip strains obtained from digital image correlation (DIC).

7.2 Materials, Experimental Method and Setup

7.2.1 COD and Strain Measurement

The material used in this study was the dentin of African elephant (Loxodonta africana) ivory, which was obtained legally from the seizures of UK customs for scientific research. The experiment setup is shown in (Fig. 7.4a). A 10x optical microscope attached with a camera was placed above the test-piece. The test-piece was loaded with a Kammrath & Weiss microtester at the rate of 0.001 μm/s. Compact tension test-pieces (10×8×2 mm^3) were designed based on ASTM E1820 [39] (Fig. 7.4b). All of the test-pieces were pre-cracked with the crack length of a = 2.26 mm. In the finite element model of the sample, an array of the zero-thickness 4-node quadrilateral cohesive elements (mesh size 10 μm) were pre-embedded in front of the crack-tip (Fig. 7.4c).

In order to measure the COD, a binary image was produced where the crack body was characterized by intensity 1 and the rest (background) was assigned 0. In each column of the segmented image, the COD was calculated by summing up the foreground pixels vertically using Matlab. The COD at r = 45 μm behind the crack-tip was chosen as the reference data and was used to fit the cohesive model to.

The interrogation window size for the DIC strain measurement is 32×32 pixels, with 25% overlap, equal to a mesh size of 15 μm. The assessment of the instrument error (i.e. vibrations, exposure variation etc) was carried out by taking 2 reference images at an interval of 1 minutes, as a result of which, the average instrument error is 0.046 pixels, corresponding to 0.018 μm in displacement and 1330 μs strain error in strain measurement.

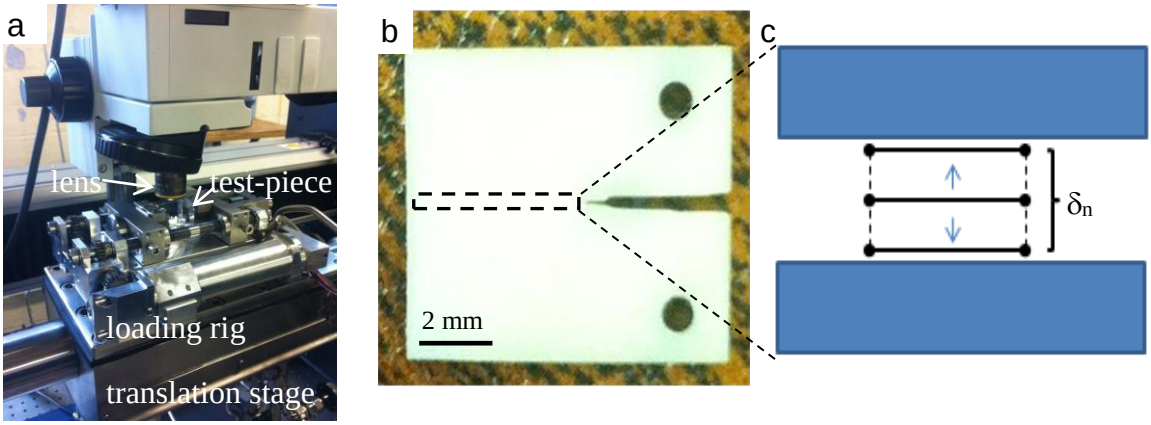

Fig. 7.4 (a) DIC experiment set-up. The whole loading stage was attached with a 10X magnification optical microscope to capture sequential images; (b) Compact tension test-piece used in the study; (c) schematic showing the 4-node bilinear quadrilateral elements.

7.2.2 Material elasticity assumptions

As is shown in Fig. 7.1g and h, the collagen fibrils are aligned perpendicular to the tubule axis. Previous work modelled dentin as an elasticity orthotropic symmetric material [40, 41], i.e. the elasticity in the collagen plane vertical to the tubule axis is isotropic. In the present study, elastic constants were calculated using Huo and Zheng's theory on the mechanical properties of dentin [42, 43] and they are listed as Table 7.1.

Table 7.1 Transverse isotropic properties of the elephant tusk used in the cohesive model

Name	E_p (GPa)	E_t(GPa)	ν_t	G_t(GPa)
value	12.8	8.7	0.3	7.7

7.3 Modelling technique

7.3.1 Multi-linear cohesive traction-separation law

A range of cohesive traction-separation shape functions [40-43] could be used to describe crack bridging. The specific shape of the cohesive zone model chosen will affect the numerical simulation of the fracture process [44]. In this paper, a multi-linear cohesive

law was proposed for the first time so as to accurately simulate the shielding effect at different stages of the cracking process (Fig. 7.5).

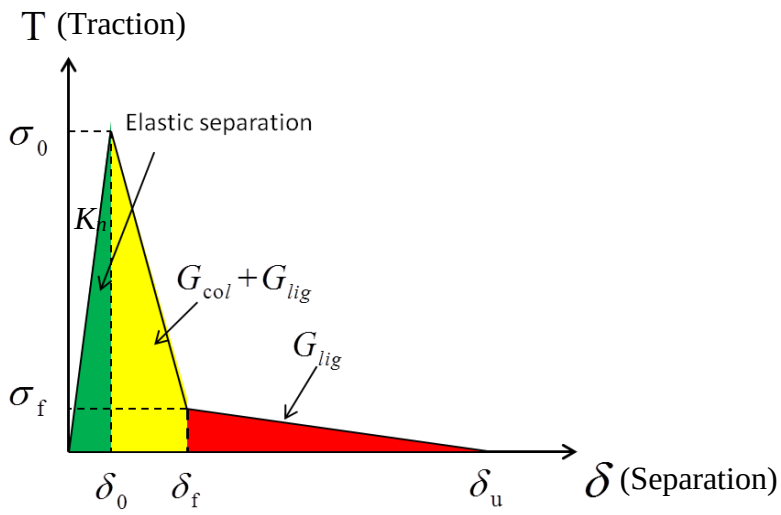

Fig. 7.5 Multi-linear cohesive law of the cohesive elements. Regions in three different colour stand for pre-damage loading (green), element softening loading (yellow + red). In the yellow region, the crack-tip is shielded by collagen and ligament bridging, whereas in red region, ligament bridging is the only working shielding mechanism.

In the first stage (green section), a linear elastic ascending process is assumed to model the uncracked material. Theoretically, this initial stiffness K_n (i.e. the gradient of the ascending line in green section) of this cohesive element should be as high as possible to simulate the original full constraint between adjacent elements. However, FE analyses encounter numerical problems if K is too large [13, 44, 45]. When the element is loaded to the material strength (σ_0), the cohesive element begins to soften as a function of the corresponding separation [46], which implies the onset of crack growth. In dentin, ligament bridging is more significant in crack-tip shielding since with the opening of cracks, the spanning collagen would break much earlier than the uncracked-ligament [28]. Accordingly, the degradation process is divided into two stages: collagen fibril + ligament bridging ($G_{lig+col}$) at low crack opening and ligament bridging (G_{lig}) at large opening. In the meantime, the strength of the cohesive elements decreases from σ_0 to 0 according to the cohesive law. Parameters δ_f and σ_f represent the separation and the crack face traction at the changing point, which indicate the transition as the crack bridging logaments fail. The cohesive element fails completely when the separation reaches δ_u. The fracture energy G_{total} equals to the whole area under the traction-separation curve,

$$G_{\text{total}} = G_{el} + G_{lig+col} + G_{lig} \tag{7.1}$$

It should be noted that this cohesive law is a phenomenological characterization of the physical process in the vicinity of the crack-tip, therefore it is difficult to clarify the proportion of these two shielding mechanisms [31]. Indeed, the cohesive law can be calibrated without any reference to, or knowledge of, the corresponding underlying mechanisms [13].

7.3.2 Tuning of cohesive law

The cohesive zone model was tuned so that the simulated COD matched with the experimentally measured COD variations as a function of load (Fig. 7.6) so as to capture: (1) the slope of the first approximately linear section (k_1); (2) the crack opening (δ_t) at which the slope of the COD curve changes; (3) the slope of the second linear section (k_2). The transition points on both of the curves indicate the initiation of the crack growth.

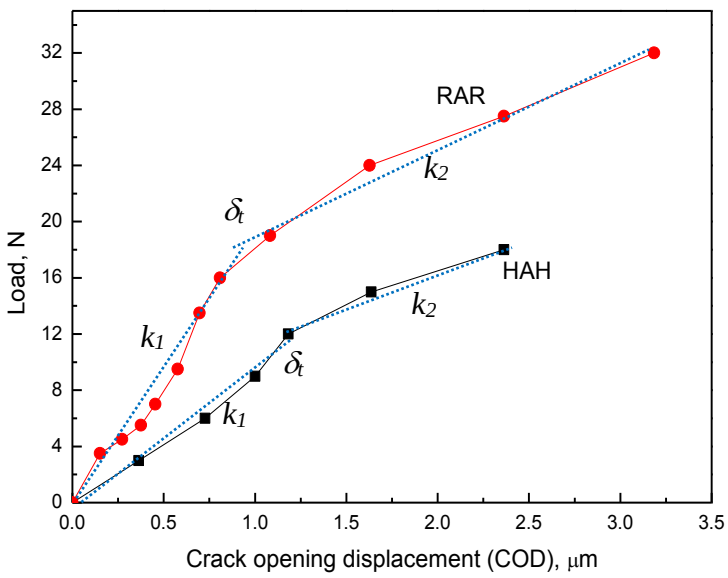

Fig. 7.6 The comparison of the COD obtained from the DIC displacement maps at r = 45 μm for both test-pieces. The two COD curves were fitted by blue dotted lines, which clearly demonstrate the bilinear gradient.

Since the bridging mechanisms are much more prominent for a crack grown in the RAR rather than HAH orientation based on previous experiment [47], the multi-linear and bilinear traction-separation laws were used for RAR and HAH respectively. The traction-

separation law was established by adapting the parameters (σ_0, σ_f, δ_0, δ_f, δ_u) and (σ_0, δ_0, δ_u) in the cohesive law to the COD data by trial and error procedures [13, 22].

The material strength measured for HAH and RAR are 40.1 ± 6.4 and 101.3 ± 11.1 *MPa* respectively, obtained from uniaxial tension experiments will be taken as σ_0. The fracture toughness of elephant tusk is quite anisotropic depending on the tubule orientation relative to the crack growth [1, 14, 48, 49]. The fracture toughness in this study for HAH and RAR are 0.77 $MPa\sqrt{m}$ and 0.93 $MPa\sqrt{m}$ respectively based on previous K_{IC} measurements at a = 2.26 mm made using DIC. The fracture toughness (K_{IC}) was then converted to G_{IC} using Eq. (7.2),

$$G_{IC} = \frac{K_{IC}^2}{E'} \tag{7.2}$$

7.3.3 Mesh sensitivity study

A mesh sensitivity study is quite necessary as the cohesive elements are known for their mesh dependent characteristics. In the present study, it is carried out by presenting the Load vs COD curve using different mesh sizes, i.e. different numbers of the cohesive elements on the way the crack propagates. Fig. 7.7 presents the COD variation with the increasing load under the same cohesive law but different mesh sizes. It is noticed that the curves overlap quite well corresponding to the mesh sizes smaller than 10 μm. However, the gradient of the curves become lower when the mesh size is larger than 20 μm. Moreover, the stability of the curve was reduced, as higher fluctuation at the end of the curve is noticeable. Accordingly, it is sensible to establish the model with a mesh size no larger than 10 μm.

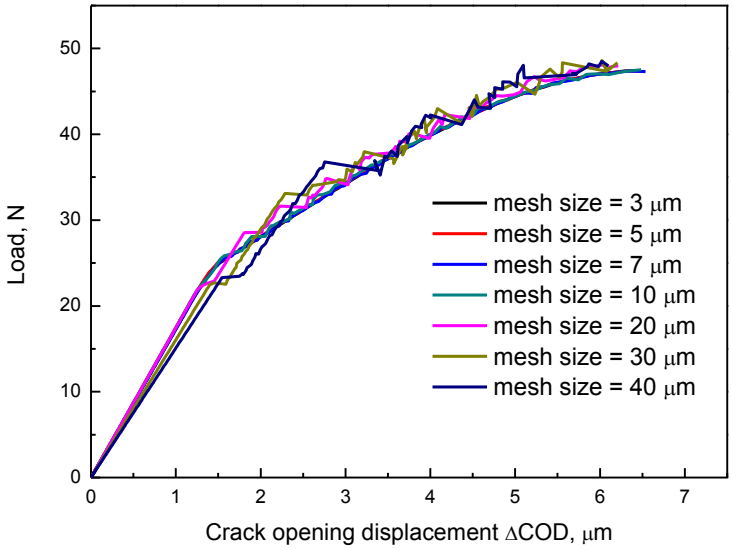

Fig. 7.7 Comparison of COD variations with the applied load using different mesh sizes and the same cohesive law

7.3.4 parametric study

The following procedure was used for the parametric study:

(1) Initial slope K_n. K_n stands for the initial stiffness of the cohesive element. It was found in Fig. 7.8a that the predicted gradient of the COD changes from 20.4 when K_n = 150 *GPa/mm* to 12.8 when K_n = 50 *GPa/mm*, which indicates a pronounced effect of K_n on the COD response. Moreover, the value of *K* changes the turning point of the curve as well: the turning point occurs at around 35 N when K_n = 100 *GPa/mm*, and decreases to 25 N when K_n = 150 *GPa/mm*. Despite the influence of K_n on the occurrence of the turning point, K_n was determined on the basis of fitting the initial slope of the COD response. This is in part because the turning point is controlled by other parameters as well, which will be discussed in the next part. In this study, K_n = 120 *GPa/mm* was chosen to give the best fit to k_1 for RAR and 100 *GPa/mm* for HAH.

(2) δ_f determines the transition between $G_{lig+col}$ and G_{lig} and so directly determines the extent of crack-tip shielding effect and how fast the damage will proceed. As is shown in Fig. 7.8b, δ_f has almost no influence on the initial slope of the COD response. However δ_f strongly influences the location of the turning point. From δ_f = 0.1 μm to 1.6 μm, the turning points changes gradually from 24.3 N to 45 N. δ_f = 0.23 μm was chosen here.

(3) σ_f represents the residual strength of the cohesive element at the transition turning point between the two damage stages. In Abaqus, the residual strength σ_f is represented in terms of a damage variable *SDEG* in Abaqus, which indicates the percentage of the strength loss during softening, ranging from *SDEG* = 0 (no damage, $\sigma_f = \sigma_0$) to *SDEG* = 1 (totally damaged $\sigma_f = 0$). Therefore, the residual strength at the separation δ_f could be calculated [50]. Fig. 7.8c illustrates the effect of varying σ_f on the *COD*-load curve. It could be concluded that all the curves have the same initial slope and turning point, the only difference being the gradient after the transition point: when σ_f = 90 *MPa* (*SDEG* = 0.1), the gradient is 0.064; when σ_f = 10 *MPa* (*SDEG* = 0.9), the gradient is 0.33. The best value of σ_f to match the experimental turning point is 20 *MPa*

(4) δ_u determines when the cohesive elements fail completely. Fig. 7.8d demonstrates that δ_u has no effect on the initial *COD* gradient, but a large influence on the gradient after the transition point. The gradient changes from 0.21 (δ_u = 1 μm) to 0.16 (δ_u = 9 μm), however, in comparison with σ_f, the influence of δ_u is negligible. The δ_u = 5.5 μm was used for this study for RAR and 2.97 μm for HAH.

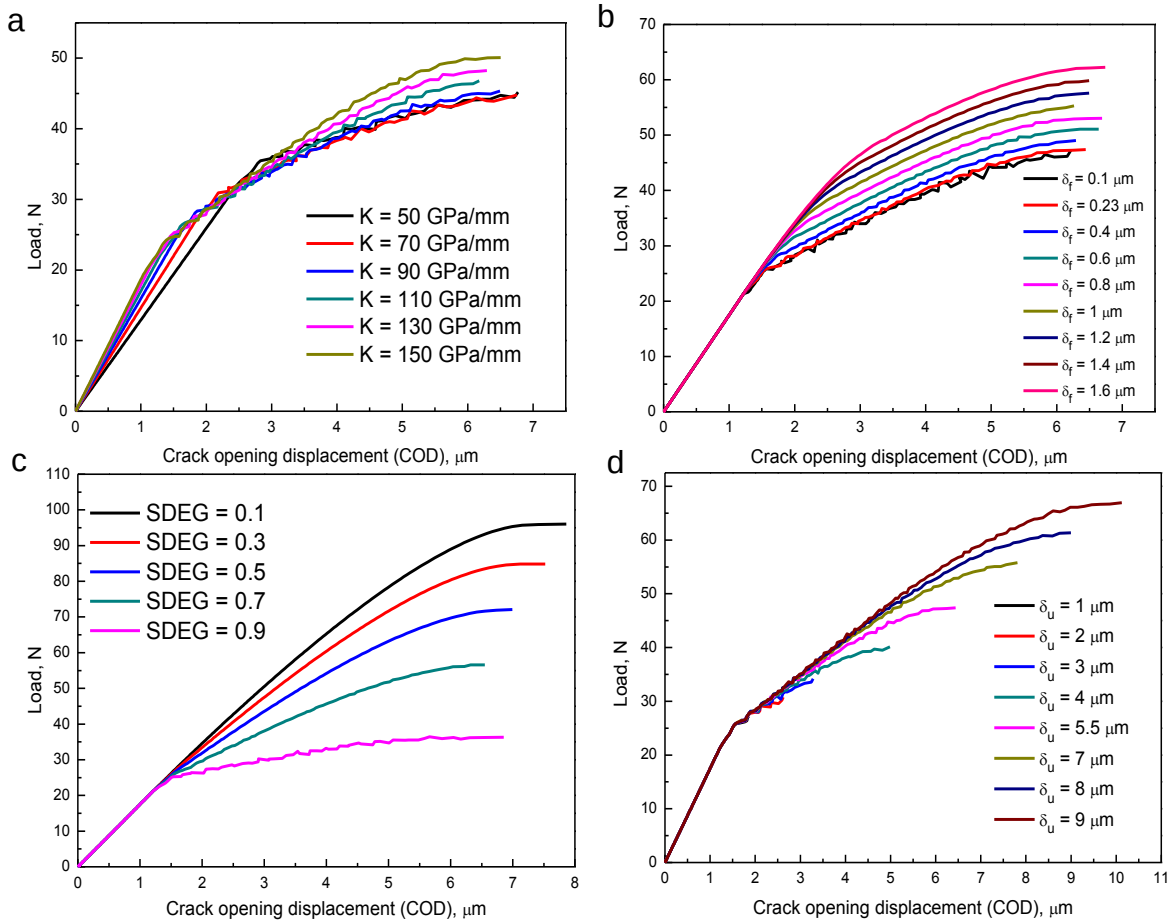

Fig. 7.8 The predicted effect on the COD response with load of varying the (a) initial stiffness K (b) δ_f (c) σ_f (d) δ_u.

The effect of each cohesive parameter on the COD response is summarized in Table 7.2. Accordingly-the optimal parameters for HAH and RAR are summarised in Table 7.3, and the fitting results are shown in Fig. 7.9, which presents a good fitting for both of the samples in terms of k_1, δ_t and k_2.

Table 7.2. Discussion of the cohesive parameters and their effect on the COD curve shape

	k_1	δ_t	k_2
Affected by K	High	Medium	No
Affected by δ_f	No	High	No
Affected by σ_f	No	No	High
Affected by δ_u	No	No	Low

Table 7.3. The cohesive parameters for HAH and RAR

Sample type	G_{total} (N/mm)	σ_0 (MPa)	K (GPa/mm)	δ_f (μm)	σ_f (MPa)	δ_u (μm)
HAH	0.059	40	100	N/A	N/A	2.97
RAR	0.066	100	120	0.23	20	5.5

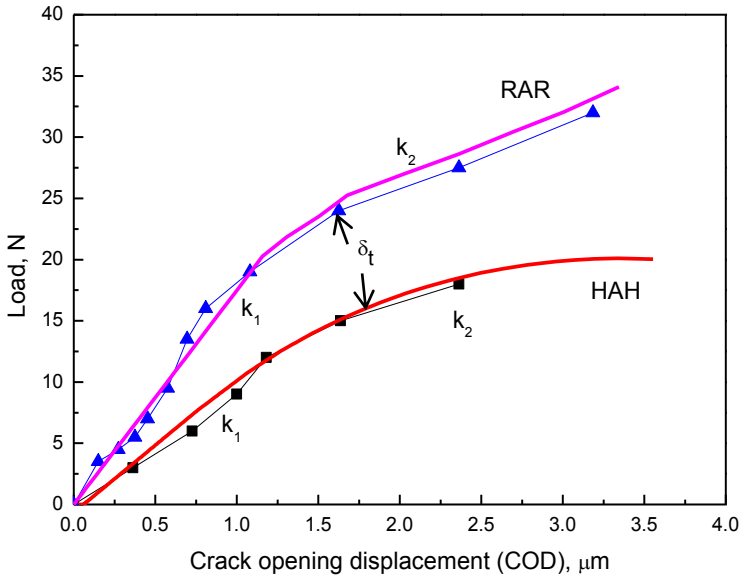

Fig. 7.9 The comparisons of the measured and the simulated COD responses obtained by tuning the cohesive model parameters iteratively for the HAH and RAR samples.

7.4 Result analysis

7.4.1 Bridging stress and energy

In order to understand crack-tip shielding from the cohesive elements bridging, Fig. 7.10 presents the distribution of the traction of the cohesive elements along the crack path at different crack extensions (e.g. Δa = 50, 100, 190, 310 μm etc) for HAH and RAR respectively. Regarding RAR, it is found that there was no element failure before Δa = 500 μm, evidenced by the non-zero traction. This indicates the cohesive element operating to bridge the crack was increasing with the extension of the crack. In contrast, the element started to fail at Δa = 320 μm for HAH. For both cases, with the crack further propagating,

it forms a balance state that the old cohesive element far away from the crack-tip failed in the mean time new cohesive elements ahead of the crack-tip start to bridge the crack. Moreover, the bridging lengths for both HAH and RAR test-pieces remain constant in balance state, which are approximate 400 and 320 μm. These values agree well with our previous observation under optical microscope [47, 51].

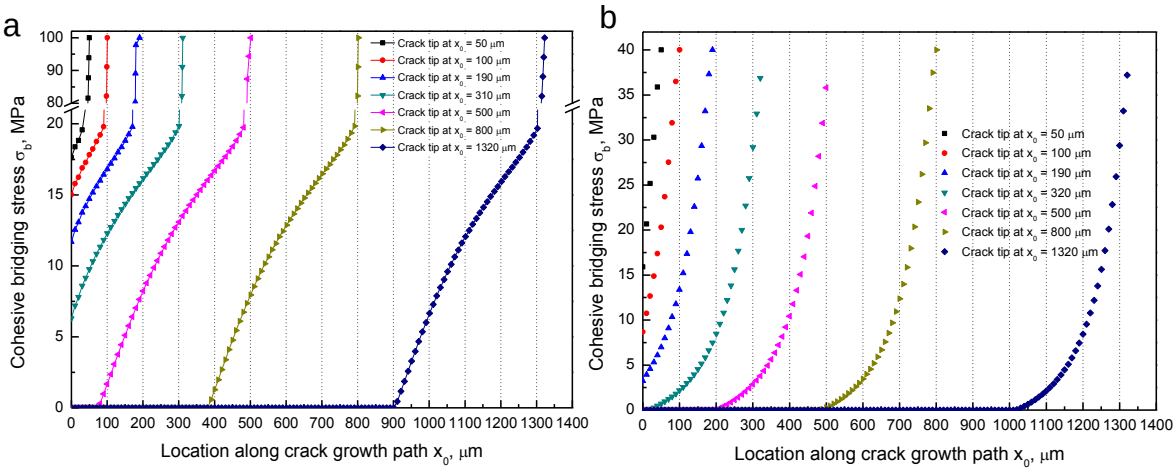

Fig. 7.10 The distribution of the traction of the cohesive elements along the crack path for (a) RAR and (b) HAH. cohesive stress at the wake of the crack as a function of crack-tip position for RAR and HAH respectively. The original crack-tip is at x_0= 0.

Subsequently, the energy dissipated due to damage of the cohesive elements and the dissipation rate at different crack extensions were plotted in Fig. 7.11. It is found that the maximum energy dissipated by element damage for RAR and HAH are 0.29 and 0.11 mJ respectively. The number of the bridging cohesive elements increases with the crack extension when $\Delta a < 400$ μm, afterwards it reaches a balance state that the pure increase of the dissipated energy from the element damage at each growth step remains constant.

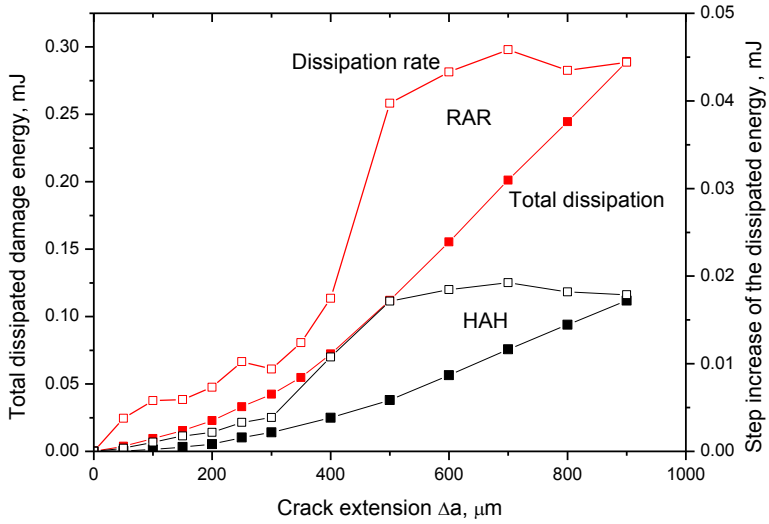

Fig. 7.11 The total dissipated damage energy of cohesive elements (solid) and increase of the dissipated energy (hollow) at each propagation length for RAR (red) and HAH (black).

7.4.2 Prediction of the R-curve response

The resistance-curve (R-curve) is a critical measure of the crack retarding effect during subcritical crack propagation (i.e. before unstable fracture occurs); The fracture toughness typically grows increasingly with the length of crack because of the activation of extrinsic toughening mechanisms [1, 16, 19-21]. This phenomenon is a particularly important toughening process and is common in natural biomaterials, e.g. teeth [1], bones [52] and tendons. Normally the fracture toughness R-curve is determined in terms of the crack-driving force (the stress intensity K) as a function of the crack extension (Δa), to quantify the increasing fracture resistance with crack length. Fig. 7.12 compares the measured sample and predicted R-curve for both samples. It is noticed that the predicted R-curve shows a reasonably good coincidence with the measured R-curve for both of the two samples. The predicted R-curve shows a distinctive turning point which splits the R-curve into two parts: in the first part fracture toughness increases drastically with the crack growth, which is caused by the increasing contribution of the bridging effect ahead of the mother crack-tip; in the second part the gradient of the R-curve reaches a plateau that implies the saturation of the bridging area and reaches a stable state, i.e. the crack bridging effects at the far end of the bridging zone (closest to the mother crack-tip) totally fail during the crack growth, and the new bridging components keep joining the bridging zone [1, 53, 54]. Tuning the cohesive model based on the COD data can effectively reflect the

physical process ahead of the crack-tip, not only on the test-piece used for setting up the model, but can be applied to the general cases as well.

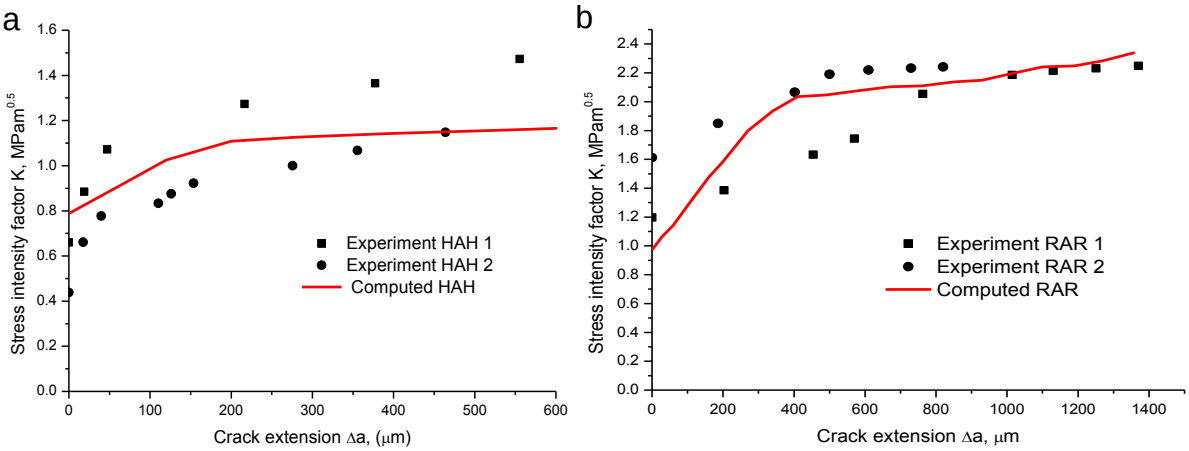

Fig. 7.12 The comparison of the measured and predicted R-curve for (a) HAH and (b) RAR respectively.

7.4.3 Prediction of the crack-tip strain field

Strain to failure is another measure characterising the fracture toughness in terms of the ability to dissipate strain energy [55]. In this section, the strain fields at the crack-tip under incremental loads are compared between DIC measurements and the simulation results from the cohesive model using the values determined above for both samples (see Fig. 7.13). The original size of the cohesive element used for the strain calculation is 1, defined when setting up the model, which means the separation of the cohesive element directly indicate the strain. This is different from the definition of the DIC measurement, which uses the central differential method to calculate the strain between the neighbouring grid. It is found that the crack-tip strain fields measured by DIC show semi-circle contours. In contrast, the strain contours from cohesive model simulations exhibit symmetrical lobe patterns (Fig. 7.13), which is a typical elastic strain pattern. RAR exhibits a much larger strain field than HAH, and the strain magnitude at the vicinity of the crack-tip in RAR reaches 0.78 %, whereas it is only 0.23 % in HAH.

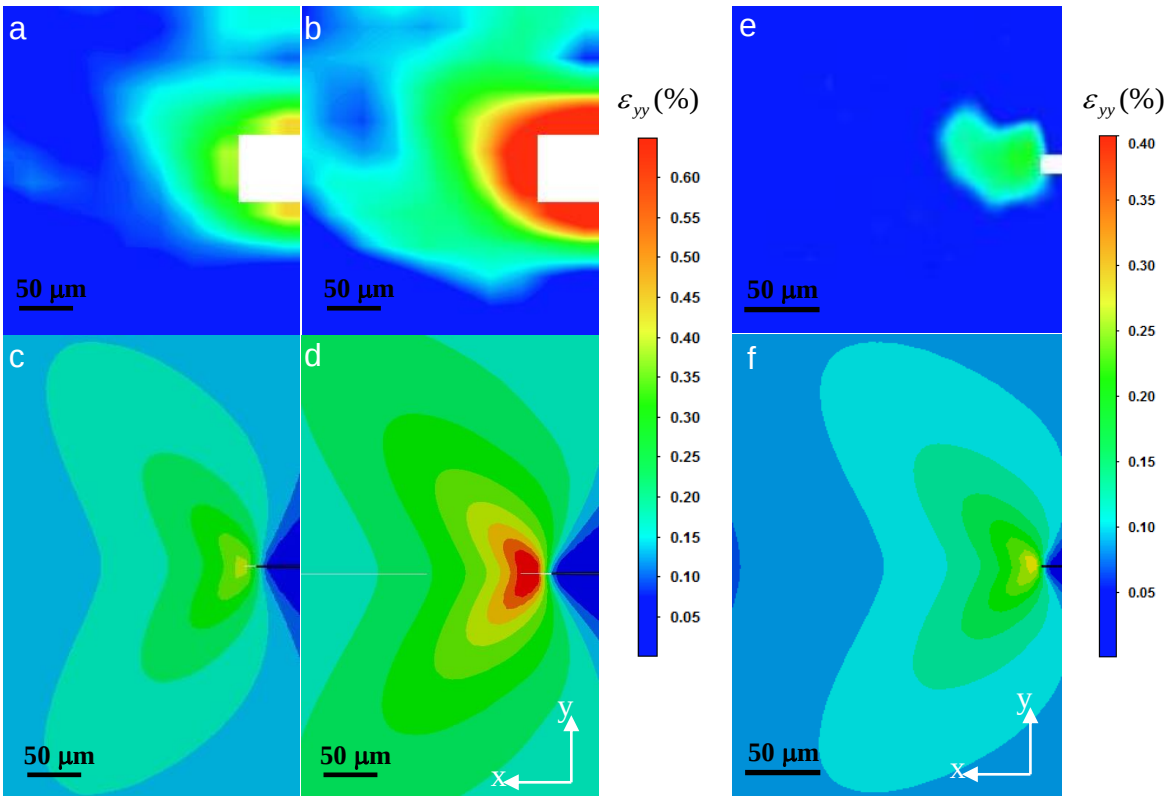

Fig. 7.13 Comparisons between the DIC strain at (a) 20 N and (b) 30 N with the simulated strain (c) 20 N and (d) 30 N for RAR. Similarly, the DIC strain and the simulated strain for HAH are shown in (e) and (f) respectively.

Fig. 7.14 plots the strain ε vs the distance d from the crack-tip (up to 90 μm) of both experimentally measurements and simulation results. The simulated strain curves match the experimental curves reasonably well for both of the samples at different loads. The DIC strain seems to be larger than the simulated curve at the vicinity of the crack-tip at 30 N, and this may result from the plastic strain at the crack-tip measured by DIC, though it is relatively small.

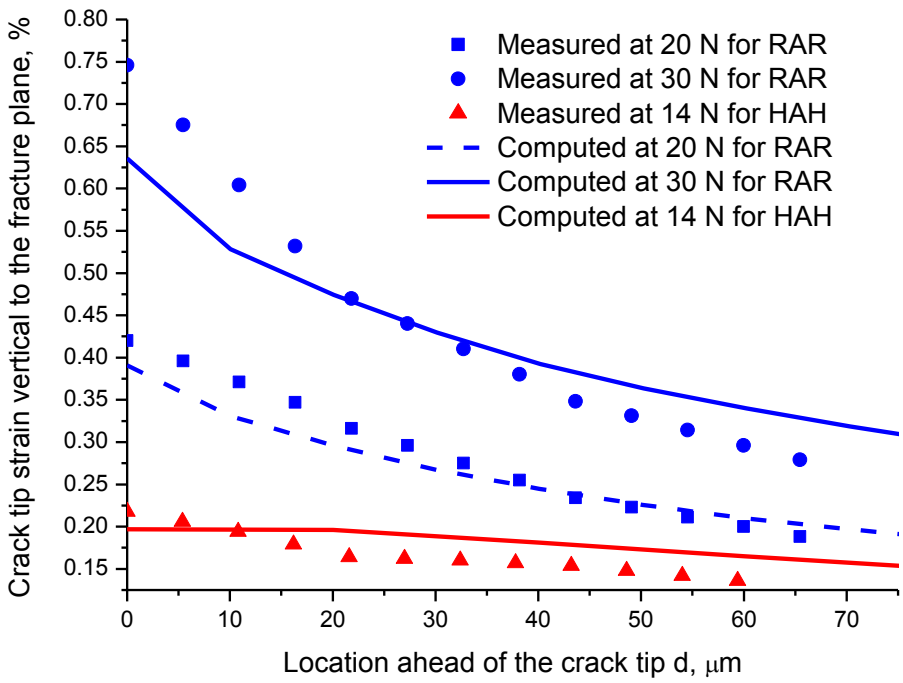

Fig. 7.14 The crack-tip strain comparisons of the measured and cohesive model for two kind of samples.

7.5 Discussion

The present work has demonstrated the feasibility of using a cohesive element equipped with a specific traction-separation law to model the physical process in the vicinity of the crack-tip and predict the crack growth resistance. Compared to the traditional cohesive zone methods, which establish the cohesive traction-separation law according to the load-displacement curve attained from mechanical test, using the measured COD is more practical and realistic since the cohesive parameters are determined directly from the behaviour of the cracks.

Among all the cohesive parameters which must be defined, the fracture energy G_{total} of cohesive elements, and the softening strength σ_0 were determined firstly. The cohesive energy G_{total} is assumed to be the fracture energy G_c released at the onset of the stable crack growth. The softening starts when the material reaches specified strength value (σ_0). Parametric method was then used to inspect the effect of each individual parameter on the COD curve. The COD curve and the dependent cohesive parameters are listed in Table 7.2. These parameters are considered to be representative for the fracture behaviour in dentin

since the cohesive model is a phenomenological characterization of the overall behaviour of the fracture process. It is necessary to specify K first since it solely determines k_1. Due to the difficulty in observing the transition between $G_{lig+col}$ and G_{lig} experimentally, δ_f can be specified based on the occurrence of the turning point δ_t, which indicates the crack initiation after cohesive element degradation. The physical crack growth observed microscopically favours the specification of the parameter δ_f. In this case, δ_f = 0.23 μm was chosen according the mechanical test which shows the crack growth occurred at 24 N. It is a coordination to determine the rest of the parameters based on the experimental COD curve and the total fracture energy.

For the multi-linear traction-separation law in RAR, the first degradation slope is much steeper than the second degradation stage since δ_u (5.5 μm) is far larger than δ_f (0.23 μm). This contributes to a fairly narrow bridging zone (10 μm) with the bridging stress larger than 80 *MPa*. The bridging stress curve of HAH is more gentle and smooth, but the bridging length is inferior to RAR (320 *vs* 400 μm), which could account for the anisotropic toughness of these two directions.

RAR test-piece has better ability than HAH (larger by 160 %) to dissipate the strain energy in terms of the damage of the cohesive element. In comparison with the experimental measurement of both samples, the successful prediction of the R-curve is convincing evidence of the feasibility to model the crack bridging effect behind the crack-tip. The turning point in RAR occurred later than HAH, which is caused by the larger critical separation (δ_u) of the cohesive elements sample. Also, δ_u is crucial to the size of the bridging zone. With a larger δ_u (5.5＞2.97 μm), RAR exhibited a larger bridging zone than HAH (400＞320 μm), and these values are in agreement with the transition point on R-curve.

The difference of the strain pattern between DIC and modelled samples may come from the fact that DIC measures the complex strain at the crack-tip, and the strain contour is determined by a range of factors, e.g. surface texture density [56], gauge volume [57], strain magnitude , ratio of elastic/plastic component. In contrast, the model only considered the elastic strain since the plastic zone is ignorable compared to the crack length and sample size. The strain *vs* distance from crack-tip shows a reasonably good match between measured and modelled strain. The mismatch between the measured and the computed strain at 30 N for RAR may result from the plastic deformation at the crack-tip in the DIC measurement.

7.6 Conclusions

1. It is feasible to simulate the physical process in the vicinity of the crack-tip using cohesive model to fit the experimentally measured COD curve. The modelled COD could fit well with the experimental one by choosing the appropriate parameter K, δ_f, σ_f (*SDEG*) respectively. Large δ_u reflected a large bridging zone, and contributed to a much more smooth bridging stress distribution at the wake of the crack, and led to a delay of the occurrence of the plateau on the R-curve.

2. The bridging length for HAH and RAR test-piece were approximate 300 and 400 μm respectively, which agreed well with the previous optical observations. The energy dissipated by cohesive element damage was 0.28 mJ for RAR, which is 163 % larger than HAH. The bridging energy remains constant after the saturation of the operating cohesive elements behind the crack-tip. Modelled R-curve exhibited the similar results with the experiment ones, which proved the ability of the cohesive model to simulate the bridging process.

3. The crack-tip strain fields obtained by cohesive model were different with the DIC strain fields in the aspect of the strain contour pattern: the modelled strain fields appear as typical symmetrical lobe pattern but the experimental measured samples were semi-circular. However, the strain gradient and magnitude obtained by the modelling were identical with the experimental ones.

References

[1] Kruzic J, Nalla RK, Kinney JH, Ritchie RO. Crack blunting, crack bridging and resistance-curve fracture mechanics in dentin: effect of hydration. Biomaterials 2003;24:5209-21.
[2] Locke M. Structure of ivory. J Morphol 2008;269:423-50.
[3] Nalla RK, Imbeni V, Kinney JH, Staninec M, Marshall SJ, Ritchie RO. In vitro fatigue behavior of human dentin with implications for life prediction. Journal of Biomedical Materials Research Part A 2003;66A:10-20.
[4] Moyes AB, Doidge DW. COMPOSITION OF THE MINERAL PHASE OF DENTIN IN SOUTHERN ELEPHANT SEAL AND ANTARCTIC FUR-SEAL TEETH. British Antarctic Survey Bulletin 1984:81-4.
[5] Povar ML. Miles,Aew - Structural and Chemical Organization of Teeth. J Am Vet Med Assoc 1967;151:1211-&.
[6] Miles AEW, Boyde A. Observations on Structure of Elephant Ivory. J Anat 1961;95:450-&.
[7] Raubenheimer EJ, Dauth J, Dreyer MJ, Smith PD, Turner ML. Structure and Composition of Ivory of the African Elephant (Loxodonta-Africana). S Afr J Sci 1990;86:192-3.
[8] Marshall GW, Inai N, Magidi ICW, Ballouch M, Kinney JH, Tagami J, et al. Dentin demineralisation: effects of dentin depth, pH and different acids (vol 13, pg 338, 1997). Dental Materials 1998;14:383-.
[9] Robert Gallegos, 2012. Maintain Dentin Bond Strength Over Time. Daily Digest;http://www.speareducation.com/spear-review/tag/dentin/page/3/.
[10] Feng Z, Rho J, Han S, Ziv I. Orientation and loading condition dependence of fracture toughness in cortical bone. Materials Science and Engineering: C 2000;11:41-6.
[11] Norman TL, Nivargikar SV, Burr DB. Resistance to crack growth in human cortical bone is greater in shear than in tension. Journal of biomechanics 1996;29:1023-31.
[12] Yeni Y, Norman T. Fracture toughness of human femoral neck: effect of microstructure, composition, and age. Bone 2000;26:499-504.
[13] Yang Q, Cox BN, Nalla RK, Ritchie R. Fracture length scales in human cortical bone: the necessity of nonlinear fracture models. Biomaterials 2006;27:2095-113.
[14] Nalla RK, Kinney JH, Ritchie RO. Effect of orientation on the in vitro fracture toughness of dentin: the role of toughening mechanisms. Biomaterials 2003;24:3955-68.
[15] Arola D, Reprogel RK. Effects of aging on the mechanical behavior of human dentin. Biomaterials 2005;26:4051-61.
[16] Koester KJ, Ager Iii JW, Ritchie RO. The effect of aging on crack-growth resistance and toughening mechanisms in human dentin. Biomaterials 2008;29:1318-28.
[17] Nalla RK, Kruzic JJ, Ritchie RO. On the origin of the toughness of mineralized tissue: microcracking or crack bridging? Bone 2004;34:790-8.
[18] Ritchie R. Mechanisms of fatigue crack propagation in metals, ceramics and composites: role of crack tip shielding. Materials Science and Engineering: A 1988;103:15-28.
[19] Nalla RK, Kruzic JJ, Kinney JH, Ritchie RO. Mechanistic aspects of fracture and R-curve behavior in human cortical bone. Biomaterials 2005;26:217-31.
[20] Malik C, Stover S, Martin R, Gibeling J. Equine cortical bone exhibits rising R-curve fracture mechanics. Journal of biomechanics 2003;36:191-8.
[21] Vashishth D, Behiri J, Bonfield W. Crack growth resistance in cortical bone: concept of microcrack toughening. Journal of Biomechanics 1997;30:763-9.
[22] Nazari A, Bajaj D, Zhang D, Arola D. A Hybrid Evaluation of Toughening in Human Dentin. 2009.

[23] Bao G, Suo Z. Remarks on crack-bridging concepts. Applied Mechanics Re 1992.
[24] Cox B, Lo C. Load ratio, notch, and scale effects for bridged cracks in fibrous composites. Acta metallurgica et materialia 1992;40:69-80.
[25] Cox BN. Extrinsic factors in the mechanics of bridged cracks. Acta metallurgica et materialia 1991;39:1189-201.
[26] Withers PJ. 3D Crack-tip Microscopy: Illuminating Micro-Scale Effects on Crack-Tip Behavior. Advanced Engineering Materials 2011;13:1096-100.
[27] Ritchie RO. Mechanisms of fatigue-crack propagation in ductile and brittle solids. International Journal of Fracture 1999;100:55-83.
[28] Ritchie RO. Mechanisms of Fatigue Crack-Propagation in Metals, Ceramics and Composites - Role of Crack Tip Shielding. Mat Sci Eng a-Struct 1988;103:15-28.
[29] Jin Z-H, Sun C. Cohesive zone modeling of interface fracture in elastic bi-materials. Engineering fracture mechanics 2005;72:1805-17.
[30] Gálvez J, Planas J, Sancho J, Reyes E, Cendón D, Casati M. An embedded cohesive crack model for finite element analysis of quasi-brittle materials. Engineering fracture mechanics 2012.
[31] Ural A, Vashishth D. Cohesive finite element modeling of age-related toughness loss in human cortical bone. Journal of Biomechanics 2006;39:2974-82.
[32] Su X, Yang Z, Liu G. Finite Element Modelling of Complex 3D Static and Dynamic Crack Propagation by Embedding Cohesive Elements in Abaqus. Acta Mechanica Solida Sinica 2010;23:271-82.
[33] Campilho R, De Moura M, Domingues J. Using a cohesive damage model to predict the tensile behaviour of CFRP single-strap repairs. International Journal of Solids and Structures 2008;45:1497-512.
[34] De Moura M, Campilho R, Goncalves J. Mixed-Mode Cohesive Damage Model Applied to the Simulation of the Mechanical Behaviour of Laminated Composite Adhesive Joints. Journal of Adhesion Science and Technology 2009;23:1477-91.
[35] Ren W, Yang Z, Sharma R, Zhang C, Withers PJ. Two-dimensional X-ray CT image based meso-scale fracture modelling of concrete. Engineering Fracture Mechanics 2015;133:24-39.
[36] Ren W, Yang Z, Withers P. Meso-scale fracture modelling of concrete based on X-ray computed tomography images. The 5th Asia-Pacific congress on computational mechanics (APCOM) Singapore2013.
[37] Guinea G, Planas J, Elices M. A general bilinear fit for the softening curve of concrete. Materials and Structures 1994;27:99-105.
[38] Ural A, Vashishth D. Anisotropy of age-related toughness loss in human cortical bone: A finite element study. Journal of biomechanics 2007;40:1606-14.
[39] E1820-08a A. Standard Test Method for Measurement of Fracture Toughness. American Society for Testing and Materials (ASTM) International, West Conshohocken, PA, USA 2008.
[40] Kinney J, Balooch M, Marshall G, Marshall S. A micromechanics model of the elastic properties of human dentine. Arch Oral Biol 1999;44:813-22.
[41] Aversa R, Apicella D, Perillo L, Sorrentino R, Zarone F, Ferrari M, et al. Non-linear elastic three-dimensional finite element analysis on the effect of endocrown material rigidity on alveolar bone remodeling process. Dent Mater 2009;25:678-90.
[42] Huo B, Zheng QS. Effect of dentin tubules on the mechanical properties of dentin. Part I: Stress-strain relations and strength criterion. Acta Mechanica Sinica 1999;15:355-65.
[43] Huo B, Zheng QS. Effect of dentin tubules on the mechanical properties of dentin - part III: Numerical, analysis. Acta Mechanica Sinica 2002;18:629-37.
[44] Yang Q, Cox B. Cohesive models for damage evolution in laminated composites. International Journal of Fracture 2005;133:107-37.

[45] Cornec A, Scheider I, Schwalbe K-H. On the practical application of the cohesive model. Eng Fract Mech 2003;70:1963-87.
[46] Yang Z, Su X, Chen J, Liu G. Monte Carlo simulation of complex cohesive fracture in random heterogeneous quasi-brittle materials. International Journal of Solids and Structures 2009;46:3222-34.
[47] Lu X, Walsh JN, Withers PJ. Anisotropic fracture toughness in elephant dentin associated with large crack deflection. Acta Biomaterialia 2015;ready for submission.
[48] Arola DD, Reprogel RK. Tubule orientation and the fatigue strength of human dentin. Biomaterials 2006;27:2131-40.
[49] Craig RG, Peyton FA. Elastic and mechanical properties of human dentin. Journal of dental research 1958;37:710-8.
[50] ABAQUS. ABAQUS 6.10 Online Documentation. Internet Manual 2010.
[51] Lu X, Withers PJ. Mapping elastic/plastic crack-tip strain fields in dentin. Biomaterials 2015;Ready for submission.
[52] Koester KJ, Barth HD, Ritchie RO. Effect of aging on the transverse toughness of human cortical bone: Evaluation by R-curves. Journal of the Mechanical Behavior of Biomedical Materials 2011;4:1504-13.
[53] Kanninen M. Advanced Fracture Mechanics. Oxford University Press 1985.
[54] Raddatz O, Schneider GA, Claussen N. Modelling of R-curve behaviour in ceramic/metal composites. Acta Materialia 1998;46:6381-95.
[55] Lopez-Crespo P, Withers P, Yates J, Steuwer A, Buslaps T, Tai Y. Study of overload effects in bainitic steel by synchrotron X-ray diffraction. Fracture and Structural Integrity 2013:Pages 153-60.
[56] Tschopp M, Bartha B, Porter W, Murray P, Fairchild S. Microstructure-dependent local strain behavior in polycrystals through in-situ scanning electron microscope tensile experiments. Metallurgical and Materials Transactions A 2009;40:2363-8.
[57] Sztefek P, Vanleene M, Olsson R, Collinson R, Pitsillides AA, Shefelbine S. Using digital image correlation to determine bone surface strains during loading and after adaptation of the mouse tibia. Journal of biomechanics 2010;43:599-605.

Chapter 8

Conclusions and Future Work

8.1 Conclusions

This study aims to characterise the anisotropic fracture toughness and crack-tip shielding mechanisms in three types of test-pieces having different crack growth directions relative to the microstructures. Crack growth resistance curves (R-curve) were measured and coupled with the corresponding microstructures. The crack-tip accumulative strain fields have been characterised for the first time using digital image correlation (DIC) techniques under both hydrated and dehydrated conditions, based on which the critical deformation and plastic zones were identified. Moreover, the effective stress intensities K_{eff} were extracted by fitting the crack-tip displacement field obtained by DIC with analytical model so as to understand the effectiveness of crack-tip shielding by comparing K_{eff} to K_{appl}. In-situ crack opening displacement (COD) measurement by 2-D (optical) and 3-D (time-lapse X-ray tomography) techniques provided an alternative way to assess the shielding effect, which was also clearly and correspondingly visualised from crack morphologies, crack-microstructure interaction, fracture topography. The physical process of crack-tip shielding was simulated using cohesive model to predict the R-curve and crack-tip strain, and were in good agreement with the experiment results.

Elephant dentin exhibited anisotropic fracture toughness in three different cracking directions. All of the three types of test-pieces HAH (crack path in hoop-radial plane, grow in hoop direction), RAR (crack path in hoop-radial plane, grow in radial direction), HRH (crack path in hoop-axial plane, grow in hoop direction) exhibited rising R-curve behaviours. HRH presented highest initiation fracture toughness Ks (2.35 $\pm$ 0.23 $MPa\sqrt{m}$) and failure fracture toughness K_C (2.94 $\pm$ 0.13 $MPa\sqrt{m}$), which were 45 % and 33 %

tougher than that in RAR test-piece and 200 % and 100 % tougher than HAH test-piece. Large angle deflection (70 ~ 90°) was so extensive for crack growing in HRH, incurring a mix-mode (type I + type II) crack-tip stress. A clear transition from rising stage and balance stage on the R-curve was shown for RAR test-piece only, and the measured bridging distance (0.4 mm) coincided well with the R-curve behaviour in terms of the entrance of the balance stage.

The critical strain fields for cracking around the crack-tip of these three types of test-piece were different. HRH test-piece demonstrated the largest crack-tip strain (4.2 %), which was 27 % larger than RAR and 250 % larger than HAH. In hydrated condition, the critical strain at the crack-tip could rose up to 200 % as large as the dehydrated test-piece for all the test-pieces. Moreover, RAR exhibited plastic zones of 78 μm at K_{app} = 0.65 $MPa\sqrt{m}$ and 107 μm at K_{app} = 0.83 $MPa\sqrt{m}$ in the hydrated condition, which was significantly larger than that in the dehydrated condition (10 μm at K_{app} = 0.65 $MPa\sqrt{m}$ and 84 μm at K = 1.17 $MPa\sqrt{m}$). Whereas the plastic strains for HAH were insignificant compared to the crack length. The discrepancies of the plastic zone indicated a larger driving force that RAR could accommodate before cracking. And this difference comes from the alignment of the collagen fibrils relative to the crack plane: as the fibrils are vertical to the crack path (RAR), in hydrated condition, dentin has better capability to accommodate deformation in terms of intra-fibrillar plasticity, coming from the mineral/collagen sliding, and this is often called intrinsic shielding. Hydrated collagen improved the efficiency of intrinsic shielding mechanisms by ~ 100 %, in terms of larger crack-tip elastic/plastic strain, crack-tip blunting and higher $\Delta K_{IC}/\Delta a$ rate, compared with the dehydrated test-piece. A reduction in moisture content could actually result in the decrease in the strain to fracture.

The yielding strength of both the hydrated and dehydrated test-pieces were inferred here using stress balance method. The yielding strength for hydrated RAR test-piece was 54 *MPa*, coincided with the reported values very well (50 ~ 65 *MPa* [1]), but the dehydrated yield strength was 40% higher [2]. Young's modulus of the dehydrated and hydrated elephant dentin inferred here were 13.8 *GPa* and 6.0 *GPa* respectively, using elastic strain comparison method. The dehydrated value was in good agreement with those found by other researchers (12 ~ 17 *GPa* [1, 2] for the dehydrated and 6.5 ~ 10.2 *GPa* [3] [4] for the hydrated dentin).

Extrinsic mechanisms were then identified using multiple characterisation methods. The crack closure effects were observed from 2-D crack morphologies. The crack-tip extrinsic shielding effect for RAR test-piece mainly resulted from uncracked-ligament bridging, which arose from the interaction between the main crack and the tubule patterns. Large angle deflection contributed mostly to the high fracture toughness for HRH test-piece, along with crack-tip meandering and micro-crack induced bridging. No obvious extrinsic shielding was noticed in HAH test-piece. The 20% difference at low load between the applied load K_{app} and effective stress intensity factor K_{eff} extracted from 2-D COD evidenced extrinsic crack-tip shielding for RAR test-piece. 3-D COD measurement from X-ray tomography experiment delineated non-uniform COD throughout the crack plane. Where there was efficient uncracked-ligament bridging, the COD was much smaller.

It is feasible to simulate the physical process in the vicinity of the crack tip using cohesive model to fit the experimentally measured COD curve. The modelled COD curve coincided well with the experimental curve in terms of the gradients and the turning point. The computed R-curve presented high similarity with the experimentally measured ones in terms of the gradients of the first linear stage and the stable plateau at balance state as well. The crack-tip strain computed by cohesive model coincides well with the measured one by DIC. The bridging length predicted for RAR was 400 μm, which agreed well with the previous optical observations, but the for HAH, it was larger than the measured value (300 μm vs 60 μm). This difference mainly comes from the difficulty defining the point of complete failure of the bridging ligament when measured optically. The energy dissipated by cohesive element damage was 0.28 *mJ* for RAR, which is 163 % larger than HAH. The bridging energy remains constant after the saturation of the operating cohesive elements behind the crack-tip. All of these validate that it is effective to simulate the physical process of the crack-tip shielding by establishing the cohesive traction-separation law according to the COD measurement.

What have been founded in present study is reasonably linked with the functions of the human teeth and elephant tusk. The different types of human teeth, e.g. incisors, canines, and molars, and elephant tusk primarily work to grasp, crush and cut the food with their sharp thin edges, as a result, significant forces normal to the biting plane are generated. Teeth are unavoidably subjected to flexure and radial shear stresses. This means high toughness in hoop-radial plane (HRH) and axial-radial plane (RAR) are most crucial to remain the structure and mechanical integrity of the teeth during functional operation. The

high fracture toughness and cracking strain in these two cracking plane is directly determined by the inter-woven collagen fibrils in hoop-axial plane (intrinsic shielding) and crack bridging (extrinsic shielding).

8.2 Future Work

The interaction between crack and the microstructure is the lynchpin to understand the anisotropic fracture behaviour and shielding mechanisms. Despite the ultra high resolution, 2-D imaging techniques have the limitations to observe the crack behaviour underneath the surface. It is essential to utilise non-destructive X-ray computed tomography to inspect the interaction between the crack and the microstructure in 3-D. Present work has accomplished the in-situ crack growth observation at the resolution of 0.7 μm, however, considering the diameter of the tubules (~ 2 μm), it is still challenging to visualise the tubules morphologies and provide the insights into crack shielding. Thus, higher resolution system is demanding.

Based on the previous work, the extent of the plastic zone has been measured. Further work can be done in terms of investigating how the plastic zone affects the crack-growth rate under fatigue loading, which is significant in this project since repetition damage can cause the fracture of the teeth without awareness. The hydration extent of the collagen can also be evaluated using thermal method.

Xradia 810 Ultra X-ray system equipped with advanced optics enables phase contrast scan at the resolution of 60 nm, which is ideal to resolve the crack and tubules at the same time. Time-lapse crack growth experiment could be designed (e.g. indentation) for test-pieces having different orientations relative to the tubules. By doing this, the information such as preferential crack growth direction, crack growth rate, crack and tubules interfaces can be extracted. This would make a complete multi-scale story explaining the crack growth mechanisms in elephant dentin, together with the micro-CT and high resolution 2-D imaging techniques.

Apart from the 3-D crack growth inspection, it is also worthwhile measuring the crack-tip strain in 3-D using digital volume correlation (DVC) technique. The tubules patterns would provided with ideal contrast to correlate the deformation between each loading step. This experiment would be significant to find out the if there is any anisotropic crack-tip

strain for different types of test-pieces, which would be a meaningful complement to the 2-D DIC work.

References

[1] Nalla RK, Kinney JH, Ritchie RO. Effect of orientation on the in vitro fracture toughness of dentin: the role of toughening mechanisms. Biomaterials 2003;24:3955-68.
[2] Kruzic J, Nalla RK, Kinney JH, Ritchie RO. Crack blunting, crack bridging and resistance-curve fracture mechanics in dentin: effect of hydration. Biomaterials 2003;24:5209-21.
[3] Guidoni G, Denkmayr J, Schöberl T, Jäger I. Nanoindentation in teeth: influence of experimental conditions on local mechanical properties. Philosophical Magazine 2006;86:5705-14.
[4] Huang TG, Schilder H, Nathanson D. Effects of moisture content and endodontic treatment on some mechanical properties of human dentin. Journal of Endodontics 1992;18:209-15.